Microstructure and Fatigue Properties of Railway Steels for Switches and Crossings

Dhar, Somrita

Publication date:
2019

Document Version
Publisher's PDF, also known as Version of record

Technical University of Denmark DTU

Microstructure and Fatigue Properties of Railway Steels for Switches and Crossings

PhD Thesis

SOMRITA DHAR

Department of Wind Energy

Technical University of Denmark

Dedicated to the loving memory of my mom, Sumana Dhar

Abstract

Switches and crossings (S&Cs) are an integral part of any rail network, allowing for necessary flexibility of directing trains from one track to another at junctions. They are also the most vulnerable part of the network due to the complex shape and the severity of the loading on them. During service, they undergo rolling contact fatigue, normal and shear stresses as well as impact loads leading to damage and severe deterioration of the mechanical properties of the steel. Therefore the choice of railway steel is very important to control material degradation and damage for safety and reliability. Understanding the damage and deformation mechanisms of the steels used for crossings, including plastic deformation, crack formation and propagation, are important in order to prevent failure. The main focus of this thesis is to study the mechanical and microstructural properties of manganese steel used in railway crossings. Worn S&C components extracted from the track were studied through extensive metallographic examinations, including optical microscopy, electron microscopy and micro-hardness profiles. X-ray tomography was used for three-dimensional mapping of fatigue crack networks within the S&Cs. The gradient in the residual stress profile from the rail wheel contact surface to different depths from the surface was analyzed using synchrotron as well as laboratory X-ray diffraction. Uniaxial, pure torsion and biaxial (in phase and out of phase) low cycle fatigue tests were performed to study the behavior of manganese steel, as well as head hardened pearlitic steel at different strain amplitudes to do a comparative analysis of their properties and deformation mechanisms under well controlled laboratory conditions. The deformed microstructures after fatigue tests were studied by transmission electron microscopy (TEM).

The hardening and the deformation of the manganese steel are quite different from that of commonly used pearlitic rail steels, but the crack morphologies were found to be quite similar. The investigations from the worn crossings revealed that the crack propagation in manganese steel crossing nose is predominately transgranular with the cracks mostly following a path free from twins through relatively soft grains. The residual stress measurements revealed significant compressive stresses on the running surface of the nose of a manganese steel crossing, but the presence of cracks reduces the residual stress significantly to around one-fifth of the original value. Large residual strains were also obtained at depths of 15 mm from the running surface. Mechanical tests of pearlitic and manganese steel showed significant differences in the cyclic response of the two materials, where hardening was prominent in case of manganese steel, the pearlitic steel showed cyclic softening. The mechanical test data correlate well with the deformation micrographs obtained by TEM. For manganese steel, under uniaxial loading dislocation cell structure formation is observed but when the shear mode is introduced in the biaxial fatigue test, formation and growth of stacking faults along with dislocation controls the mechanical properties. For pearlitic steel, the dislocation morphologies are similar under all conditions; the change in mechanical properties is thus due to differences in density of dislocations.

Abstrakt

Sporskifter er en integreret del af ethvert jernbanenetværk da de giver den nødvendige fleksibilitet så togene kan skifte fra et spor til andet ved disse krydsninger. De er også den mest udsatte del af jernbanenetværket på grund af deres komplicerede form og de store belastninger som de bliver udsat for. Under brug udsættes sporskifter for rolling contact fatigue, normalspændinger og forskydningsspændinger såvel som slagbelastninger der kan lede til skader og forværring af de mekaniske egenskaber af stålet. Derfor er valget af stål typen meget vigtigt for sikker og pålidelig drift af jernbanenettet. Ligeledes er forståelse af skades og deformations mekanismer i de stål der bliver brugt til sporskifter, inklusiv plastisk deformation, revnedannelse og revnevækst, helt nødvendige. Denne afhandling fokuserer på studier af de mekaniske og mikrostrukturelle egenskaber af manganstål brugt i sporskifter. Brugte sporskiftekomponenter, skåret ud af det Fynske jernbanenet,er karakteriseret ved hjælp afmetallografiske undersøgelser, inklusiv optisk mikroskopi, elektron mikroskopi og mikro-hårdhedsmålinger. Røntgen tomografi er blevet brugt til tre-dimensional kortlægning af udmattelsesrevnenetværker. Restspændinger, både nær overfladen og i dybden er karakteriseret ved hjælp af laboratorie og synkrotron røntgen diffraktion.. Endelig er der lavet kontrollerede laboratorie forsøg til bestemmelse af de mekaniske egenskaber af både mangan stål og pearlitisk stål, under betingelser der er typiske for normal jernbanedrift. En-aksial, vridning og bi-aksial (i fase og ud af fase) lavcyklus udmattelsestest er blevet foretaget ved forskellige tøjningsamplituder for at lave en komparativ analyse af de to materialers egenskaber og deformationsmekanismer. Den deformerede mikrostruktur efter udmattelsestestene blev studeret med transmissions elektron mikroskopi (TEM).

Hærdning og deformation af manganstål er ret forskelligt fra det normalt brugte perlitiske skinnestål, men revnemorfologien blev fundet at være ret ens for dem begge. Undersøgelserne af de slidte sporskifter viste at revneudbredelsen for manganstålssporskifter hovedsagligt går igennem kornene hvor revnen for det meste følger en retning som ikke indeholder tvillinger men går igennem relativt bløde områder i kornene. Restspændingsmålingerne viste signifikante kompressive spændinger på køreoverfladen af et manganståls sporskifte, mens dannelsen af revner reducerer restspændingerne signifikant til omkring en femtedel af den originale værdi. Store restspændinger blev også fundet ved dybder på 15 mm fra køreoverfladen. Mekaniske test af perlitisk og mangan stål viste signifikante forskelle i den cykliske respons af de to materialer, hvor hærdning var prominent for manganstål, mens det perlitiske stålblev blødere ved cyklisk deformation. De mekaniske test data er i god overensstemmelse med deformationsmikrostrukturenobserveret med TEM. For manganstålet, giveren-aksial belastninger en dislokationscellestruktur, men når forskydningsretninger bliver introduceret i bi-aksiale udmattelsestest, er det formation og vækst af stabelfejl der sammen med dislokationer kontrollerer de mekaniske egenskaber. For perlitiske stål er dislokationsmorfologien den samme i alle de undersøgte tilfælde; ændringen i mekaniske egenskaber er her grundet forskellige dislokationstætheder.

Keywords: Switches and crossings (S&Cs), residual stress, synchrotron X-ray diffraction, 3D X-ray tomography, low cycle fatigue(LCF), multiaxial fatigue, TEM, EBSD, rolling contact fatigue (RCF), twinning, 2D & 3D crack network, stacking faults, dislocations, manganese steel.

Preface

The thesis is based on the research carried out at the Department of Wind Energy at Technical University of Denmark under the supervision of Senior Researcher Hilmar Danielsen and Professor Dorte Juul Jensen during the period December 2015 to January 2019. The project has been funded by Innovation Fund Denmark through the project “INTELLISWITCH – Intelligent Quality Assessment of Railway Switches and Crossings” (Grant no 4109-00003B). Part of the work has been funded by Interreg ESS & MAX IV: Cross Border Science and Society (Project number DTU-009). The experimental work presented in this thesis has been performed at Department of Wind Energy and Department of Mechanical Engineering at Technical University of Denmark, Department of Industrial and Materials Science at Chalmers University of Technology, and Argonne National Laboratory in USA. The Danish rail network company Banedanmark is a collaborative partner in this project.

This thesis consists of an introductory part followed by the appended papers and additional results:

Paper 1: Crack formation within a Hadfield manganese steel crossing nose

S. Dhar, H. K. Danielsen, S. Fæster, C. Rasmussen, Y. Zhang and D. Juul Jensen

Submitted for publication in Wear

My supervisors and I together formulated the concepts, framework, and design of the paper. The experiments, data collection and analysis, and interpretation of the results were done by me. Søren Fæster and Yubin Zhang helped with some experiments. The article was written by me and revised by co-authors.

Paper 2: 2D and 3D characterization of rolling contact fatigue cracks in a manganese steel crossing wing rails

S. Dhar, H. K. Danielsen, S. Fæster, C. Rasmussen and D. Juul Jensen

Submitted for publication in Wear

My supervisors and I together formulated the concepts, framework, and design of the paper. The experiments, data collection and analysis, and interpretation of the results were done by me. Søren Fæster helped with one experiment. The article was written by me and revised by co-authors.

Paper 3: Synchrotron X-ray measurement of residual strain within the nose of a worn manganese steel railway crossing

S. Dhar, Y. Zhang, R. Xu, H.K. Danielsen and D. Juul Jensen

IOP Conf. Series: Materials Science and Engineering 219 (2017) 012016 doi:10.1088/1757-899X/219/1/012016

My supervisors and I together formulated the concepts, framework, and design of the paper. The experiments, data collection and analysis, and interpretation of the results were done by me. Yubin Zhang helped with experiment and data analysis. The article was written by me and revised by co-authors.

Paper 4: Synchrotron and laboratory X-ray measurements of residual strains in manganese steel from a railway crossing

S. Dhar, H. K. Danielsen, R. Xu, Y. Zhang, C. Rasmussen and D. Juul Jensen

To be submitted for international publication

My supervisors and I together formulated the concepts, framework, and design of the paper. The experiments, data collection and analysis, and interpretation of the results were done by me. Yubin Zhang helped with synchrotron experiment and data analysis. The article was written by me and revised by co-authors.

Paper 5: Multi-axial Fatigue Deformation of Head Hardened Pearlitic and Austenitic Manganese railway steels: A comparative study

S. Dhar, J. Ahlstrom, X. Zhang, H.K. Danielsen, and D. Juul Jensen

To be submitted for international publication

My supervisors, Johan Ahlstrom and I together formulated the concepts, framework, and design of the paper. The experiments, data collection and analysis, and interpretation of the results were done by me. Johan Ahlstrom and Xiaodan Zhang helped with some experiments. The article was written by me. Reviews from other co-authors were also incorporated.

Acknowledgments

It’s a great pleasure to thank the many people whose help made this thesis possible.

First, I would like to thank my supervisors, Senior Researcher Hilmar Danielsen and Professor Dorte Juul Jensen who gave me this opportunity to work on this exciting project. I gratefully acknowledge their continuous support, patience encouragement, scientific inputs and valuable feedback throughout the project. My sincere thanks to senior researchers: Søren Fæster, Yubin Zhang and Xiaodan Zhang who has helped me with many of my experimental work, data analysis and scientific suggestions on my articles. I am sincerely grateful to Professor Johan Ahlstrom for helping with my work and other things during my external stay at Chalmers University of Technology. I highly appreciate his valuable insight, suggestions and scientific feedback on the work during my external stay. Special thanks to Carsten Rasmussen from Banedanmark for his practical understandings and insight about railways and its problems.

I would like to thank physicist Ruqing Xu at Argonne National Laboratory, USA and development engineer Steffen Rasmussen at Denmark Technical University for their help in some experiments. Special thanks to the very skillful technicians Flemming Grumsen, Lars Lorentzen, Gitte Christiansen, and Preben Olsen, without their help, this thesis would not have been possible.

I would like to express my deepest gratitude to my parents who have been a constant source of inspiration, encouragement, and support for me.

I would also like to thank my colleagues at work for their support and great environment at work and also to my friends who was there always to encourage and inspire me at every stage of my life.

Table of Contents

1. Introduction

Railways are one of the oldest forms of transport which date back to the 16th century. The rails were made of woods and hauled by horses in the early days. The development of steam locomotives in the 19th century marked the beginning of modern rail transport. At that time and in the following years, the rails were made of wrought iron. However, the soft rails often had slag defects and failed quickly. Upon the advent of steel making processes iron was replaced with steel with better mechanical properties, longer lifetime and reduced cost thus becoming the standard for all railways. Modern technological advancements have increased the efficiency of the rail network. Steam engines are now replaced by diesel driven and electric locomotives. High speed trains have been introduced in many countries worldwide. Railways are often considered as faster and one of the safest compared to other modes of transport. According to literature, the number of fatalities in railway transport is substantially less compared to those occurring on roads [1-2]. Recent studies suggest transportation accounts for 25% of global environmental pollution. According to 2010 International Transport Forum on Greenhouse Gas Emissions, railways only account for 2% transport emission compared to 73% from road transport, 11% from domestic and international aviation and rest from other means of transport, making railways one of the environment conscious forms of transportation [3]. The latest white paper on transport from the European Union suggests that railways are the key to obtaining a sustainable multi-modal interoperable transport network [4]. Therefore it is important to maintain the reliability, efficiency, and safety of railway systems and a lot of research has been undertaken worldwide to improve the environment, safety and economic aspects of the railway system.

Switches and Crossings(S&Cs) are an integral part of any railway network. They enable trains to be directed from one track onto another at railway junctions providing the necessary flexibility during train operations. The complex geometry and moving parts of S&Cs, however, makes them quite vulnerable to damage due to high stress and impact loading. Poorly maintained S&Cs have a detrimental impact on railway operations. Recent incident of S&C failure in the Danish rail network includes derailment of a freight train in Southern Jutland during the winter of 2012 which caused disruption of traffic to Germany. A significant portion (estimated 50%) of the maintenance budget of the Danish rail network is spent on the repair and renewal of S&Cs [5].

The work carried out in this thesis is a part of the INTELLISWITCH project which deals with intelligent quality assessment of railway S&Cs. The project is in collaboration between the Technical University of Denmark (DTU) and the Danish rail infrastructure provider Rail Net Denmark and is funded by INNOVATION FUND, Denmark. The INTELLISWITCH project aims to improve the fault prediction techniques used for detecting damages and defects in S&Cs by providing sophisticated tools to detect hidden faults before they can cause failure [5]. This will help in optimization of maintenance procedures thus avoiding unscheduled repairs and delays in the railway traffic. The main objectives of the INTELLISWITCH project include developing a model by which the condition of individual S&Cs can be assessed. This will be done by combining the inputs from measuring cars, data from the sensors installed at S&Cs selected for this project, metallurgical investigation of damaged components and also from dynamic modeling of wheel rail interaction and study of material behavior. The model will produce one or more maintenance performance indicator(s) by which appropriate maintenance can be predicted in advance. The project is aiming at having significant impact on the maintenance procedures and renewal of railway infrastructure [5].The present PhD thesis deals with the metallurgical investigation of the damaged components and study of their materials behavior.

S&Cs fail due to many reasons, but the rail components most commonly fail due to impact and rolling contact fatigue. Generally, fatigue failure starts with crack initiation and repeated transient loading causing crack propagation and finally failure of the component. Repeated loading also causes wear of the surface of the rails leading to material loss. Progression of rolling contact fatigue and wear creates degradation of the rail profile and redistribution of contact stresses, elevated noise, and vibration levels and further continuation of damage can cause catastrophic failures. Identification of possible failure modes will help to identify the most critical components and the likely failure mechanisms. Therefore, a better insight into material selection for S&Cs along with understanding their degradation and damage behavior through detailed metallurgical investigation may contribute to the development of optimal maintenance schemes and have a significant future impact on railway operations. A contribution to this large field is the overarching objective of the present thesis work.

1.1 Research Objective and Scope of Work

To focus the project, it was decided together with Banedanmark to concentrate the work on the crossing nose since it is the most critical component in the S&C from a maintenance point of view. It was further decided to divide the project into two fundamentally different parts: Part I- Metallurgical Investigation of crossing noses which have been in operation for many years and Part II- Mechanical Testing of steels typically used for crossing noses. The work focuses on the fatigue properties and microstructural changes associated with damage in crossing steels with the aim of investigating the damage mechanisms for obtaining better failure predictions. Straight railway tracks used in Denmark are produced from standard pearlitic grade steels, however, the crossing noses are made from a head hardened pearlitic steel variant or the austenitic manganese steel, often called Hadfield steel. Therefore these two materials are investigated.

A crossing component is subject to normal, rolling as well as impact stresses during operation. Since the crossing components are subjected to a different load state than normal tracks, and the materials microstructures are different, different damage mechanisms are also expected. While there is a large quantity of investigations done on pearlitic steels in standard tracks [6-13], the information on S&C and crossing steels is very limited. The literature studies on crossings mostly deal with modelling and simulation [14-18].

Thus the main aim of this thesis is to investigate the microstructure and fatigue properties in head hardened pearlitic and austenitic manganese steels using novel experiments and characterization techniques in order to understand the damage and degradation mechanism of the most critical S&C component. Using specimens extracted from crossings which have been in service as well as laboratory testing of crossing materials, the focus has been on three topics: crack propagation, residual stress and fatigue properties.

Crack propagation: Understanding of the damage and deformation of the steels used for crossings including plastic deformation, crack formation and propagation are important in order to develop maintenance performance models. Only few studies deal with manganese steel crossings extracted from networks and those studies focus mostly with *local* microstructure changes and crack initiation [19-22]. The objective of this work is to investigate the crack morphology for larger volumes in crossing components extracted from the rail network, and to compare it to the damage progression in normal pearlitic rails from straight track. Failed crossings extracted from the track have been studied through

extensive metallographic examinations, including optical microscopy, electron microscopy and micro-hardness profiles, where the damage was correlated to the deformation and associated microstructural changes. To study the complete morphology of the developed crack network, 3D X-ray computerized tomography was used for the first time for three-dimensional mapping of fatigue crack networks as well as other defects in the individual components of the crossings.

Residual stress: Apart from external loads, due to the rail wheel contact, the damage and deformation of any engineering component is also dependent on residual stresses present within the material. Residual stresses can be present due to manufacturing and may also develop during service. Compressive residual stresses are beneficial to counteract crack growth while tensile residual stresses have the opposite effect. The combination of applied stress together with the residual stress influences further deformation and cracking. Measurements on residual stresses have mostly been carried out on normal track pearlitic rail steels [23-26], while manganese steel crossings have only been investigated through simulations [27]. Understanding the residual stress state in a crossing component extracted from service is needed when the goal is to understand the failure mechanism. The objective of this part of the work is to investigate the magnitude and distribution of the residual stresses within a crossing nose which has been in service. Conventional laboratory X-ray diffraction is used to determine the macro stresses and, as something new, this work includes differential aperture synchrotron X-ray diffraction to evaluate the potentials of this method to determine local micro strain inside the crossing.

Fatigue properties: Cyclic loading induces large strains in the surface layers of rails due to low cycle fatigue, from where cracks initiate. The overall resistance to fatigue crack growth depends on the strength, ductility and work hardening properties of the material. Previous laboratory scale fatigue tests on manganese steels have mostly focused on uniaxial loading [28-29] rather than complex multiaxial loading. The latter is assumed to be a better model for the real in-track situation. The objective of this part of the work is to perform a comparative study of the mechanical performance for two different crossing steels under different loading conditions (uniaxial and biaxial), as well as to investigate the microstructural changes associated with it. Uniaxial and biaxial (in phase and out of phase) low cycle fatigue tests were performed at different strain amplitudes to understand the materials behavior. Microstructural analysis of the fatigue deformed material involving optical microscopy and transmission electron microscopy is performed and related to the mechanical properties to analyze the deformation mechanisms. The present work presents the first results of biaxial testing of crossing manganese steels and all together, the results contribute to the understanding of the suitability of these two steels as crossing material under different loading conditions as well as to predict fatigue damage.

1.2 Background

1.2.1 Switches and Crossings(S&Cs)

In 1832, Sir Charles Fox designed the first S&C which has been modified over the course of time. A railway S&C is also referred to as a turnout. The typical parts of a railway S&C are described in Figure 1.1 and Figure 1.2.

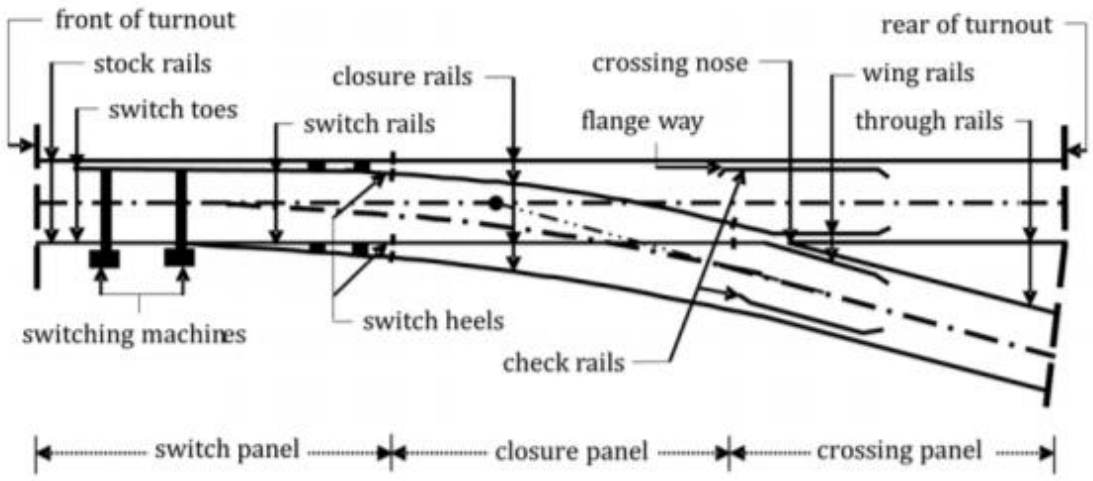

Figure 1.1: Schematic diagram of an S&C with its components [18].

The typical parts of an S&C are:

(a) Switch panel: The switch panel consists of two fixed fully profiled stock rails and two movable rails called switch rails. The movable rails guide the wheels towards either the straight or the diverging track. They are tapered on most switches. The switching function is operated by switching machines or actuators that position the switch rails according to the desired traffic direction [18]. The switch rails are of the flexible type and are milled from dedicated switch rail specimens with a lower height and a thicker and asymmetrical rail foot compared to standard rails. The steel used for switch blades and stock rails are mostly pearlitic steel. The position of switch rail decides the direction of traffic as can be seen in Figure 1.3 below. In Figure 1.3a it can be observed that the switch rails are positioned to the top, in contact with the top stock rail to catch the wheel flange, while the bottom switch rail is positioned away from the bottom stock rail to allow wheels to pass through on the stock rail. This causes the train to move through the diverging track. In Figure 1.3b the situation is reverse with the bottom switch rail in contact with the bottom stock rail while the top switch rail is maintained away from the top stock rail to allow the wheels to keep continuing on the top stock rail. This position of the switch blades causes the train to move towards the straight track. The common defects within the switch panel are broken stretcher bars, switch anchor losing, broken bolts etc.

(b) Closure panel: The closure panel is the section between the switch panel and the crossing panel. It consists of the closure rails for guiding the wheel sets into the crossing panel. This part is made of ordinary pearlitic steel as used in normal tracks.

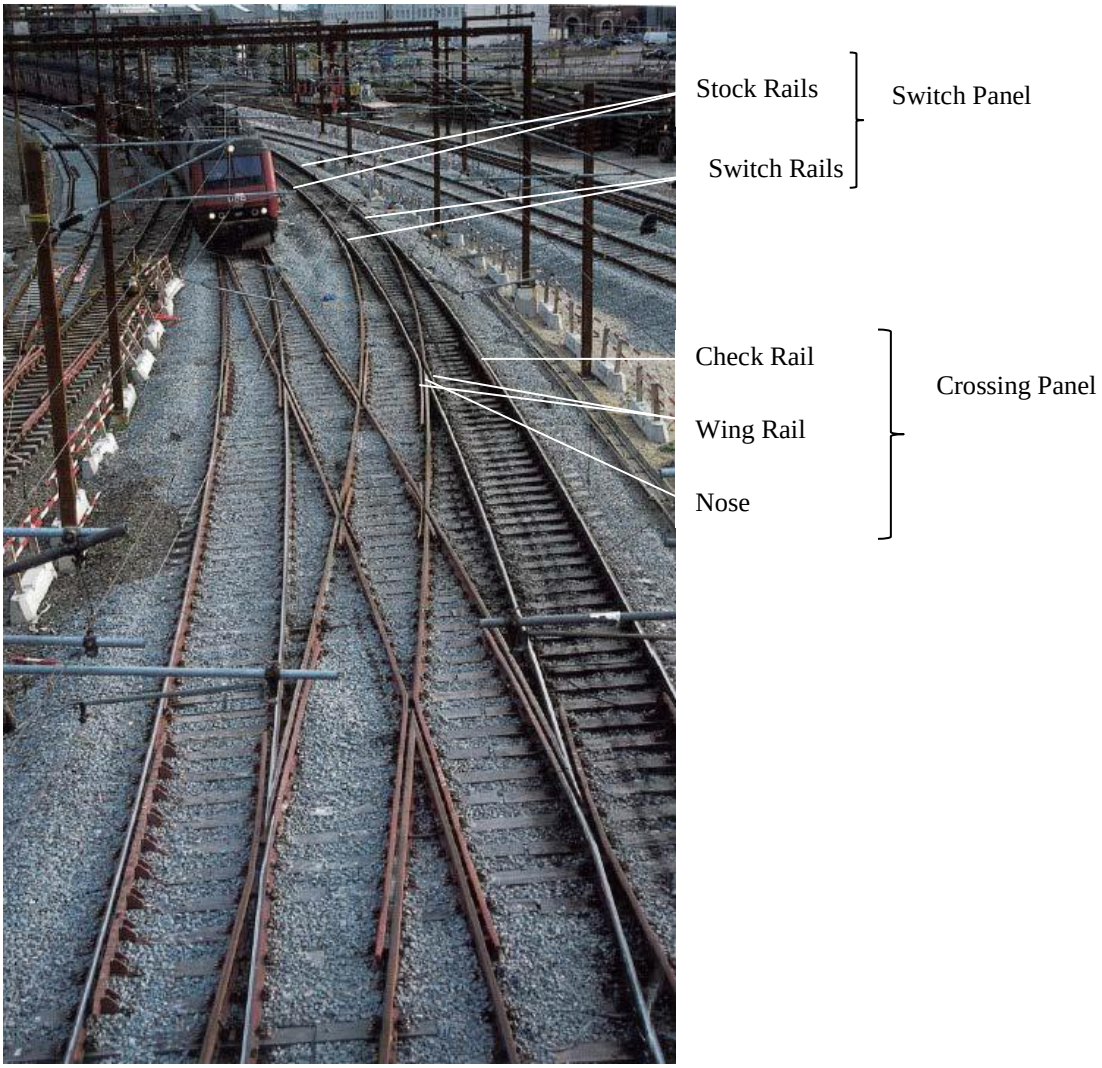

Figure 1.2: Rail network near Copenhagen Central Station showing the components of S&Cs [5].

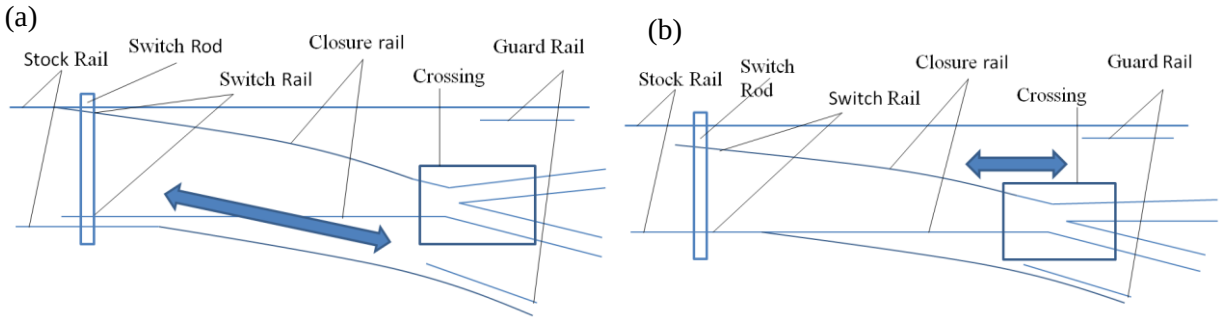

Figure 1.3: Schematic diagram of a railway S&C showing the position of switch rails when the train moves in the (a) diverging track and (b) straight track.

(c) Crossing panel: A crossing panel consists of through rail, check rail or guard rail, wing rail, and a nose, see Figure 1.1. It allows trains to travel along both directions. The crossing or the V-shaped portion of the panel is the crossing point of two rails. It consists of a nose and two wing rails. The three different parts are either assembled by bolts

(pearlite crossing) or casted together (manganese crossing). Crossings can either be fixed type (the ones investigated in this study) or movable typically used when high axle loads or high speed are required. Check rails or guard rails are present on either side of the crossings parallel to the stock rails. The check rails constraint the lateral movements of the train wheels. S&Cs are very intricate components of the rail network as it contains variations and discontinuities which results in increased dynamic loading and thus increased degradation of these components compared to straight track. Irrespective of the direction of traffic (diverging or straight track), either the wheel will pass from the nose to the wing rail or from the wing rail to the nose in the crossing area. The discontinuity between the wing rail and nose causes impact loading and damage to the components. The common failures experienced in the crossing rails are wear, rolling contact fatigue, plastic deformation, rail head cracks, rail foot fractures, rail web cracks etc. The investigations in this study focus on the nose and wing rails of the crossing.

1.2.2 Damage due to rail wheel contact

Tracks are subjected to variable loading depending on the axle load and the speed of the trains passing. In addition to this, the geometry of S&Cs causes very different service conditions that are also dependent on the direction of traffic. If the direction of traffic is towards the nose, the nose generally undergoes contact friction and impact stresses from the wheels while the wing rail mostly experiences rolling contact stresses and wear deformations in this situation [22] and vice versa if the direction of traffic is towards the wing. In addition, the horizontal stresses on the crossing further increase the adverse effect on it. Numerical calculations suggest stress and strain analyses are key to understanding and predicting wear and fatigue behavior of contacting and impacting systems like the crossing and the wheel of trains. The contact forces between the wheel and the nose range from two to four times that of the static wheel load [30], and in some cases, due to the poor quality of track and wheel, the stresses can be even five times higher than the static load [31]. Since crossings are subjected to impact loadings, the vertical contact forces during the impact of the wheel on the crossing nose generally increase with higher running velocities of the train, thus it is necessary to control the train speed while passing through the crossing. The maximum von Mises stress and maximum equivalent plastic strain in the crossing are very sensitive to train speed and axle load and they increase linearly with an increase in speed or load [32-33]. The von Mises stress calculations also indicate that manganese crossings deform more plastically whereas harder steel resists plastic deformation [34]. High loads on the crossings cause damage leading to rolling contact fatigue, wear, and cracks.

Rolling Contact Fatigue (RCF)

Rolling Contact Fatigue (RCF) is an important concern for today's railway industry where increased traffic, acceleration and loads impose serious safety and economic risks. It occurs due to repeated passage of wheels over the rails which lead to application of loads along with rolling contact between the materials. The catastrophic derailment at Hatfield on the East Coast Main Line in October 2000 is a classic example of rail failure due to RCF initiated cracks. The variation of loading condition results in difference in the contact patch of the rail and wheel and leads to various types of defects in the rails as shown in Figure 1.4 [35]. In Figure 1.4a, vertical loading causes the growth of surface and subsurface cracks within the contact zone. Figure 1.4b demonstrates surface crack initiation due to both vertical and lateral loading. Figure 1.4c shows the formation of subsurface initiated RCF cracks due to vertical loading of a rolling object. Plastic deformation of the contact surface leads to crack initiation and growth if the rolling contact is

accompanied by interfacial shear and slip (Figure 1.4d). Material defects and inhomogeneities which can cause surface irregularities can also lead to surface cracking under such loading (Figure 1.4e) [35].

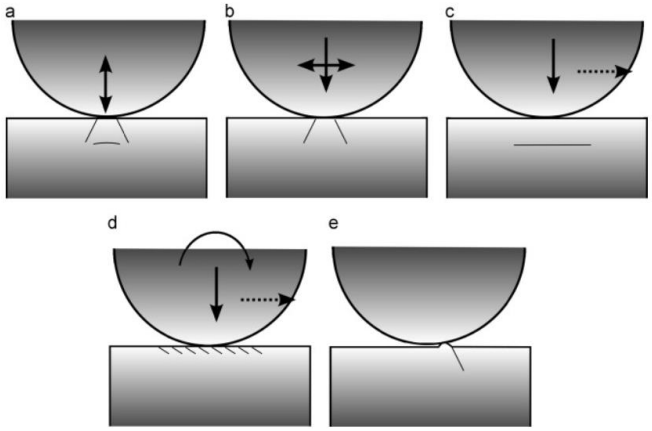

Figure 1.4: Different types of contact loading and resulting crack formation (a) vertical loading causing growth of surface and subsurface cracks, (b) both vertical and lateral loading causing surface initiated cracks, (c) vertical loading of a rolling object causing subsurface initiated cracks, (d) rolling contact with interfacial shear and slip causing surface cracks and (e) surface irregularities causing cracking [35].

Deformation

The rail wheel contact in the above mentioned loading scenarios causes plastic deformation of the rails. The material response to contact loading is strongly influenced by the magnitude of the contact loads, the material hardening, the residual stress state and the change in contact conditions due to plastic deformation [36]. Plastic shakedown and ratcheting normally occur in the wheel rail contact zone, causing the steel to exceed the elastic limit and deform plastically. Plastic deformation of the microstructure causes an increase in hardness of the rail material, which again increases the load bearing capacity of the material [37]. Plastic deformation in a crossing is highly influenced by high normal loads, tangential or shear load as well as impact from the wheel in the transition zone.

The depth of plastic deformation and thus hardening is dependent on the loading and also on the material. High normal loads cause thicker plastically deformed layers with smaller hardness gradients [38] while shear loads cause thinner plastically deformed layers but with a higher strain in the material with a higher hardness gradient [39]. Higher depths of hardening is observed for manganese steels compared to pearlitic grade due to the extreme strain hardening ability of manganese steels [40, 6], where the increase in hardness can reach three times higher values than that of the base material [40]. In pearlitic steel, heavy plastic deformation causes the microstructure to align in the shear strain direction whereas for manganese steel no shearing of grains is observed (See Figure 1.5); instead the plastic deformation causes the formation of deformation bands in the microstructure [41].

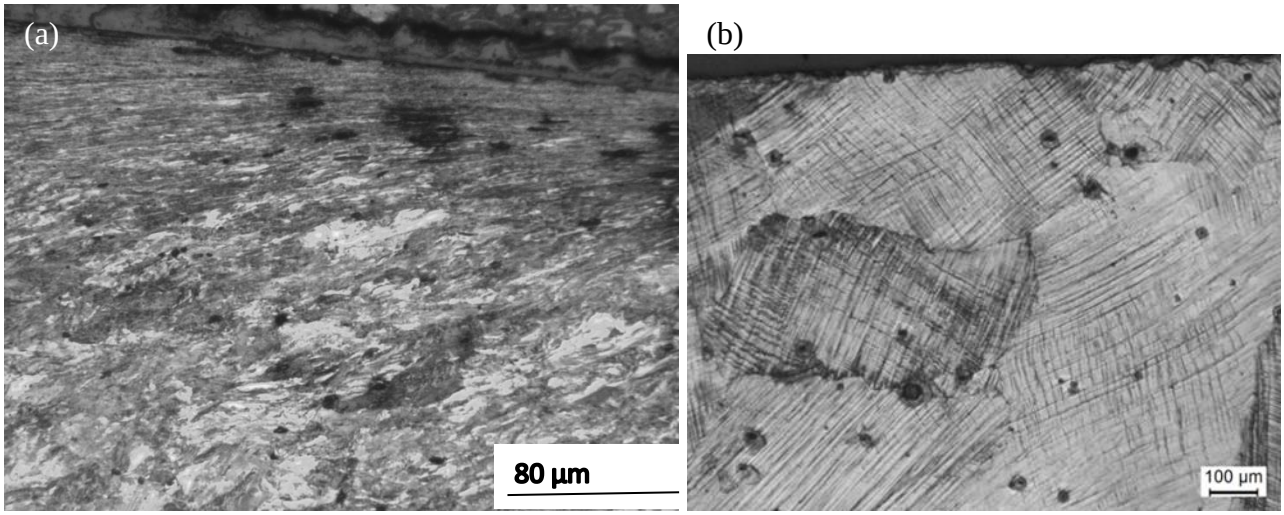

Figure 1.5: Deformation of rail microstructure at the rail wheel contact surface (a) pearlite steel and (b) manganese steel [41].

Crack formation

The accumulation of deformation continues until the material's ductility limit is exceeded. When the deformation exceeds the fracture strain of the material, RCF cracks appear [42]. The initiation and early growth of RCF cracks is a critical stage in the development of rail damage, and various numerical models are available in the literature to predict crack initiation due to RCF [42-43]. The most plausible explanation for crack initiation is brittleness of the material due to hardening from plastic deformation, but harder materials produce shallower cracks [44]. Cracks generally initiate at different angles to the surface and have different directions of propagations, as the deformation of the microstructure causes anisotropy in the material, which in turn leads to decreasing toughness making way for crack growth in certain directions with the least resistance [45].

When a crack has nucleated, the possibility of its propagation can be assessed by comparing the applied stress intensity factor to the fatigue threshold for the proper mode of crack opening. The life of a fatigue crack is normally divided into three phases mainly involving crack initiation and growth. The first phase is initiation at the surface due to shear stresses also called as Stage I. The second phase (ii) is transient crack growth behavior and the third phase (iii) is subsequent tensile and/or shear driven crack growth. Phase ii and phase iii together comprise Stage II crack growth (See Figure 1.6) [42]. After its initiation, the crack propagation is dependent on crack length, crack angle, crack face friction, and coefficient of surface friction near the contact load [43]. The cracks may grow back to the surface, causing spallation, or propagate deeper into the material, causing rail breakage.

The crack growth can also be promoted by fluid entrapment in the cracks [46] under compressive loading, as in the case of a rail under a wheel. Laboratory scale experiments of RCF on rail steels indicate the theory that surface crack growth by fluid pressurization is a dominant phenomenon [47-48].

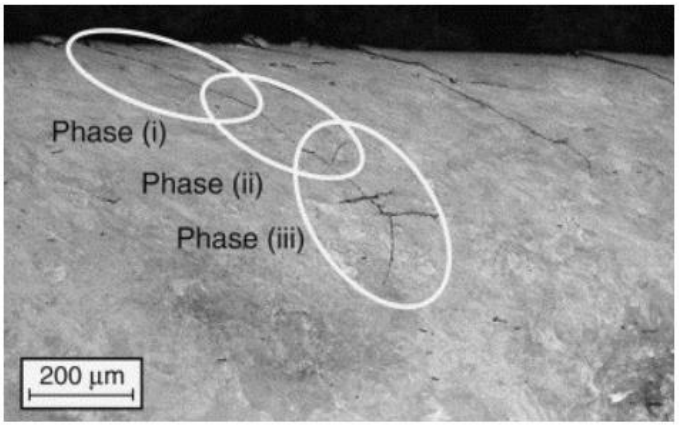

Figure 1.6: The three phases of a fatigue crack on a rail head [42].

Wear

Wear refers to the loss of material due to rail wheel contact, and is another important aspect in RCF. Wear plays an important role in determining the service life of rails [49] and wear-fatigue interaction is important in determining the life of components which undergo both processes simultaneously, as is the case for rail-wheel contact. Increasing speed or decreasing axle load reduces the wear volume [50], friction modifiers can also be used to counteract the wear [51-53]. It is further suggested that reversing the direction of rolling would also decrease wear [54], although this is not always feasible in the rail network. Wear can also be decreased by using harder rail steel grades [55-56]. Laboratory scale experiments on RCF indicate steels with high hardness have better wear resistance [47, 50], with increased hardness the plastically deformed layer on the rail surface is reduced. The thickness of the flow layer, or plastically deformed layer, indicates the extent of wear degree of material, the thicker the flow layers, the more severe the wear [57]. In pure rolling RCF dominates over wear, as the wear rate is negligible with the removal of only a thin surface layer and no removal of cracks. Increased slip ratio causes an increase in friction coefficient and higher wear volume [58]. In rolling/sliding conditions wear is a dominant mechanism, which produces large thin metallic flakes and removes surface micro-cracks [36]. The changes in rail profile due to wear causes change in the contact area between the rail and wheel that affects the contact dynamic forces, which sometimes leads to detrimental effects damaging to the rail.

Higher wear rate can reduce materials load bearing capacity leading to increased accumulation of plastic strain. However, wear can have beneficial effects in reducing the RCF crack propagation, by reducing crack growth by crack truncation or by simply crack being worn out as wear debris before attaining a critical size. If the wear rate is low, the surface cracks may not be eliminated which might lead to crack propagation and sudden fracture. Therefore an optimal combination of RCF and wear can be beneficial for rail wheel contact conditions. High wear also improves the conformity of contact between rail and wheels, thus reducing the contact stresses due to increase in the actual area of contact pressure. On the other hand, a high wear rate causes a larger accumulation of plastic deformation and subsequently damage in the long run.

1.2.3 Failure modes

As mentioned above, rail wheel contact induces a lot of damage and defects in the rails, due to RCF and wear. Two most important defects due to RCF are head checks and squats. Head checks are clustered fine surface cracks appearing on the gauge corner of the rail [59]. They initiate at angles around 15-30˚ to the surface, where the cracks are shallow and confined within thin surface layers. A combination of wear and grinding removes the thin layer of head checks. Squat defects are characterized by the appearance of microcracks below the rail surface and are of major concern due to the high occurrence of this type of defects.

Squats on normal rails are surface or near surface initiated cracks occurring because of local plastic deformation due to high dynamic load leading to RCF [60-61]. Squats are visible on the running surface as a widening and a localized depression of the surface of the rail, which appears as a dark spot containing cracks with a circular arc or V-shape [62]. Figure 1.7 shows typical squat type defects on the rail surface. The cracks generally appear at shallow angles to the surface, but might propagate deep within the material causing rail break, or may cause branching moving upward leading to spallation. A lot of research has been carried out on the origin of squats [63-64] and their growth mechanisms [65-66] but still, their development is not fully understood.

Figure 1.7: Squats formed on a normal grade rail track [62].

Studies on squats on normal grade rails from straight tracks indicate there is a leading and trailing branch of the crack. The leading branch of the crack is shear induced fatigue crack whereas the trailing branch is driven by the transverse shear loading. Squat defects are also strongly influenced by the anisotropy of the microstructure when it grows within the material. Leading cracks are initiated by delamination or fracture of white etching surface material and the propagation is dictated by the anisotropic microstructure when growing into the railhead [63]. However, other studies indicate white etching material is not related to crack initiation on head-hardened rails [64]. Squats on premium grade steels are found to occur due to locally increased microslip under redistributing tangential contact stresses in the presence of an already initiated crack [64]. Once a leading crack is formed, a transverse failure mechanism is initiated under tangential stresses, which cause branching of the leading crack to form a trailing crack. The trailing crack of a branched squat breaks through the material texture and is related to transverse, wedge-shaped failure mechanism of the surface layer of the rail [63]. In premium grade steels, the trailing crack and the accompanying surface depression

precede the leading RCF induced crack and the accompanying larger surface depression in the running direction [64]. The leading crack generally can propagate over long lengths and greater depths of millimeters as compared to trailing crack planes. Typically, the depth of propagation is around 2-3 mm. When the crack growth reaches the undeformed structure, branching and oxidation processes are found to be important metallurgical factors of crack growth. The rail wheel contact surface gets modified with redistribution of normal and shear stresses due to the squat formation. This may cause high-frequency impact, resulting in progressive internal crack growth and rail fracture [66]. In recent years, 3D Computerized Tomographic (CT) scanning non-destructive technique for characterizing internal 3D geometry defects in rails has been developed and is much superior to ultrasonic or eddy current methods. CT scanning allows for a 3D visualization of RCF defects in rails with very high resolution of data on the geometry of the internal cracks [67-69].

1.2.4 Microstructure of rails

The RCF phenomenon is dependent on the microstructure present in the steels. Several laboratory scale experiments on RCF on rail steel have established the importance of microstructure on RCF damage [6, 70]. The difference in composition and heat-treatment leads to refinement of the microstructure (varying grain size, pro-eutectoid ferrite, cementite content, and pearlite lamellae spacing) and mechanical properties (hardness, tensile strength, yield strength etc.).

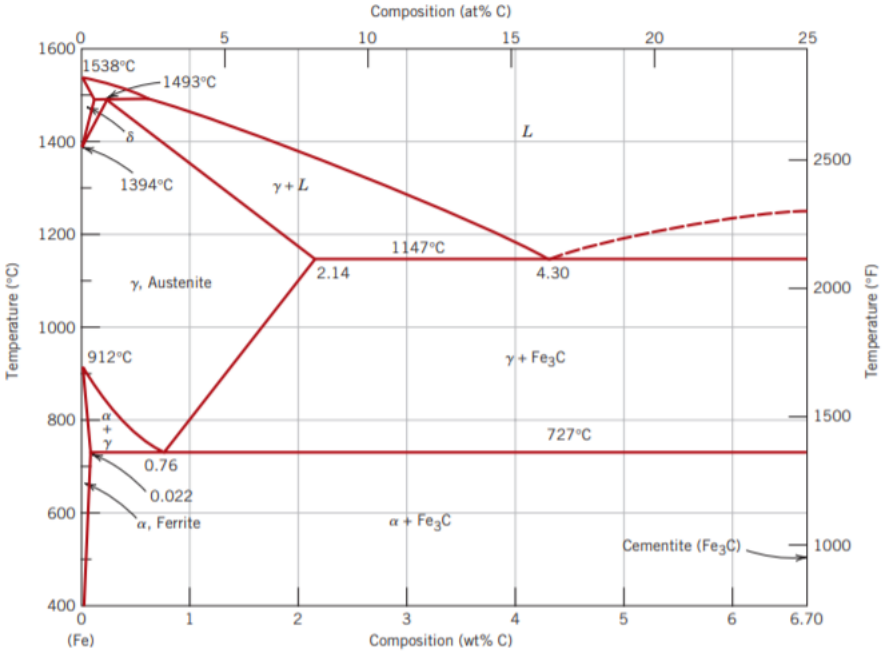

Figure 1.8: Iron-carbon phase diagram showing the different phases at different compositions of carbon and temperatures [71].

The iron carbon phase diagram is shown in Figure 1.8. The left side of the diagram up to 2% iron is related to steel alloys of different compositions. Up to 0.8% carbon, it is referred to as hypo-eutectoid steel whereas steel with more than 0.8% carbon is referred to as hyper-eutectoid steel. The microstructural phases (as can be seen in the phase diagram) vary depending on the carbon percentage resulting in steel of different mechanical properties. The eutectoid

point for steels is around 0.8% carbon, thus proeutectoid ferrite will be present if the percentage of carbon is lower than 0.8%, and if the carbon content is greater than 0.8% proeutectoid cementite will be present. With increasing carbon content, the proeutectoid ferrite percentage decreases and at 0.8% C, it only contains eutectoid pearlite with no proeutectiod ferrite. The difference in the phases and their amount present in the structure cause very significant changes in material behavior and deformation.

Pearlitic steels

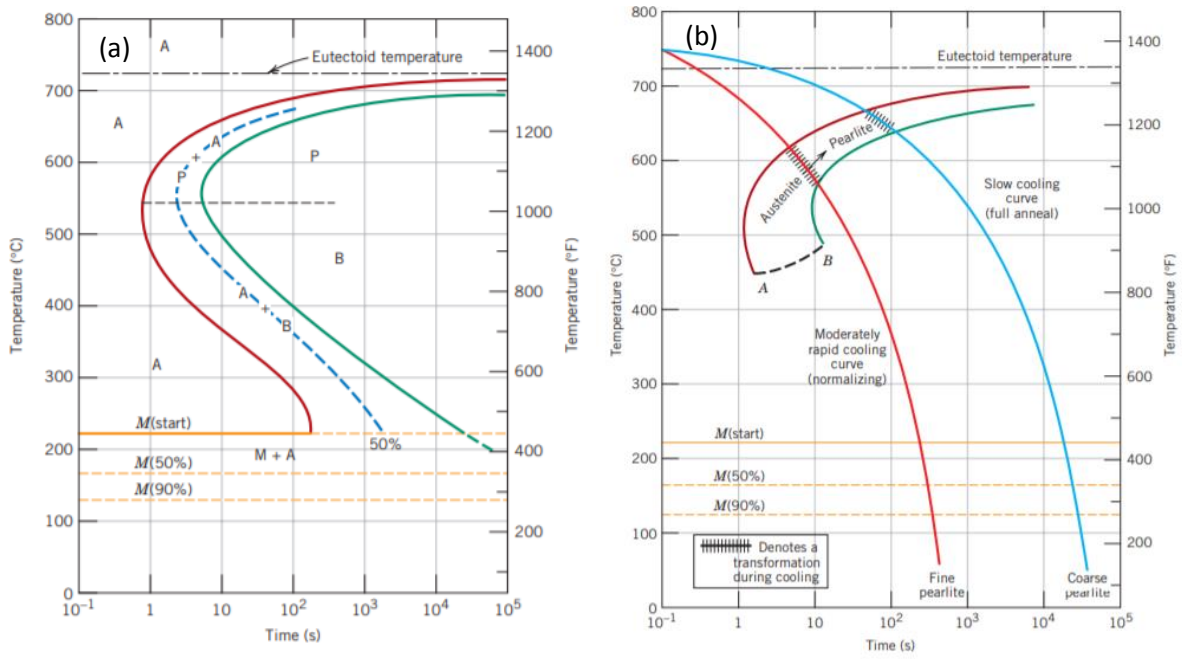

Figure 1.9: (a) time temperature transformation (TTT) diagram for an iron-carbon alloy of eutectoid composition: where A-austenite, B-bainite, M-martensite, P-pearlite and (b) a continuous cooling transformation (CCT) diagram for a eutectoid iron-carbon alloy [71].

Most rail steels are manufactured with a pearlitic microstructure, with a carbon percentage between 0.6-0.8% depending on the exact grade used. Figure 1.9a shows the time temperature transformation diagram for the eutectoid steel. From the austenite phase on cooling, transformation occurs to pearlite, bainite or martensite depending on the cooling rate. The pearlite steel microstructure consists of an alternate network of ferrite and cementite. The carbon content alters the proportion of ferrite and cementite in the microstructure. Depending on the carbon and alloying element content the morphology of the ferrite and cementite changes. Previous studies indicate that the volume of proeutectoid ferrite contributes significantly to RCF damage. RCF cracks are predominantly initiated at the rail surface along the edges of highly strained, proeutectoid ferrite zones. The ferrite is the softer phase in the matrix and they facilitate early stage crack propagation [7]. The ferrite gets more strained than the pearlite as evident from the significant percentage increase in the nano hardness measurements of the deformed rail [8]. At lower strains, the softer ferrite deforms plastically while the cementite is still in the elastic stage leading to increased internal stresses. Strain partitioning between the proeutectoid ferrite and pearlite occurs where the ferrite exhausts its ductility. Cracks can initiate within the proeutectoid ferrite or at the ferrite/pearlite interface, and short cracks initiated in the vicinity of major cracks run along

the strained proeutectoid ferrite. An increase in the amount of proeutectoid ferrite in rail steel, therefore, is detrimental to fatigue life [7-8]. Higher carbon percentage causes formation of less proeutectoid ferrite and therefore better resistant to stress partitioning. However, internal stress incompatibility can also arise between the soft ferrite and hard cementite in pearlite structure leading to crack initiation.

Head hardened steels

Since the stress state in a crossing differs to a large extent from normal tracks, several new grades or modification of the basic pearlitic grade with superior mechanical properties have been adapted to be used for crossings. Pearlitic steels for crossings generally have carbon percentage on the higher side, around 0.7-0.8%, which leads to higher hardness and better resistance to RCF [72]. Modifications in the microstructure and mechanical properties of pearlite can also be obtained by varying the heat treatment. By using a faster cooling rate, the interlamellar spacing between the ferrite and cementite in the pearlitic steel can be reduced, giving a higher hardness which provides better wear resistant properties in service [73]. The head hardened pearlitic steel is obtained by heat treating the head of the rail, followed by fast cooling which leads to fine interlamellar spacing (See Figure 1.9b). Finer interlamellar spacing controls the dislocation movement within the ferrite channels and thus increases the strength. Head hardened steels have better RCF resistance than normal hardened or non-hardened pearlitic steel [47, 74]. The most frequent grade used for the crossings is premium grade 350HT steel, which is a low alloy carbon steel with an average hardness of 350-370 in the Brinell scale (HBN). The average chemical composition of this steel is 0.72 – 0.80% C, 0.15 – 0.58% Si, 0.70 – 1.20% Mn, ≤ 0.15% Cr, max. 0.020% P max, 0.025% and rest Fe. This steel is often referred as to as head hardened pearlitic grade due to the rail head being hardened to 370 HBN, and has improved resistance to wear, corrugation and RCF compared to standard R260 grade pearlitic steels [75].

Manganese steels

Manganese austenitic steel, often referred to as Hadfield steel, is a common material choice for railway crossings due to its excellent work hardening ability, large stress intensity factor, suitable strength, high toughness, and good wear resistance. The addition of high Mn content stabilizes the austenitic phase in the microstructure. The average chemical composition of this steel is 1-1.4% C and 12-13% Mn with the addition of other alloying elements like ~0.18% Cr, 0.4-0.6% Si, 0.022-0.033% P. The typical heat treatment for most manganese steels consists of a solution anneal followed by a water quench. The temperature is raised slowly to the soaking temperature which is generally high (mostly above 1000˚ C) for dissolution of carbides and also to obtain the austenitic microstructure (see Figure 1.10). Very high-solution temperatures should be avoided as it causes incipient fusion at the grain boundaries resulting in embrittlement [76]. The steel is then rapidly quenched to prevent any precipitation of carbides and also to maintain the austenitic microstructure. Manganese steels are used either in rolled, as-cast or explosion hardened condition. Manganese steels used in crossings have a single phase austenitic microstructure, where different substructures are formed within the grains due to the difference in the degree of deformation in different grains, and also with different regions of the same grain. Depending on the stress and orientation, some grains may deform by twinning whereas other grains might only have slip bands or stacking faults [20, 77]. The non-uniform distribution of microstructure causes local regions of strain concentration due to mismatch of deformation, initiating cracking and damage [20]. Compared to normal pearlitic grade, the manganese steel has properties better suited to the handle repeated impacts at crossing [78]. The threshold stress intensity factor (ΔK_{th}) of manganese steel is quite large compared to common structural steel; therefore it has a

lower crack growth rate [79]. An important property of manganese steel is its excellent work hardening capacity [80] which makes is extremely resistant to wear as well. When it comes to maintenance inspection, a disadvantage of using manganese steel is that it allows ultrasonic waves to pass through the material, which might lead to cracks being undetected during routine ultrasonic testing of rails. Also, welding procedures for manganese steels have to be carefully designed because it is very sensitive to reheating especially in the range above 260˚ C which causes carbide precipitation and pearlite formation with subsequent embrittlement and loss in toughness [76].

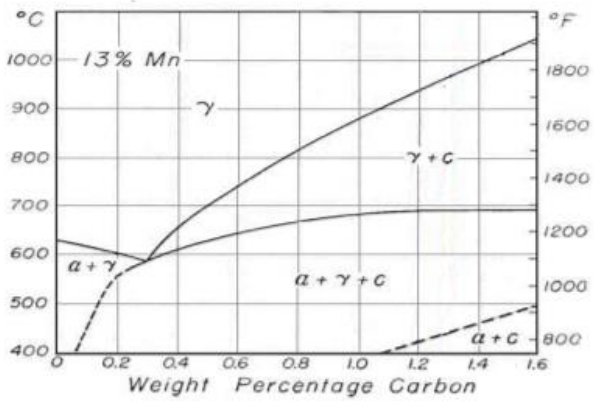

Figure 1.10: The phase diagram of manganese steel containing 13% manganese [81].

Bainitic steels

In recent years, bainitic steels have also been used in railway S&Cs. Bainitic steels are harder and have better wear resistance than pearlitic grade [82], as well as good RCF resistant properties under similar loadings [83]. The bainitic steel is obtained from the isothermal cooling of the steel from the austenitic temperature i.e., by the decomposition of austenite at a temperature which is above the martensite formation temperature but below that at which fine pearlite forms. Several types of bainite can be obtained during the cooling process, such as granular bainite and lath bainite depending on the composition of alloying elements, temperature and time of holding (See Figure 1.9a). The complex and inhomogeneous microstructure of the bainitic steel makes it more vulnerable to crack initiation. Bainitic steel crossings are in use in several countries including Germany, where manganese steels are not used due to the problem with ultrasonic measurements. Research is ongoing on the suitability of bainitic steel as crossing material under different loading conditions.

1.2.5 Deformation mechanisms

Plastic deformation in metallic materials generally occurs by slip due to dislocation motion or by twinning. In pearlitic steel, slip is the only deformation mechanism whereas in manganese steel both slip and twinning can be observed. An overview of the mechanisms is given below:

Slip

The process of slip involves sliding of one atomic plane over another along definite crystallographic planes called slip planes by dislocation movements [84]. When the applied shear stress exceeds the critical shear stress, the atoms move an integral number of atomic distances along the slip plane so that the lattice is left unaltered and a step is produced

called the slip line. The dislocation is the boundary between the slipped and unslipped part of the plane of the partly glided crystal [85]. Slip generally occurs on planes of greatest atomic density and the slip direction is the closest-packed direction within the slip plane. The slip plane and the slip direction constitute the slip system [84]. In fcc crystals, the {111} planes and <110> directions are the close packed systems. There are four possible individual planes and three directions which together give a total of 12 slip systems. The bcc crystals have 48 different slip systems, from the combination of {110}, {112} and {123} slip planes and <111> direction [85]. Slip lines in bcc crystals have a wavy appearance due to slip occurring on several slip planes.

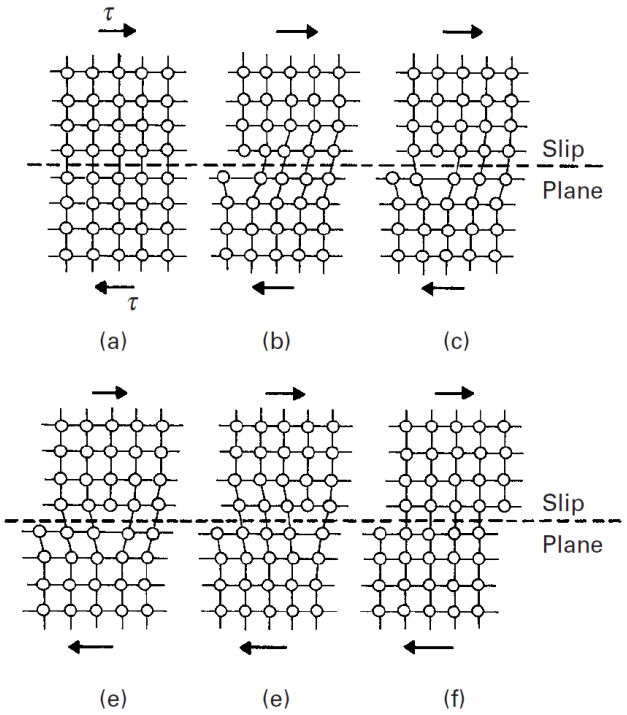

Figure 1.11: (a-f) Schematic illustration of the slip process on the application of shear stress [86].

Twinning

Another important deformation mechanism is twinning. Twinning is dominant when deformation by dislocation slip is limited. However, both slip and twinning can occur simultaneously. Twinning occurs when deformation causes reorientation of a portion of the crystal lattice in a symmetric way such that the twinned portion is the mirror image of the parent untwinned crystal. The plane of symmetry between the two orientations is termed as twinning plane [84]. Twinning like slip also occurs in definite direction on a specific crystallographic plane. For fcc systems, the twin plane and directions are {111} and <112> respectively. For bcc systems the twin plane is {112} and the twin direction is <111>. Slip and twinning vary in many aspects. While the slipped region has the same orientation as that of the original unslipped grain, the twinned region of a grain is a mirror image of the original lattice, which causes a change in orientation across the twin plane. Slip occurs in discrete multiples of atomic spacing whereas in twinning the atom movements are much less than an atomic spacing [86]. Twinning can be caused either due to deformation called mechanical twins or as a result of annealing following plastic deformation called annealing twins [86].

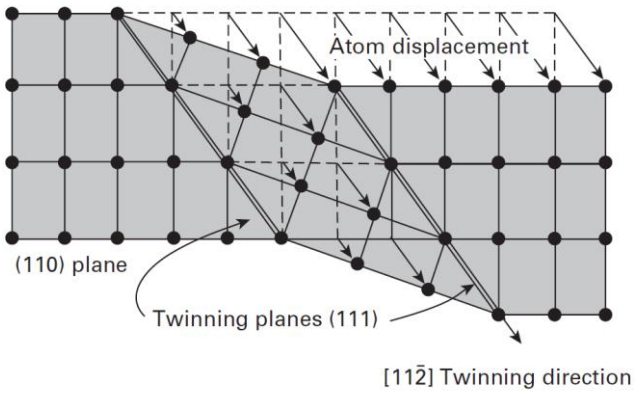

Figure 1.12: Schematic of twinning in FCC metals [86].

1.2.6 Residual Stress in rails

Residual stresses are elastic stresses present within the material without external loading. The presence of residual stresses in materials and components are often overlooked, in spite of they could significantly affect the mechanical properties both in a positive and negative way. Residual stresses are generated in a rail due to manufacturing processes like hot rolling, cooling, roller straightening and head hardening [87]. Due to rail-wheel contact, the material at the top surface will harden and when residual stresses exceed the yield cracks will eventually appear [88]. The rate of crack growth also in rails is affected by contact stresses due to rail-wheel interaction, thermal stresses due to temperature changes as well as residual stresses induced by both manufacturing process and rail wheel contact [89]. Research has been carried out to estimate the extent of development of residual stresses in new rails after manufacturing [90-91].

It is generally accepted that compressive residual stresses are beneficial to counteract crack growth while tensile residual stresses have the opposite effect. A C-shaped longitudinal residual stress pattern has been observed with tensile longitudinal residual stresses in the rail head and foot, and compressive stresses in the web of a rail. European Committee for Standardization has set limits to the value of residual stress, for example to 250 MPa in the middle of the rail foot for new rails [92]. The state of stress changes while the rail is in service. Typically, compressive stress in both the longitudinal and transverse directions in the rail develops near the running surface, with balancing tensile stresses appearing beneath this region. Therefore the contact stresses are reduced by the superposition of the compressive residual stresses [23].

The residual stresses in rails are usually determined by a destructive method using strain gauges. Non-destructive methods include X-ray and neutron diffraction as well as ultrasonic and magnetic methods. However, ordinary X-rays are limited in terms of intensity and penetration depth. Neutrons have a significantly larger penetration depth compared to ordinary X-rays, but low intensity. Synchrotron X-Ray diffraction has higher intensity and penetration depth compared to neutrons. In recent years, both X-ray diffraction and neutron diffraction has been used to determine residual stresses in the rail head [23-26, 93]. The residual stresses developed in new rail depend on the manufacturing technique it has been subjected to, and in worn rails, on the load, it has been subjected to. Residual stress measurements by various techniques on normal rail heads after several years of service indicate compressive stresses can reach values as high as 500 MPa on the rail wheel contact surface depending on the service loading.

Variation in stress is obtained depending on the direction of stress measurement, with compressive stresses being higher in the transverse direction for rails. The thickness of the compressive layer depends on the tonnage and the wear suffered as well as the rail grade. The plastic deformation of 350HT rail differs from normal grade rails, causing different residual stress state even under similar loading. Harder steels have better resistance to wear and also plastic deformation, forming thinner compressive residual stress layers. The layer of compression is balanced beneath by a tensile stress layer. Thinner compressive stress layer is detrimental to crack propagation as it causes early turning down of cracks towards the tensile layer in harder 350HT rails. Unfortunately, all studies on residual stresses require rail specimens to be sectioned for measurements which cause stress relaxation and redistribution. Studies performed on the bulk specimen and sliced rail specimen indicates a difference of residual stress of around three times [93]. However, various approaches are available to account for the amount of stress relaxation and measure the exact stress fields.

Most studies on residual stress measurement of rails have been done on normal pearlitic steel from straight tracks. The geometry and the imposed stress on a crossing are totally different from a normal track. The residual stress distribution, therefore, is expected to differ from a normal track. There is little experimental data on residual stress measurements on crossing components. Numerical simulations of residual stresses on manganese crossings indicate equivalent residual stress is complex and irregular after wheel contact loading [27]. According to simulations, the maximum residual stress is obtained at certain depth below the surface of the nose rail, rather than at the contact surface of wheel and crossing, and is also dependent on the train speed and loading. The combined effects of the maximum contact stress and the maximum residual stress is responsible for fatigue crack initiation, which occur at the intermediate position between the maximum contact stress and the maximum residual stress in a crossing rail [27]. Residual stresses are therefore an important parameter to be considered while studying RCF as it influences the state of stress within the material, which in turn will affect the cracks and other defects in the rails.

2. Experimental procedure and details

In this section, a detailed description of the experimental techniques and procedures used for the characterization and mechanical testing of the rail steel specimens is given. For better understanding, detailed diagrams and descriptions of the different types of crossings examined in this study along with their different components are given at first.

2.1 Crossings investigated in this work

Three different railway crossings have been investigated in this study. The first one is a pearlite steel crossing labeled as AP 104. It was from the year 2004 and was extracted from Vestfyn in Denmark. The individual components of wing rail and nose were bolted together. Most of the traffic was in the direction of the nose. The Figures 2.1-2.3 below show the different components of the crossings.

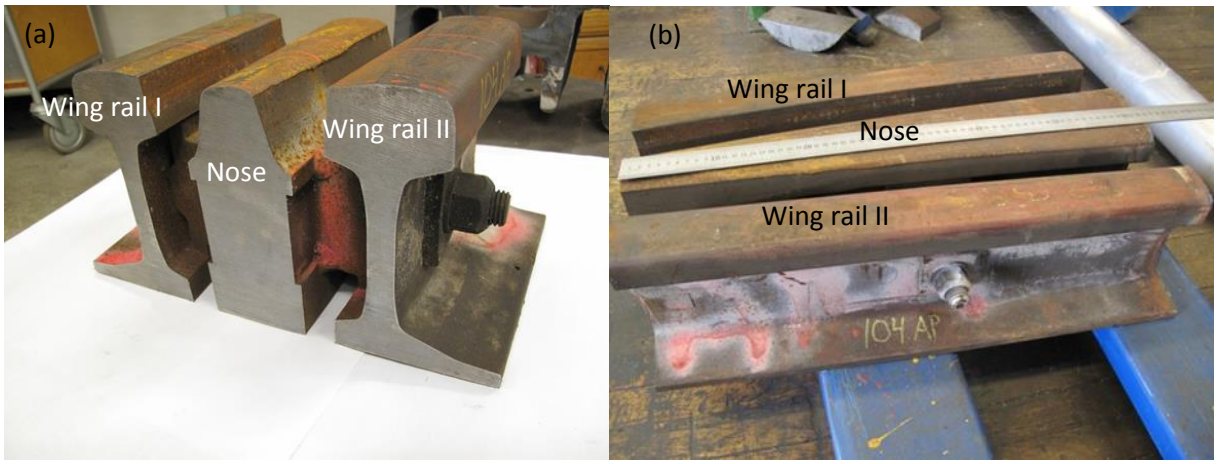

Figure 2.1: AP 104 pearlitic crossing extracted from Vestfyn (a) and (b) the cut out portions of crossing AP 104 with wing rail and nose bolted together (a) the first part and (b) the second part of the same crossing.

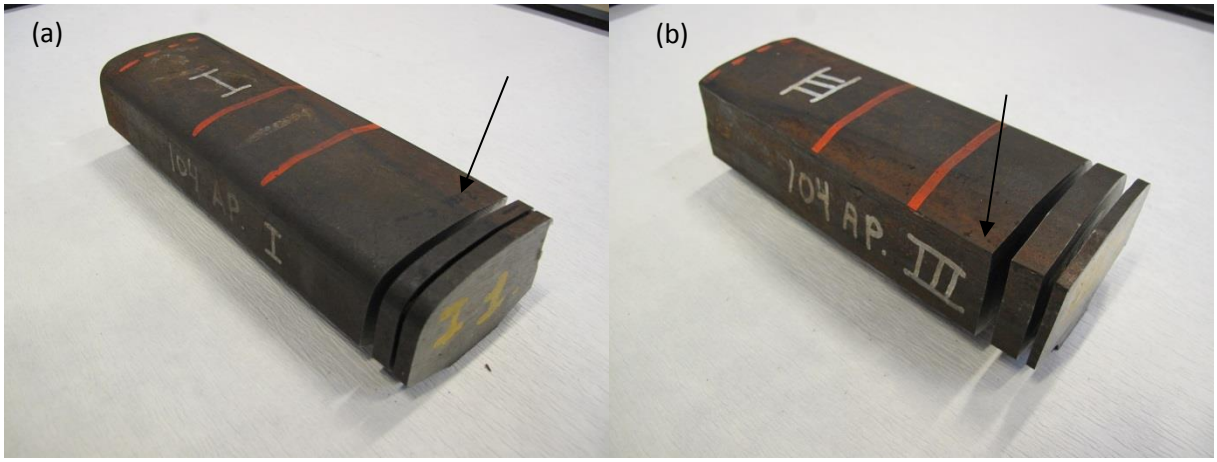

Figure 2.2: The head portions of (a) wing rail I and (b) wing rail II after unbolting and separating it from the pearlite crossing showing the pieces cut out for metallurgical investigation. The rail wheel contact area is evident from the deformation and is marked with black arrows.

Figure 2.3: The nose of the pearlitic crossing after unbolting and separating it from the crossing showing the pieces cut out for metallurgical investigation.

Two manganese crossings were also investigated. They were extracted from Tommerup in Denmark and labeled as ATP 110 and BTP 102 respectively. Unlike pearlite crossings where the individual components are manufactured and bolted together, the manganese crossings are cast as a single piece. The ATP 110 crossing is from 2010 and had been in service for five years with a traffic density of approximately 14 MGT. The majority of the traffic was towards the nose from wing rail and the nose rail was severely damaged with visual cracking and spallation. Figures 2.4-2.5 show the ATP 110 crossing with the various components.

BTP 102 crossing is from 2002 and had been in service for 13 years. The crossing was severely damaged and had been repaired by welding. Nearly all traffic goes in the direction from the nose to the wing rail in BTP 102. The majority of the traffic is straight through the switches for both the cases. Figures 2.6-2.7 show the BTP 102 manganese crossing with its individual components.

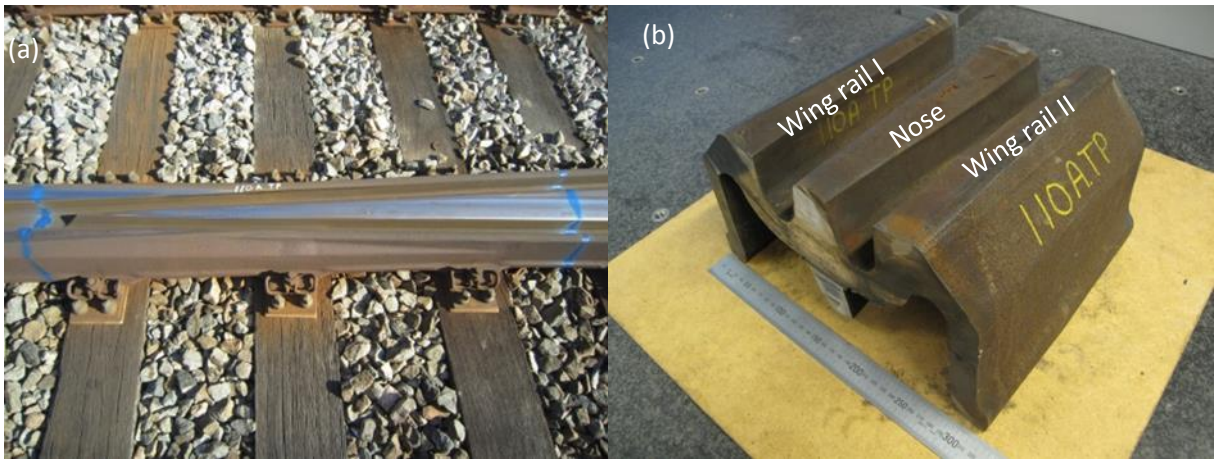

Figure 2.4: (a) ATP 110 manganese crossing in the track before extraction. The blue markings indicate the region that was cut out and (b) a cut out portion of the same crossing with the wing and nose rail for detailed investigation.

Figure 2.5: Individual components of the ATP 110 crossing after separating them (a) the nose of the crossing showing distinct visual cracking and spallation, (b) and (c) the two wing rails, the rail wheel contact area is evident from the deformation and is marked by arrows.

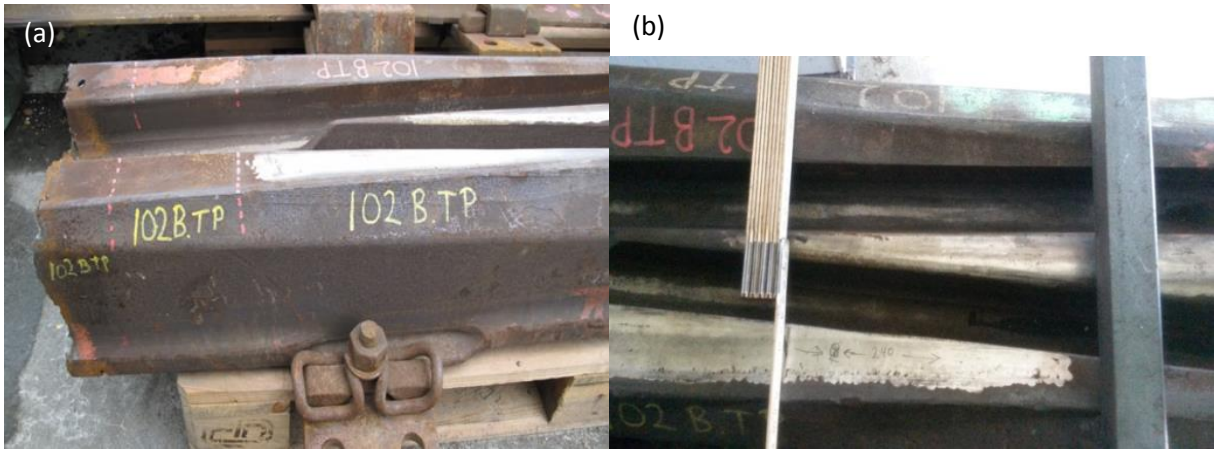

Figure 2.6: BTP 102 manganese crossing extracted from Tommerup (a) the initial part, the red mark shows the area which was cut out further for detailed investigation, (see Figure 2.7a) and (b) the second part of the crossing; the welding is evident in the nose and the second wing rail.

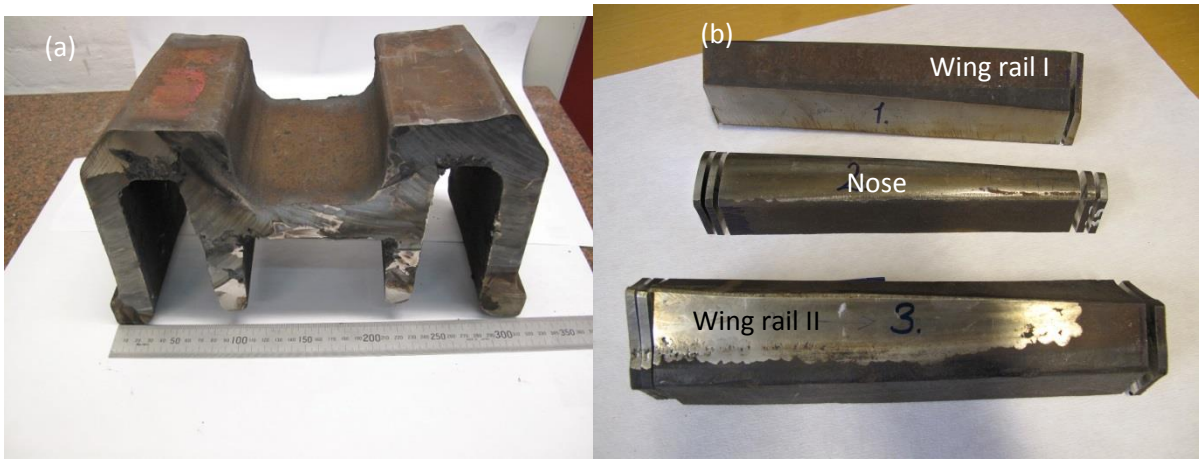

Figure 2.7: (a) Part of the BTP 102 crossing before the starting of the nose cut out for metallurgical investigation and (b) individual components of the wing rail and nose separated from the crossing for further investigation.

The experimental characterization techniques are mentioned in the following sections.

2.2 3D X-Ray Computerized Tomography (CT)

Absorption contrast X-ray tomography can measure non-destructively the three dimensional (3D) structure of inner defects of an object which has absorption difference to the bulk of the specimen with a spatial resolution down to 1 μm. In a computerized tomography (CT) system, the specimen is placed on a stage in between the radiation source and an imaging system. The specimen is then rotated up to a full angle of 360˚ during the scan, and the digital detector registers thousands of individual 2D images from many angles. An algorithm uses these 2D images to reconstruct the structure into a complete 3D representation. This helps in the characteristics of the internal structure of the specimen including dimensions, shape, defects, and density from the whole volume of the specimen. The 3D X-Ray tomography scans were done on a ZEISS Xradia 510 Versa machine. A polychromatic X-ray beam was used with energies ranging up to 160 kV from a tungsten target. For all the present experiments, a total of 1601 projections were acquired during a full specimen rotation. 3D maps were reconstructed by a Feldkamp algorithm for cone beam reconstruction [94] to 2k×2k×2k voxel volumes with a voxel size of around 10 μm, depending on exact specimen size. The crack network and other defects were segmented and visualized using Avizo 3D software. X-ray tomography reconstructions are 3D density maps, which allow detection of cracks due to the difference in density by applying an appropriate intensity threshold value.

For the manganese steel crossing (ATP 110), 5 specimens were cut from the nose from an area showing distinct visual spallation and cracking (Figure 2.8a). Each of the specimens was 10x10x40 mm in height, width, and length respectively. Each of the specimens was individually scanned and reconstructed, after which they were stitched together to give an overview of the crack network in 3D over a large volume. Pieces were also cut from the wing rail of manganese steel crossing (BTP 102) having dimensions 50x10x10 mm in length, breadth, and height respectively for scanning and crack reconstruction in 3D using the above procedure. For the pearlitic crossing (AP 104), the nose of the crossing was welded having welding cracks and defects. A piece was cut from the nose having dimensions 10x5x10 mm and scanned similarly with 3D Xradia to visualize the defects and porosities in the welding.

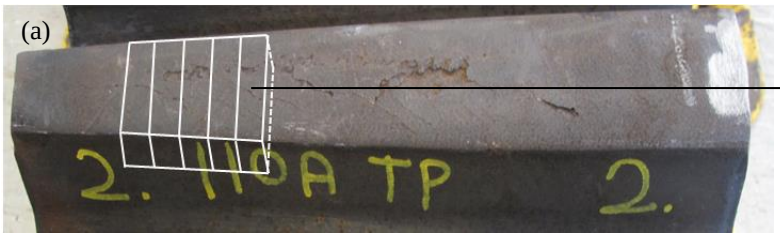

Area in the nose of the manganese crossing from where five specimens for tomographic imaging were taken.

Areas from where specimens for tomographic scanning were taken

Figure 2.8: The areas where the specimens for the tomographic reconstruction was obtained from the different crossings (a) nose of ATP 110 manganese crossing showing the five individual specimens, (b) nose of AP 104 pearlitic crossing and (c) BTP 102 manganese crossing.

2.3 X-Ray diffraction

Residual stresses were measured on the worn manganese steel crossing (ATP 110) by X-ray diffraction at laboratory source and by synchrotron at Advanced Photon Source (APS).

Residual stresses are stresses present within a material body in absence of external loading. Residual strains are elastic in nature. Elastic strains generally cause a shift in peak positions whereas inelastic stresses cause peak broadening in diffraction. There is no direct method available to measure stresses, they are calculated or derived from measured elastic strain which is then converted to stress by using elastic strain relation (See Equation 8). The strain is defined as:

$$\varepsilon = \frac{d_n - d_0}{d_0} \quad (1)$$

Where d_n is the deformed lattice spacing due to the residual stress/strain and d_0 is the unstrained lattice spacing.

X-ray diffraction is a useful method that provides information on the atomic structures of crystalline materials. An incoming X-ray wave interacts with the crystalline material and diffracts in certain direction depending on the symmetry of the unit cell. Strain free crystalline material has a well-defined inter-planar spacing and produces a characteristics diffraction pattern when exposed to X-rays. Under strained condition, the inter-planar spacing changes

which cause a shift in the diffraction pattern. The inter-planar spacing can be calculated by using the Bragg's Law (Equation 2) which states that the planes of a crystalline material diffract X-rays at certain angles [95].

$$n\lambda = 2d\sin\theta \quad (2)$$

where λ is the wavelength of the X-Ray, d is the inter-planar spacing of the reflecting planes, θ is the reflection angle and n is the integer. Therefore by measuring the inter-planar spacing of the strained and unstrained specimen, the residual strains can be calculated by using Equation 1.

Strains in a material can either be macro (Type I) or micro (Type II/Type III). Macro strains are homogeneous over several grains and can be measured by a shift in peak position (Δ2θ). In this study, we use the conventional laboratory X-ray to determine the macro (Type I) strains. Micro strains can be either homogeneous (Type II) or inhomogeneous (Type III) within the same grains and can be measured by a shift in peak position (Δ2θ) and change in full width half maxima (ΔFWHM) of the diffracted peak. We use differential aperture synchrotron X-Ray diffraction to determine the local micro (Type II/Type III) strains.

2.3.1 Laboratory X-ray Stress Measurement

While measuring stresses on the free surface of the material, a plane stress condition is assumed where the stress perpendicular to the surface (normal direction) is supposed to be zero (σ_3=0) as shown in Figure 2.9 [96]. However, there are non-zero strains present in the normal direction. The inter-planar spacing of planes oriented at different tilt angles of ψ is measured for different directions of φ. The strains for lattice planes of different tilt angles ψ and different directions of φ [97] can be expressed as:

$$\varepsilon_{\varphi\psi} = \frac{d_{\varphi\psi} - d_0}{d_0} \quad (3)$$

From Hooke's law, the relationship between elastic stress and strain in an isotropic material is defined as [97]

$$\varepsilon_{\varphi\psi} = \frac{d_{\varphi\psi} - d_0}{d_0} = [\frac{1+v}{E}\sigma_\varphi sin^2\psi] - [(\frac{v}{E})(\sigma_1 + \sigma_2)] \quad (4)$$

Where v is the Poisson's ratio, E is the elastic modulus. By rearranging,

$$d_{\varphi\psi} = [(\frac{1+v}{E})\sigma_\varphi d_0 sin^2\psi] - [(\frac{v}{E})d_0(\sigma_1 + \sigma_2)] + d_0 \quad (5)$$

Therefore we find a linear relationship between the lattice spacing $d_{\varphi\psi}$ and $\sin^2\psi$. The stresses for each direction of φ can be calculated by

$$\sigma_\varphi = \frac{E}{1+v} \text{ x } \frac{1}{d_0}(\frac{\partial d_{\varphi\psi}}{\partial sin^2\psi}) \quad (6)$$

The stress thus can then be calculated by determining the gradient of the $\sin^2\psi$ vs d curve. This assumes a zero stress at d intercept on the y-axis when $\sin^2\psi = 0$. This assumption is based on the fact that Young's modulus is greater than the summation of the principal stresses (σ_1 and σ_2) and d_0 can be used from the inter-planar spacing measured at ψ=0 with less than 1% accuracy [97]. In this way, the stresses are measured at minimum three different directions of φ to obtain

the principal stresses σ_1 and σ_2. This technique of using multiple ψ and φ is often referred to as the $\sin^2\psi$-d method. An example of such a plot is given in Figure 2.10.

The laboratory X-ray residual stress measurements were made using a Xstress 3000 G2R diffractometer equipped with a Cr-Kα X-ray source. Measurements were made on the wheel running surface of the nose on a specimen (B) (see Figure 2.11a) at two positions, center, and the gauge corner. The specimen was cut out from the nose having dimensions 40x10x10 mm (See Figure 2.11d). X-ray diffraction measurements for determining the lattice spacing were done with 9 ψ tilts from -45˚ to +45˚ along three directions of φ=0˚, 45˚ and 90˚. The operating voltage was 30kV and the current was 6.7mA with an exposer time of 60 sec. The lattice spacing of the {220} austenitic iron peak around 2θ=128˚ was measured. Higher 2θ positions are preferable as at high 2θ angles small changes in the d-spacing due to strain gives measurable changes in 2θ. At low angles, the difference will be too small to be measured precisely [96]. A circular collimator of 1.5 mm diameter was used to irradiate the specimen with the X-ray. The diffraction peaks were fitted using the Stress Tech Xtronic software, using a cross relation method with a linear background. Strains were measured by the method described above and converted into stress by the software assuming a Poisson's ratio of 0.28 and elastic modulus of 196 GPa.

X-ray diffraction (XRD) measurements were also performed using a Bruker X-ray diffractometer operated in the Bragg-Brentano configuration applying Cr-Kα radiation (λ = 2.2897 Å). X-ray diffractograms were recorded with a a step size of 0.07° in 2θ and an operative voltage of 35 kV and a step time of 10s in the angular range of 2θ in 122°-133° to record the austenitic peak around 2θ=128˚.

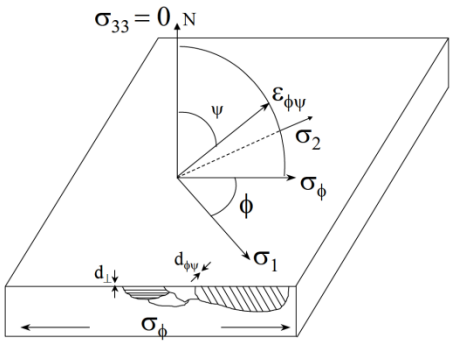

Figure 2.9: Schematic showing diffraction planes parallel to the surface and at an angle φψ. Here both $\sigma_1$and σ_2 both lie in the plane of the specimen surface whereas according to plane stress condition σ_3=0 [96].

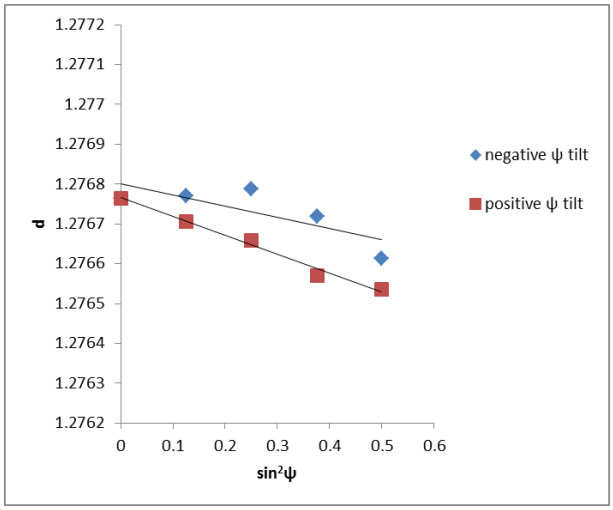

Figure 2.10: A typical $\sin^2\psi$ vs d plot (own work).

Measurements were made on two specimens, specimen A and specimen C, see Figure 2.11f. A bulk specimen C from the nose having dimensions 95x50x25 mm was selected. The measurements were made on the running surface. Here also the standard $\sin^2\psi$ vs d technique was used with 9 positive ψ tilts from 0 to 65 ˚ along the two φ directions of 0˚and 90˚. Another set of measurements were made on the transverse surface of Specimen A cut from the nose having dimensions 40x5x20 mm. Both positive and negative ψ tilts were considered and only the normal direction φ=90˚ stresses were calculated. Measurements were made on the transverse surface at 5 locations from the running surface at 3 mm interval till 15 mm from the surface.

2.3.2 Synchrotron X-Ray Stress Measurements

Synchrotron measurements were conducted on the transverse surface of a specimen cut out from the nose of the manganese crossing having dimensions 40x5x2 mm, (Specimen A). Measurements were made at depths of 3 mm, 4 mm, 6.5 mm and 15 mm from the wheel running surface at beam line 34-ID-E at Advanced Photon Source (APS), Argonne National Laboratory (see Figure 2.11b). The transverse surface was electropolished to avoid mechanical stresses induced due to the cutting procedure. Strains were measured at different depth along the transverse or the running direction for each of the four locations. The deformed lattice spacing *d* at each of the locations at different depths were calculated based on differential aperture X-Ray microscopy (DAXM) measurements. To calculate the strains, the strain free lattice spacing d_0 was obtained from laboratory X-Ray diffraction measurements with Cr-Kα radiation (λ = 2.2897 Å) source using a specimen taken from the base of the nose at a depth of 20 mm from the running surface. Hardness measurements and optical micrographs suggested that there is no deformation due to rail wheel interaction at that depth. The strain free lattice parameter obtained from the diffraction of {220} peak was calculated to be 1.2802 Å. For synchrotron measurements, the specimen was mounted with an inclination of 45˚ to the incoming X-rays. A polychromatic beam was used to determine the orientation of the matrix grains. The resulting microbeam had a Lorentzian profile with a full width half maximum of ~0.5 µm. The Laue diffraction patterns from the scanned volume were recorded on a detector which was mounted in 90^0 reflection geometry at a distance of 510.3 mm above the specimen. A Pt-wire of 50 mm diameter was used as a differential aperture to obtain the diffraction patterns at different depths. The Laue patterns at each depth were reconstructed by the use of the LaueGo software available at APS

beamline. The patterns were indexed, from which the hkl indices of individual spots as well as their corresponding X-ray energies were determined. A spot with high intensity and a diffraction vector normal to the specimen surface was then selected for monochromatic energy scan to determine the absolute lattice spacing. The strains were calculated using equation (1). Only one component of the strain was determined (along the running direction).

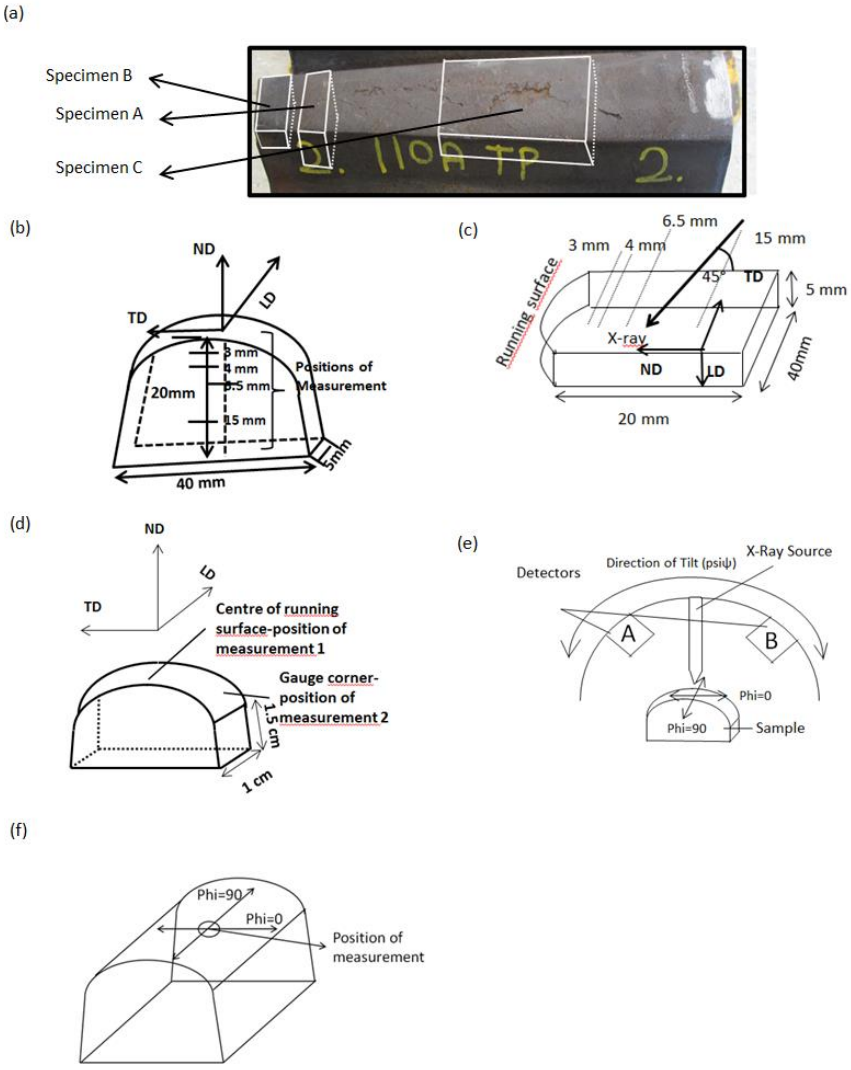

Figure 2.11: Photo and schematic diagrams showing where specimens A, B and C were cut out from the nose for the strain measurements (a) photograph showing the nose studied, (b) schematic diagram of specimen A. The positions of the synchrotron X-ray diffraction measurements are also shown, (c) sketch showing the experimental synchrotron X-ray set up for specimen A and the points of measurement on the specimen, (d) schematic diagram of Specimen B for laboratory X-ray diffraction scans showing the positions of measurements at the running surface and at the gauge corner, (e) Sketch showing the experimental set-up for the laboratory X-ray measurements and (f) Schematic diagram of specimen C used for laboratory X-ray diffraction scans showing the position of the measurement.

2.4 Mechanical Testing

2.4.1 Hardness Measurements:

Hardness measurements were made on the individual components of the damaged and deformed crossings (AP 104, ATP 110 and BTP 102) which were extracted from the network and also on the fatigue deformed specimens.

Hardness refers to the resistance of a material to localized plastic deformation. It can also be used as a measure to quantify the amount of deformation of any component. At higher plastic deformation, the material becomes harder. The general method followed is a small indenter is forced into the surface of the specimen under controlled loads. The depth or size of the indents is measured and then the hardness number is calculated. There are different methods for hardness measurement namely Brinell, Vickers, Knoop, and Rockwell. Vickers hardness measurements were used in this study. The formula to calculate the hardness:

$$HV = \frac{2P\ sin(\frac{\theta}{2})}{d^2} = \frac{1.8544P}{d^2} \quad (7)$$

Where P is the applied load in kg, θ is the angle between opposite faces of diamond indenter and d is the average of the two diagonals in mm. The Vickers indenter is a square based diamond pyramid indent with an included angle between opposite faces of 136 ˚. The Vickers Hardness number is defined as the load divided by the surface area of the indentation [84]. Since the loads used are small, the indent size is also small. Therefore for accurate measurement of the diagonal length, a well polished surface is required. Also, the surface should be free from any defects and the specimen should be mounted properly so that the test surface is perpendicular to the axis of the indenter.

Hardness measurements were made on both the manganese and pearlitic crossings: For the manganese crossing (ATP 110), measurements were made on both the wing rail and nose. Vickers hardness measurements with a load of 1kg and a dwell time of 20 seconds were used to study the hardness distributions in the transverse section of the nose and wing rail. A grid of measurements was made at intervals of 2 mm along the transverse direction and 0.3 mm from the rail running surface along the normal direction throughout the transverse section, and from these measurements, hardness maps were constructed. The same procedure was used to measure the hardness distribution of the wing rail of BTP 102 manganese crossing at different locations as shown in Figure 2.12 c & d below. Finally, hardness maps were constructed from the measurements. For the pearlite crossing (AP 104), hardness measurements were made on the wing rail and nose using the same load and dwell time. However, only a few series of measurements were made on the transverse section from the wheel running surface at intervals of 0.3 mm.

Figure 2.12: The areas where hardness measurements were made on the different components of the crossings (a) ATP 110 manganese wing rail, (b) ATP 110 manganese nose, (c) and (d) BTP 102 manganese crossing, the numbers in the figure indicate the area for hardness profile maps, (e) pearlite wing rail showing the surface of hardness measurements and (f) pearlite nose rail showing the surface of hardness measurement.

2.4.2 Tensile Testing

The tensile test is used to obtain the basic mechanical properties of the materials. In the tensile test, a continuously increasing tensile load is applied to the specimen until it breaks. Simultaneous measurements of the elongation are also done. The tests are performed at a specific strain rate as mechanical properties of some materials have strong strain rate dependence. Engineering stress-strain or true stress-strain curves can be constructed from the load elongation data. The important parameters obtained from the stress-strain curve of metal are the tensile strength, yield strength, percent elongation and reduction of area. The initial portion of the stress-strain curve is fairly linear, the stress is linearly proportional to strain. This is the elastic portion of the stress-strain curve which follows the Hooke's law:

$$\sigma = E\varepsilon \quad (8)$$

where σ is the applied stress, E is the modulus of elasticity, and ε the strain experienced by the material. The modulus of elasticity also referred to as Young's Modulus (E) is calculated from the slope of the elastic portion of the curve:

$$E = \text{slope} = \frac{\Delta\sigma}{\Delta\varepsilon} \quad (9)$$

When the stress exceeds a certain value, the material is plastically deformed. This value is called the yield strength of the material. The yield strength is the stress required to produce a small specified amount of plastic deformation. The usual way of determining the yield strength is by the stress corresponding to the intersection of the stress-strain curve for a line parallel to the elastic part of the curve offset by a strain of 0.2%. After the yield point, the material strain hardens and the stress to produce further deformation increases with plastic strain. With continued deformation, the specimen elongates but the cross section decreases uniformly along the gauge length. Initially, the strain hardening rate is more to compensate for the decrease in cross sectional area and the load continues to rise with increasing elongation. After the highest point on the load-elongation curve, called the ultimate point the cross sectional area decreases at a faster rate than the strain hardening rate. Therefore the load and hence the engineering stress required for deformation decreases until fracture occurs [84]. Tensile strength or ultimate tensile strength is the maximum load (P_{max}) divided by original cross-sectional area (A_0):

$$S_u = \frac{P_{max}}{A_o} \quad (10)$$

The ductility of the material is measured either from the % elongation i.e., the engineering strain, expressed in % at the fracture or the % reduction of area at fracture:

$$e_f = \frac{L_f - L_o}{L_o} \ \% \quad (11)$$

where e_f is the engineering strain at fracture also called the % elongation, L_f is the gauge length after fracture and L_o is the original gauge length before the test.

$$q = \frac{A_0 - A_f}{A_o} \ \% \quad (12)$$

where q is the % reduction of area at fracture and A_f and A_0 are the cross sectional area at fracture and before test respectively.

The engineering stress-strain curve does not give the full description of the deformation characteristics of a material because it is based on the original cross sectional area of the specimen which continues to decrease during the test. A material strain hardens all the way to fracture so the stress required for deformation also increases. But since the engineering stress-strain curve is based upon initial cross sectional area, stress falls after maximum tensile strength. The true stress-strain curve is based on the instant cross sectional area of the specimen and continues to increase until failure. This curve is also called the flow curve of the material.

The true stress expressed as:

$$\sigma = \frac{P}{A_0}(e+1) = s(e+1) \quad (13)$$

where σ and ε are the true stress and strain respectively and s and e are the engineering stress and strain respectively. P refers to engineering load and A_o refers to the original cross sectional area. The true strain is expressed as:

$$\varepsilon = ln\,(e+1) \quad (14)$$

Since constancy of volume and a homogeneous distribution of strain along gauge length are assumed, the above equations are applicable only up to the onset of necking.

The flow curve of many metals in the region of uniform plastic deformation can be expressed with a power law relation as:

$$\sigma = K\varepsilon^{n} \quad (15)$$

where n is the strain hardening exponent and K is the strength coefficient. The values of n and K can be obtained from a log-log plot of true stress and true strain up to maximum load.

Tensile tests until failure at room temperature were performed on the two different materials (pearlite and manganese steel) at a strain rate of 10^{-2} s^{-1} on an Instron 8801 100 kN universal testing machine. Cylindrical dog bone shaped specimens having gauge length 10 mm and gauge diameter 5 mm were made from the undeformed portion of the crossings. For the manganese steel, the specimens were obtained from a depth of 15 mm from the surface, as it is assumed that at this depth the area will be free from any service deformation. For pearlite, specimens were taken from the head hardened part only leaving a few millimeters from the running surface which was severely deformed during service.

2.4.3 Fatigue Testing

Metal subjected to repeated cyclic or fluctuating stresses fails at lower stresses than required to cause fracture under monotonic application of load. This phenomenon is called fatigue failure. The fatigue tests can be divided into low cycle fatigue (LCF) and high cycle fatigue (HCF). The LCF often shows plastic strains and lasts up to 10^5 cycles. The HCF is elastic in nature, at least in the beginning, and by definition HCF is over 10^5 cycles. Any fluctuating stress cycle or strain cycle can be considered to be made up of two components, a mean or steady stress or strain and alternating or variable stress or strain. The mean stress or strain is defined as the algebraic mean of the maximum and minimum stress or strain in a cycle:

$$\sigma\,/\,\varepsilon_{\,mean} = \frac{(\sigma/\varepsilon_{max} + \sigma/\varepsilon_{min})}{2} \quad (16)$$

Another important term in this respect is the stress or strain range which is the algebraic difference between the maximum and minimum stress or strain in a cycle:

$$\sigma\,/\,\varepsilon_{\,range} = (\sigma/\varepsilon_{max} - \sigma/\varepsilon_{min}) \quad (17)$$

The alternating stress or strain often expressed as the stress or strain amplitude which is one half of stress or strain range:

$$\sigma/\varepsilon_{\ amplitude} = \frac{(\sigma/\varepsilon_{max} - \sigma/\varepsilon_{min})}{2} \tag{18}$$

Two ratios are used in presenting fatigue data. One is the stress/strain ratio denoted by R which is the ratio of minimum stress/strain to maximum stress/strain and another is the amplitude ratio denoted by A which the ratio of stress/strain amplitude to mean stress/strain:

$$R = \frac{\sigma_{min}}{\sigma_{max}} \tag{19}$$

$$A = \frac{\sigma_{amplitude}}{\sigma_{mean}} \tag{20}$$

LCF tests under strain controlled mode where the strain amplitude is fixed are performed in this work. The specimen is cycled between a maximum and minimum strain and the stress response is measured. The usual way of presenting low cycle fatigue results is by a plot of plastic strain range or amplitude against number of cycles to failure. The Coffin Mansion equation describes the relationship between plastic strain amplitude and fatigue life [85].

$$\frac{\Delta\varepsilon_p}{2} = \varepsilon'_f(2N)^c \tag{21}$$

Where $\Delta\varepsilon_p/2$ is plastic strain amplitude, $\varepsilon_f^{/}$ is the fatigue ductility coefficient, 2N is number of strain reversals to failure and c is the fatigue ductility exponent. $\varepsilon_f^{/}$ and c are considered as material specific parameters [85]. The equation holds true for uniaxial loading. Most components in real life are subjected to multiaxial loading. In rail wheel contact there is both normal and shear stresses acting. Various modified theories have been proposed to predict fatigue life under multiaxial loading [97].

Cyclic stress-strain curves help in assessing the durability of structures and components subjected to repeated loading. The material response of any specimen subjected to cyclic inelastic loading is in the form of a hysteresis loop. The total height of the loop is the stress range and the width of the loop is the total strain range which includes both elastic and plastic strain. The area within the loop is the energy per unit volume which is a measure of the plastic deformation work of the material. An example of a hysteresis loop is shown in Figure 2.13. The material is first loaded in tension and then to compression range after reaching the maximum strain amplitude. Yielding in compression occurs at lower stress upon reversed loading due to the Bauschinger effect [99]. After the initial transient in the stress amplitudes for the first few cycles, the material stabilizes in the subsequent cycles with very little variation in stress amplitude (cyclic stabilization). In some materials, due to high strain hardening, the stabilization phase does not occur. The peak stress amplitude keeps on increasing (cyclic hardening) whereas in some materials the stress amplitude decreases throughout the test (cyclic softening). Finally, cracks start to develop in the material which causes a decrease in peak stress eventually leading to the failure of the material.

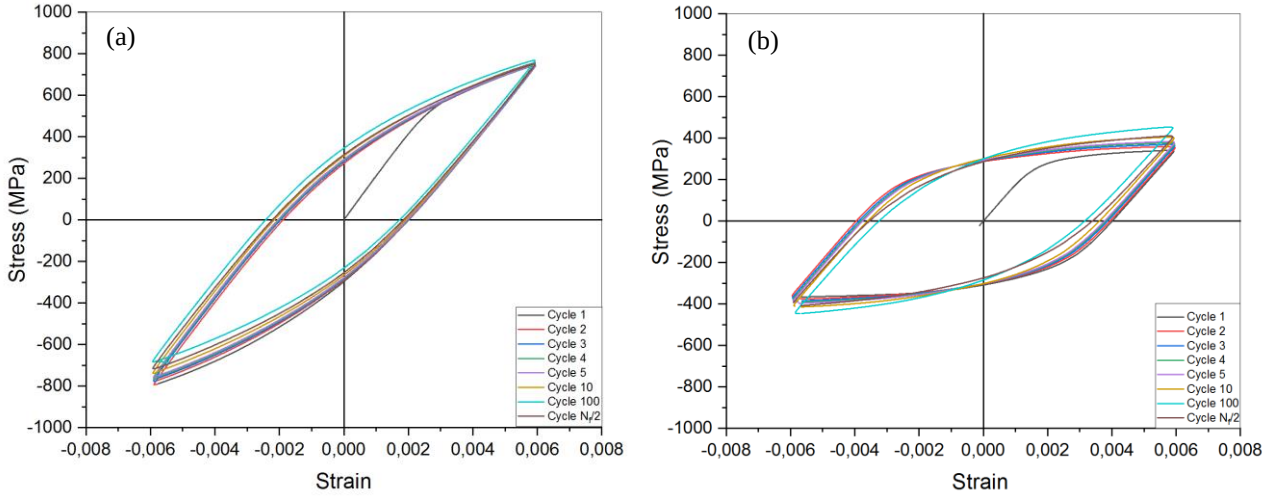

Figure 2.13: Typical Hysteresis loops for strain controlled LCF test in uniaxial cyclic loading with a constant strain amplitude of 0.6%. (a) Head hardened pearlite steel, where the registered stress amplitude decreased throughout the test (b) manganese steel, where the registered stress amplitude increased for the first hundred cycles and then decreases for the remaining life time [own data].

Specimens for the experiments were extracted from actual crossings from the track. For the pearlitic grade, the head hardened part was confined to within the first 20 mm from the surface, after which the hardness falls off from 400 HV to 330 HV. Specimens for fatigue testing were taken from the head hardened part only leaving a few millimeters from the running surface which was severely deformed during service. Thus slight variations in hardness levels in volumes from which the test bars were taken are expected. For the manganese steel, the specimens were obtained from a depth of 15 mm from the surface, as it is assumed that the area will be free from any service deformation. Hardness studies for the pearlitic and manganese grade suggested the depth of deformation during service was confined to first 2-3 mm for the pearlite and 10 mm for the manganese steel. This means that both types of specimens were essentially free from any in-service deformation. A schematic diagram of the fatigue specimens is given in Figure 2.14. The specimens had a gauge diameter of 10 mm and a gauge length of 20 mm. The specimens were ground and polished to mirror finish before testing. Low cycle strain controlled fatigue tests (strain amplitude was kept constant) were performed using a strain rate of 10^{-2} s^{-1} on an MTS 809 axial/torsion testing system. All tests were conducted at room temperature. The conditions for the tests were:

1. Uniaxial (tension-compression) tests at strain amplitudes of 0.6%, 1% and 1.5%.

(a) For 0.6% strain amplitude, tests were done at 0 mean strain (R=-1) and with a compressive mean strain of 0.9% (R= 5).

(b) For the 1% strain amplitude tests were done at 0 mean strain (R=-1) and with a compressive mean strain of 0.5% (R=-3).

(c) For 1.5% strain amplitude tests were done at 0 mean strain (R=-1).

2. Pure torsion tests at shear strain amplitudes of 1.3 % and 2.16% (R=-1).

3. In and out of phase biaxial tests under tension-compression and torsion at strain amplitudes which would give equivalent strain amplitudes of 0.6% and 1%. Both axial and shear strain maintained R=-1.

A schematic diagram of the strain loading paths under fatigue is shown in Figure 2.7.

According to von Mises theory [100], the equivalent strain, axial strain, and shear strain can be related as:

$$\varepsilon_{eq} = \sqrt{\varepsilon^2 + \frac{\gamma^2}{3}} \tag{22}$$

where ε_{eq} is the equivalent strain, ε is the axial strain and γ is the shear strain.

In the case of uniaxial loading, there is no shear strain and the equivalent strain is the same as axial strain. In the case of pure torsion, to obtain an equivalent strain amplitude of 0.6% or 1%, the shear strain should be 1.04% and 1.732% respectively. However, in the case of torsion, a strain gradient is obtained with the maximum at the surface and zero at the center. For pure torsion tests, surface strain amplitudes were calculated to be 1.3% and 2.16% assuming the strain decreases linearly from the surface. For biaxial tests at equivalent strain amplitude of 0.6% and 1%, both in-phase (0 ˚ phase difference) proportional and out of phase (90 ˚ phase difference) nonproportional loadings were conducted. For this case, the axial strain was selected to be 0.424% and the shear strain was 0.735% to obtain an equivalent of 0.6% strain. For 1% equivalent strain the axial strain and shear strain were calculated to be 0.707% and 1.225 % respectively. A schematic diagram of the different strain amplitude variations under the various loading conditions is shown in Figure 2.15-2.16.

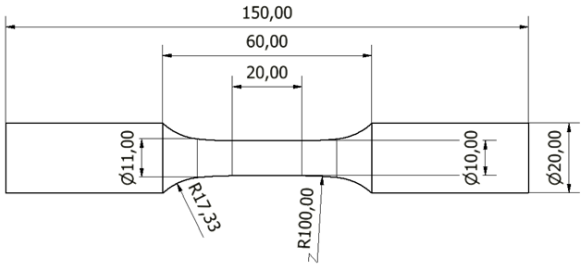

Figure 2.14: Specimen geometry of the specimen used for fatigue testing (All dimensions in mm)

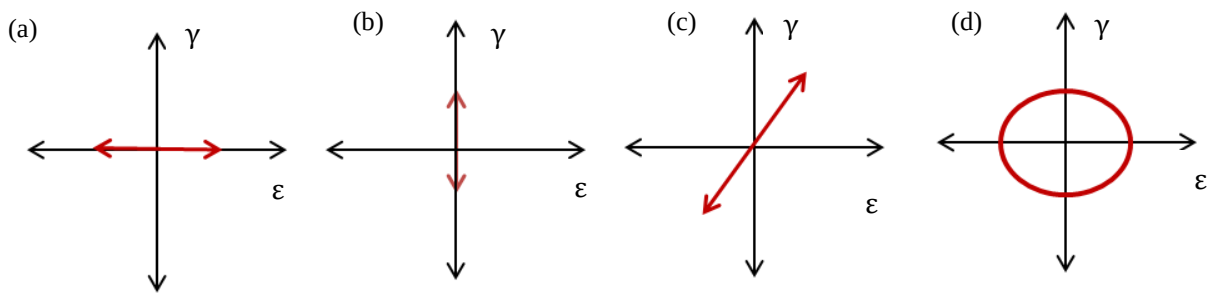

Figure 2.15: Schematic diagram of the loading strain paths for different conditions of fatigue testing (a) linear axial (uniaxial), (b) linear shear (pure torsion), (c) linear with axial and shear in phase loading (biaxial proportional loading) and (d) circular with axial and shear strain out of phase loading (biaxial non proportional loading).

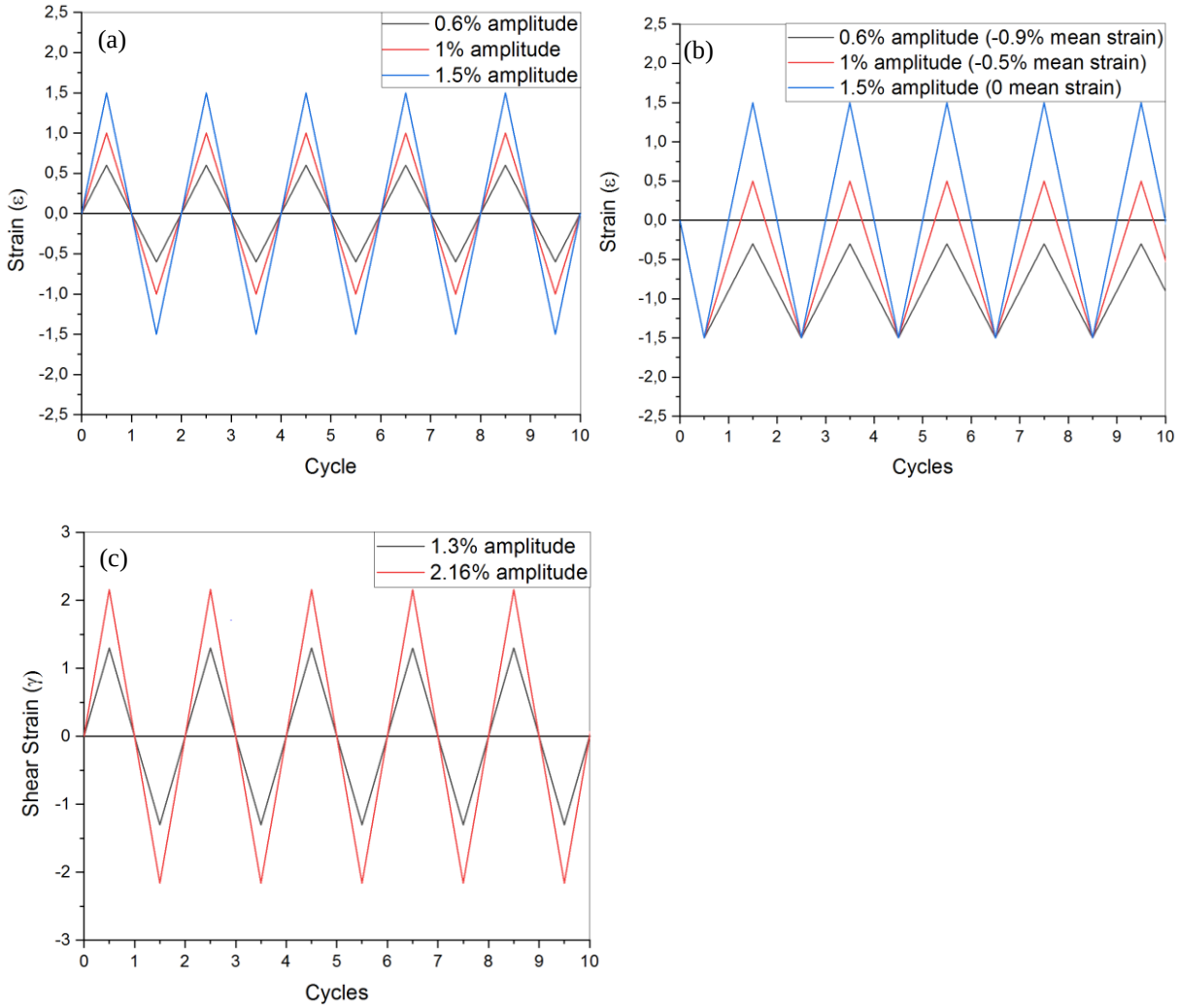

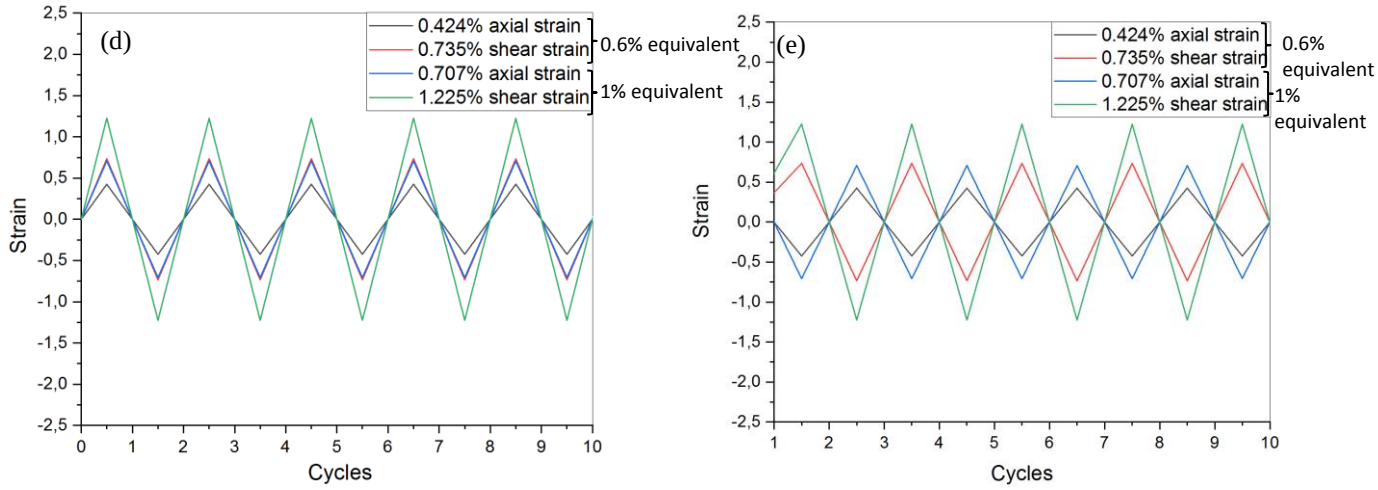

Figure 2.16: Schematic diagram of the load time history for the different conditions of fatigue testing (a) uniaxial loading at different strain amplitudes with 0 mean strain (R=-1), (b) uniaxial loading with different strain amplitudes and different mean strains but the same minimum strain of -1.5%, (c) pure torsion tests at different shear strain amplitudes (R=-1), (d) biaxial in phase tension-compression and torsion at equivalent strain amplitude of 0.6% and 1% and (e) biaxial out of phase tension-compression and torsion at equivalent strain amplitude of 0.6%. and 1%.

Intermittent uniaxial fatigue testing at different intervals of time was also done to study the evolution of microstructure during fatigue for the pearlite steel. The material was subjected to 0.4% strain amplitude and the tests were interrupted at 0.4 cycle, 100 cycles and finally failure. These fatigue tests were conducted at a strain rate of 10^{-2} s^{-1} on an 8801 100 kN servo hydraulic universal testing machine at room temperature. The specimens had a gauge length of 10 mm and a gauge diameter of 5 mm.

2.5 Material Characterization

2.5.1 Optical Microscopy

Optical microscopes can be used to investigate the microstructure at relatively low magnifications. It consists of a light source or illumination system, objective lens, eyepiece, photo micrographic system, and specimen stage. Light rays from the object first converge at the objective lens and are then focused to form a magnified inverted image. The light path then goes through an eyepiece to form a virtual image on the human eye retina. A modern microscope is commonly equipped with a device to switch from eyepiece to projector lens for either recording images on photographic film or sending images to a computer screen [101]. The damaged and deformed microstructure of the wing and nose of the pearlite and manganese crossings as well as the deformed structure of the fatigued manganese and pearlitic steel specimens were studied by optical microscopy. The specimens for optical microscopy were first ground with Si-C paper ranging from grain 320 to 4000 followed by polishing by diamond paste to 1 µm. Finally, the specimens were etched with 4% Nital.

2.5.2 Scanning Electron Microscopy (SEM)

The scanning electron microscope has better spatial image resolving capabilities due to the lower wavelength of radiation and better depth of field to explore finer details in the microstructure. In SEM, a beam of electrons emitted

from an electron gun is focused down on the specimen surface with the help of condenser and magnetic lenses. This results in the formation of a pear-shaped interaction volume within the specimen. Electron material interaction leads to the emission of back scattered electrons, secondary electrons as well characteristics X-rays which are then detected by different detectors. The images in the SEM can either be due to electrons which are back scattered from or near to the surface of the specimen, the contrast of which strongly depends on the atomic number and crystallographic orientation of the specimen, or due to the secondary electrons which helps in external morphology and topographical investigations. SEM can also be used to study the microstructures, revealing texture, defects, grain morphology and deformation through electron back scattered diffraction mode (EBSD). In EBSD arrangement, the specimen is mounted at a 70^{o} tilt to the incident electron beam. The electron beam is diffracted from the specimen and a pattern of Kikuchi lines is obtained on the phosphor screen. The positions of the Kikuchi bands can be utilized to determine the orientation of the diffracting crystal. The analysis of these Kikuchi lines helps the determination of orientation and texture of grains. In this study, the SEM was used in the EBSD mode to study the deformation structure of the nose of the manganese steel crossing and also in secondary electron imaging mode to study the fracture surface of the deformed fatigue specimens.

A Zeiss Supra-35 scanning electron microscope, equipped with HKL Channel 5 EBSD system was used in the present study. The EBSD measurements were made using an acceleration voltage of 20 kV, aperture size of 60 µm and a working distance of 13.3 mm. The focus of this study was to investigate the highly deformed microstructure near the surface cracks in the nose of the manganese crossing. A specimen was cut from a damaged nose, as shown in Figure 2.17, having dimensions 40x5x20 mm. The transverse surface of the specimen was ground with Si-C paper ranging from grain 320 to 4000 followed by polishing by diamond paste to 1 µm. The final polishing consisted of colloidal silica or OPS for 40 minutes. The specimen was scanned on the transverse surface in a square grid with a step size of 0.5µm.

Figure 2.17: Nose of ATP 110 manganese crossing showing the region where specimen for EBSD scanning was obtained.

2.5.3 Transmission Electron Microscopy

The transmission electron microscope (TEM) has better spatial resolution compared to SEM. The operative voltage range from 100-300 kV and the lower wavelength of the electrons allows resolutions below 1 nm. The TEM can also be used for different operation modes, but for this study, the TEM has been used for imaging only. The TEM system consists of the electron gun, electromagnetic lenses and a viewing screen, all enclosed in a vacuum. The electron from the gun passes through the lenses and is focused on a very thin specimen. Thin specimens are required to allow the electrons to transmit through the thickness of the specimen. Two types of interactions occur with the specimens namely, either the electrons get diffracted or the electrons remain parallel to their initial path and transmit through the

specimen. After passing through the specimen the electrons are focused again by an objective lens and create an intermediate image which finally produces a magnified image after passing through a projector lens on a fluorescent screen, photographic film or on a CCD camera.

A Jeol 2000FX electron microscope operating at 200KV was used in this work. The deformed microstructure of the two types of steel after fatigue testing under different loading conditions was studied. The dislocation density and also the stacking fault width were calculated from the TEM images by using a linear intercept method. Test lines were drawn randomly in areas showing dislocations in the micrographs and the dislocation density was calculated as:

$$\rho d = N/Lxt \tag{22}$$

where N is the number of dislocations intersecting the given drawn line, L is the length of the line and t is the thickness of the foil.

The specimens for TEM studies were obtained from the gauge part of the fatigue deformed specimens. The transverse surface was studied and specimens were obtained as close to the surface as possible. Thin TEM foils were prepared by electropolishing down to 0.1-0.5 μm thickness so that electrons can pass through it. Thin slices are cut from bulk specimens and then electropolished until a small hole appears in the middle of the slice which indicates the area near the hole is thin enough for electrons to pass. Typically, large areas transparent for the electrons were obtained.

3. Summary

This section contains a summary of results obtained from the experimental and analysis work carried out for this thesis. Five papers were written based on the results obtained, focusing mostly on the manganese steel. The main findings of the papers are summarized here. Apart from the results reported in the papers, some additional results are also presented.

3.1 Results from the papers

3.1.1 Crack formation within a Hadfield manganese steel crossing nose (Paper 1)

This paper focuses on the microstructure and crack network in a damaged Hadfield manganese steel crossing nose. The damage and deformation have been studied by hardness measurements, optical microscopy and scanning electron microscopy (SEM) including electron back scattering diffraction (EBSD). The complex crack network within the nose of the crossing has been investigated using 3D X-ray tomography. Rail wheel contact causes high deformation hardness of over 600 HV and the strain hardening extends up to a depth of about 10 mm from the running surface. Microscopy indicates that the deformation microstructure is composed of both deformation twins and deformation induced dislocation boundaries. Extensive crack networks with both surface and subsurface cracks having crack branching and shielding have been observed. Microstructure plays an important role in the crack behavior. The crack propagation is predominately transgranular with the cracks mostly following a path free from twins through relatively soft grains causing waviness in the crack path. The crack network is confined in top layers of the plastically deformed rail with surface cracks at shallow angles to the surface and after reaching a certain depth of 2-3 mm, they run parallel to the contact surface. The hardening and the deformation of the manganese steel are quite different from that of commonly used pearlitic rail steels but the crack morphologies are found to be quite similar for both of them.

3.1.2 2D and 3D characterization of rolling contact fatigue cracks in manganese crossing wing rails (Paper 2)

This paper focuses on the microstructure and crack network in damaged Hadfield manganese steel crossing wing rails. Damaged and deformed wing rails of a manganese steel crossing were studied through characterization of the microstructure, hardness, and 3D crack network. High deformation induced hardness of over 600 HV which is three times that of the base material and also strain hardening up to a depth of about 10 mm from the running surface was observed which is similar to what observed in case of the nose of the manganese crossing studied in paper 1. Rail wheel interaction causes high deformation and a high density of the deformation induced twins and dislocation boundaries in the austenitic grains near the surface with decreasing density away from the surface. Presence of cracks parallel to the running surface was observed through 3D X-Ray tomographic reconstruction. While most of the cracks run parallel to the running surface, the crack network is extensive and continuous. The damage and deformation in the manganese wing rail are found to be quite similar to the manganese nose rail studied previously although the geometry and loading of a wing rail are different from the nose. Cracks were mostly observed at regions having relatively less hardness than regions which had a higher hardness. The change of rolling planes from wing rail to nose, or vice versa, introduces high impact stresses which most likely are the reason for the crack formation beside the plastic deformation.

3.1.3 Synchrotron X-Ray measurement of residual strain within the nose of a worn manganese steel railway crossing (Paper 3)

In this work, the residual strains inside the bulk of a damaged nose of a manganese steel crossing have been investigated by using differential aperture synchrotron X-ray diffraction. The main purpose of this paper was to describe how this method allows non-destructive measurement of local micro residual strains in selected local volumes in the bulk of the nose. To the best of my knowledge, this is the first time synchrotron radiation was employed to measure the strains in a nose of a manganese railway crossing. Measurements were made at a depth of 6.5 mm from the rail wheel contact surface and significant compressive strains were present along the longitudinal direction even at such high depths. Residual stresses alter the state of stress in the material which affects further deformation and damage in the material, especially the crack propagation. Therefore further work on the residual stress measurements on the nose of the same crossing was done and explained in paper 4.

3.1.4 Synchrotron and laboratory X-ray measurements of residual strains in manganese steel from a railway crossing (Paper 4)

In this work, two X-ray techniques were applied to quantify the residual stresses in the nose of the manganese crossing. Conventional laboratory X-ray $\sin^2\psi$ method was used to determine the macro (Type I) stresses along the running surface and perpendicular to it while differential aperture synchrotron X-ray diffraction was used to determine the local micro (Type II/Type III) strains along the longitudinal direction (i.e. running direction) at four different depths down to 15 mm from the rail surface. Besides the information on the magnitude of the residual stresses in the worn nose, the potentials and limitations of the two X-ray methods for the present component are also discussed. High compressive stresses, as large as 615 MPa, have been observed on the hardened rail-wheel interaction surface which is higher than the yield strength of the undeformed material. The presence of cracks reduces the residual stress significantly to around one-fifth of the original value. Micro X-ray measurements of residual revealed significant residual strains when measured on the transverse surface of the nose which could not be detected by macro X-ray measurements due to the lower penetration depth of the laboratory X-rays and significant stress relaxation on the cut transverse surface. The micro X-Rays shows that the residual strains at a depth of 15 mm it is more than twice as large than at depths of 3, 4 and 6.5 mm. This increase in residual strain at the large depth is related to an interaction of elastic and plastic deformation. The large compressive residual stresses at e.g. 15 mm depth may contribute to explaining why cracks generally move parallel to the surface at certain depths instead of continuing perpendicular to the surface deep into the material.

3.1.5 Multi-axial Fatigue Deformation of Head Hardened Pearlitic and Austenitic Hadfield railway steels: A comparative study (Paper 5)

In this paper, a comparative study on the cyclic deformation characteristics and fatigue behavior of a head hardened pearlitic and Hadfield manganese steel have been made and explained with respect to low cycle fatigue behavior under conditions of uniaxial and biaxial, as well as proportional and non-proportional, loading. Also, the different microstructures developed in the two different types of steels are compared and related to mechanical properties. Low cycle fatigue tests at 0.6% strain amplitude were performed. Distinct difference in the cyclic response of the two materials was obtained. While profound hardening was observed in case of manganese steel, the pearlitic steel showed cyclic softening behavior except for biaxial loading where initial hardening for the first one or two cycles was observed.

Pearlite steel was insensitive to mean strain application but the manganese steel showed significant hardening due to mean strain. The maximum hardening is observed in case of biaxial non-proportional loading due to activation of multiple slip systems for both the steels, however, the hardening is more significant in the case of manganese compared to pearlite. The optical microscopy reveals no observable changes in the morphology of the phases in the microstructure of pearlitic steel under the different loading cases. TEM images also reveal the dislocation morphologies are similar in all the samples where threading dislocations and dislocation tangles have been observed in all three samples. The variation in mechanical properties can be attributed to the change in dislocation density in the ferrite channels. The biaxial out of phase loading leads to maximum dislocation density leading to highest hardening and stress/torque amplitudes. Deformation of manganese steel caused the formation of deformation bands in the austenite grains. TEM micrographs reveal the microstructures in manganese steel under different conditions are composed of dislocation cells with dislocation tangles inside, intersected by straight stacking fault lamellae. Under uniaxial loading, dislocation cell structure formation is the prominent mechanism but when the shear mode is introduced in bi-axial low cycle fatigue test, formation and growth of stacking faults play an important role together with the dislocations. Higher dislocation density with low stacking fault width is observed for biaxial out of phase loading causing maximum hardening.

3.1 Additional Results

3.1.1 Characterization of damage within a head hardened pearlitic steel crossing

The damage and deformation of the wing rail and nose of a pearlitic steel crossing have been studied by optical microscopy, hardness measurements, and 3D X-ray tomography. Rail wheel interaction induces normal and shear loads which cause shearing of grains towards the rolling direction in the pearlitic structure. The contact area of the wheel with the rail influences deformation which is evident from the higher depths of shearing of the gauge corner region than in regions near the center of rail head. The hardness of the deformed surface layer was around 500 HV and the hardening extended up to a depth of about 2-3 mm from the running surface. The nose of the crossing was repair welded. Multiple surface and subsurface cracks, as well as porosities, were found in the weld layer. Improper welding has resulted in the formation of defects in particular porosities and cracks growing from them. 3D X-ray tomography of the defects and crack network revealed multiple pores of various shapes and dimensions with sizes as large as 1 mm are present. Some of the pores are connected to the surface (for example through a crack) whereas many pores are deep inside the specimen.

3.1.2 Mechanical testing of two different rail steels used in crossings

The main focus of this work was to do a comparative analysis of the mechanical properties and deformation characteristics of two different grades of steels used for crossings: head hardened pearlite and austenitic manganese steel. Room temperature tensile testing, as well as low cycle fatigue uniaxial (at 1% and 1.5% strain amplitudes), biaxial experiments (at 1% equivalent strain amplitude) and pure torsion experiments (at 0.8 and 1.3% equivalent strain amplitudes), was performed. The microstructural analysis of the fatigue deformed specimens was made to correlate the mechanical behavior with the mechanical properties. The uniaxial tensile test results reveal that pearlitic steel, which is harder compared to manganese steel, strain hardens rapidly and saturates due to the low value of strain hardening exponent (n=0.2). Manganese steel is soft compared to pearlitic steel but strain hardens steadily, with a constant work hardening rate over a large strain range with a higher strain hardening exponent of 0.4. The low cycle fatigue behavior

of the two materials was similar to the behavior as described in paper 5 for tests performd at the lower strain amplitude of 0.6%. Hardening was observed in case of manganese steel, and softening for pearlitic steel, except for the biaxial loading. For uniaxial loading, at lower strain amplitude the plastic strain energy density per cycle is nearly equivalent for both the materials but at higher amplitudes the pearlitic steel has higher plastic strain energy density per cycle compared to the manganese steel. Higher number of cycles to failure was observed for pearlitic steel under all cases of uniaxial loading compared to the manganese steel and thus caused much higher accumulated plastic strain energy. Both the Coffin-Manson strain life model and the energy life model gave a good match between the modeled and actual number of cycles to failure. Pure torsion loading gave improved fatigue life due to a delay in crack initiation for both the materials. In biaxial loading, the maximum hardening was observed in case of non-proportional loading, similar to that reported in paper 5. However, the hardening is more significant in the case of manganese steel compared to pearlitic steel and at high amplitudes, the stress/torque amplitude for manganese steel is higher compared to pearlitic steel. The rate of hardening increases linearly with strain amplitude. For pearlitic steel, the cyclic softening is less compared to other conditions of loading because it is compensated by non-proportional hardening.

4. Conclusions and Outlook

4.1 Conclusions

This thesis focuses on the mechanical and microstructural properties of manganese steel railway crossings. The combined effect of contact, impact and frictional loading on manganese crossings after several years of service have been evaluated in terms of the microstructural changes and crack formation, comparing it to normal track behavior. Residual stress in a failed manganese nose was measured and correlated with the crack direction in the nose. In addition, low cyclic fatigue testing under different loading conditions has been done for both pearlitic and manganese steel used in crossings, where a comparative analysis of the mechanical and microstructural properties has been done. A main aspect of this investigative work was to apply non-conventional experiment techniques like 3D X-ray tomography, synchrotron X-ray radiation and biaxial fatigue testings on a crossing component for the first time for a detailed investigation for S&C components.

This work has shown:

1. Investigations of damaged manganese steel crossings extracted from track showed an extensive transgranular crack network which mostly followed a path free from twins through relatively soft regions within the grains. Presence of both surface and subsurface cracks was observed with most cracks confined within the first few millimeters from the running surface. The manganese steel work hardened to a larger degree than standard pearlitic rail steel, evident from the depth of hardening extending up to 10 mm from the contact surface with a hardness of 600 HV at the surface. The deformed microstructure contained a high density of deformation induced dislocation boundaries and twins. Though the deformed microstructure is different from that of pearlitic steel, the crack morphologies were found to be similar to those in pearlitic steel straight tracks, with mostly shallow cracks that return to the surface.

2. Residual stress measurements were performed on the damaged nose extracted from the manganese steel crossing by synchrotron and laboratory X-ray diffraction techniques. It is the first time synchrotron X-ray have been used to determine the local distribution of micro strains in a railway crossing. The synchrotron X-ray micro strain measurements could determine strains at depths from the measured surface which was not possible to access with laboratory X-ray diffraction. Significant macro compressive residual stresses were observed in the manganese steel crossing on the running surface by standard laboratory X-ray diffraction measurements. The synchrotron measurements reveal that residual stresses were also present at distances below the running surface. The residual stresses at distances of 3, 4 and 6.5 mm from the running surface are nearly comparable but those at greater depths were significantly higher. The effect of crack on residual stress is evident as the presence of cracks near the surface of the nose released the residual stresses significantly to very small values.

3. Mechanical testing on head hardened pearlite and manganese steel from railway crossings revealed differences in both the static and cyclic response. The pearlite steel was found to have high yield strength but limited work hardening capability over small plastic strain, thus pearlite is a good candidate for fatigue loading where the

plastic deformation is limited. The manganese steel was capable of accommodating large plastic deformation and having extensive work hardening over a large plastic strain range, retaining its capability to absorb plastic energy. Therefore, it might be a good candidate material for impact loading which occurs at the crossing. Manganese steel also has less ductility exhaustion in fatigue compared to pearlite steel and can accommodate larger plastic deformation in non-proportional loading as well as in mean strain applications, which is a typical case for railway crossing. Microstructural analysis of the fatigue specimens revealed that the deformed microstructure of the pearlitic steel is dominated by slip only, while the microstructures in manganese steel are composed of dislocations, stacking faults and a few twins. Therefore additional hardening in manganese steel is imparted to stacking faults and twinning along with dislocation slip.

Seen in the bigger perspective it can be concluded that:

The crack network in the failed crossing nose can be correlated to the state of stress in the material. Crack propagation in preferred directions are sometimes related to connecting high strain energy zones formed due to the residual/external stress distribution and thereby forming a crack network which releases the residual stress. The stresses developed in a crossing nose component are mostly compressive in nature and maybe highest at higher depths from the surface. This could be one of the explanations why cracks are mostly confined to the top few millimeters from the surface of the nose rather than moving down into the material.

Although the biaxial tests were performed to replicate the rail wheel contact situation in a crossing, the microstructure characterization indicated this was not entirely successful. Hardness measurements on the failed fatigue deformed manganese steel specimens indicated the maximum hardness at the surface reached up to 350Hv in biaxial 0.6% strain tests, which is far below the 600Hv found in the extracted crossing components at the running surface. The microstructure obtained from the failed crossing nose also showed extensive twinning along with dislocation induced boundaries, however only a few twins were observed in 0.6% strain amplitude fatigue specimens. Therefore, this indicates the biaxial fatigue tests done, could not correlate exactly to the real in service conditions in tracks. One reason could be the impact loading existent in the tracks, which was not replicated in these tests, could lead to higher deformation and work hardening. It should also be considered that the loading during testing was displacement controlled rather than force controlled as in real crossings, which could cause a difference in behavior.

This work has significantly advanced the understanding on the topic of microstructure and mechanical properties of railway crossing steel. For the first time, cracks in crossing components have been mapped in 3D, providing information on damage mechanism and crack propagation that could be used in the maintenance of manganese steel crossings. Mapping the length and depth of the crack network will be helpful for scheduling grinding or welding procedures. The residual stress developed during service in a crossing nose was measured for the first time. This helps explain the crack propagation and will be useful for designing future crossing components. For the first time, a comparative study has been carried out on the cyclic response of two different crossing steels under biaxial loading conditions. Although the tests could not replicate the exact rail wheel situation in crossing, the difference in mechanical properties between the two steels could be understood based on the microstructural differences, and the suitability of the

two materials under different conditions of loading could be explained. Finally, the extensive experimental data obtained during this work could be used for future modelling and simulations works on crossings under complex loading situations.

4.2 Outlook

While this work has provided useful insight into the microstructure and fatigue properties of railway crossings, a more in depth investigation on certain topics could be carried out, which time limitations did not allow for during this work.

Further low cycle fatigue studies of the strengthening mechanisms and microstructural changes in manganese steel crossings are needed. An important concern here is that, only a few twins were found in 0.6% tests compared to the extracted crossing. There was not enough time to do TEM studies of the 1% strain amplitude fatigue tests. Studies of the evolution of microstructure with number of cycles using intermittent fatigue testing should also be done at different fractions of the life cycle for different types of loading.

Other types of tests conducted under controlled conditions would also be relevant for mechanical behavior in crossings. Since the loading is force controlled rather than displacement controlled in crossings, stress controlled fatigue tests can also be relevant for comparative studies. The development and evolution of cracks could be studied in rolling contact fatigue tests in order to investigate the crack initiation, direction and branching in manganese steel with respect to the microstructure. Also impact toughness tests (Charpy V notch tests) would be highly relevant for crossings, as well as fracture toughness tests together with fatigue crack growth tests.

The residual stress in the nose of the manganese crossing has been studied in this work to some extent, but a more detailed stress mapping on a bulk component of the nose through synchrotron X-ray diffraction with all the three components and its relation with cracks should be studied. Residual stresses alter the state of stress in the material effecting crack propagation mechanism and hence needs to be included when interpreting failure mechanisms, and should be considered both in design and lifetime predictions of crossings.

In the larger perspective, it would be of great value for rail infrastructure providers, if metallurgical investigations, methods and results as those presented in this thesis, could be incorporated into their maintenance scheme. Here it would be beneficial to relate the presence and extend of cracks and other faults to signals recorded by the measuring car, various sensor systems mounted on S&Cs, noise measurements and alike, which are tools the infrastructure providers already use or possibly will use in the future.

References

[1] https://ec.europa.eu/eurostat/statistics-explained/index.php/Archive:Transport_accident_statistics.

[2] V. Eksler, Intermediate report on the development of railway safety in the European Union, May 2013. https://www.era.europa.eu/sites/default/files/library/docs/safety_interoperability_progress_reports/railway_safety_performance_2013_en.pdf.

[3] H. Schwarz, Improving the sustainability of transport-the rail sector as a case study, New York 2011.

[4] White Paper on transport-Roadmap to a single European transport area-Towards a competitive and resource-efficient transport system, 2011. https://ec.europa.eu/transport/sites/transport/files/themes/strategies/doc/2011_white_paper/white-paper-illustrated-brochure_en.pdf.

[5] INTELLISWITCH project website: http://www.intelliswitch.dk/about-us.

[6] J. E. Garnham and C. L. Davis, Very early stage rolling contact fatigue crack growth in pearlitic rail steels, Wear 271 (2001) 100-112.

[7] J. E. Garnham and C. L. Davis, The role of deformed rail microstructure on rolling contact fatigue initiation, Wear 265 (2008) 1363-1372.

[8] H. C. Eden, J. E. Garnham and C. L. Davis, Influential microstructural changes on rolling contact fatigue crack initiation in pearlitic rail steels, Materials Science and Technology 21(6) (2005) 623-629.

[9] J. E. Garnham, F. J. Franklin, D. I. Fletcher, A. Kapoor and C. L. Davis, Predicting the life of steel rails, Proceedings of the Institution of Mechanical Engineers, Part F: Journal of Rail and Rapid Transit 221(1) (2007) 23-33.

[10] S. L. Graissie, Rolling contact fatigue on the British railway system: treatment, Wear 258 (2005) 1310–1318.

[11] M. Matsui and Y. Kamiya, Evaluation of material deterioration of rails subjected to rolling contact fatigue using x-ray diffraction, Wear 304 (2013) 29-35.

[12] W. Lojkowski, M. Djahanbakhsh, G. Bürkle, S. Gierlotka, W.Zielinski and H. J. Fecht, Nanostructure formation on the surface of railway tracks, Materials Science and Engineering: A 303 (1-2) (2001) 197-208.

[13] H.W. Zhang, S. Ohsaki, S. Mitao, M. Ohnuma and K. Hono, Microstructural investigation of white etching layer on pearlite steel rail, Materials Science and Engineering A 421 (2006) 191-199.

[14] A. Johansson, B. Palsson, M. Ekh, J. C. O. Nielsen, M. K. A. Ander, J. Brouzoulis and E. Kassa, Simulation of wheel-rail contact and damage in switches & crossings, Wear 271 (2011) 472-481.

[15] D. Nicklisch, E. Kassa, J. Nielsen, M. Ekh and S. Iwnicki, Geometry and stiffness optimization for switches and crossings, and simulation of material degradation, Proceedings of the Institution of Mechanical Engineers, Part F: Journal of Rail and Rapid Transit 224 (2010) 279-292.

[16] C. Wan, V. L. Markine and I. Y. Shevtsov, Improvement of vehicle–turnout interaction by optimising the shape of crossing nose, Vehicle System Dynamics: International Journal of Vehicle Mechanics and Mobility 52 (2014) 1517-1540.

[17] B. A. Palsson and J. C.O. Nielsen, Wheel–rail interaction and damage in switches and crossings, Vehicle System Dynamics: International Journal of Vehicle Mechanics and Mobility 50 (1) (2012) 43-58.

[18] B. A. Palsson, Optimisation of Railway Switches and Crossings, PhD thesis, Department of Applied Mechanics, Chalmers University of Technology, 2014, Sweden.

[19] B. Lv, M. Zhang, F. C. Zhang, C. L. Zheng, X. Y. Feng, L. H. Qian and X. B. Qin, Micro-mechanism of rolling contact fatigue in Hadfield steel crossing, International Journal of Fatigue 44 (2012) 273–278.

[20] L. Qian, X. Feng and F. Zhang, Deformed microstructure and hardness of Hadfield high manganese steel, Materials Transactions 52(8) (2011) 1623-1628.

[21] X. Y. Feng, F.C. Zhang, C.L. Zheng and L. Bo, Micromechanics behavior of fatigue cracks in Hadfield steel railway crossing, Science China Technological Sciences 56 (5) (2013) 1151–1154.

[22] F. C. Zhang, B. Lv, T. S. Wang, C. L. Zheng and M. Li, Microstructure in working surface of Hadfield steel crossing, International Journal of Modern Physics B 23 (2009) 1185-1190.

[23] J. F. Kelleher, D. J. Buttle, P. M. Mummery and P. J. Withers, Residual Stress Mapping in Railway Rails, Materials Science Forum 490-491 (2005) 165-170.

[24] K. H. Lo, P. Mummery and D. J. Buttle, Characterisation of residual principal stresses and their implications on failure of railway rails, Engineering Failure Analysis 17 (2010) 1273-1284.

[25] J. Kelleher, M. B. Prime, D. Buttle, P. M. Mummery, P. J. Webster, J. Shackleton and P. J. Withers, The measurement of residual stress in railway rails by diffraction and other methods, Journal of Neutron Research 11(4) (2003) 187-193.

[26] T. Sasaki, S. Takahashi, Y. Kanematsu, Y. Satoh, K. Iwafuchi, M. Ishida and Y. Morii, Measurement of residual stresses in rails by neutron diffraction, Wear 265 (2008) 1402-1407.

[27] J. H. Xiao, F. C. Zhang and L. H. Qian, Contact stress and residual stress in the nose rail of a high manganese steel crossing due to wheel contact loading, Fatigue and Fracture of Engineering Materials and Structures 37 (2014) 219-226.

[28] J. Kang, F. C. Zhang, X. Y. Long, B. Lv, Cyclic deformation and fatigue behaviors of Hadfield manganese steel, Materials Science and Engineering A 591 (2014) 59-68.

[29] C. Chen, B. Lv, F. Wang and F. Zhang, Low-cycle fatigue behaviors of pre-hardening Hadfield steel, Materials Science & Engineering A 695 (2017) 144-153.

[30] M. Wiest, W. Daves, F. D. Fischer and H. Ossberger, Deformation and damage of a nose rail due to wheel passages, Wear 265 (2008) 1431–1438.

[31] R. Harzallah, A. Mouftiez, E. Felder, S. Hariri and J. P. Maujean, Rolling contact fatigue of Hadfield steel X120Mn12, Wear 269 (2010) 647–654.

[32] J. Xiao, F. Zhang and L. Qian, Numerical simulation of stress and deformation in a railway crossing, Engineering Failure Analysis 18(8) (2011) 2296-2304.

[33] S. L. Guo, D. Y. Sun, F. C. Zhang, X. Y. Feng and L. H. Qian, Damage of a Hadfield steel crossing due to wheel rolling impact passages, Wear 305 (2013) 267-273.

[34] M. Pletz, W. Daves and H. Ossberger, A wheel passing a crossing nose: Dynamic analysis under high axle loads using finite element modelling, Proceedings of the Institution of Mechanical Engineers, Part F: Journal of Rail and Rapid Transit 226(6) (2012) 603-611.

[35] A. Ekberg, B. Akesson and E. Kabbo, Wheel/rail rolling contact fatigue-Probe, predict, prevent, Wear 314(1-2) (2014) 2-12.

[36] G. Donzella, M. Faccoli, A. Ghidini, A. Mazzù and R. Roberti, The competitive role of wear and RCF in a rail steel, Engineering Fracture Mechanics 72 (2005) 287-308.

[37] C. Jones, W. R. Tyfour, J. H. Beynon and A. Kapoor, The effect of strain hardening on shakedown limits of a pearlitic rail steel, Proceedings of the Institution of Mechanical Engineers, Part F: Journal of Rail and Rapid Transit 211(2) (1997) 131-140.

[38] M. Schilke, N. Larijani and C. Persson, Interaction between cracks and microstructure in three dimensions for rolling contact fatigue in railway rails, Fatigue and Fracture of Engineering Materials and Structures 37(3) (2014) 280–289.

[39] A. Ekberg, Rolling contact fatigue of railway wheels-a parametric study, Wear 211(2) (1997) 280-288.

[40] S. Dhar, H. K. Danielsen, S. Fæster, C. J. Rasmussen, Y. Zhang and D. Juul Jensen, Crack formation within a Hadfield manganese steel crossing nose, Submitted to Journal of Wear.

[41] S. Dhar, H. K. Danielsen, S. Fæster, C. J. Rasmussen and D. Juul Jensen, 2D and 3D characterization of rolling contact fatigue cracks in a manganese steel crossing wing rail, Submitted to Journal of Wear.

[42] J. W. Ringsberg, Life prediction of rolling contact fatigue crack initiation, International Journal of Fatigue 23(7) (2001) 575-586.

[43] J. W. Rinsberg and A. Bergkvist, On propagation of short rolling contact fatigue cracks, Fatigue and Fracture of Engineering Materials and Structures 26 (2003) 969-983.

[44] R. Heyder and G. Girsch, Testing of HSH® rails in high-speed tracks to minimise rail damage, Wear 258(7-8) (2005) 1014-1021.

[45] A. Hohenwarter, A. Taylor, R. Stock and R. Pippan, Effect of Large Shear deformation on fracture behavior of fully pearlitic steel, Metallurgical and Materials Transactions A 42(6) (2011) 1609-1615.

[46] A. F. Bower, The influence of crack face friction and trapped fluid on surface initiated rolling contact fatigue cracks, ASME Journal of Tribology 110 (1988) 704-711.

[47] J. H. Beynon, J. E. Garnham and K. J. Sawley , Rolling contact fatigue of three pearlitic rail steels, Wear 192(1-2) (1996) 94-111.

[48] M. Ishida, M. Akama, K. Kashiwaya and A. Kapoor, The current status of theory and practice on rail integrity in Japanese railways-rolling contact fatigue and corrugations, Fatigue and Fracture of Engineering Materials and Structures 26(10) (2003) 909-919.

[49] A. Kapoor, D. I. Fletcher and F. J. Franklin, The role of wear in enhancing rail life, Tribological Research and Design for Engineering Systems 41 (2003) 331-340.

[50] W. Zhong, J. J. Hu, P. Shen, C. Y. Wang and Q. Y. Lius, Experimental investigation between rolling contact fatigue and wear of high-speed and heavy-haul railway and selection of rail material, Wear 271 (2011) 2485-2493.

[51] R. Stock, D. T. Eadie, D. Elvidge and K. Oldknow, Influencing rolling contact fatigue through top of rail friction modifier application-A full scale wheel-rail test rig study, Wear 271(1-2) (2011) 134-142.

[52] D. T. Eadie, D. Elvidge, K. Oldknow, R. Stock, P. Pointner, J. Kalousek and P. Klauser, The effects of top of rail friction modifier on wear and rolling contact fatigue: Full-scale rail-wheel test rig evaluation, analysis and modelling, Wear 265 (2008)1222-1230.

[53] W. J. Wang, T. F. Liu, H. Y. Wang, Q. Y. Liu, M. H. Zhu and X. S. Jin, Influence of friction modifiers on improving adhesion and surface damage of wheel/rail under low adhesion condition, Tribology International (75) (2014) 16-23.

[54] W. R. Tyfour and J. H. Beynon, The effect of rolling direction reversal on the wear rate and wear mechanism of pearlitic steel, Tribology International 276(6) (1994) 401-412.

[55] M. Sato, P. M. Anderson and D. A. Rigney, Rolling sliding behavior of rail steels, Wear 162-164 (2002) 159-172.

[56] A. J. Perez-Unzueta and J. H. Beynon, Microstructure and wear resistance of pearlitic rail steels, Wear 162-164 (1993) 173-82.

[57] H. B. Qiu, Y. F. Pei and Y. S. Jin, An experimental investigation into the influences of plastic deformation on rail steel wear, Tribology 16 (1996) 80-84.

[58] J. W. Seo, H. K. Jun, S. J. Kwon and D. H. Lee, Rolling contact fatigue and wear of two different rail steels under rolling-sliding contact, International Journal of Fatigue 83 (2016) 184–194.

[59] Y. Jin, F. Aloki, M. Ishida and A. Namura, Investigation and analysis of the occurrence of rail head checks, International Journal of Railway(IJR) 2(2) (2009) 43-49.

[60] Z. Li, X. Zhao, C. Esveld, R. Dollevoet and M. Molodova, An investigation into the causes of squats-Correlation analysis and numerical modelling, Wear 265 (2008) 1349-1355.

[61] S. L. Graissie, Squats and squat type defects in rails: the understanding to date, Journal of Rail Rapid Transit 226 (2011) 235-242.

[62] Operational failure modes of Switches and Crossings: Public deliverable D 1.3.1 for Capacity 4 rails: http://www.capacity4rail.eu/IMG/pdf/c4r_-_d131_-_operational_failure_modes_of_scs_public_pdf.

[63] M. Steenbergen and R. Dollevoet, On the mechanism of squat formation on train rails-Part I: Origination, International Journal of Fatigue 47 (2013) 361-372.

[64] M. Steenbergen, Squat formation and rolling contact fatigue in curved rail track, Engineering Fracture Mechanics 143 (2015) 80-96.

[65] Z. Li, R. Dollevoet, M. Molodova and X. Zhao, Squat growth-some observations and the validation of numerical predictions, Wear 271 (2011) 148-157.

[66] M. Steenbergen and R. Dollevoet, On the mechanism of squat formation on train rails-Part II: Growth, International Journal of Fatigue 47 (2013) 373-381.

[67] M. Naeimi, Z. Li, Z. Qian, Y. Zhou, J. Wu, R. H. Petrov, J. Sietsma and R. Dollevoet, Reconstruction of the rolling contact fatigue cracks in rails using X-ray computed tomography, NDT and E International 92 (2017) 199-212.

[68] C. Jessop, J. Ahlström, L. Hammar, S. Fæster and H. K. Danielsen, 3D characterization of rolling contact fatigue crack networks, Wear 366-367 (2016) 392–400.

[69] Y. Zhou, X. Zheng, J. Jiang and D. Kuang, Modeling of rail head checks by X-ray computed tomography scan technology, International Journal of Fatigue 100 (2017) 21–31.

[70] H. Chen, C. Zhang, W. Liu, Q. Li, H. Chen, Z. Yang and Y. Weng, Microstructure evolution of a hyper eutectoid pearlite steel under rolling-sliding contact loading, Materials Science and Engineering A 655 (2016) 50-59.

[71] W. D. Callister and D. G. Rethwisch, Materials Science and Engineering-An Introduction, Wiley, 2014.

[72] R. Stock and R. Pippan, RCF and wear in theory and practice-The influence of rail grade on wear and RCF, Wear 271(1-2) (2010) 125-133.

[73] P. Clayton and D. Danks, Effect of interlamellar spacing on the wear resistance of eutectoid steels under rolling-sliding conditions, Wear 135(2) (1990) 369-389.

[74] H. Muster, H. Schmedders, K. Wick and H. Pradier, Rail rolling contact fatigue, The performance of naturally hard and head-hardened rails in track, Wear 191 (1996) 54-64.

[75] Innotrack Concluding Technical Report, edited by Anders Ekberg & Björn Paulsson, 2010. **http://publications.lib.chalmers.se/records/fulltext/129645/local_129645.pdf**.

[76] J. Tasker and M. O. H Amuda, Austenitic Steels: Non-Stainless, Encyclopedia of Materials Science and Technology (2001) 411-415.

[77] C. Efstathiou and H. Sehitoglu, Strain hardening and heterogeneous deformation during twinning in Hadfield steel, Acta Materialia 58 (2010) 1479-1488.

[78] R. Harzallah, A. Mouftiez, S. Hariri, E. Felder and J. P. Maujean, Impact and Sliding Wear Resistance of Hadfield and Rail Steel, Applied Mechanics and Materials 146 (2012) 112-123.

[79] M. Takeshi and I. Atsushi, Fatigue crack propagation rate of austenitic high manganese steel, Structural Engineering 11 (1995) 165-172.

[80] W. Yang, L. Fang, K. Suna and Y. Xub, Effect of work hardening on wear behavior of Hadfield steel, Materials Science and Engineering A 460–461 (2007) 542-546.

[81] C. S. Mahlami and X. Pan, An Overview on high manganese steel casting, Advanced sustainable foundry: 71st World Foundry Congress (WFC 2014) Bilbao, Spain, 19 - 21 May 2014 Vol. 2 420-428.

[82] R. Devanathan and P. Clayton, Rolling-sliding wear behavior of three bainitic steels, Wear 151(2) (1991) 255-267.

[83] Y. Jiang and H. Sehitoglu, A model for rolling contact failure, Wear 224 (1999) 38–49.

[84] G. E. Dieter, Mechanical metallurgy, McGraw-Hill book Company, 1988.

[85] W. F. Hosford, Mechanical behaviour of materials, Cambridge University Press, 2005.

[86] M. A. Anders and K. K. Chawla, Mechanical behaviour of materials, Cambridge University Press 2009.

[87] G. Schleinzer and F. D. Fisher, Residual stress formation during the roller straightening of railway rails, International Journal of Mechanical Science 43 (2001) 2281-2295.

[88] A. Ekberg and E. Kabo, Fatigue of railway wheels and rails under rolling contact and thermal loading - an overview, Wear 258 (2005) 1288-1300.

[89] A. Kapoor and D. I. Fletcher, Post Hatfield rolling contact fatigue-The effect of residual stress on contact stress driven crack growth in rail, New Rail Report No. WR061106-2 (2006) 1–30.

[90] G. Schleinzer and F. D. Fischer, Residual stresses in new rails, Material Science and Engineering A 288(2) (2000) 280-283.

[91] S. L. Srimani, A. C. Pankaj and J. Basu, Analysis of end straightness of rail during manufacturing, International Journal of Mechanical Science 47(12) (2005) 1874-1884.

[92] CEN/TC256/WG4. Draft standard railway applications-track heavy rail. Part 1: flat bottom symmetrical railway rails 46 kg/m and above. European Committee for Standardization; 1997.

[93] V. Luzin, H. J. Prask, T. Gnaupel-Herold, J. Gordon, D. Wexler, Ch. Rathod, S. Pal, W. Daniel and A. Atrens, Neutron residual stress measurements in rails, Neutron News 24(3) (2013) 9-13.

[94] L. A. Feldkamp, L. C. Davis and J. W. Kress, Practical cone-beam algorithm, Journal of the Optical Society of America A 1(6) (1984) 612-619.

[95] B. D. Cullity, Elements of X-ray diffraction, Addison-Wesley Publishing Company, Inc., 1956.

[96] M. E. Fitzpatrick, A. T. Fry, P. Holdway, F. A. Kandil, J. Shackleton and L. Suominen, Determination of Residual Stresses by X-ray Diffraction – Issue 2, Measurement Good Practice Guide No. 52, National Physical Laboratory, Teddington, Middlesex, United Kingdom, 2005.

[97] P. S. Prevey, X-ray diffraction residual stress techniques, Metals Handbook Ohio: ASM 10 (1986) 380-390.

[98] V. M. Radhakrishnan, Multiaxial fatigue - An overview, Sadhana 20 (1995) 103-122.

[99] J. Bauschinger, Mitteilung XV aus dem Mechanisch-technischen Laboratorium der Königlichen Technischen Hochschule in München 1886 13 115.

[100] R. von Mises, Mechanik der festen Körper im plastisch deformablen Zustand. Göttin. Nachr. Math. Physics 1 (1913) 582–592.

[101] Y. Leng, Materials Characterization-Introduction to Microscopic and Spectroscopic Methods, John Wiley and Sons, 2010.

Appendix

Part I- Appended Papers

Part II- Additional Results

Part I- Appended Papers (1-5)

Paper 1:

Crack formation within a Hadfield manganese steel crossing nose

S. Dhar, H. K. Danielsen, S. Fæster, C. Rasmussen, Y. Zhang and D. Juul Jensen

Submitted for publication in Wear

Crack formation within a Hadfield manganese steel crossing nose

Somrita Dhar[1], Hilmar K Danielsen[1], Søren Fæster[1], Carsten Rasmussen[2], Yubin Zhang[3] and Dorte Juul Jensen[3]

[1]Department of Wind Energy, Technical University of Denmark, Risø Campus, Roskilde, DK- 4000, Denmark
[2]Banedanmark, Amerika plads 15, Copenhagen, DK-2100, Denmark
[3]Department of Mechanical Engineering, Technical University of Denmark, Kgs. Lyngby, DK-2800, Denmark

Abstract:

Switches and crossings in rail networks suffer from complex loading which may induce severe damage and defects, including formation of cracks that can result in rail breakage. This paper focuses on the microstructure and crack network in a damaged Hadfield manganese steel crossing nose. The extent of deformation has been quantified by hardness measurements, optical microscopy and scanning electron microscopy (SEM) including electron back scattering diffraction (EBSD). It is found that the wheel contact causes high deformation hardness of over 600 HV, around three times that of the base material, and the strain hardening extends up to a depth of about 10 mm from the running surface. Microscopy indicates the deformation microstructure is composed of bands of both deformation twins and deformation induced dislocation boundaries. The complex crack network within the nose of the crossing has been investigated using 3D X-ray tomography, where both surface and subsurface cracks are detected with the majority of the cracks originating from the surface. The crack network has been related to the observed deformation microstructure and it has been found that although the hardening and the deformation of the Hadfield manganese steel is quite different from that of commonly used pearlitic rail steels, the crack morphologies are found to be quite similar for the two materials.

Keywords: Rail, rolling contact fatigue (RCF), Hadfield manganese steel, twinning, 3D X-ray tomography, EBSD.

1. Introduction:

Switches and crossings (S&Cs) are an essential part of any railway network, enabling trains to be directed from one track onto another at railway junctions, allowing for the necessary flexibility during train operations. At the same time they are also the most vulnerable part of the railway network, suffering from peak stresses due to their greater geometric complexity compared to normal tracks. When a train passes, from the wing rail to the nose or vice versa depending on the direction of the traffic, either the nose or the wing will suffer from impact stresses due to the discontinuities in the rail as well the normal rolling contact stresses, often causing fatigue cracks and spallation [1]. In this work a Hadfield manganese steel crossing nose is investigated and the crack formation is characterized.

Various numeric studies [2-6] have been conducted in the past to assess the severity of loading and damage on railway crossings. It has been calculated that the stresses and the equivalent plastic strain in the crossing are very sensitive to train speeds as well as track conditions. Large contact and impact forces can lead to plastic deformation as well as severe defects such as squashing and lipping or crack formation and spallation, which may ultimately lead to catastrophic failures.

Hadfield manganese steel has an austenitic fcc structure and is a common material choice for railway crossings due to its excellent work hardening ability, large stress intensity factor, suitable strength, high toughness and good wear resistance. Repeated transient impact and contact stresses will harden the top surface of a Hadfield manganese crossing. However eventually fatigue cracks may develop both at the surface and beneath it. There are only few studies of the relations between the deformation microstructure and the crack propagation within the nose of Hadfield manganese steel crossings published in the open literature [7-8]. These studies indicate that the deformation in this steel is not uniform and several deformation mechanisms have been reported. A discontinuous dynamic recrystallized layer was observed on the worn surface of a manganese crossing in one study, whereas the aggregation of vacancy clusters due to deformation leading to cracking has been reported in another study.

Previous works [9-12] on crack formation in rail steels have almost exclusively been done on normal pearlitic steel grades. Here it is found that the microstructure changes during service due to plastic deformation, which is important for crack propagation as it influences the crack path. Cracks tend to follow the direction of least resistance (minimum energy), which depends on the properties and the microstructure in front of the crack tip [13]. With service surface cracks on the rails are unavoidable, and they generally appear at an angle to the surface due to rolling contact fatigue, where they may continue to propagate downwards into the rail causing rail break or reverse the path returning to the surface causing spallation. Brouzoulis et al [14] demonstrated that cracks with shallow angles to the surface are expected to propagate back to the surface while deeper cracks propagate downwards, however inhomogeneity in the microstructure may influence the crack path [9].

Mapping of rail cracks has traditionally been done by serial sectioning which is a destructive test with repeated grinding, polishing and imaging of the cross section in order to acquire data of the crack network in three dimensions. Examples include Garnham et al [12] making schematic representations of the crack geometries in pearlitic rails and Schilke et al [9] studying the crack growth on normal pearlitic grade R350HT rail steel. A non-destructive 3D X-ray computerized tomography technique was used by Jessop et al [10] and Zhou et al [11] for visualizing crack networks, where the crack and its side branches could be visualized with high resolution in 3D in pearlitic grade rail steels. Naeimi et al [15] also reconstructed squat defects at different growth stages using this technique. However, all of these studies on 3D crack networks were done on normal grade pearlitic steel used in straight tracks. Crack propagation for crossing noses in Hadfield manganese steel has not been investigated to the best of the authors' knowledge. The load cases in the nose of crossings are quite different from straight tracks, with the material and microstructure behavior also being quite different in case of the Hadfield manganese steel; thus there may be significant differences in the damage mechanisms and nature of crack propagation.
This paper characterizes the deformation and damage induced by rolling contact fatigue and impact on a Hadfield manganese steel crossing nose, which has been in service in the rail network for five years. An extensive crack network had developed in the nose, which is analyzed in detail using X-ray tomography measurements, providing 3-D mapping of the crack network within a fairly large volume. The deformed microstructure and its correlation to the crack network are studied by optical and scanning microscopy. The results are compared to pearlitic grade steel-similarities and differences are discussed.

2. Experimental Procedure:

The Hadfield manganese steel crossing investigated in this study was obtained from the Danish rail network and had been in service for five years with a traffic density of approximately 14 MGT. While some Hadfield manganese steel crossings are explosion hardened, this one was not. Most of the traffic was in the direction towards the nose from the wing rail; hence the nose was the most severely damaged component. Hadfield manganese steel include 1-1.4% C, 12-13% Mn and addition of other alloying elements like ~0.18% Cr, 0.4-0.6% Si, 0.022-0.033% P.
The mechanical properties of the steel were obtained from tensile tests done at room temperature and 10^{-3} s^{-1} strain rate. The specimen for tensile testing was obtained at a depth of 20 mm from the wheel running surface (i.e at a position assumed to be free from any deformation due to wheel contact) along the longitudinal direction from a wing rail. The specimen was cylindrical dog bone shaped with a gauge length of 10 mm and gauge diameter of 5mm. The tensile test results are given in Table 1.

Table 1: Mechanical properties of undeformed Hadfield manganese steel.

Tensile Strength	Yield Strength	Young's Modulus	Elongation	Hardness
~750 MPa	~365 MPa	~203 GPa	20%	~220 HV

For investigations of the crack network and the deformation layers, specimens were cut from the damaged nose, as shown in figure 1. Vickers hardness measurements with a load of 1kg and a dwell time of 20 seconds were used to study the microhardness distributions in the transverse section (i.e the TD/ND section) of the nose. A grid of measurements were made at intervals of 2 mm along the transverse direction and 0.3 mm from the rail running surface along the normal direction throughout the transverse section, and from these measurements a hardness map was constructed.
The microstructures were investigated using optical microscopy (OM) and scanning electron microscopy (SEM). Specimens for microstructural observations in OM were ground with Si-C paper ranging from grain 320 to 4000 followed by polishing by diamond paste to 1 µm and etched with 4% Nital.
For EBSD in the SEM, the specimen was ground and polished similarly down to1 µm and then polished with colloidal silica or OP-S for 40 minutes. The EBDS measurements were made using an acceleration voltage of 20 kV, aperture size of 60 µm and working distance of 13.3 mm. The specimen was scanned on the transverse surface in a square grid with a step size of 0.5µm.

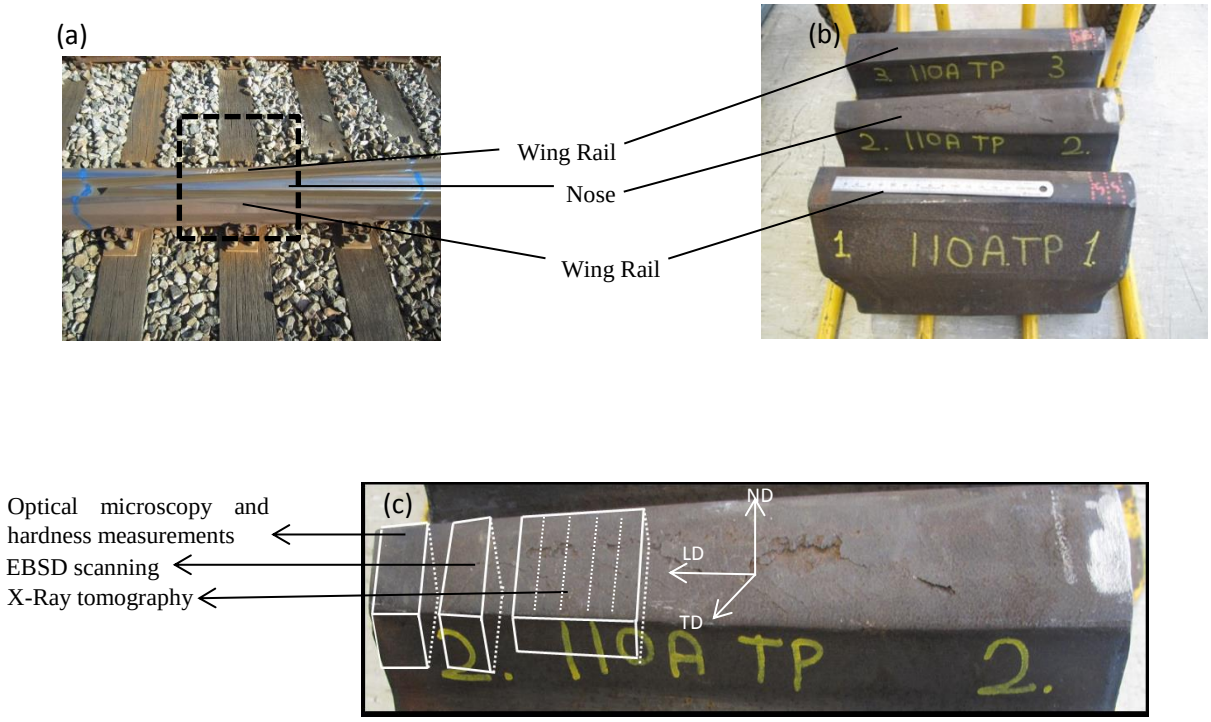

Figure 1: Sketches and photos showing where the specimens are taken. (a) A Hadfield manganese railway crossing with nose and wing rail on the track. (b) Part of Hadfield manganese steel crossing cut out from the track for the investigation. (c) Image with indications of the selected areas in the nose extracted for metallurgical characterization. ND, TD, LD represents normal direction, transverse direction and longitudinal direction respectively.

For X-ray computerized tomography, 5 specimens were cut from an area of the nose which had visual fatigue spallation (see figure 1c), each of them having a cross section of ≈10 mm by 40 mm by 10 mm. Each of the specimens was scanned individually using a Zeiss Xradia Versa 520. A polychromatic X-ray beam was used with energies ranging up to 160 kV from a tungsten target. A total of 1601 projections were acquired during a full specimen rotation. 3D maps were reconstructed by a Feldkamp algorithm for cone beam reconstruction [16] to 2k×2k×2k voxel volumes with a voxel size of 10 µm. The crack network was segmented and visualized using Avizo 3D software. The crack networks from different specimens were then stitched together to provide a 3D map of the crack morphology within a 50 mm by 40 mm by 10 mm volume of the nose.

3. Results:

3.1 Hardness Measurements

Figure 2 shows the hardness map of the nose. The wheel contact surface of the rail receives the maximum deformation where the deformation induced hardness is very high, nearly 600 HV, whereas the undeformed material hardness is only 220 HV. The black area at the top of the hardness map in figure 2 is caused by the lack of data due to the presence of cracks. Moving down from the running surface in to the material the hardness decreases as the extent of deformation decreases. The deformation gradient however extends quite deep into the rail, hardness values above 220 HV are observed as deep as 10 mm from the running surface. This is visualized in figure 3, which shows the hardness profile along the normal direction at three positions in the hardness map. For all three positions, a similar exponential decrease in hardness is observed. Compared to pearlitic grade steel, the depth of hardening is significantly higher for a Hadfield manganese steel nose. In normal 260 grades pearlitic steel the hardness is reported to fall off to base hardness within the first 3-4 mm from the running surface [9].

3.2 Optical Microscopy

Figure 4 (a-d) shows the microstructure of the nose at different depths from the running surface. The microstructure of undeformed Hadfield manganese steel (figure 4d) is composed of very large equiaxed grains with an average grain size of 500 µm and some inclusions in the microstructure. At the rolling contact surface, deformation bands can be seen in the grains (figure 4a). In normal pearlitic grade steel deformation causes the grains to become elongated in the direction of shear. However shearing of grains is not observed in the present Hadfield manganese steel, instead deformation bands form inside the grains. As the contact surface receives the maximum deformation, the density of these bands is highest at the surface. At increasing depth from the running surface (figure 4b-4c) the density of the deformation bands decreases in agreement with the deformation hardening decreasing as seen in figure 3. At the contact surface the deformation bands cross each other within the grains whereas at deeper locations the grains mostly have deformation bands in a single direction. The deformation bands are inhomogeneously distributed and have a wavy appearance, with the orientation and direction of the bands differing from grain to grain. These deformation bands can either be deformation induced mechanical twins or dislocation boundaries, which the optical microscopy is not capable of differentiating between. In some austenitic steels, martensitic transformation also imparts additional hardening, but in this investigation no martensite was found.

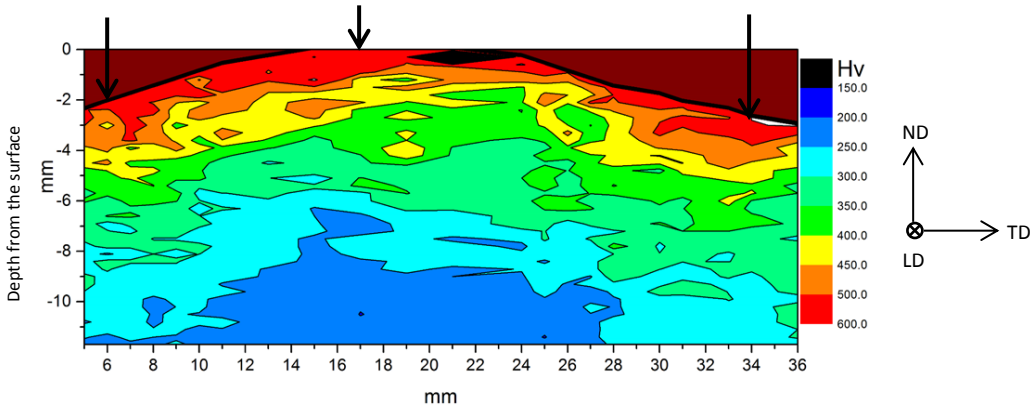

Figure 2: Hardness contour map of the transverse section of the nose of the Hadfield manganese crossing showing the gradient of deformation. The black area at the top running surface is due to lack of data points because of the presence of cracks. The black arrows at the top show where the hardness decrease profiles shown in figure 3 are taken.

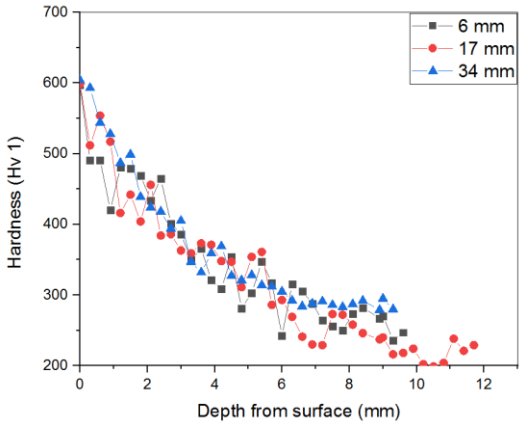

Figure 3: Decrease in hardness as a function of distance from the surface at the positions 6mm, 17 mm and 34 mm along the transverse direction (see arrows in figure 2).

In figure 5, an optical micrograph of the crack network on the transverse surface is shown. Most of the cracks seem to originate from the wheel contact surface. The bigger cracks are at angles of nearly 35 degrees from the surface, extending around 2-3 mm into the rail and then change direction parallel to the running surface, which may lead to spallation. This is similar in nature to what is found in pearlitic grade steel subjected to rolling contact fatigue. There are some shallow angled small surface cracks as well, which also run parallel to the surface. The smaller cracks have angles

ranging from 15 degrees to 30 degrees to the surface. Plastic deformation plays an important role in the propagation of the crack. Sometimes cracks can penetrate beneath, exceed the plastically deformed layer, however in this case the crack is confined within the first 2-3 mm from the running surface, well within the 10 mm thick plastically deformed layer. Indication of crack shielding can be observed, where two cracks initiate close to each other and only one of them grows and shields the propagation of the other due to stress relief. In figure 5, the propagation of crack 1 might have shielded the growth of crack 2. Crack shielding can also be observed in case of branched cracks as we see for crack 3, where the main crack propagation may have been interrupted by the growth of the branched crack.

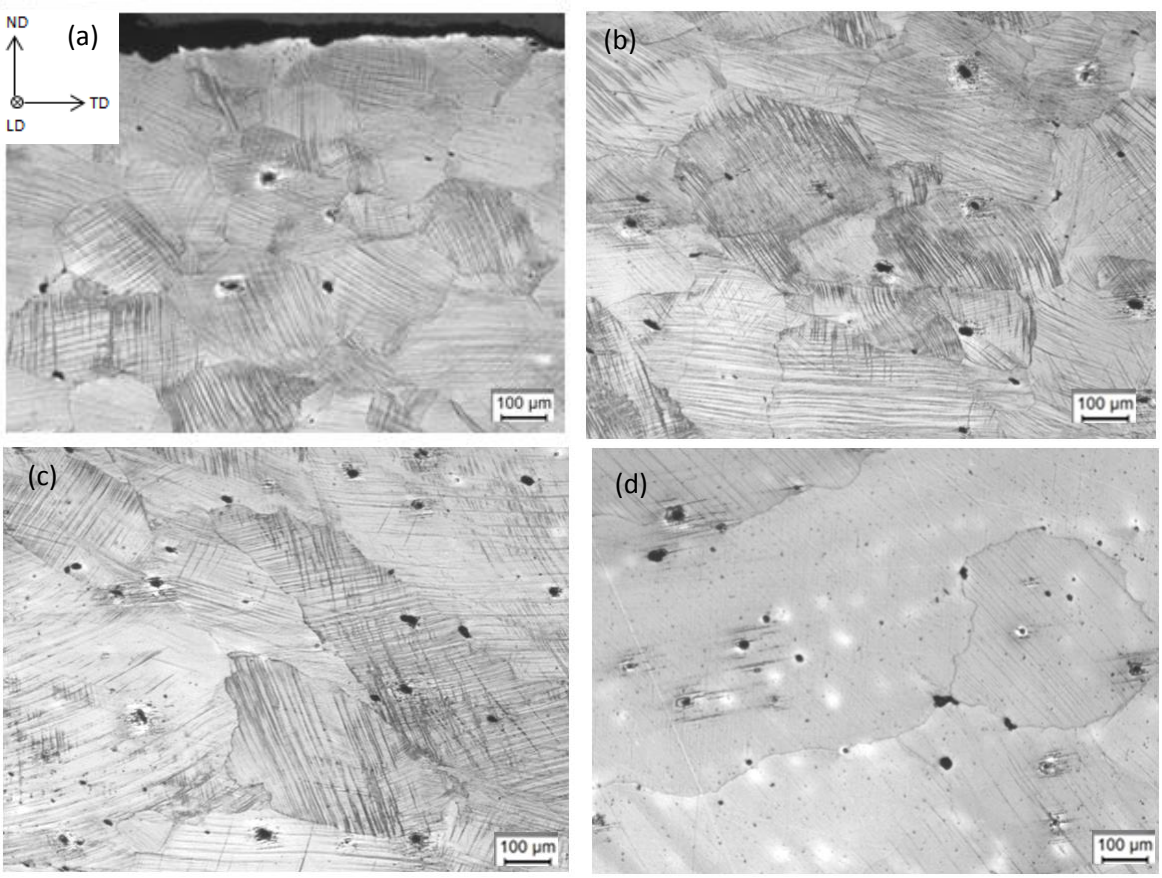

Figure 4: Optical microscope images of the transverse surface of the deformed Hadfield manganese steel crossing nose (a) at the rolling contact surface (b) 2 mm from the surface (c) 8 mm from the surface (d) 15 mm from the surface (largely without deformation).

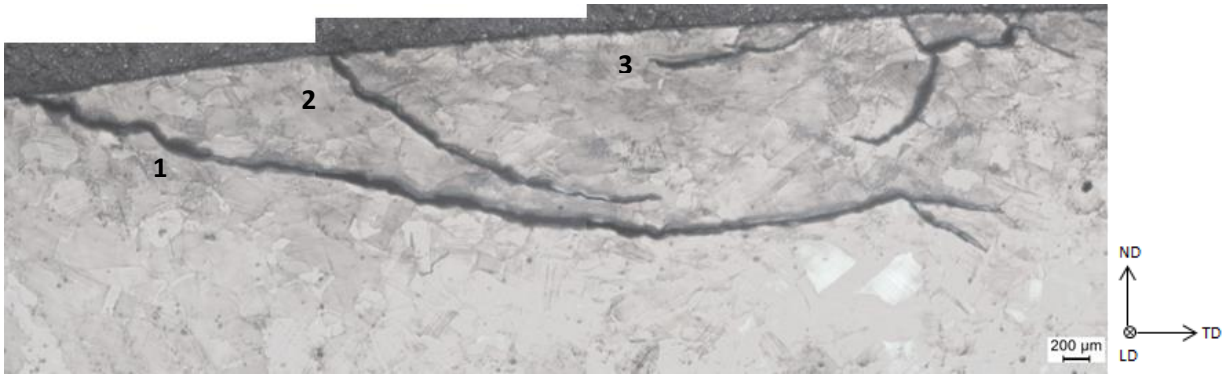

Figure 5: Optical microscope image of a crack network in the transverse surface showing a wavy crack propagation path along with crack branching.

3.3 X-ray Computerized Tomography

3D X-ray computerized tomography was used to get a 3D representation of the crack morphology. X-ray tomography reconstructions are 3D density maps, which allow detection of cracks due to the difference in density by applying an intensity threshold value. Each of the specimens were individually scanned and reconstructed, after which they were stitched together to give an overview of the crack network in a large volume. Figure 6(a) shows the 3D tomography image of the volume within the crack shown in figure 5 and a 2D section from the 3D data set is shown in figure 6(b). The surface morphology of the crack is much more evident in the 3D image although it is hard to show in a non-3D media. A comparison between the optical microscopy imaging of the crack (figure 5) and the 2D tomography section of the same cracks in figure 6(b) illustrates that with tomography it is possible to reconstruct the crack network with good spatial resolution and sufficient detail even though the voxel size in the reconstructions are 10 µm.

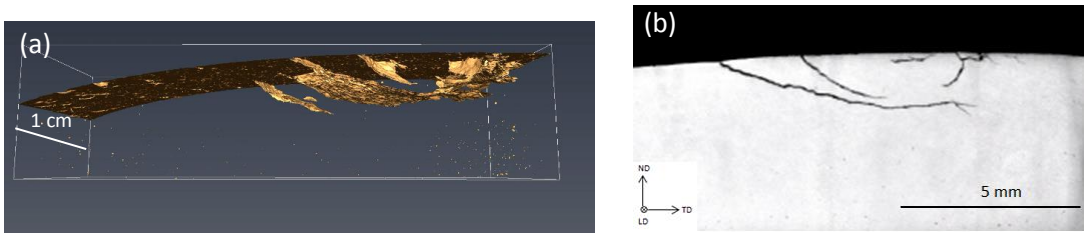

Figure 6: X-ray tomography of a volume containing the crack network shown in figure 5. (a) crack network in 3D revealing the complete morphology of the crack network. (It is chosen to show the steel and air as transparent and the interface between them in yellow which makes the cracks as well as the rail surface visible) (b) A 2D section taken from the data in figure (a) at a location close to shown in figure 5.

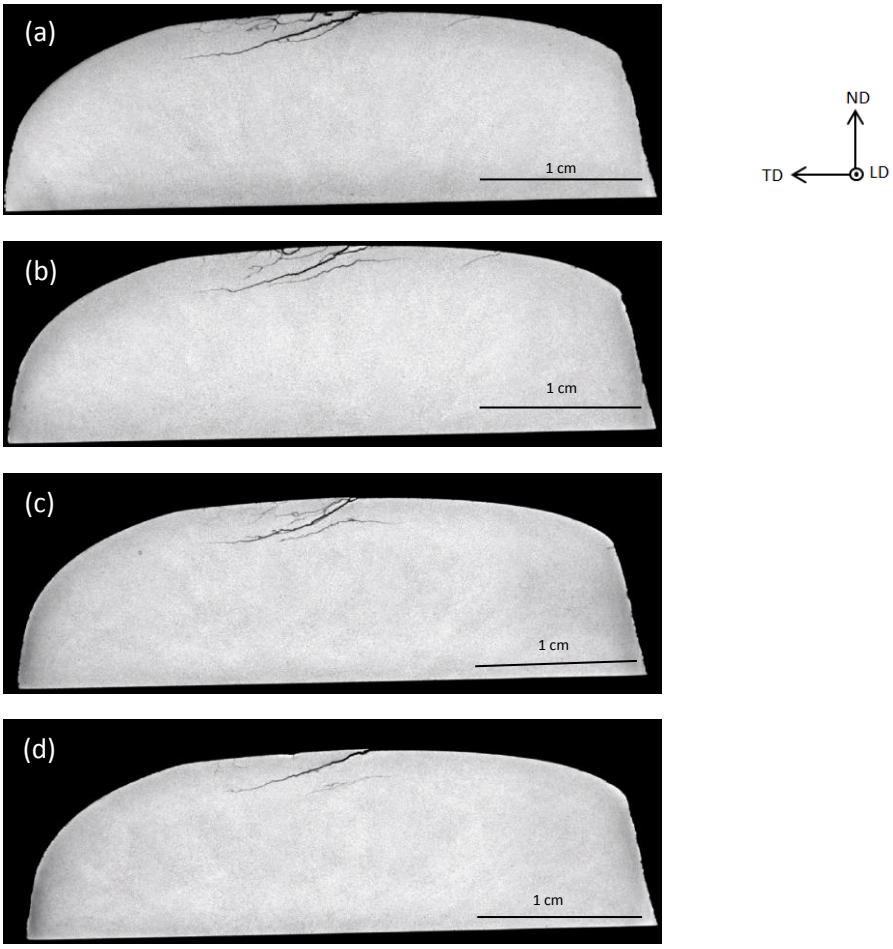

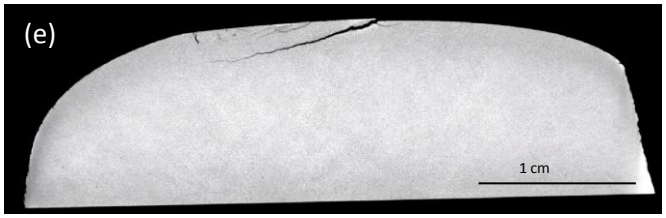

Figure 7: X-ray tomography of the crack network from one of the specimens visualized by 2D slices at different locations within 10 mm along the running direction.

Five adjacent specimens were cut out from the area shown in figure 1, which contained some spallation. Figure 7(a-e) shows 2D slices from the tomographic reconstruction for one of the five specimens. The different images are from different positions along the longitudinal direction within a length of 10 mm. From these images we can identify a big crack originating from the surface and running throughout the entire cross section of the specimen. The crack network is extensive and continuous through all the five scanned specimens, with different cracks and branches interacting with each other. These 2D images clearly show the need for a large overview in order to comprehend the crack network. For example, in figure 7(b–d) we see a sub-surface crack present, which is not evident in figure 7a or 7e. The crack shape changes continuously with location and may have connections to the surface at other locations, which are not evident from 2D slices.

Figure 8 shows the stitched 3-D tomography images of the crack network obtained from the five adjacent specimens. The samples are aligned next to each other separated by the width of the cutting blade. The steel and air are represented as being transparent and the colored area is the interface between them, making the crack network as well as the crossing nose surface visible. The figure shows the extent and severity of cracks beneath the surface of the crossing nose, also giving an overview of the spallation and the cracking related to it. At higher magnification the cracks are rough with ridges which are typical for rolling contact fatigue. Apart from the larger surface crack, the 3D scans shows that some smaller subsurface cracks are located at various depths. Within the nose, many of the surface and subsurface cracks are interconnected, whereas some are propagating individually. Most of the cracks have a definite direction of propagation. The main crack network seen here continues throughout the 50 mm of the running direction, it is over 10 mm in length in the transverse direction and extends up to a depth of 3 mm from the running surface.

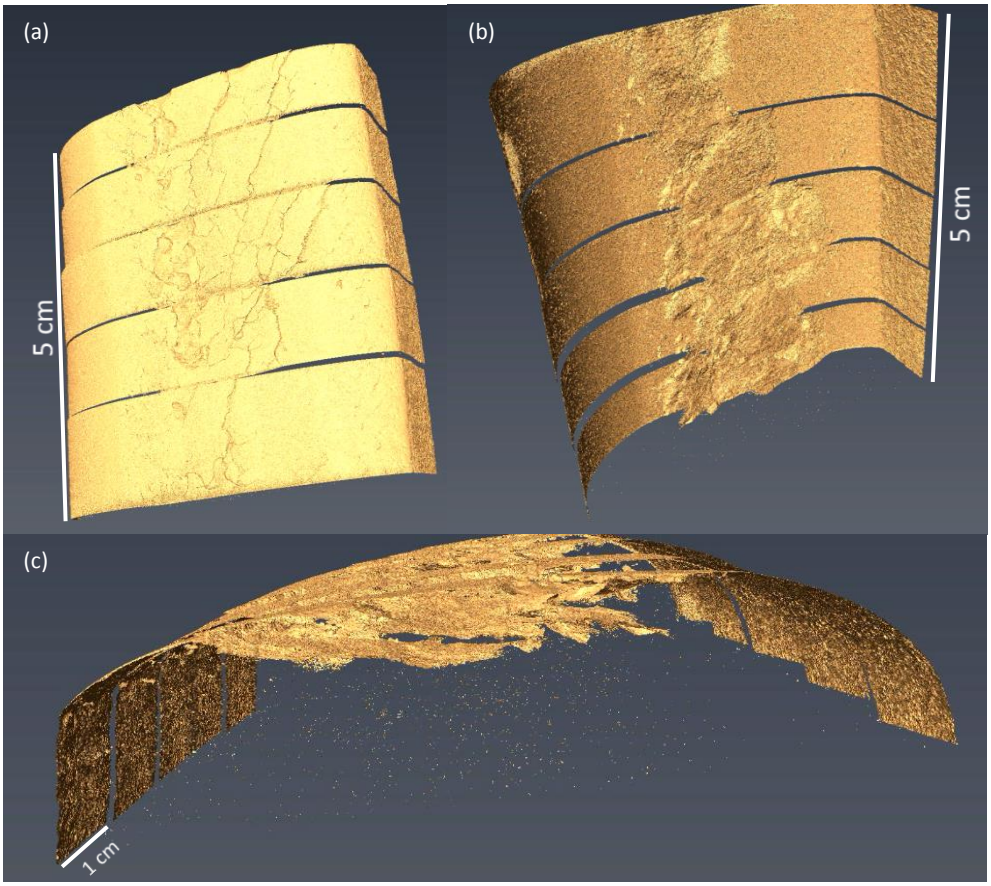

Figure 8: 3-D tomographic representation of the crack network in a volume of size 50 mm by 40 mm by 10 mm. The surface of the rail including crack openings is made visible by performing a global segmentation thresholding. The steel and air are transparent and the interface between them is yellow which makes the cracks as well as the rail surface visible. (a) Top view of the nose showing the running surface with evident surface cracks and spallation. (b) The crack network as seen from within the crossing nose. (c) Transverse view of the crack network.

3.4 EBSD

Figure 9 shows maps of the microstructure near two of the cracks, close to the crack tips, obtained by EBSD. The maps show high density of mechanical twins (colored in white) and also deformation induced dislocation boundaries (colored in black). The density of these bands is not uniform through the grains and the direction of these bands also varies for different grains. Some orientations are more favorable for twin formation and have multiple twins whereas other grains are totally free from any deformation twins, consisting only of dislocation boundaries. All the deformation induced dislocation boundaries have only low (< 15 ˚) misorientation even at the severe deformation near the surface.

(a)

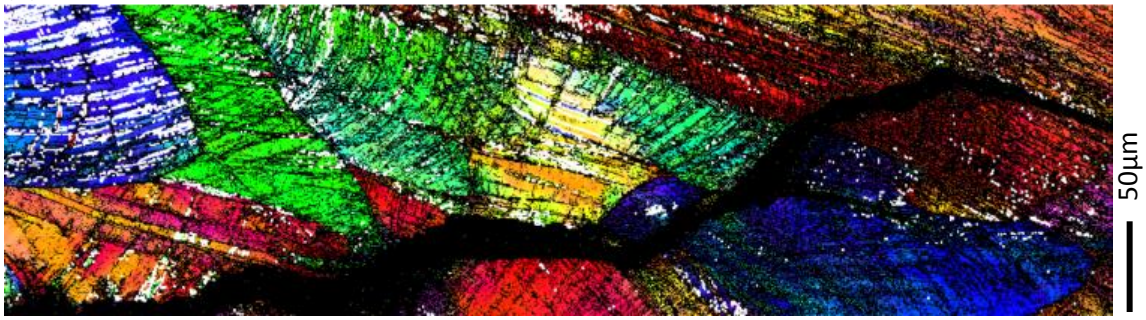

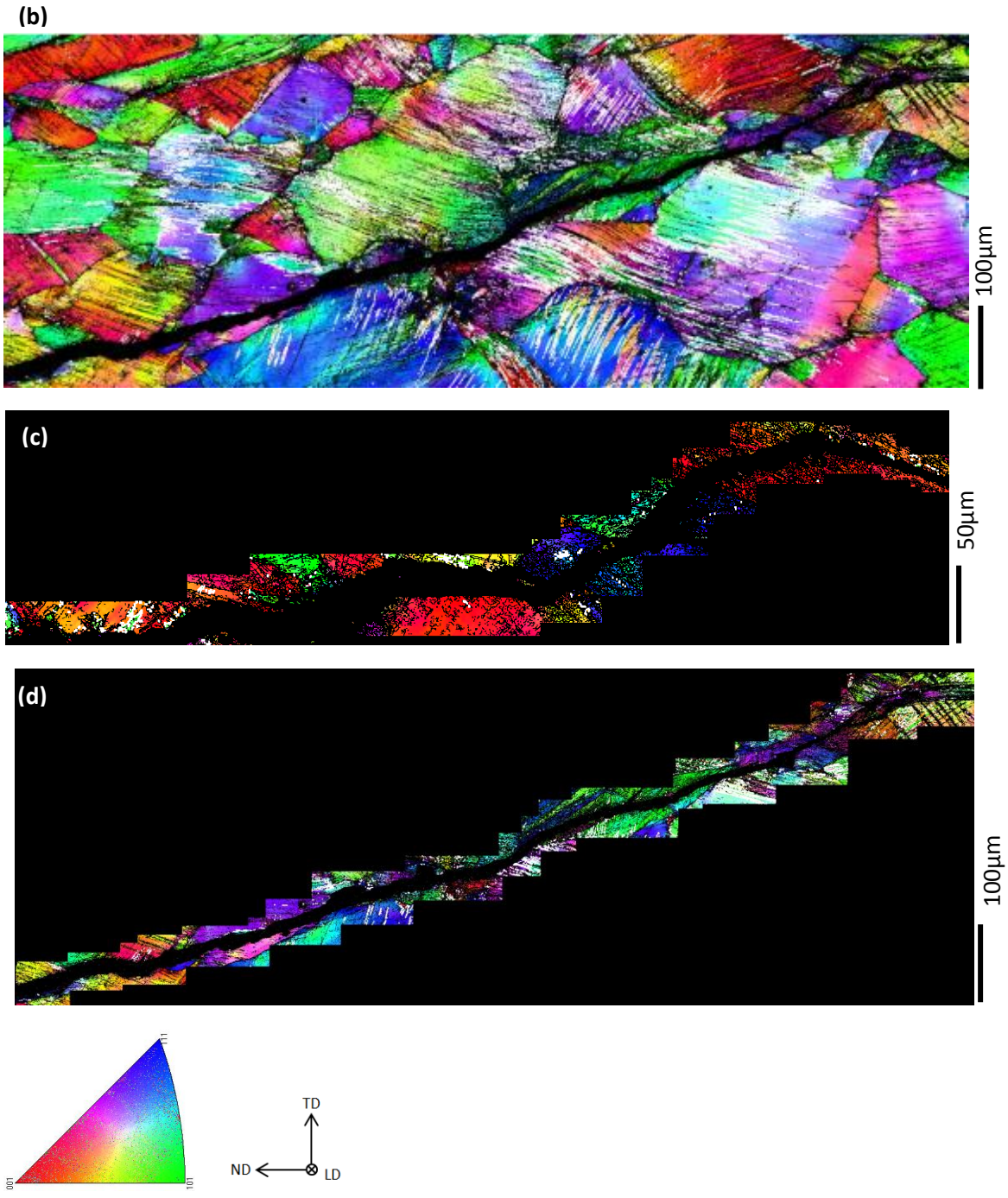

Figure 9: Maps obtained by EBSD showing the distribution of crystallographic orientations near two of the cracks within the nose. The colors correspond to the crystallographic orientation along the specimen surface normal direction, the white bands are deformation twins and the black bands are dislocation boundaries. (a) & (b) the matrix around the two cracks, (c) & (d) the area near the cracks selected for detailed analysis.

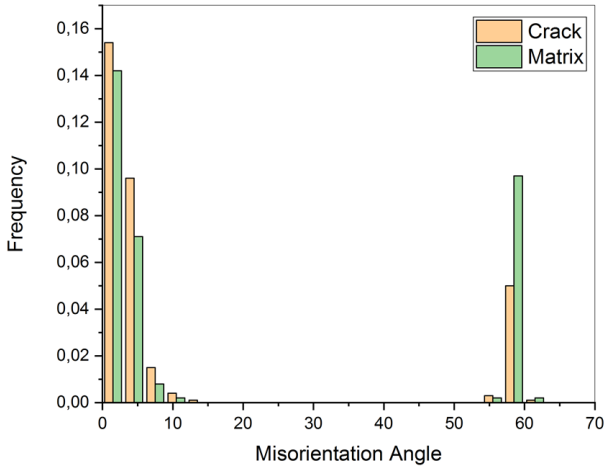

Figure 10: The frequency distribution of misorientation angles across boundaries within the area near cracks (see figure 9 c and d) and the matrix away from the crack.

A comparison of misorientations in areas near the cracks and in the matrix away from them reveal that the matrix has a significantly higher twinning density compared to the areas near the cracks, see figure 10. Thus the cracks tend to propagate through regions, which are free from twinning resulting into a wavy crack path. The crack network is mostly transgranular with only about 35% of the crack length along the grain boundaries (see Table 2) and it passes through grains of many different crystallographic orientations. There appears to be no preference for the crack to pass through any specific orientation, other than grains with twins are less likely to be cracked.

Table 2: Analysis of crack path, the percentage of crack length passing through grain interiors or along grain boundaries is given. Crack 1 is from figure 9c and crack 2 is from figure 9d.

Crack	Grain interior	Grain boundary
1	65.33 %	34.66 %
2	62.31 %	37.68 %

4. Discussion

Rail-wheel contact causes both normal and shear strains in the rails due to rolling and sliding at the contact surface, which induces hardening at the surface. When the hardening reaches saturation, the surface becomes brittle and fatigue cracks start appearing leading to failure. The work hardening behavior is generally characterized by the strain hardening exponent (n); the greater the value of n, the greater is the work hardening. A hardening exponent of n~0.4 was obtained from tensile testing of this Hadfield manganese steel whereas the exponent is ~0.2 for pearlitic grade steel also used for crossings. In pearlitic steels the microstructure becomes aligned in the shear strain direction at high plastic deformation. The two phase microstructure of ferrite and cementite in the pearlitic steel plays a role in the deformation mechanism and eventually crack initiation and propagation. The ferrite generally gets strained in the direction of the plastic deformation and cracks generally form along the proeutectoid ferrite grain boundaries as they are the soft part of the microstructure and strain harden the most [17-18]. Cracks tend to follow the weakest link in the microstructure, which causes waviness in the crack path. Beside the soft ferrite, inclusions, slags and other defects are weak links in the microstructure, which can lead to a change in direction of the crack or in many cases the formation of branches.

The deformation mechanism of Hadfield manganese steel is quite different from pearlitic grade rail steel. Although containing inclusions, the microstructure of the Hadfield manganese steels is more homogenous, being single phase austenite. In Hadfield manganese steel, deformation occurs by both dislocation and twinning mechanisms while for pearlitic grades it is only by dislocations. Apart from dislocation movements, generally the extra work hardening is associated with the low stacking fault energy of Hadfield manganese steels, which is favorable for twinning deformation [19-20]. Another reason contributing to the extra hardening in Hadfield manganese steel may be rearrangement of the carbon atoms from octahedral to tetrahedral sites [19]. Therefore, the deformation mechanism of

Hadfield manganese steel can be attributed to interactions between different slip systems, dislocations and twins [21], interstitial carbon atoms and dislocations [22-23], and between twinning systems [24].

Optical and EBSD imaging in this work show the deformation of the austenite grains in Hadfield manganese steel is not uniform. Depending on the stress direction and orientation of the grains, some grains are more favorable for twinning whereas other grains only have deformation induced dislocation substructures. Even within the same grain different substructures can be present. This non-uniform deformation of the grains can lead to local stress concentrations and crack formation in Hadfield manganese steel. Once a crack forms it seems to be confined within the plastically deformed layer and follows the direction of plastic flow. The crack has a shallow angle to the surface, and after a certain distance of propagation within the material, it changes direction and runs parallel to the surface. Crack branching is also evident, as well as indications of crack shielding. The crack network is found to preferentially propagate through regions free from twinning as that is relatively softer compared to twinned regions.

The crack propagation morphology found in a Hadfield manganese steel crossing in this work is similar to what can be found in pearlitic grade steel used in normal tracks. Plastic deformation occurs leading to crack formation in both cases. The crack originates mostly at the surface where the loads are highest. After initiation, most of the cracks are confined within the plastically deformed layer, following the weakest links in the microstructures, ferrite grain boundaries in case of pearlite and softer non-twinned grains in Hadfield manganese steel. Although the mechanism of plastic deformation is different in the two types of material, the crack network developed in both of them seems to be more or less comparable. The observed crack network passes through several grains and most cracks have a shallow angle of origin propagating back to the surface, which is generally the same behavior seen in pearlite.

5. Conclusion:

The deformation and damage induced during service on the nose of a non-explosion hardened Hadfield manganese steel crossing has been investigated in this paper. The direction of traffic from the wing rail to the crossing nose had caused high impact stresses from the train wheels, leading to high deformation and severe crack formation of the crossing nose. The running surface has a very high deformation induced hardness of around 600 HV, with a hardness profile extending to a depth of 10 mm. A high density of the deformation induced twins and dislocation boundaries in the austenitic grains was observed near the surface with decreasing density away from the surface related to the decrease in hardness.
The deformed microstructure of the Hadfield manganese steel contains a high density of deformation twins and dislocation boundaries but no shearing of grains are observed. EBSD imaging of the microstructure near the cracks indicate the crack propagation is predominately transgranular. The cracks mostly follow a path free from the twins through relatively soft grains causing the waviness in the crack path.
An extensive crack network was mapped in the damaged crossing nose using 3D X-ray tomography, capable of non-destructive scans accurately detecting the cracks in large sized specimens. Both surface and subsurface cracks were detected, some of them interconnecting. While Hadfield manganese steel has very different deformation mechanisms compared to normal pearilitic rail steels, the crack morphology is similar to cracks observed in the pearlitic grades. The crack network is confined in top layers of the plastically deformed rail with surface cracks originating at shallow angles to the surface and after reaching a certain depth of 2-3 mm running parallel to the contact surface.

6. Acknowledgements:

The authors gratefully acknowledge support from the Innovation Fund Denmark through the project “INTELLISWITCH – Intelligent Quality Assessment of Railway Switches and Crossings” (Grant no 4109-00003B).

References:

[1] B. Lv, M. Zhang, F. C. Zhang, C. L. Zheng, X. Y. Feng, L. H. Qian and X. B. Qin, Micro-mechanism of rolling contact fatigue in Hadfield steel crossing, International Journal of Fatigue 44 (2012) 273–278.

[2] S. L. Guo, D. Y. Sun, F. C. Zhang, X. Y. Feng and L. H. Qian, Damage of a Hadfield steel crossing due to wheel rolling impact passages, Wear 305 (2013) 267–273.

[3] M. Wiest, W. Daves, F. D. Fischer and H. Ossberger, Deformation and damage of a nose rail due to wheel passages, Wear 265 (2008) 1431–1438.

[4] J. H. Xiao, F. C. Zhang and L. H. Qian, Numerical simulation of stress and deformation in a railway crossing, Engineering Failure Analysis 18 (2011) 2296–2304.

[5] A. Johansson, B. Palsson, M. Ekh, J. C. O. Nielsen, M. K. A. Ander, J. Brouzoulis and E. Kassa, Simulation of wheel–rail contact and damage in switches & crossings , Wear 271 (2011) 472–481.

[6] A. Tejada, A. Lau, I. Santos and R. Fongemie, Numerical simulation of track settlement using a multibody dynamic software a holistic approach, in A.T. Fleury, D.A. Rade and P.R.G. Kurka (Ed), Proceedings of the XVII International Symposium on Dynamic Problems of Mechanics, Sao Paolo, Brazil, March 5-10, 2017, ABCM - Brazilian Society of Mechanical Sciences.

[7] L. Qian, X. Feng and F. Zhang, Deformed microstructure and hardness of Hadfield high manganese steel, Materials Transactions 52(8) (2011) 1623-1628.

[8] F. C. Zhang, B. Lv, T. S. Wang, C. L. Zheng, M. Li and M. Zhang, Microstructure in worn surface of Hadfield steel crossing, International Journal of Modern Physics B 23(6 & 7) (2009) 1185–1190.

[9] M. Schilke, N. Larijani and C. Persson, Interaction between cracks and microstructure in three dimensions for rolling contact fatigue, Fatigue and Fracture of Engineering Materials and Structures 37 (2014) 280-289.

[10] C. Jessop, J. Ahlström, L. Hammar, S. Fæster and H. K. Danielsen, 3D characterization of rolling contact fatigue crack networks, Wear 366-367 (2016) 392–400.

[11] Y. Zhou, X. Zheng, J. Jiang and D. Kuang, Modeling of rail head checks by X-ray computed tomography scan technology, International Journal of Fatigue 100 (2017) 21–31.

[12] J. E. Garnham, D. I. Fletcher, C. L. Davis and F. J. Franklin, Visualization and modelling to understand rail rolling contact fatigue cracks in three dimensions, Proceedings of the Institution of Mechanical Engineers, Part F: Journal of Rail and Rapid Transit 225 (2016) 165–178.

[13] W. Zhong, J. J. Hu, Z. B. Li, Q. Y. Liu and Z. R. Zhou, A study of rolling contact fatigue crack growth in U75V and U71Mn rails, Wear 271 (2011) 388–392.

[14] J. Brouzoulis and M. Ekh, Crack propagation in rails under rolling contact fatigue loading conditions based on material forces, International Journal of Fatigue 45 (2012) 98-105.

[15] M. Naeimi, Z. Li, Z. Qian, Y. Zhou, J. Wu, R. H. Petrov, J. Sietsma and R. Dollevoet, Reconstruction of the rolling contact fatigue cracks in rails using X-ray computed tomography, NDT and E International 92 (2017) 199–212.

[16] L. A. Feldkamp, L. C. Davis and J. W. Kress, Practical cone-beam algorithm, Journal of the Optical Society of America A 1(6) (1984) 612-619.

[17] M. Steenbergen, Squat formation and rolling contact fatigue in curved rail track, Engineering Fracture Mechanics 143 (2015) 80–96.

[18] H. C. Eden, J. E. Garnham and C. L. Davis, Influential microstructural changes on rolling contact fatigue crack initiation in pearlitic rail steels, Materials Science and Technology 21(6) (2007) 623–629.

[19] P. H. Adler, G. B. Olson and W. S. Owen, Strain hardening of Hadfield manganese Steel, Metallurgical Transaction A 17A (1986) 1725-1737.

[20] I. Karaman, H. Sehitoglu, K. Gall, Y. I. Chumlyakov and H. J. Maier, Deformation of single crystal Hadfield steel by twinning and slip, Acta Materialia 48 (2000) 1345-1359.

[21] E. G. Astafurova, M. S. Tukeeva, G. G. Zakharova, E. V. Melnikov and H. J. Maier, The role of twinning on microstructure and mechanical response of severely deformed single crystals of high-manganese austenitic steel, Materials Characterization 62 (2011) 588-592.

[22] Y. N Dastur and W.C. Leslie, Mechanism of work hardening in Hadfield manganese steel, Metallurgical Transaction A 12A (1981) 749-759.

[23] W. S. Owen and M. Grujicic, Strain ageing of austenitic Hadfield manganese steel, Acta Materialia 47(1) (1999) 111-126.

[24] C. Efstathiou and H. Sehitoglu, Strain hardening and heterogeneous deformation during twinning in Hadfield steel, Acta Materialia 58 (2010) 1479–1488.

Paper 2

2D and 3D characterization of rolling contact fatigue cracks in a manganese steel crossing wing rails

S. Dhar, H. K. Danielsen, S. Fæster, C. J. Rasmussen and D. Juul Jensen

Submitted for publication in Wear

2D AND 3D CHARACTERIZATION OF ROLLING CONTACT FATIGUE CRACKS IN A MANGANESE STEEL CROSSING WING RAILS

S Dhar[1*], HK Danielsen[1], S Fæster[1], CJ Rasmussen[2] and D Juul Jensen[3]

[1] Department of Wind Energy, Technical University of Denmark, Risø Campus, Roskilde, DK- 4000, Denmark
[2] Banedanmark, Amerika plads 15, Copenhagen, DK-2100, Denmark
[3] Department of Mechanical Engineering, Technical University of Denmark, Kgs. Lyngby, DK- 2800, Denmark

[*] E-mail: sodh@dtu.dk

Abstract: Rail wheel contact at switches and crossings (S&Cs) induces impact stresses along with normal and shear contact stresses, resulting in plastic deformation and eventually crack formation. Damaged and deformed wing rails of a manganese steel crossing are studied. This includes a characterization of the microstructure, hardness and 3D crack network. The surface of the rail receives the maximum deformation resulting in a hardened top layer. The deformation is manifested in a high density of twins and dislocation boundaries in the microstructure. A complex crack network is revealed in high resolution by X-ray tomography.

Keywords: Switches and crossings (S&Cs); deformation; 3D X-Ray tomography; 2D & 3D crack network; rolling contact fatigue (RCF); manganese steel

1. Introduction

Switches and crossings (S&Cs) are more susceptible to damage compared to normal tracks because of their moving parts and complex geometry. Therefore, poorly maintained S&Cs encounter frequent failures and large maintenance cost. The direction of traffic plays an important role in the damage evolving in the crossing. When a wheel passes from nose to wing rail or vice versa, the component suffers from high impact stresses as well as normal and rolling contact stresses causing severe damage like fatigue cracks and spallation if not maintained in time [1].
Pearlitic steels are most commonly used in normal tracks as well as crossings. However in recent years manganese steel has been the preferred choice for crossings because of superior mechanical properties. Most studies on deformation and cracks in rail steels are done for pearlitic steel taken from normal tracks [2-8]. Not much work has been published in the literature on the damage and degradation behaviour of manganese steels used in crossings. In a previous work [9] we investigated the nose of a manganese steel crossing which was in service in the Danish rail network for five years. The direction of traffic was mostly towards the nose and hence the nose was severely damaged with cracking and visual spallation. A complex crack network had developed in the nose, which is similar to crack networks developed in pearlitic steels from straight track although the microstructural characteristics and deformation mode in the two steels are very different. It was obvious that the nose was heavily deformed due to rolling contact stresses, normal stresses as well as impact loadings. Deformation causes formation of twins and dislocation boundaries in the austenitic grains near the surface but no shearing of grains were observed.
The wing rails can also be heavily damaged when the direction of traffic is from the nose to the wing rail. In this case, the wing rail will suffer from impact loadings due to discontinuity in rail wheel contact at the transition zone. It is thus of interest to compare the damage and deformation of a wing rail to the nose rail. This is the main aim of the present work in which the damage and deformation of a manganese steel crossing has been investigated, focusing on the wing rails. The crossing investigated in this work was in service in the Danish rail network for 13 years with a yearly traffic density of 14 MGT (million tons) where more than 90 % of the traffic was from the nose to the wing rail in straight track; hence one of the wing rails was severely damaged by impacts and contained cracks. The experimental techniques used for the present investigation are the same as those used in the previous study for the crossing nose, namely characterization with optical microscopy and hardness measurements, as well as X-ray tomography for 3D mapping of the crack network. With X-ray tomography cracks can be mapped non-destructively and with good resolution compared to the traditional method of repeated grinding, polishing and imaging of the crack cross section by optical microscopy [9].

2. Experimental Procedure

The two wing rails of a manganese steel crossing were studied. Although nowadays most of the manganese steel crossings are explosion hardened for better mechanical properties, this one was not explosion hardened. Visual inspection showed the wing rails were heavily deformed and damaged, and the presence of repair welds was evident on

one of the wing rails. A schematic diagram of a switch and crossing (S&C) assembly is given in Figure 1a and 1b, which shows the position of the switch blades when the train is moving on to the diverging track or straight track respectively. Depending on the direction of the traffic, one of the wing rails or the nose will receive heavy impact. Figure 1c shows a schematic diagram of the crossing panel indicating the regions from where the parts of the crossing in Figure 1d and 1e are cut from.

Small samples for investigation were cut from the wing rails. Wing rail 2 (as well as the nose) had received extensive repair welding, no samples were taken from the welded sections. The micro hardness measurements on the transverse surface (TD, ND) of the wing rails at five different locations (as shown by roman numbers in Figure 1d and 1e) were conducted using a Vickers hardness measurement tester with a load of 1 kg and dwell time of 20 seconds. The hardness map was constructed from a series of measurements, which were done from the rail wheel contact surface down to a depth of 10 mm with a step size of 0.3 mm and 1 mm along the normal and the transverse direction, respectively.

The deformed microstructure of the transverse section was studied using optical microscopy (OM). The samples were ground with Si-C paper ranging from grain 220 to 4000 then polished by diamond paste down to 1 µm and etched with Nital.

The crack network developed in the wing rail was studied by X-ray computerized tomography. For these measurements, samples having a cross section of 10 mm by 10 mm and 40 mm in length were cut out from the wing rail. A Zeiss Xradia Versa 520 was used for the measurements. A polychromatic X-ray beam with energies ranging up to 160 kV from a tungsten target was used. A total of 1601 projections were acquired during a full sample rotation. 3D maps were reconstructed by a standard filtered back-projection method to 2k×2k×2k voxel volumes with each voxel of 10 μm^3 size. The crack network was segmented and visualized by using the Avizo 3D software.

3. Results

3.1 Hardness

Figure 2 shows the hardness maps of the two wing rails at different locations. The positions (i), (iii) and (iv) belong to wing rail 1 and (ii) and (v) to wing rail 2, which had been repair welded. As shown, the hardness measurements were made on wing rail 2 at locations away from the weld. The figures show that the hardness gradient is different at different locations, due to the difference in rail wheel contact at those places. In positions (ii), (iv) and (v), the deformation hardening is most severe at the top layer showing a high hardness of more than 600 Hv. The hardness maps from locations (i) and (iii) show that these locations are comparatively less deformed. The extent of deformation varies due to difference in direction of traffic (diverging track or straight track). Below the wheel running surface the hardness values decrease, indicating less deformation at larger depths, with the undeformed region having a base hardness of around 220 Hv. Cracks were found at region (ii), although the hardness as well as depth of hardening are higher at region (iv) and (v). No cracks are found in these very hard regions; (iv) and (v).

Region (i) has the least deformation and maintains the original rail profile shape, whereas in the other cases, the rail profile changes with deformation. With increased deformation, the depression of the surface profile (as in Figure 2b, 2d and 2e) compared to the original profile gets more severe. The work hardened layer is observed to extend to 10 mm below the surface. This depth of deformation in the investigated wing rails is found to be nearly the same as found in case of the manganese nose rail studied previously [9]. Although the previously studied crossing was fairly a new one (5 years in service) compared to the crossing in the present study (13 years in service), the yearly traffic density through both the switches was the same around 14MGT. The depth of hardening was the same in both cases. Similar depth of hardening is reported for manganese crossing experiencing 130 MGT loads during service in another study [10]. Depth of hardening by other deformation mechanisms like explosion hardening can be much higher up to 25 mm from the surface [11]. The depth of hardening from wheel/rail contact is significantly higher in manganese grade crossings as compared to normal pearlite grade. In literature it has been reported that in pearlitic grade the depth of hardening extends to only 3-5 mm from the wheel running surface [12-13].

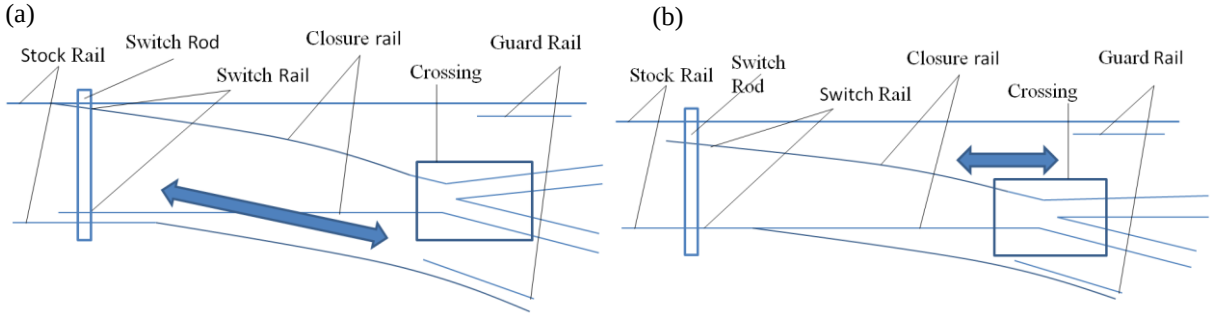

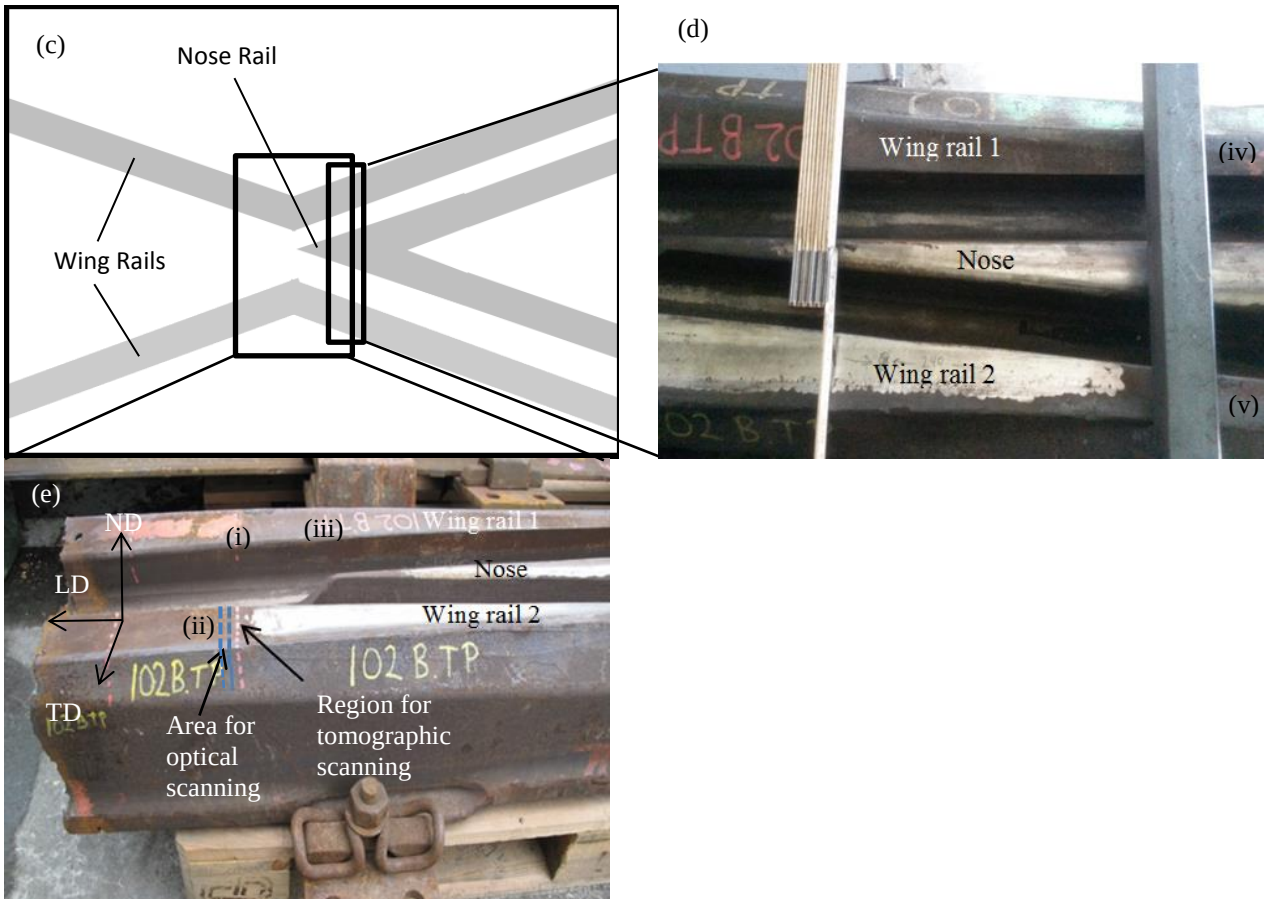

Figure 1: Schematic diagram of a railway switch and crossing showing the position of switch rails when the train moves on to the (a) diverging track and (b) straight track. (c) Schematic diagram of only the crossing panel showing the different components, with (d) and (e) showing the parts of the manganese steel crossing cut out for investigations. The roman numbers within the figure (in black) indicate the locations of hardness measurements. ND, TD, LD represents normal direction, transverse direction and longitudinal direction respectively.

3.2 Microstructure

The microstructure is austenitic in manganese steel. The grain size is coarse, ranging up to 500 µm, and the grains do not deform by shearing as in pearlitic rails. Figure 3(a-d) shows optical micrographs of the deformed wing rail at different depths from the wheel running surface. At the rolling contact surface, Figure 3a, a large number of bands can be seen crossing each other within the grains. The deformation in manganese steels is manifested in the form of these bands and not by the usual elongation of grains as seen in pearlite. The surface receives the maximum deformation and hence the density of the bands is higher here and decreases with depth from the surface (Figures 3a-d). At around 12 mm in depth (Figure 3d) the microstructure is almost free from deformation bands. The deformation bands are inhomogeneously distributed with a wavy appearance and the direction of the bands varies from one grain to another. From optical microcopy it is not possible to reveal whether the deformation bands are mechanical twins or dislocation boundaries. The deformed microstructure in the wing rail was found to be similar to the manganese nose rail investigated previously [9].

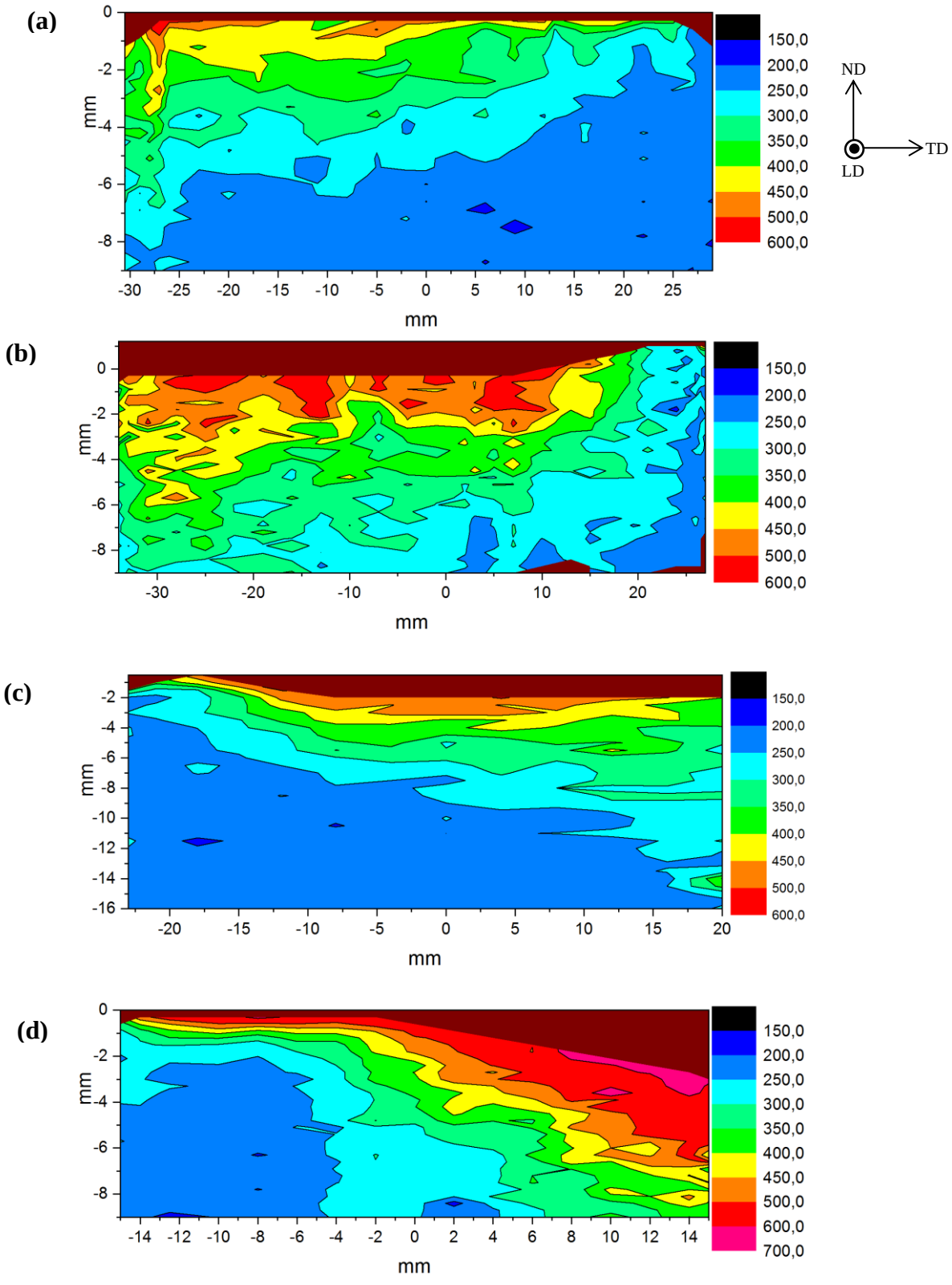
(a)
(b)
(c)
(d)
mm
150,0
200,0
250,0
300,0
350,0
400,0
450,0
500,0
600,0
700,0
ND
TD
LD

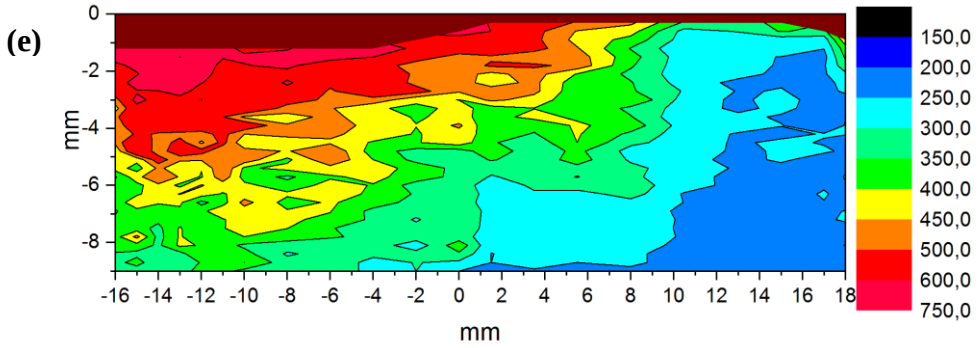

Figure 2: Hardness contour maps of the wing rails at different locations: (a) Wing rail 1 position i, (b) Wing rail 2 position ii, (c) Wing rail 1 position iii, (d) Wing rail 1 position iv and (e) Wing rail 2 position v.

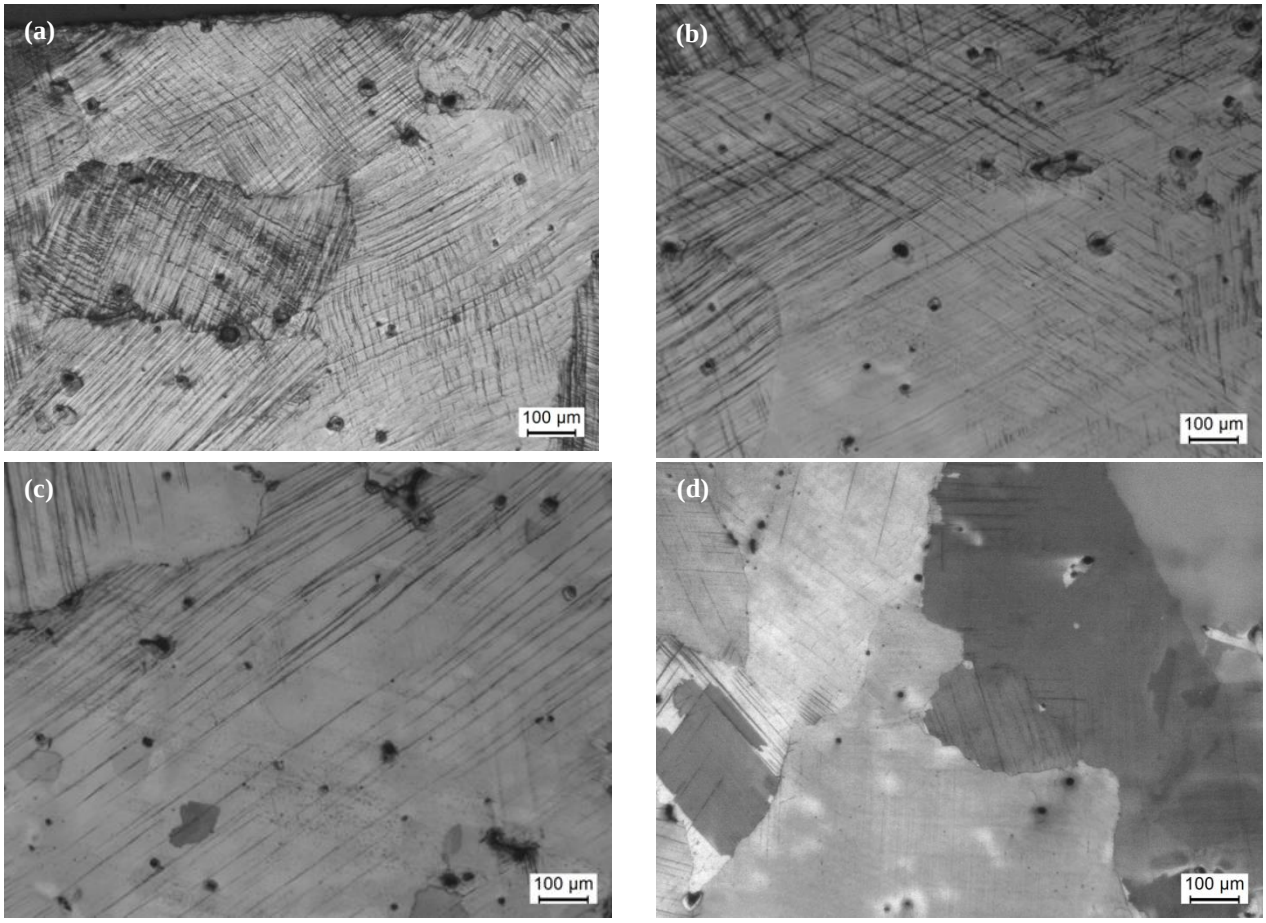

Figure 3: Optical microscopy images of the transverse section (a) at the rolling contact surface, (b) at 6 mm depth from the surface, (c) at 10 mm from the surface, and (d) at 12 mm from the surface, where the base hardness has been reached.

3.3 X-ray Computerized Tomography

Two samples with size 10 mm by 10 mm by 40 mm from wing rail 2 (see Figure 1e) were characterized by X-ray tomography. Figure 4(a-d) shows 2D slices from one of the 3D tomographic reconstructions. Tomographical reconstructions are 3D density maps, which allow detection of even small cracks due. Figure 4 shows a very long subsurface crack parallel to the running surface across the entire cross section of the specimen. However, the full 3D reconstruction also reveals the presence of cracks in contact with the surface. While most of the cracks run parallel to the running surface, the crack network is extensive and continuous.
Figure 5 shows the 3D reconstructions of another crack network in sample 2. In this figure, the steel is represented as

transparent and the blue colored areas represent air, including air inside the cracks, thereby making the crack network and running surface visible. The white box represents the volume of the wing rail which has been scanned. The interior crack surface has a rough and wavy appearance with ridges which are quite similar to the failure surfaces often seen in rolling contact fatigue. Figure 5 also reveals that the crack network is spreading quite deep into the rail, with seemingly random crack propagation. Most of the cracks move parallel to the running surface, as apparent from Figure 4, but there is also some diverging downward branching cracks which could cause rail break in the long run. The wing rail contains both surface and sub surface cracks, where some are interconnected and some propagate individually.

Figure 4: 2D slices showing the crack network within the wing rail at different locations along the longitudinal direction (a) at the trasverse cut (0 mm), (b) 10 mm from the transverse cut, (c) 18 mm from the transverse cut and (d) 29 mm from transverse cut.

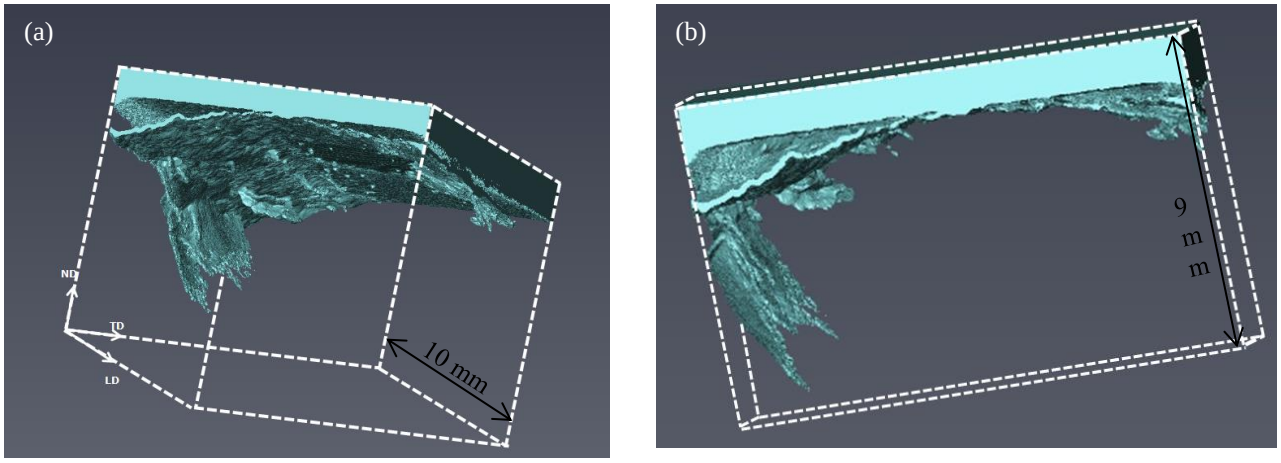

Figure 5: (a and b) 3-D tomographic representations of the crack network within the wing rail of a manganese crossing seen from different directions. The steel is represented as transparent and the blue coloured area represent air, making the crack network and running surface visible.

4. Discussion

The damage and deformation in the manganese wing rail is found to be quite similar to that in the manganese nose rail studied previously [9]. Although the geometry of a wing rail is different from the nose, the microstructural characteristics are similar. The deformation is manifested in the formation of a high density of deformation bands. The depth of hardening in both cases reached as high as 10 mm from the rail running surface. In case of the nose rail, cracks were found in the highly deformed top surface layers having high hardness of 600 Hv. In this study it was found that locations on the wing rail having very high hardness, position iv and v, were crack free whereas cracks were mostly found in regions of comparatively less hardness, position ii. Therefore high deformation cannot be the only reason for crack formation in switches and crossings. Rail wheel interaction induces both normal and shear contact stresses when a train moves over a crossing, however the change of rolling planes from wing rail to nose, or vice versa, introduces high impact stresses as well. Most likely it is the impact from the wheel that is the reason for crack formation.

The two-phase microstructure in a pearlite grade material, consisting of ferrite and cementite, affects the deformation mechanism and eventually the crack initiation and propagation [18], where cracks tend to propagate through the softer ferrite phase, resulting in a wavy appearance. Figure 6 shows a rolling contact fatigue crack in pearlite grade steel from a straight track with a wavy crack propagation that passes through several grains. Figure 7 shows an optical micrograph of a subsurface crack in the wing rail of the manganese steel crossing investigated in this work having the same wavy appearance intersecting several grains with several crack branches and a seemingly random crack propagation. This is in correspondence to the cracks found in a manganese steel crossing nose studied previously in [9], where a more detailed study showed the cracks avoided the twinned regions (harder areas of the matrix) and were mostly transgranular giving the wavy appearance by following the weakest link in the microstructure. Therefore, although the plastic deformation is caused by slip in pearlitic grade without twinning, and for manganese steel deformation is from both dislocation motion as well as twinning, the crack networks have a similar appearance for pearlitic steel straight tracks and manganese steel crossings.

5. Conclusions

The deformation and degradation of the wing rails of a damaged non explosion hardened manganese steel crossing, which has been in service in the Danish rail network, was studied. More than 90% of the traffic through this crossing was in straight track, from the nose to the wing rails and hence one of the wing rails is severely damaged from impacts and cracks are present. Heavy deformation is evident with the formation of a high density of deformation bands at the running surface. The hardening reaches to a depth around 10 mm from the running surface, with the surface having a very high hardness of above 600 Hv which gradually drops to a base hardness of 220 Hv. Cracks were not found at the locations with highest hardness, thus it is likely that the wheel impact causes the cracks and not the deformation. The nondestructive 3D mapping of the crack network using X-ray tomography reveals the crack network and its minute branches with high resolution. The presence of both surface and sub surface cracks is evident in the wing rail. Though the material and the deformation mechanism of the manganese steel is quite different from that of normal pearlitic grade steel, the crack network seems to be similar to rolling contact fatigue cracks found in pearlitic grade steel used in

normal straight tracks. The cracks tend to be concentrated mostly within the plastically deformed layer and have a wavy surface appearance which is common for rolling contact fatigue cracks.

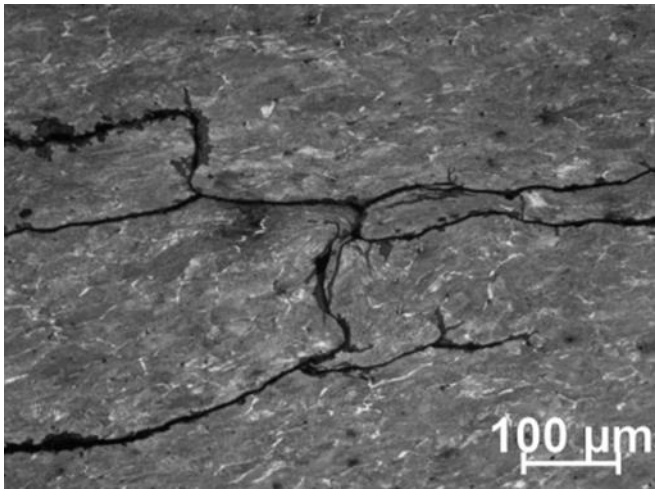

Figure 6: Optical micrograph of a rolling contact fatigue crack in a rail from straight track of pearlitic steel [19].

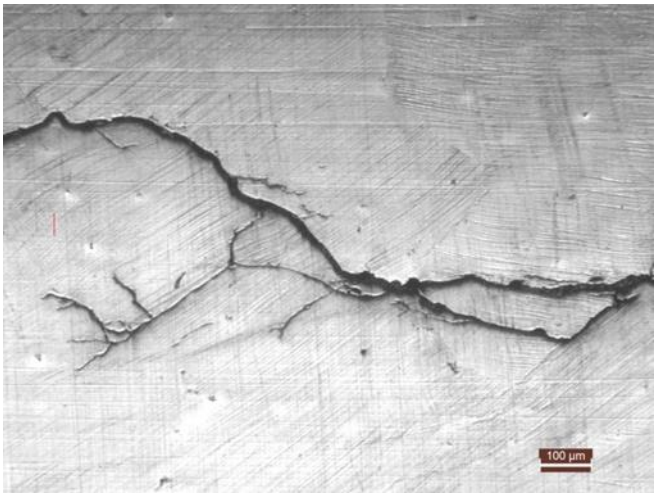

Figure 7: Optical micrograph of a rolling contact fatigue crack in the wing rail of manganese steel crossing.

Acknowledgments

The authors gratefully acknowledge support from the Innovation Fund Denmark through the project "INTELLISWITCH – Intelligent Quality Assessment of Railway Switches and Crossings" (Grant no 4109-00003B).

References

[1] B. Lv, M. Zhang, F. C. Zhang, C. L. Zheng, X. Y. Feng, L. H. Qian and X. B. Qin: *Micro-mechanism of rolling contact fatigue in Hadfield steel crossing*, International Journal of Fatigue, 2012, 44, 273–278.

[2] M. Schilke, N. Larijani and C. Persson: *Interaction between cracks and microstructure in three dimensions for rolling contact fatigue*, Fatigue and Fracture of Engineering Materials and Structures, 2014, 37, 280-289.

[3] C. Jessop, J. Ahlström, L. Hammar, S. Fæster and H. K. Danielsen: *3D characterization of rolling contact fatigue crack networks*, Wear, 2016, 366-367, 392–400.

[4] Y. Zhou, X. Zheng, J. Jiang and D. Kuang: *Modeling of rail head checks by X-ray computed tomography scan technology*, International Journal of Fatigue, 2017, 100, 21–31.

[5] M. Steenbergen and R. Dollevoet: *On the mechanism of squat formation on train rails – Part I: Origination*, International Journal of Fatigue, 2013, 47, 361-372.

[6] M. Steenbergen and R. Dollevoet: *On the mechanism of squat formation on train rails – Part II: Growth*, International Journal of Fatigue, 2013, 47, 373-381.

[7] L. Wang, A. Pyzalla, W. Stadlbauer and E. A. Werner: *Microstructure features on rolling surfaces of railway rails subjected to heavy loading*, Materials and Engineering A, 2003, 359, 31-43.

[8] M. Masoumi, E. Anderson Ariza, A. Sinatora and H. Goldenstein: *Role of crystallographic orientation and grain boundaries in fatigue crack propagation in used pearlitic rail steel*, Materials and Engineering A, 2018, 722, 147-155.

[9] S. Dhar, H. K. Danielsen, S. Fæster, C. Rasmussen, Y. Zhang and D. Juul Jensen: *Crack formation within a Hadfield manganese steel crossing nose*, Submitted to Journal of Wear.

[10] F. C. Zhang, B. Lv, T. S. Wang, C. L. Zheng, M. Zhang, H. H. Luo, H. Liu and A. Y. Xu: *Explosion hardening of Hadfield steel crossing*, Materials Science and Technology, 2010, 26:2, 223-229.

[11] S. L. Guo, D. Y. Sun, F. C. Zhang, X. Y. Feng and L. H. Qian: *Damage of a Hadfield steel crossing due to wheel rolling impact passages*, Wear, 2013, 305, 267–273.

[12] J. E. Garnham and C. L. Davis: *Very early stage rolling contact fatigue crack growth in pearlitic rail steels*, Wear, 2011, 271, 100–112.

[13] H. C. Eden, J. E. Garnham and C. L. Davis: *Influential microstructural changes on rolling contact fatigue crack initiation in pearlitic rail steels*, Materials Science and Technology, 2007, 21(6), 623–629.

[14] E. G. Astafurova, M. S. Tukeeva, G. G. Zakharova, E. V. Melnikov and H. J. Maier: *The role of twinning on microstructure and mechanical response of severely deformed single crystals of high-manganese austenitic steel*, Materials Characterization, 2011, 62, 588-592.
[15] P.H. Adler, G.B. Olson and W.S. Owen: *Strain hardening of Hadfield manganese steel*, Metallurgical Transaction A, 1986, 17A, 1725-1737.
[16] Y. N. Dastur and W. C. Leslie: *Mechanism of work hardening in Hadfield manganese Steel*, Metallurgical Transaction A, 1981, 12A, 749-759.
[17] Y. I. Chumlyakov, I. V. Kireeva, H. Sehitoglu, E. I. Litvinova, E. G. Zaharova and N. V. Luzginova: *High-strength single crystals of austenitic stainless steels with nitrogen content: mechanisms of deformation and fracture*, Materials Science Forum, 1999, 318–320, 395–400.
[18] F. D. Fischer, W. Daves, R. Pippan and P. Pointner: *Some comments on surface cracks in rails*, Fatigue and Fracture of Engineering Materials and Structures, 2008, 29, 938-948.
[19] M. Schilke: *Degradation of railway rails from materials point of view*, PhD Thesis, Department of Materials and Manufacturing Technology, Chalmers University of Technology, 2013, Sweden.

Paper 3

Synchrotron X-Ray measurement of residual strain within the nose of a worn manganese steel railway crossing

S. Dhar, Y. Zhang, R. Xu, H. K. Danielsen and D. Juul Jensen

IOP Conference Series: Materials Science and Engineering 219 (2017) 012016
doi:10.1088/1757-899X/219/1/012016

Synchrotron X-Ray measurement of residual strain within the nose of a worn manganese steel railway crossing

S Dhar[1], Y Zhang[1], R Xu[2], HK Danielsen[1] and D Juul Jensen[1]

[1] Section for Materials Science and Advanced Characterization, Department of Wind Energy, Technical University of Denmark, Risø Campus, Roskilde, DK- 4000, Denmark
[2] Advanced Photon Source, Argonne National Laboratory, Argonne, IL, 60439-4800, USA

E-mail:sodh@dtu.dk, yubz@dtu.dk

Abstract. Switches and crossings are an integral part of any railway network. Wear plastic deformation and rolling contact fatigue due to repeated passage of trains cause severe damage leading to the formation of surface and sub-surface cracks which finally may result in rail failure. Knowledge of the internal stress distribution adds to the understanding of crack propagation and may thus help to prevent catastrophic rail failures. In this work, the residual strains inside the bulk of a damaged nose of a manganese railway crossing which was in service for five years has been investigated by using differential aperture synchrotron X-ray diffraction. The main purpose of this paper is to describe how this method allows non-destructive measurement of residual strains in selected local volumes in the bulk of the rail. Measurements were conducted on the transverse surface at a position about 6.5 mm from the rail running surface of the crossing nose. It was observed that significant compressive residual strains along the train running direction exist in the tested sample.

1. Introduction

Switches and crossings (S&Cs) are of great importance for any railway network as they allow trains to be directed from one track to another. The geometry, as well as the loading situations, in the nose of a crossing (see figure 1) differs from that of normal rails. It has been observed that the majority of the track problems are associated with switches and crossings which lead to higher maintenance costs than for any other part of the track. There have been studies performed on the deformation behavior of the crossing nose [1-5], which clearly indicate that very high contact stress occurs at the rail/wheel contact surface due to repeated passage of wheels. The stress levels are higher than the yield strength of the material causing plastic deformation of the material. The nose rail undergoes contact, friction, and impact stresses, which leads to wear and rolling contact fatigue. Many defects appear including surface and subsurface cracks. The stress distribution (of both contact and residual stresses) plays an important role in generation of cracks in the material which may lead to failure. Residual stresses are generated in a rail during manufacturing as well as while in service. There are quite a few studies on measurement of residual stresses in normal rail heads in literatures, including both modelling and experimental work [6-15]. Mostly tensile residual stresses are present in the rail head after the

straightening process during manufacturing, however in service the state of stress changes due to variable loading situations and generate a complex stress field.

There are different experimental techniques to measure the residual stress in any material. The non-destructive methods include use of X-rays or neutrons. However, ordinary X-rays are limited by intensity and penetration depth. This means they typically give a mean stress averaged over the penetration depth within a small area. In recent years, neutron diffraction has been used to determine residual stresses in the rail head [8-11]. Neutrons have significantly more penetration depth than ordinary X-rays, but due to relative low intensity only stresses averaged over fairly large volumes in the mm^3-cm^3 range can be determined. Alternatively, with the advent of high energy synchrotron radiation, local residual stresses can be determined in the bulk of the samples. Measurements of residual stresses on worn rails [12-14] as well as roller-straightened new rail heads [15] using synchrotron X-Ray diffraction method have been published.

The novelty of the present work is that we focus on stresses in the heavily loaded nose of an S&C and that the selected S&C is made of manganese steel optimized to improve wear and fatigue resistance compared to conventional pearlitic steel. Moreover the manufacturing process of manganese steel railway crossings is different from normal rails. It is cast as a single piece and then explosion hardened.

The purpose of this work is to apply synchrotron X-ray measurements to the nose of a rail crossing, and to determine the depth profiles of residual strains. The crossing rail sample used in the experiment was taken from the rail network which was in service for five years on a major railway line in Denmark with both freight and passenger trains.

2. Experimental Procedure

The residual strains in the nose of manganese steel crossing were investigated in this study. Visual inspection of the nose revealed severe damage with cracks and spallation. The chemical composition and mechanical properties of the steel are given in table 1 and table 2, respectively. The sampling area of the nose for synchrotron measurements is described in figure 1. The slice for the measurement was 5mm thick and strain measurements were made on the transverse surface at various depths along the longitudinal direction. To avoid mechanical strains induced during grinding and cutting of the slice, the free surface was electropolished before measurements.

Table 1. Chemical composition of the manganese steel (wt%).

C	Mn	Si	Cr	P	S	Fe
1.14	12.81	0.26	0.12	0.05	0.05	balance

Table 2. Mechanical properties of the manganese steel.

Tensile strength	Yield Strength	Elongation	Hardness
~750 MPa	~365 MPa	~20%	~220 HV

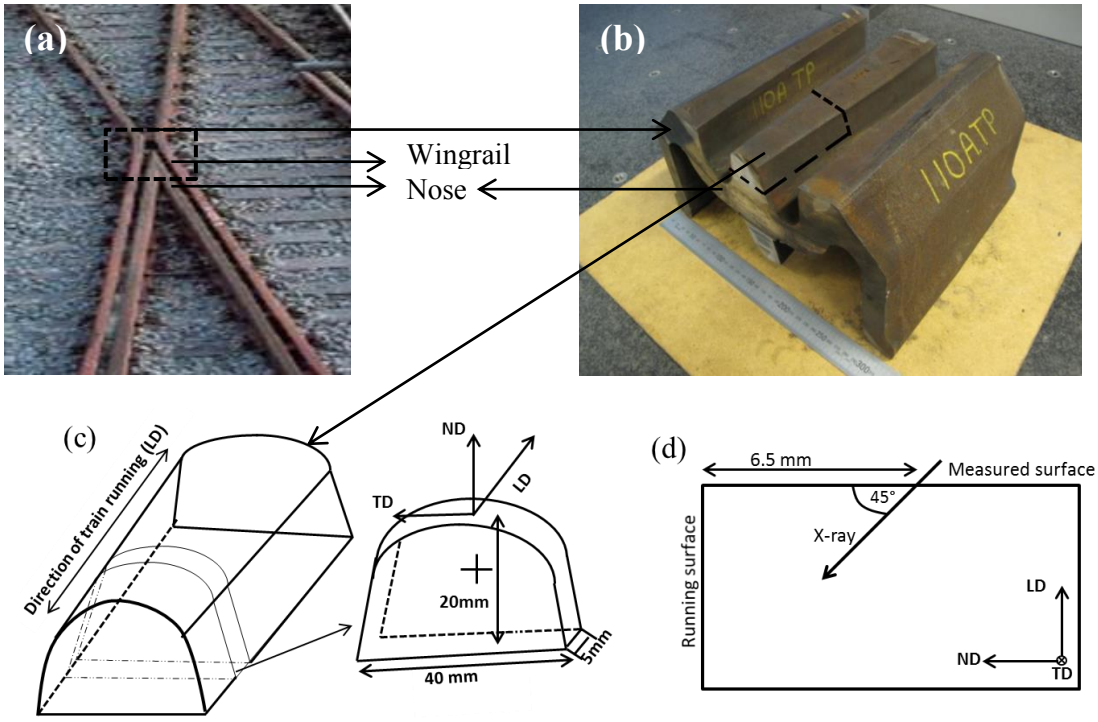

Figure 1. Nose specimen used for the synchrotron strain measurement: (a) A crossing (with nose and wingrail) (b) Part of a manganese steel crossing cut out from the track for investigation, (c) Final sampling slice for strain measurements showing the normal direction (ND), transverse direction (TD) and longitudinal direction (LD). The black cross marks the position for synchrotron measurement. (d) Sketch showing the experimental set-up for synchrotron measurement.

Synchrotron measurements were conducted on the transverse section at a position about 6.5 mm from the rail running surface of the crossing nose (see figure 1d) at beam line 34-ID-E at the Advanced Photon Source (APS), Argonne National Laboratory [16].

A focused polychromatic beam was first used to determine the orientations of the matrix grains. The use of non-dispersive Kirkpatrick-Baez (K-B) focusing mirrors helps in focusing of the beam on to the specimen. The resulting microbeam had a full-width half maximum of ~0.5 µm. The X-ray microbeam scanned the specimen which was mounted on a holder at an inclination of 45º to the incoming beam (see figure 1d). The Laue diffraction patterns from the polychromatic scans were recorded on an area detector mounted in 90º reflection geometry 510.3 mm above the specimen. The diffraction patterns from different depths were obtained by the use of a Pt-wire of 100 µm diameter as a differential aperture. The Laue patterns at each depth were reconstructed by the use of the LaueGo software [17] available at APS beamline 34-ID-E. The patterns were indexed, from which the (hkl) indices of individual spots as well as their corresponding X-ray energies were determined. From these data, a spot with high intensity and its corresponding plane parallel to the specimen surface was selected for monochromatic energy scan to determine the absolute lattice spacing. Thereby the strain (in one direction) was measured as:

$$\varepsilon = \frac{d - d_0}{d_0} \tag{1}$$

where d is the lattice spacing of the sample and d_0 is the lattice spacing of the sample in the stress-free state. For the present study, d_0 was calculated based on the lattice parameter determined at the base of the nose (at a depth of 20 mm from the running surface) using laboratory X-ray measurements

assuming that, apart from manufacturing stresses, this place is free from stresses induced due to wheel rail interaction. These measurements were done at Department of Materials and Manufacturing Technology at Chalmers University of Technology, Sweden. Chromium source (X- Ray wavelength λ = 2.2897 Å) was used. The lattice parameter determined from the (220) peak at a diffraction angle of 126.85º is a = 3.621 Å which is used as reference d_0.

3. Results and Discussion

The crystallographic orientations measured using polychromatic beam differential aperture X-ray diffraction (DAXM) at four locations, 0.5 mm apart, are shown in figure 2. The grain orientations within depth of 0-50 µm from the measurement surface are shown. The result shows that the grain at position of 6.5 mm from the running surface has the least orientation spread (see figure 2b) and the highest indexed percentage. This grain is therefore chosen for the monochromatic energy scan.

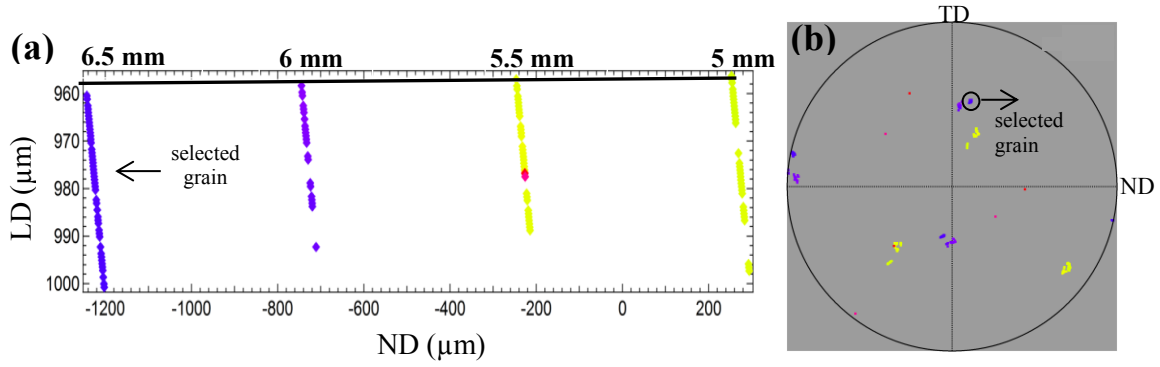

Figure 2. Grain orientation at different depths and different locations on the transverse surface (a) and their corresponding (001) pole figure (b). The grain selected for monochromatic energy scan for determination of lattice absolute spacing is marked. The black line in (a) marks roughly the measurement surface. The colors in (a) and (b) are corresponding to the crystallographic orientations.

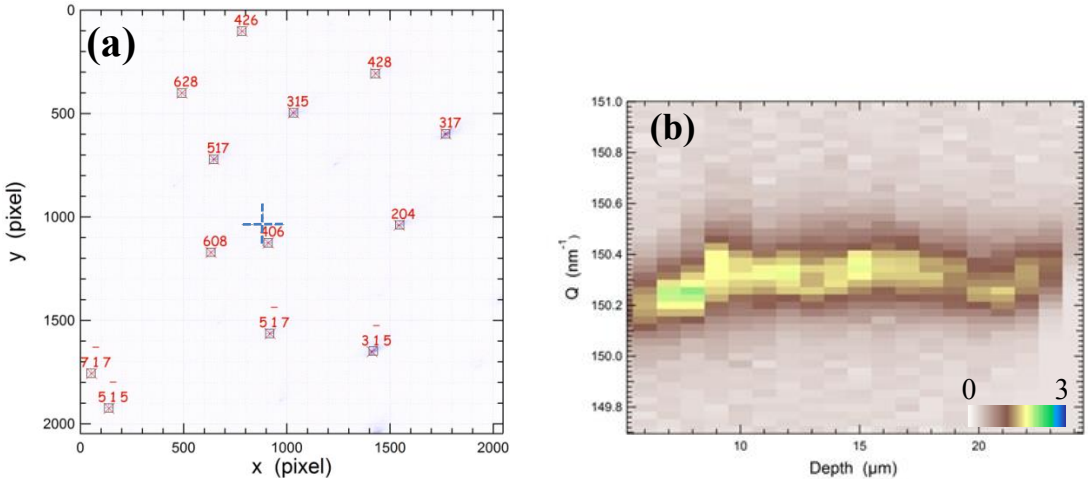

Figure 3. (a) Indexing of a polychromatic beam Laue diffraction patterns, (b) Intensity distributions as a function of diffraction vector Q at each depth.

Figure 3a shows an indexed Laue pattern with the (hkl) indices obtained at one of the depths from polychromatic beam diffraction for the selected grain. Based on this diffraction pattern the spot (517) was selected for the monochromatic energy scan as the intensity of this spot is relatively high and the

corresponding X-Ray energy is high about 21 keV. The normal of the chosen (517) plane is about 2º away from sample normal direction, which is marked by the dashed cross in figure 3a.

From the monochromatic energy scan, the diffraction images around the (517) spot at each energy step for each depth are reconstructed. As each energy corresponds to a specific diffraction vector Q ($Q = 2\pi/d$), the integrated intensity of each diffraction image as a function of the diffraction vector can be determined at all X-ray penetrated depths (see figure 3b). A few examples of the Q distribution at different depths are given in figure 4a, which clearly shows that the strain distribution varies within the sample from tensile to compressive strains. The dashed line marks the Q value for d_0 of the (517) crystallographic plane. A shift to the right relative to the dashed line indicates compressive strains and vice versa for tensile strains. At each depth, the Q distribution was fitted using a Gaussian function and the center of the distribution, Q_c was used to determine the crystallographic plane spacing, d.

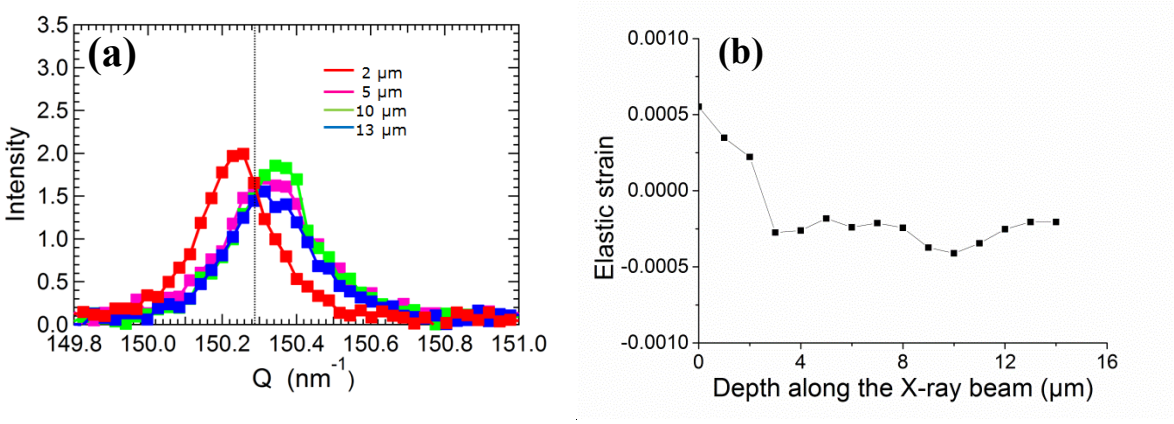

Figure 4. (a) Intensity variation as a function of Q at different depths within the sample (The dashed line marks the Q value for d_0 of the (517) crystallographic plane). (b) The residual strain along LD as a function of depth along the incoming X-ray.

Figure 4b shows the elastic strain (component which is normal to the transverse surface of the sample) developed in the nose crossing at different depths from the measuring surface. It can be seen that in the bulk of the material there are residual compressive strains in the range of 2×10^{-4} up to 4.11×10^{-4}.

Whereas theoretically the out of plane normal strain at a free surface is zero, tensile strains are seen within the first 3 μm from the free surface in figure 4b. Two possible explanations for this tensile strain are: i) the reference d_0 is not strain free. It is very likely that the grains even at depth of 20 mm below the running surface are also under compression, thus the dashed line in figure 4a should be shifted to the left, and the curve in figure 4b should move down towards more compressive strain. ii) Due to a small experimental error, the free surface may be wrongly identified by about 2-3 μm from the currently assumed position. If the measurement surface in figure 4b (i.e. 0 point) changes about 2-3 μm to the right, the tensile strain at the measurement surface is reduced. Irrespective of this, we can conclude the bulk volume is under compressive residual strains.

The problem of railway damage and failure can be caused by multiple mechanisms but it is evident that interaction between residual stresses and the defects (cracks etc.) can lead to severe problems. Generally compressive stresses are beneficial because they are supposed to inhibit crack propagation whereas tensile stresses are conducive for crack propagation. Although we find the longitudinal stresses are compressive, the normal or the transverse component of the stress may have a tensile component which could lead to crack evolution and failure. Also, generally the presence of a significant compressive stress is counterbalanced by a tension zone underneath. A complete map of all the components of the stresses in the three directions at different depths from the running surface would be helpful to understand the interaction of residual stress with damage mechanisms. This will

be investigated in future work. Also the synchrotron data will be compared with those measured using standard laboratory X-rays.

4. Conclusion

The residual strain distribution within a 5 mm thick slice of the nose of a manganese railway crossing was analyzed in the longitudinal direction at a distance of 6.5 mm from the rail surface. To our knowledge this is the first time synchrotron radiation was employed to measure the strains in a nose of of a manganese railway crossing. It was found that compressive strains exist along the longitudinal direction (with some small oscillations in the values) even at a depth of 6.5 mm from the wheel contact surface. Rail wheel interaction at the nose of the crossing induces severe plastic deformation of the nose, the effect of which is thus evident even at a depth of 6.5 mm from the contact surface.

Acknowledgement

The authors gratefully acknowledge support from the Innovation Fund Denmark through the project "INTELLISWITCH – Intelligent Quality Assessment of Railway Switches and Crossings" (Grant no 4109-00003B) and grant from Interreg ESS & MAX IV: Cross Border Science and Society (Project number DTU-009). Use of the Advanced Photon Source was supported by the U.S Department of Energy, Office of Basic Energy Sciences, under Contract No.DE-AC02-06CH11357. The authors would also like to thank the Department of Materials and Manufacturing Technology at Chalmers University of Technology, Sweden for helping with the laboratory X-ray measurements.

References

[1] Johansson A, Pålsson B, Ekh M, Nielsena JCO, Ander MKA, Brouzoulis J and Kassa E 2011 *Wear* **27**1 472–481

[2] Wiest M, Daves W, Fischer FD and Ossberger H 2008 *Wear* **265** 1431–38

[3] Guo SL, Sun DY, Zhang FC, Feng XY and Qian LH 2013 *Wear* **305** 267-273

[4] Lv B, Zhang M, Zhang FC, Zheng CL, Feng XY, Qian LH and Qin XB 2012 *Int J Fatigue* **44** 273-278

[5] Harzallah R, Mouftiez A, Felder E, Hariri S and Maujean JP 2010 *Wear* **269** 647–654

[6] Xiao JH, Zhang FC and Qian LH 2014 *Fatigue Fract Engng Mater Struct* **37** 219–226

[7] Kaiser R ,Stefenelli M , Hatzenbichler T, Antretter T, Hofmann M, Keckes J and Buchmayr B 2015 *J Strain Anal Eng* **50(3)** 190–198

[8] Sasaki T, Takahashi S, Kanematsu Y, Satoh Y, Iwafuchi K, Ishida M and Morii Y 2008 *Wear* **265** 1402–07

[9] Jun TS, Hofmann F, Belnoue J, Song X, Hofmann M and Korsunsky AM 2009 *J Strain Anal Eng* **44(7)** 563-568

[10] Luzin V, Prask HJ, Herold TG, Gordon J , Wexler D , Rathod C, Pal S , Daniel W and Atrens A 2013 *Neutron News* **24(3)** 9-13

[11] Rathod C, Wexler D, Luzin V, Boyd P and Dhanasekar M 2014 *Mater Sci Forum* **77** 213-218

[12] Webster PJ, Hughes DJ, Mills G and Vaughan GBM 2002 *Mater Sci Forum* **404-407** 767-772

[13] Pyzalla A, Wang L, Wild E and Wroblewski T 2001 *Wear* **251** 901–907

[14] Kelleher JF, Buttle DJ, Mummery PM and Withers PJ 2005 *Mater Sci Forum* **490-491** 165-170

[15] Kelleher J, Prime MB, Buttle D, Mummery PM, Webster PJ, Shackleton J and Withers PJ 2003 *J Neutron Res* **11(4)** 187-193

[16] Liu W, Zschack P, Tischler JZ, Ice GE and Larson BC 2010 *AIP Conf. Proc.* **1365** 108-111

[17] Tishchler JZ 2014 Reconstructing 2D and 3D X-ray orientation map from white beam Laue *Strain and Dislocation Gradients from Diffraction* eds R Barabash and GE Ice (London: Imperial College Press) chapter 10 pp 358-375.

Paper 4

Synchrotron and laboratory X-ray measurements of residual strains in manganese steel from a railway crossing

S. Dhar, H. K. Danielsen, R. Xu, Y. Zhang and D. Juul Jensen

To be submitted for international publication

Synchrotron and laboratory X-ray measurements of residual strains in manganese steel from a railway crossing

Somrita Dhar[1], Hilmar K Danielsen[1], Ruqing Xu[2], Yubin Zhang[3], Carsten Rasmussen[4] and Dorte Juul Jensen[3]

[1]Department of Wind Energy, Technical University of Denmark, Risø Campus, Roskilde, DK- 4000, Denmark
[2]Advanced Photon Source, Argonne National Laboratory, Argonne, IL, 60439-4800, USA
[3]Department of Mechanical Engineering, Technical University of Denmark, Kgs. Lyngby, DK-2800, Denmark
[4]Banedanmark, Amerika plads 15, Copenhagen, DK-2100, Denmark

Abstract:

Several X-ray methods exist for determination of residual strains in metallic components. In this work we have used differential aperture synchrotron X-ray diffraction to map the local distribution of residual strains and the standard $\sin^2\psi$ vs d laboratory X-ray method to determine macroscopic residual strains. The nose of a worn manganese steel railway crossing was investigated. The laboratory X-ray measurements revealed significant residual strains are induced in the longitudinal and transverse directions on the rail running surface due rail wheel contact, while the synchrotron X-ray measurements documented that high local compressive residual strains exist at depths as deep as 15 mm from the running surface.

Introduction:

The presence of residual stresses in materials and components are often overlooked in spite of they may be significant and affect the mechanical properties both in a positive and negative way. As an example shot peening may be used to introduce compressive residual stresses in the surface layers to improve crack resistance [1]. While on the contrary tensile stresses of half or more of the yield stresses may upset engineering design and contribute to the need for significant safety factors in the design in many components [2].

A main reason why residual stresses are often ignored is that it is not so straight forward to measure them experimentally. The available techniques may be classified into two groups: destructive and nondestructive ones. The destructive ones include hole drilling, sectioning and the more recently developed contour method [3]. The destructive nature of these methods is problematic, making them prohibited for testing critical components in operation and for following the evolution in residual stresses over time. The non-destructive methods include X-ray and neutron diffraction as well as ultrasonic and magnetic methods [4]. The ordinary X-ray methods have limited penetration depth while the neutrons can penetrate significantly deeper but suffer from poor spatial resolution [5]. X-rays from high energy synchrotron sources allow both high penetration power and good spatial resolution [6-7]. Drawbacks here are the limited access to relevant synchrotron sources and the restrictions on specimen/component size that can be investigated here. The non-destructive ultrasonic and magnetic methods suffer from being less direct in nature and the results thus need interpretations based on assumptions. For an excellent overview of various methods see [4].

The present work deals with residual stresses in a rail component; namely the nose of a manganese steel railway crossing which has been in service for five years in the Danish rail network and is heavily damaged. For rail components, in particular the fatigue life and the dimensional stability are affected by the presence of residual stresses. Both these properties are critical for safe operation of the railway. Whereas many experimental and theoretical studies have been published on residual stresses on conventional pearlitic rail steel of straight rails [8-13], to the authors' best knowledge residual stresses in used noses made of the more complex manganese steel have not been reported before. The nose is in particular interesting as it is exposed to both contact friction and impact stresses which lead to more severe wear and rolling contact fatigue than straight rail [14-15]. Furthermore preliminary measurements indicate that significant stresses are present even deep in the nose [16].

In the present work, we apply two X-ray techniques to quantify the residual stresses in the selected nose. We use the conventional laboratory X-ray $\sin^2\psi$ vs d method to determine the macro (Type I) stresses along the running surface and perpendicular to it while we use differential aperture synchrotron X-ray diffraction to determine the local micro (Type II/Type III) strains along the longitudinal direction (running direction) at four different depths down to 15 mm from the rail surface. Besides the information on the magnitude of the residual stresses in the worn nose, the potentials and limitations of the two X-ray methods for the present component will be discussed.

Experimental procedure:

The residual strain within a damaged and deformed nose from a manganese steel crossing is investigated in this study. The crossing was in service in the Danish railway network for five years and had both freight and passenger traffic through it. The approximate traffic density through it was around 14 MGT. Visual inspection of the crossing reveals severe spallation and cracks. The Hadfield steel has a chemical composition of 1-1.4% C, 12-13% Mn and addition of other alloying elements including ~0.18% Cr, 0.4-0.6% Si, and 0.022-0.033% P. The undeformed manganese steel has a hardness of 220 Hv, yield strength of 363 MPa and elastic modulus of 203 GPa [15]. The undeformed microstructure is composed of large equiaxed austenitic grains with an average grain size of 500 µm. The surface of the nose receives the maximum deformation and the microstructure here contains a large number of deformation induced bands. The direction of these bands varies from grain to grain and in some grains they intersect each other (see Figure 1). The density of these bands is maximum at the surface and decreases through the depth.

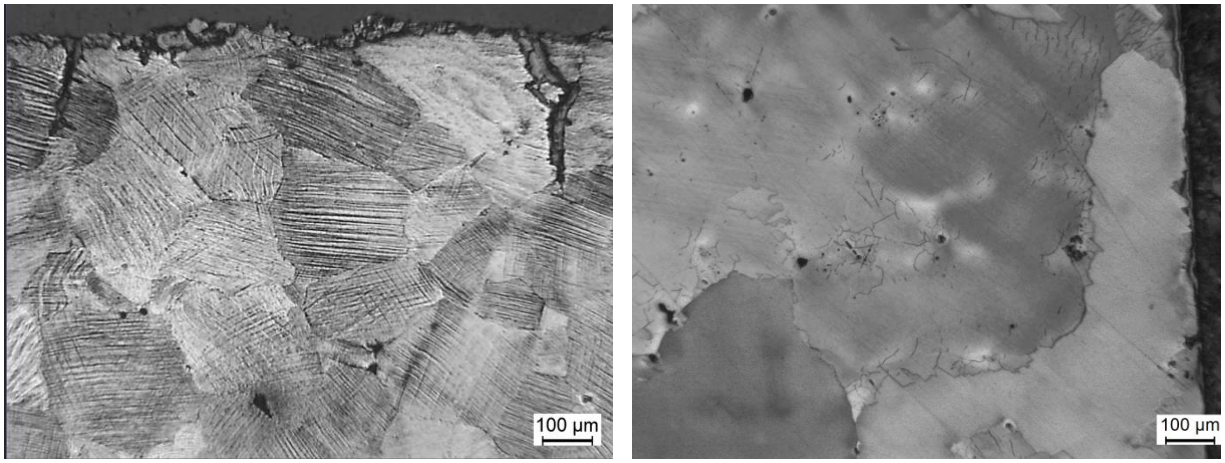

Figure 1:Optical micrographs of the microstructure of the manganese steel nose. (a) Specimen taken at the running surface showing a deformed microstructure with deformation induced bands. (b) Specimen taken from 20 mm below the running surface showing large equiaxed grains (the few bands here originate from the casting process).

Synchrotron Measurements:

Synchrotron measurements were conducted on the transverse (TD, ND) surface of a specimen cut out from the nose (Specimen A, see Figure 2a) at beam line 34-ID-E at the Advanced Photon Source (APS), Argonne National Laboratory. The sampling positions are shown in Figure 2b and 2c. The specimen was 5mm in thickness (see Figure 2b) and measurements were made at various depths along the longitudinal direction (running direction) for each of the four sampling position. The transverse surface was electro polished to avoid mechanical stresses induced due to cutting and polishing.

The strain was calculated as

$$\varepsilon = \frac{d-do}{do} \quad \ldots\ldots\ldots\ldots\ldots\ldots\ldots\ldots\ldots\ldots\ldots\ldots\ldots\ldots\ldots\ldots . (1)$$

where d is the lattice spacing at the measured position and d_0 is the lattice spacing of the specimen in stress-free state. This spacing (d_0) was obtained from laboratory X-ray diffraction measurements with a chromium source (X-ray wavelength = 2.2897 Å) using a specimen taken from the base of the nose at a depth of 20 mm from the running surface. Optical microscopy suggests that at this depth there is no effect of deformation due to wheel rail interaction (see Figure 1b). The undeformed lattice parameter was determined from the {220} peak to be 1.2802 Å.

The lattice spacings d of the selected strained volumes were determined based on differential aperture X-ray microscopy (DAXM) using synchrotron radiation [17].

(a)

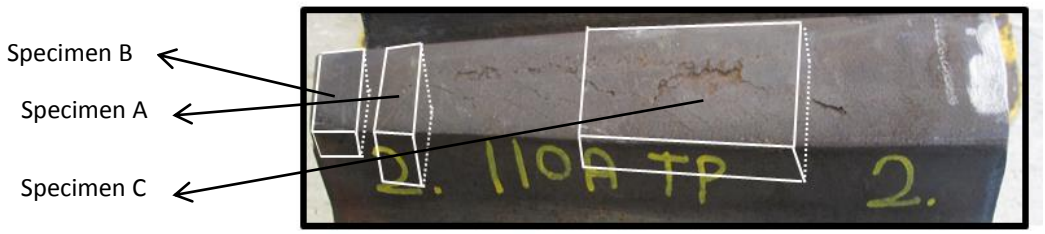

(b)

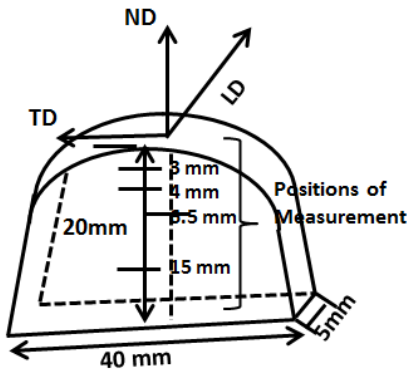

(c)

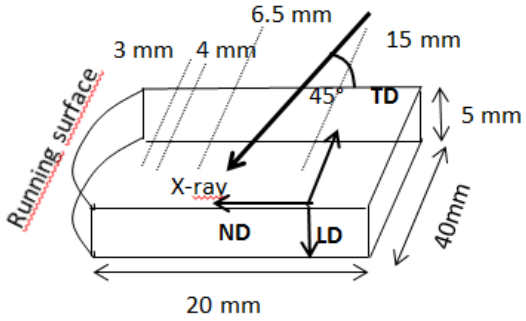

(d)

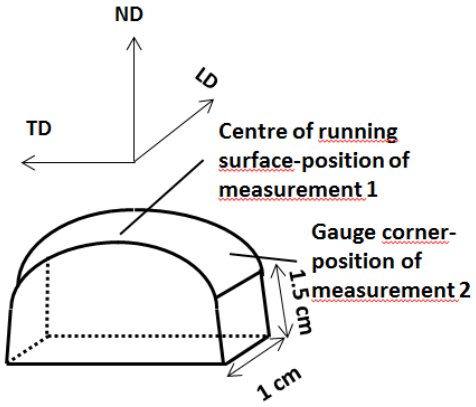

(e)

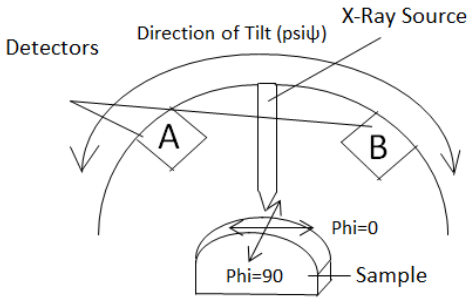

(f)

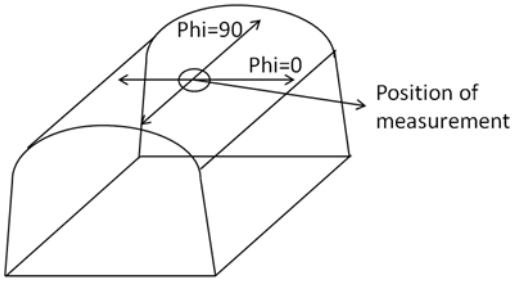

Figure 2: Photo and schematic diagrams showing where specimens A, B and C were cut out from the nose for the strain measurements. (a) Photograph showing the nose studied. (b) Schematic diagram of specimen A. The positions of the synchrotron X-ray diffraction measurements are also shown. (c) Sketch showing the experimental synchrotron X-ray set up for specimen A and the points of measurement on the specimen. (d) Schematic diagram of Specimen B for laboratory X-ray diffraction scans showing the positions of measurements at the running surface and at the gauge corner. (e) Sketch showing the experimental set-up for the laboratory X-ray measurements. (f) Schematic diagram of specimen C used for laboratory X-ray diffraction scans showing the position of the measurement.

The specimen was mounted on a holder with an inclination of 45 ˚ to the incoming X-ray beam. A polychromatic beam was used first to determine the orientations of the matrix grains. The focusing of the beam was done with the help of non-dispersive Kirkpatrick-Baez (K-B) focusing mirrors. The resulting microbeam has a Lorentzian profile and a full-width half maximum of ~0.5 µm. The Laue diffraction patterns from the scanned volume were recorded on a detector which was mounted in 90 ˚ reflection geometry at a distance of 510.3 mm from the specimen. A Pt-wire of 50 mm diameter was used as a differential aperture to obtain the diffraction patterns at different depths. The Laue patterns at each depth were reconstructed by the use of the LaueGo software available at APS beamline 34-ID-E [18]. The patterns were indexed, from which the hkl indices of the individual spots as well as their corresponding X-ray energies were determined. A spot with high intensity and the diffraction vector normal to the specimen surface was then selected for monochromatic energy scans to determine the lattice spacings, d, at the selected positions, within the specimen A.

Laboratory X-ray Diffraction measurements:

The laboratory X-ray measurements of Type I macro stresses were done at two different diffractometers. This was simply due to our possibility of getting access.
One set of measurements were made using a Xstress 3000 G2R diffractometer equipped with a Cr Kα X-ray source. Measurements were made on the wheel running surface of specimen B at two positions as shown in Figure 2d. The standard $\sin^2\psi$ vs d technique [19-20] with 9 tilts from -45˚ to +45˚ along three directions of 0˚, 45˚ and 90˚ was used for determining the stress values. The operating conditions were: voltage 30 kV, current 6.7 mA and exposure time 60 secs. The {220} austenitic peak around 2θ=128˚ was measured. The incident X-ray beam was collimated to a diameter of 1.5 mm. The diffraction peaks were fitted using the Stress Tech Xtronic software, using a cross relation method with a linear background [21]. XRD measurements are made at different psi (ψ) tilts of the specimen to measure the peaks and the inter-planar spacing, d from them. The inter-planar spacings, d are then plotted as a function of $\sin^2\psi$. The stress is determined from the slope of the curve. This assumes a zero stress ($d = d_o$) at $\sin^2\psi = 0$. The stress is calculated as $\sigma = \left(\frac{E}{1+\nu}\right) m$ where m is the slope of the curve, E is the Young's Modulus and ν is the Poison's ratio [19]. For the present material ν=0.28 and E= 203 GPa. This procedure was followed for all the three directions (0˚, 45˚ and 90˚).

X-ray diffraction (XRD) measurements were also performed using a Bruker X-ray diffractometer operated in the Bragg–Brentano configuration still applying Cr-Kα radiation. X-ray diffractograms were recorded with a step size of 0.07° in 2θ, a voltage of 35 kV and exposure time of 10s in the angular range of 2θ in 122°–133° to record the austenitic {220} peak. The measurements were made on two specimens. (i) The specimen used for synchrotron measurements (Specimen A). For this specimen measurements were made on the transverse section at 5 locations from the running surface at 3, 6, 9, 12 and 15 mm from the surface. (ii) A larger specimen with dimensions 95x50x25 mm (specimen C :see Figure 2f). For this large specimen, the measurements were made on the running surface. The standard $\sin^2\psi$ vs d technique was used for both specimens with 9 tilts from 0 to 65 ˚ along the two directions of 0˚and 90˚ for specimen C whereas both positive and negative psi tilts were performed for specimen A. The stresses were measured along the running direction and also perpendicular to the running direction for the large specimen C.

Results:

Synchrotron Measurements:

The Laue diffraction pattern obtained from the polychromatic diffraction scan of specimen A at one of the four locations (6.5 mm depth) is shown in Figure 3. The (hkl) indices of the individual spots are also given. Based on this, the spot (517) was selected for the monochromatic energy scan as the intensity of this spot is relatively high and the corresponding X-ray energy is high; about 21 keV. This high energy is necessary to achieve a good penetration depth. With this X-ray energy, it is found that good a diffraction signal is obtained for penetration depths up to 70µm from the specimen surface. Monochromatic X-ray scans were performed for all the four selected positions (see Figure 1b) at different depths from the running surface.

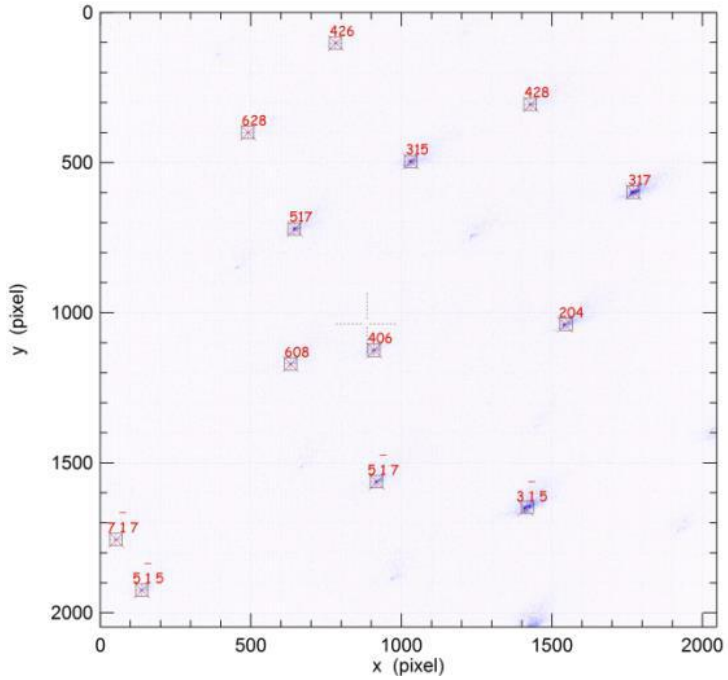

Figure 3: Indexing of the polychromatic Laue diffraction pattern for specimen A measured at a depth of 6.5 mm from the running surface [16].

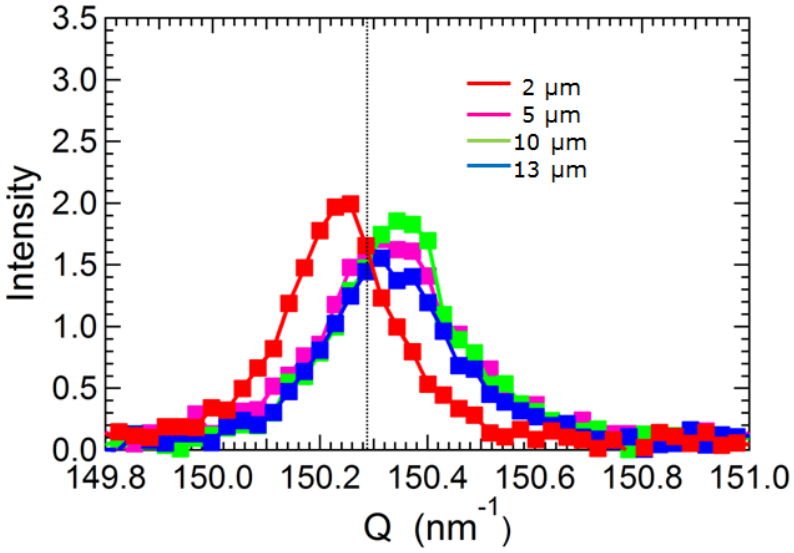

Figure 4: Intensity variation as a function of Q at different penetration depths within specimen A measured at a depth of 6.5 mm from the running surface. The dashed line marks the Q value for d_o of the (517) peak [16].

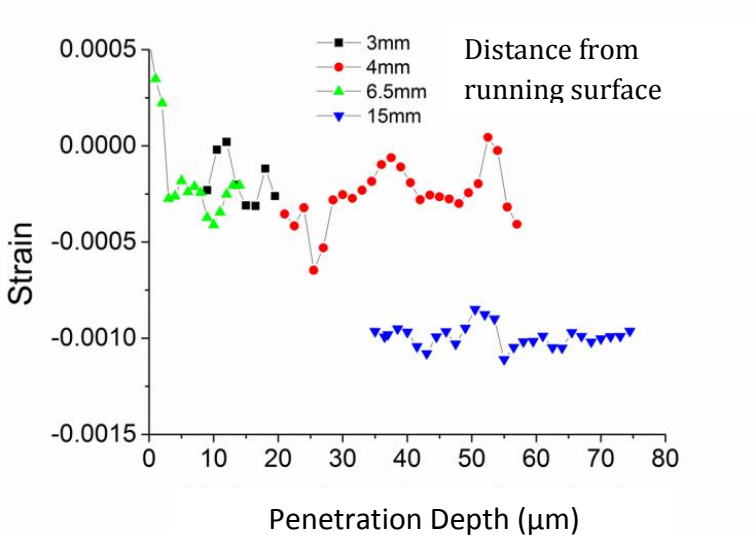

Figure 5: The residual strain measured nondestructively along the longitudinal direction to a penetration depth within the specimen of upto 75µm at different distances from the running surface.

For the location of 6.5 mm from the running surface, the intensity and the Q distribution are plotted at different penetration depths. At each depth, the Q distribution is fitted using a Gaussian function and the center of the distribution, Qc is determined from which d is calculated. The dashed line marks the Q value for d_0 of the (517) peak. As can be seen from Figure 4 the peaks of the Q distribution shift from the left to the right side of the dashed line with increasing penetration depth. This means that the residual strain near the specimen surface is observed to be tensile whilst it is compressive at higher penetration depths at this distance from the running surface.
Figure 5 gives an overview of all the measured strains at the four selected depths from the running surface. The figure reveals that there are significant residual micro strains at all depths which are mostly compressive, and that the strains are fairly constant as a function of penetration depth from the specimen surface down to 70 µm below this free surface. It is remarkable that the compressive residual strain at 15 mm from the running surface is twice as large as the strains at 3, 4 and 6.5 mm.

Laboratory Measurements:

For the large specimen C, measurements were made in two directions (the transverse and the longitudinal direction). The $\sin^2\psi$ vs d plots for the two directions are given in Figure 6. Nice straight lines are observed in both cases indicating absence of shear stresses. Based on the slopes and the standard software, the stress values calculated are -460 MPa and -615 MPa respectively. This means that very large compressive residual stresses are present in both directions.

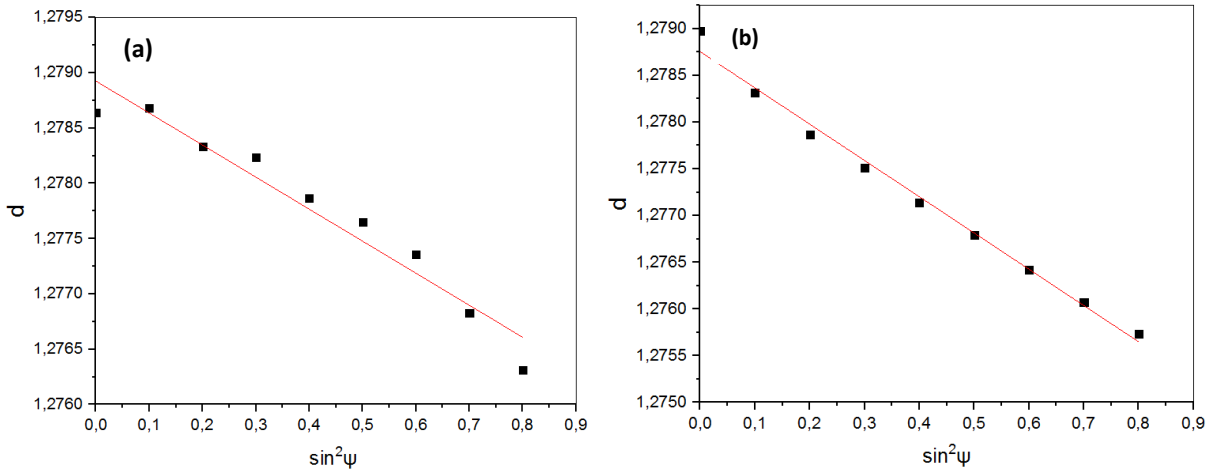

Figure 6: The $\sin^2\psi$ vs d plot measured on the running surface of Specimen C for the two directions. (a) Transverse. (b) Longitudinal.

Whereas these measurements were done on specimen C taken at some distance from the tip of the nose (see Figure 2a) and at a position away from any visual cracks and spallation, we performed similar measurements on specimen B which is much nearer the nose tip. It should however be noted that a large crack is present in this specimen B running from the center to a depth of 2-3 mm from the surface. Measurements were taken in an area away from but still near the crack network. For Specimen B, examples of $\sin^2\psi$ vs d plots for two locations at the center of the running surface and at the gauge corner are given in Figure 7. Since both positive and negative psi tilts were used, the average of the slopes of the positive and negative curves was used to calculate the stress values using standard software. The stress values thus measured at 3 different directions (i.e. $\varphi=0^\circ$, 45° and 90°) and are given in Table 1.

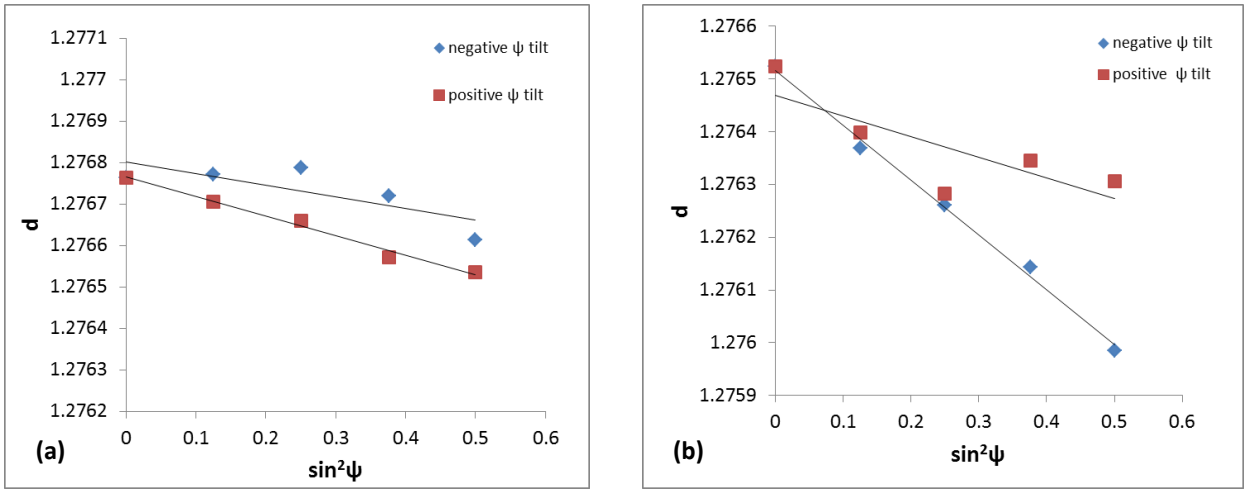

Figure 7: The $\sin^2\psi$ vs d plot for the laboratory X-ray measurements on running surface of specimen B at $\varphi=0^\circ$. (a) Center of the specimen. (b) At the gauge corner.

Table 1: Stress values obtained at different directions on two locations of specimen B.

Location	Stress at $\varphi=0^\circ$ (MPa)	Stress at $\varphi=45^\circ$ (MPa)	Stress at $\varphi=90^\circ$(MPa)
Centre	-59.78	-180.25	-121.99
Gauge corner	-113.34	-103.79	-82.48

The difference in stress values in different directions at different locations may be due to difference in wheel rail contact when a train passes over the nose. The area of contact of the wheel on the nose will affect the stresses developed. The results are however also affected by the presence of the crack which has released part of the stresses

Laboratory X-ray measurements were also performed for specimen A, at five different depths from the running surface (3, 6, 9, 12 and 15 mm) to supplement the synchrotron X-ray measurements on the same specimen. At all these depths the resulting $\sin^2\psi$ vs d plots show only points which are too scattered for the standard software to determine any stress values from. An example is shown in Figure 8. The likely reason for this is stress relaxation occurring at the cut out free surface. So the laboratory X-rays ($\lambda=2.2897$ Å) which only penetrates roughly 10 µm into the specimen will record no macro stresses.

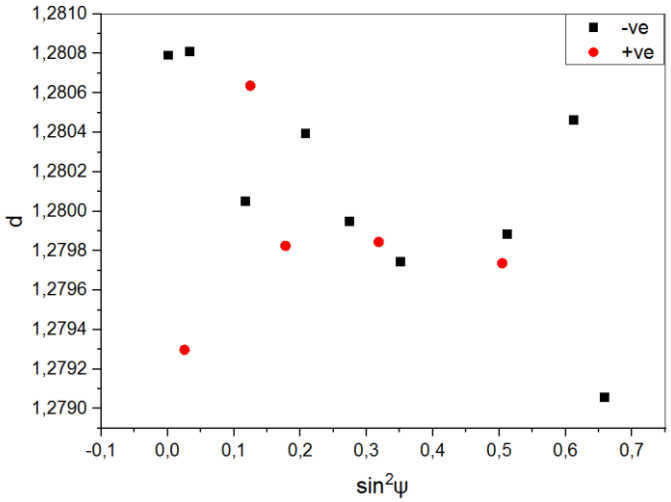

Figure 8: The $\sin^2\psi$ vs d plot for the laboratory X-ray measurements on the transverse surface of specimen A at a depth of 15 mm from the running surface. The black and red dots are from negative and positive ψ tilts respectively.

Discussion:

Residual stresses are present in essentially all engineering components originating from the manufacturing processes itself and evolving during in-service operations. For freshly manufactured straight rails, residual stresses up to 250 MPa is generally accepted [22] and studies published in the open literature reports compressive values in the range 300-500 MPa for rails which have been in operation in the open track [23-24].

In the present work we have characterized the residual stresses present in the nose of a crossing made of manganese steel which has been in operation for five years and experienced 14 MGT traffic density from both passenger and freight trains.

By laboratory X-ray measurements we found that very large compressive macro stresses of values up to -615 MPa were present at the running surface. A first point to notice here is that the reported macro stress are calculated using standard software and procedures, assuming a biaxial stress state at the free surface, i.e. $\sigma_{33} = 0$. This assumption implies also that the normal strain, ε_{33} should be close to 0. However, as can be seen in Fig. 6 and 7, the d values at $\sin^2\Psi = 0$ are in the range 1.2765-1.290Å, values which are significantly different from the d_0 of 1.2802Å we measured from the undeformed base of the nose. There could be two reasons for the differences: i) The stress state at the investigated positions are not simple biaxial and the assumption underlying the macro stress calculation is not fulfilled. More experimental measurement and a more comprehensive data analysis could clarify how large or how small an effect the non-biaxial stress state has on the macro stress reported here. ii) The different d_0 measured from the two laboratory X-ray instruments implies a difference in 2Θ of 0.45°, which may be a result of a misalignment between the X-ray instruments. Another notable aspect is that a macro stress of -615 MPa largely exceeds the yield stress of the material. It however has to be noted that 363 MPa is the yield stress for the *undeformed* manganese steel. As the present steel is significantly plastically deformed (See Figure 1a); its yield point will be much higher. For Hadfield steel deformed by explosion hardening, yield values as high as 660 MPa has been reported in literature [25]. It is therefore realistic that a residual stress of 615 MPa can be present in a severely deformed crossing near the nose where the largest impact forces and rolling contact fatigue occurs.

Residual stresses can be relaxed by several mechanisms; by crack formation and growth, which is critical for the railway switches and crossings, and by plastic deformation occurring when the residual stresses exceeds the actual yield point and which hardens the material. The latter in general has a positive effect increasing wear resistance.

Effects of cracks on residual stress relaxation were investigated in the present study by measuring the residual stresses present in a specimen taken at a location where a large crack has evolved (Specimen B). For this specimen we found that the macro residual stresses are significantly reduced to values in the range -50 to -180 MPa at the running surface and that the stress state is converted to include shear components. The latter is not surprising due to the presence of the crack. At the gauge corner, residual stress values of -80 to -113 MPa are observed. It is therefore clear that cracks can fully relax the residual stresses build up during operation however of course with the negative effect that the nose is damaged.

Another important parameter to investigate is how deep into the rail away from the running surface the residual stresses extend to. We tried to determine that by laboratory X-ray macro stress measurements. We cut a specimen out (Specimen A) and performed the measurements on the cut-out transverse section. However as can be seen in Figure 8,

the attempt was unsuccessful. A reason could be that the grain size of the steel is too large compared to the size of the X-ray beam. The grain size of the present steel is around 500 µm and the X-ray beam is 1.5 mm. This may explain why measurements are unsuccessful deep below the running surface where grains may be undeformed. However the measurements are also unsuccessful nearer to the running surface, 2, 4, 6 mm below the surface, where optical microscopy documents that the grains are heavily subdivided by twins and high angle deformation induced dislocation boundaries with a distance of around 3-4 µm [15]. The large grain size can therefore not explain why these measurements fail. This conclusion is substantiated by the fact that the measurements directly on the running surface are successful (Figure 6). Stress relaxation occurring near the surface when the transverse surface becomes free during the cutting out of the specimen is a much more likely explanation

We thus used synchrotron X-ray of 21 keV which readily penetrates 75 µm in iron to measure the residual stresses below the cut out free transverse surface as a function of depth from the running surface. Figure 5 reveals that micro compressive residual strains are present at all measured depths and is actually the highest at the largest depth measured at 15 mm below the running surface. The micro residual stresses, of which we only measured one component, cannot be directly compared to the more conventional macro stresses determined by the $\sin^2\psi$-d method using laboratory X-rays. The present micro strain results however document that the residual stresses are not only at the running surface but on the contrary extends to significant depths. For the present data (Figure 5), it is of interest to note that the largest micro strain exists at a distance of 15 mm from the running surface and the micro strains at 4mm are about half of that. Stress relaxation by cracks cannot be the explanation for this. It is however observed that the microstructure near the running surface are heavily deformed while at 15mm only few deformation induced boundaries are observed [15]. It is therefore suggested that residual stresses build up to the yield point at the near to the running surface layers after which they are at least partly relaxed by introducing plastic deformation into the material. At 15mm the residual strain values are around 0.001. Using a simple conversion, from strain to stress with Poison's ratio of 0.28 and E=203 GPa, the stress values 158 MPa are obtained. Therefore the residual stress at this depth has not yet reached the yield point of the material.

Large strains given by the wheel rail interaction deform the top surface layers plastically as the stresses here exceed the yield point. Deeper in the nose the external load is below the yield point and is therefore manifested as residual stresses as in the present specimen. A similar phenomenon was observed in ductile cast iron where volumes near the graphite nodules were plastically deformed and large residual stresses were seen further away [7].

The present depth profiles of residual stresses are of importance when interpreting crack propagation. The measured stresses are compressive except very near (the artificially) free transverse section surface. This means they are actually beneficial and contribute to crack closure within the measured layers. That the compressive strains are largest at significant depth may contribute to explaining why cracks formed near the surface of the nose typically evolve to a certain depth and then move parallel to the running surface instead of moving deeper into the material.

Conclusions:

The residual stresses in the nose of Hadfield manganese steel crossing extracted from the Danish rail network after five years in operation were studied. Both standard $\sin^2\psi$-d laboratory X-ray measurements of macro stresses and synchrotron X-ray measurements of micro strains were performed. It was found that.

- Macro residual stress measurements on the running surface of the crossing nose revealed compressive stresses as large as -615 MPa determined by standard procedure. This is higher than the yield stress of the undeformed material. High deformation by rail wheel contact has hardened the top layers increasing the yield strength in the running surface layers, and it is suggested that very large residual stresses thus can exist here.
- The presence of cracks extending to the surface of the nose can reduce the residual stresses significantly as observed in this study where the residual stresses on the running surface near the vicinity of the crack are reduced to values below -200 MPa.
- Micro residual stresses are not only present at the running surface but are observed to extend to a depth of at least 15 mm. For the present nose, the micro residual stresses are about twice as large at the depth of 15 mm from the running surface than at depths nearer to the surface (depths of 3, 4 and 6.5 mm). It is suggested that this difference is related to the fact that the load at the near surface layers exceeds the yield and thus plastically deform the material. The large compressive residual stresses at. 15 mm depth may contribute to explaining why cracks generally move parallel to the surface at certain depths instead of continuing perpendicular to the surface deeper into the material.

As the present work has demonstrated significant and complex residual stress profiles existing the nose of a railway crossing, it is suggested that the residual stresses have to be included both in the design of crossings, while interpreting failure mechanisms, and in lifetime predictions.

Acknowledgments:

The authors would like to thank Interreg ESS & MAX IV: Cross Border Science and Society (Project number DTU-009) for their grant for allowing this research. Use of the Advanced Photon Source was supported by the U.S Department of Energy, Office of Basic Energy Sciences, under Contract No.DE-AC02-06CH11357. The authors would also like to thank Dr. Dinesh Mallipeddi from the Department of Materials and Manufacturing Technology at Chalmers University of Technology, Sweden and Flemming Bjerg Grumsen from the Department of Mechanical Engineering at the Technical University of Denmark for helping with the laboratory X-ray measurements. Dorte Juul Jensen and Yubin Zhang further wish to acknowledge support from the European Research Council (ERC) under the European Union's Horizon 2020 research and innovation programme (grant agreement No 788567-M4D).

References:

[1] H. Wohlfahrt, Shot Peening and Residual Stresses, in: Kula E., Weiss V. (Eds.), Residual Stress and Stress Relaxation, Sagamore Army Materials Research Conference Proceedings (28) Springer, Boston, MA, 1982.

[2] Handbook of Residual Stress and Deformation of Steel, Editors: G. Totten, M. Howes, T. Inoue, ASM International, 2002.

[3] M. B. Prime, Cross-Sectional Mapping of Residual Stresses by Measuring the Surface Contour After a Cut, Journal of Engineering Materials and Technology 123(2) (2000) 162-168.

[4] P. J Withers and H. K. D. H. Bhadeshia, Residual stress Part 1 – Measurement techniques, Journal of Materials Science and Technology 17 (4) (2001) 355-365.

[5] P. J. Webster, X. Wang, G. Mills and G. A. Webster, Residual stress changes in railway rails, Physica B: Condensed Matter 180–181 (2) (1992) 1029-1031.

[6] S. C. Wu, T. Q. Xiao and P. J. Withers, The imaging of failure in structural materials by synchrotron radiation X-ray micro tomography, Engineering Fracture Mechanics 182 (2017) 127-156.

[7] Y. Zhang , T. Andriollo , S. Fæster , W. Liu , J. Hattel and R. I. Barabash, Three-dimensional local residual stress and orientation gradients near graphite nodules in ductile cast iron, Acta Materialia 121 (2016) 173-180.

[8] T. Sasaki, S. Takahashi, Y. Kanematsu, Y. Satoh, K. Iwafuchi, M. Ishida and Y. Morii, Measurement of residual stresses in rails by neutron diffraction, Wear 265 (2008) 1402–1407.

[9] K. H. Lo, P. Mummery and D. J. Buttle, Characterisation of residual principal stresses and their implications on failure of railway rails, Engineering Failure Analysis 17 (2010) 1273–1284.

[10] P. J. Webster, D. J. Hughes, G. Mills and G. B. M. Vaughan, Synchrotron X-Ray Measurement of Residual Stress in a Worn Railway Rail, Materials Science Forum 404-407 (2002) 767-772.

[11] R. Kaiser, M. Stefenelli, T. Hatzenbichler, T. Antretter, M. Hofmann, J. Keckes, and B. Buchmayr, Experimental characterization and modelling of triaxial residual stresses in straightened railway rails, Journal of Strain Analysis for Engineering Design 50(3) (2015) 190-198.

[12] A. Pyzalla, L. Wang, E. Wild and T. Wroblewski, Changes in microstructure, texture and residual stresses on the surface of a rail resulting from friction and wear, Wear 251(1–12) (2001) 901-907.

[13] W. Solano-Alvarez, M. J. Peet, E. J. Pickering J. Jaiswal, A. Bevan and H. K. D. H. Bhadeshia, Synchrotron and neural network analysis of the influence of composition and heat treatment on the rolling contact fatigue of hypereutectoid pearlitic steels, Materials Science and Engineering A 707 (2017) 259-269.

[14] M. Wiest, W. Daves, F. D. Fischer and H. Ossberger, Deformation and damage of a nose rail due to wheel passages, Wear 265 (2008) 1431–1438.

[15] S. Dhar, H. K. Danielsen, S. Fæster, C. Rasmussen, Y. Zhang and D. Juul Jensen, Crack formation within a Hadfield manganese steel crossing nose, Submitted to Journal of Wear.

[16] S. Dhar, Y. Zhang, H. K. Danielsen and D. Juul Jensen, Synchrotron X-Ray measurement of residual strain within the nose of a worn manganese steel railway crossing,38th Risø International Symposium on Materials Science, IOP Conf. Series: Materials Science and Engineering 219 (2017) 012016.

[17] W. Liu, P. Zschack, J. Z. Tischler, G. E. Ice, B. C. Larson, X-ray laue diffraction microscopy in 3D at the advanced photon source, AIP Conf. Proc. 1365 (2010) 108-111.

[18] J. Z. Tishchler, Reconstructing 2D and 3D X-ray orientation map from white beam Laue, in: R. Barabash, G.E. Ice (Eds.), Strain and Dislocation Gradients from Diffraction Chapter 10, Imperial College Press, London, 2014.

[19] M. E. Fitzpatrick, A. T. Fry, P. Holdway, F. A. Kandil, J. Shackleton and L. Suominen, Determination of Residual Stresses by X-ray Diffraction – Issue 2, National Physical Laboratory Teddington (2005) Middlesex, United Kingdom.

[20] U. Welzel, J. Ligot, P. Lamparter, A. C. Vermeulen and E. J. Mittemeijer, Stress analysis of polycrystalline thin films and surface regions by X-ray diffraction, Journal of Applied Crystallography 38 (2005) 1-29.
[21] E. Brinksmeier, Improvements in X-Ray stress analysis, Advances in Surface Treatment 2 (1986) 109-115.
[22] CEN/TC256/WG4. Draft standard railway applications-track heavy rail. Part 1: flat bottom symmetrical railway rails 46 kg/m and above. European Committee for Standardization; 1997.
[23] V. Luzin, H. J. Prask, T. Gnaupel-Herold, J. Gordon, D. Wexler , Ch. Rathod, S. Pal , W. Daniel and A. Atrens, Neutron residual stress measurements in rails, Neutron News 24:3 (2013) 9-13.
[24] J. Kelleher, M. B. Prime, D. Buttle, P. M. Mummery, P. J. Webster, J. Shackleton and P. J. Withers, The measurement of residual stress in railway rails by diffraction and other methods, Journal of Neutron Research 11 (4) (2003) 187-193.
[25] F. C. Zhang, B. Lv, T. S. Wang, C. L. Zheng, M. Zhang, H. H. Luo, H. Liu and A. Y. Xu, Explosion hardening of Hadfield steel crossing, Materials Science and Technology 26 (2) (2010) 223-229.

Paper 5

Multi-axial Fatigue Deformation of Head Hardened Pearlitic and Austenitic Manganese railway steels: A comparative study

S. Dhar, J. Ahlstrom, X. Zhang, H. K Danielsen and D. Juul Jensen

To be submitted for international publication

Multi-axial Fatigue Deformation of Head Hardened Pearlitic and Austenitic Manganese railway steels: A comparative study

S.Dhar[1], J.Ahlstrom[2], X. Zhang[3], H.K Danielsen[1,] and D. Juul Jensen[3]

[1]Department of Wind Energy, Technical University of Denmark, Risø Campus, Roskilde, DK- 4000, Denmark

[2] Department of Industrial and Materials Science, Chalmers University of Technology, Gothenburg, SE-41296, Sweden

[3] Department of Mechanical Engineering, Technical University of Denmark, Kgs. Lyngby, DK- 2800, Denmark

* E-mail: sodh@dtu.dk

Abstract:

Switches and Crossings in a rail network suffer from damage and deformation due to severe loading and complex geometric shape. Therefore a thorough knowledge of the mechanical behavior and microstructure changes associated with materials used in crossings is needed. A comparative study on the cyclic deformation characteristics and fatigue behavior of head hardened pearlitic and Hadfield manganese steel, which are used as crossing material, have been made and explained with respect to low cycle fatigue behavior under conditions of uniaxial and biaxial, as well as proportional and non-proportional loading. Also, the different microstructures developed in the two different types of steels after deformation are analyzed by optical and transmission electron microscopy. The pearlitic steel endured higher life cycles compared to manganese steel under all conditions. The cyclic response of manganese steel was significant hardening whereas softening was present for pearlitic steel except for biaxial non proportional loading. TEM micrographs reveal that the deformed microstructure of the pearlitic steel consisted of threading dislocations and dislocation tangles. The microstructures in manganese steel under different conditions are composed of dislocation cells with dislocation tangles inside, intersected by straight stacking fault lamellae.

Introduction:

Rail wheel contact induces very high contact stresses due to rolling and sliding. Different parts of the rail network are subjected to different types of stress conditions. Switches and crossings are of very much importance in this respect. They are more susceptible to damage and deformation due to their complex geometric shape as compared to other parts of the rail, experiencing high contact and impact stresses. This leads to more frequent failures and large maintenance cost. The two most common types of steels used in railway crossings are head hardened pearlitic steels and austenitic manganese steel, also known as “Hadfield steel”. Pearlitic steels possess properties like good strength, toughness and wear resistance whereas Hadfield steel possesses excellent work hardening ability as well as good toughness and wear resistance. The stresses encountered by the rail surface are transient, multiaxial, non-proportional and in different directions [1]. The rolling contact cyclic loading induces large strains in the surface layers of the rail from where cracks initiate by Rolling Contact Fatigue (RCF) mechanisms. Rail wheel interaction induces cyclic elastic stresses in the entire rail, which can lead to High Cycle Fatigue (HCF). But the surface layer, close to the rail/wheel contact, plastic deformation and ratcheting strains accumulate which are often evaluated using Low Cycle Fatigue (LCF) experiments [2]. The aim of this work is to improve the understanding of how the material behavior of the surface layers of rails

develops under RCF loading. To investigate well-defined conditions, different laboratory scale low cycle fatigue experiments have been performed on the two different grades of steel which are used as crossing material and an attempt has been made to correlate the mechanical properties with the microstructure developed in the materials.

Several studies have been conducted on cyclic plasticity over the last decades. It has been demonstrated that damage is dependent on many factors including the type of loading, the presence of stress raisers and residual stresses in the material [1]. Under the conditions of strain controlled loading, the material can exhibit cyclic hardening, cyclic softening or cyclic saturation. This is strongly dependent on the material microstructure including dislocation density and arrangement, as well as sub-structure formation [3].

Fatigue properties of manganese steels have been examined in some previous studies. Rittel et al. [4] studied the cyclic properties of coarse grained cast manganese steel and found pronounced hardening effect. Studies by Schilke et al. [5] and Kang et al. [6] on LCF of manganese steel found initial cyclic hardening followed by cyclic softening until failure. Chen [7] studied the effect of pre hardening on the LCF behavior of manganese steel. Pronounced hardening followed by cyclic stability with no softening was observed. Pre deformation induced twins in the structure which influenced fatigue life. Fatigue behavior of manganese steel is affected by both dislocation and twinning mechanisms. It has been generally accepted that the high strain hardening in manganese steel is due to the deformation twinning [8-10]. The interaction of twins with dislocations provides additional hardening to the material. Another theory suggests a reorientation of C-atoms in C-Mn cluster in the core of the dislocations imparts additional hardening [11-12]. Fatigue studies by Kang et al. suggested that the LCF process and failure of manganese steel at low strains are mainly controlled by dislocation dominated cyclic deformation structures. The role of twinning or stacking faults and their interaction with dislocations in LCF is not quite understood. Also, most of the previous studies were performed under uniaxial loading. It is expected that a change in the mode of loading for example pure torsion or biaxial will generate differences in structure as well as the mode of fracture.

Diverse softening-hardening behavior of pearlitic steels has been reported in the literature by different authors. Previous studies of uniaxial LCF on rail steels [13-15] have indicated initial softening for the first 10% of fatigue life followed by cyclic stabilization. Asitha et al. [16] showed that the microstructural features like the pearlite inter-lamellar spacing have strong correspondence with the cyclic plasticity behavior of the material. Also, the ferrite cementite content can affect the cyclic behavior. Sunwoo et al. [17] studied the effect of interlamellar spacing on the cyclic deformation behavior of pearlitic steels. In recent years few experimental studies on multiaxial fatigue of rail steels have been attempted [18-20]. However, the correlation between the mechanical properties and the microstructure under uniaxial or multiaxial fatigue is not clear.

In this paper, a comparative study on the cyclic deformation characteristics and fatigue behavior of a head hardened pearlitic and manganese steel has been made and explained with respect to low cycle fatigue behavior under conditions of uniaxial and biaxial loading including proportional and non-proportional loading. Also, the different microstructures developed in the two different types of steels are compared and related to mechanical properties.

Experimental Procedure:

Materials

The two types of materials examined are a head hardened pearlitic steel (0.8 wt.% C) and an austenitic manganese steel (13 wt.% Mn). The nominal chemical composition of the pearlite steel is 0.72 – 0.80% C, 0.15 – 0.58% Si, 0.70 – 1.20% Mn, ≤ 0.15% Cr, ≤ 0.020% P, ≤ 0.025% S and rest Fe. The average chemical composition of manganese steel is 1-1.4% C and 12-13% Mn with addition of other alloying elements like ~0.18% Cr, 0.4-0.6% Si and 0.022-0.033% P. The microstructure of the pearlitic steel consists of two phases: ferrite and cementite, whereas the manganese steel has single phase austenitic grains with very large grain size in the order of 500 µm. Figure 1 shows the microstructures of the two steels. The average hardness of the manganese steel in the bulk is 220 HV. The pearlitic steel was head hardened and thus has a gradient of hardness which would cause the properties of the rail to vary over the cross-section. Head hardening is done in production and encompasses forced cooling of the head of the rail, giving higher cooling rates resulting in a finer pearlitic structure in the rail head surface. The average hardness is 400 HV near the surface decreasing gradually with increasing depth down to 330 HV at 20 mm from the surface.

Samples for the experiments were extracted from actual crossings taken from the track. Hardness studies for the pearlitic and manganese grade suggested the depth of deformation during service was confined to first 2-3 mm for the pearlite and 10 mm for the manganese steel. Samples for fatigue testing of the pearlitic rail grade were thus taken from the rail head a few millimeters beneath the running surface. Because of the head hardening, slight variations in hardness levels in the volumes from which the test bars are taken is expected. For the manganese steel, the samples were obtained from a depth of 15 mm from the surface, as it is found that the volumes here will be free from any service induced deformation [21]. This means that both types of samples were essentially free from any in-service deformation.

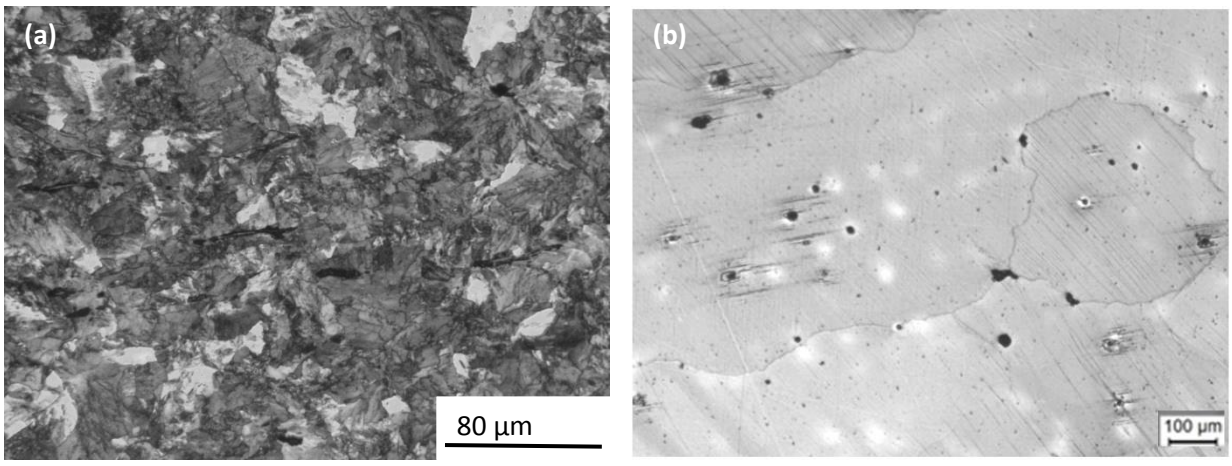

Figure 1: Optical Microstructure of (a) pearlite and (b) manganese steel.

Mechanical Testing

A schematic drawing of the fatigue test bars is given in Figure 2. The test bars had a gauge diameter of 10 mm and a gauge length of 20 mm. Outside the gauge length, a large radius (100 mm) was adopted to minimize the stress

concentration without compromising buckling stability. The samples were extracted so that the axis of the test bars was parallel to the rolling direction. The test bars were ground and polished to mirror finish before testing. Low cycle strain controlled fatigue tests (strain amplitude was kept constant) were performed using a strain rate of 10^{-2} s^{-1} on an MTS 809 axial/torsion testing system. Throughout testing, peak tensile and compressive stresses were recorded for each cycle. In addition, complete strain–stress loops were obtained at defined intervals to acquire the hysteresis loop development. All tests were conducted at room temperature. The conditions for the tests were:

1. Uniaxial (tension-compression) tests at strain amplitude of 0.6%.
2. Biaxial tests under tension-compression and torsion at strain amplitudes, which would give an equivalent strain amplitude of 0.6% in the gauge surface.

According to von Mises theory, the equivalent strain, axial strain, and shear strain can be related as

$$\varepsilon_{eq}=\sqrt{\varepsilon^2+\frac{\Upsilon^2}{3}}$$

where ε_{eq} is the equivalent strain, ε is the axial strain and Υ is the shear strain.

In case of uniaxial loading, there is no shear strain and the equivalent strain is the same as the axial strain. Two sets of uniaxial tests were done at the strain amplitude of 0.6%: strain controlled equal tension compression giving R_ε = -1 and strain controlled axial fatigue with a mean compressive strain of 0.9% giving R_ε = 5. For biaxial loading both in phase proportional (0˚ phase difference) and out of phase non-proportional loading (90˚ phase difference) were conducted. For both these cases, the axial strain was selected to be 0.4243% and the shear strain was 0.7348% to obtain an equivalent of 0.6% nominal strain amplitude, even if the non-proportional loading in each moment yields an equivalent strain below 0.6%.

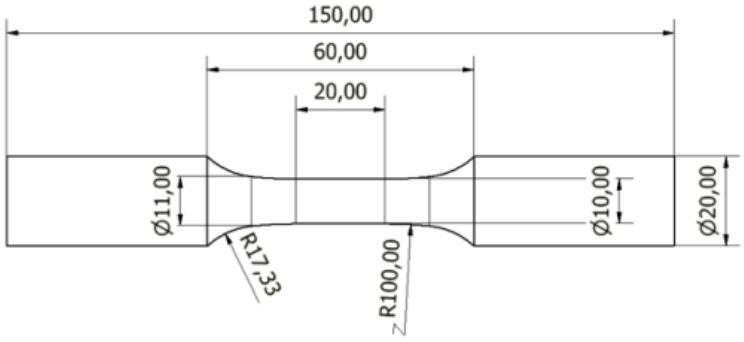

Figure 2: Schematic drawing of fatigue specimens (all dimensions in mm).

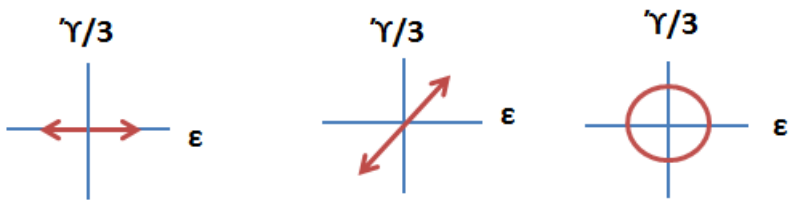

Figure 3: The loading paths for different conditions (a) linear strain path (uniaxial strains with no shear strain), (b) oblique strain path (uniaxial with in-phase shear strains) and (c) circular path (uniaxial with out of phase shear strains).

Microstructure study

The microstructures of the deformed specimens were studied using optical microscopy (OM). For optical microscopy, the samples were ground and polished and finally etched with Nital. The detailed features of the cyclic deformation microstructure under different cyclic loading conditions after the failure of the two different steels were analyzed using a Transmission Electron Microscope (TEM). The specimens for TEM studies were obtained from the gauge part of the fatigue deformed specimens. The transverse surface was studied and specimens were obtained as close to the surface as possible. A Jeol 2000FX electron microscope operating at 200KV was used in this work. The dislocation density and also the stacking fault width were calculated from the TEM images by the linear intercept method.

Results:

Cyclic plasticity and fatigue behavior

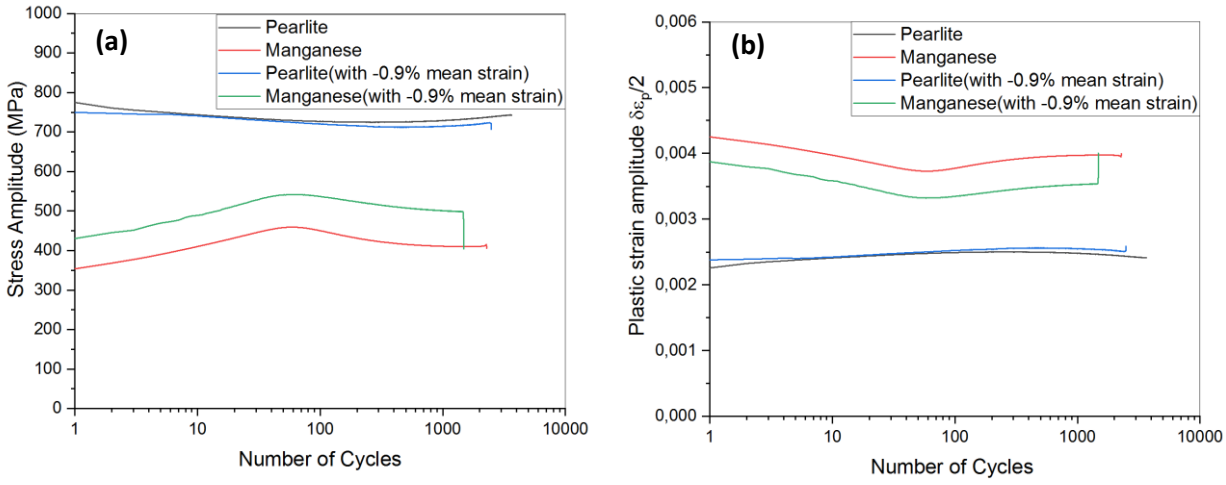

Figure 4: Uniaxial LCF (a) axial stress amplitude vs number of cycles and (b) plastic strain amplitude vs number of cycles.

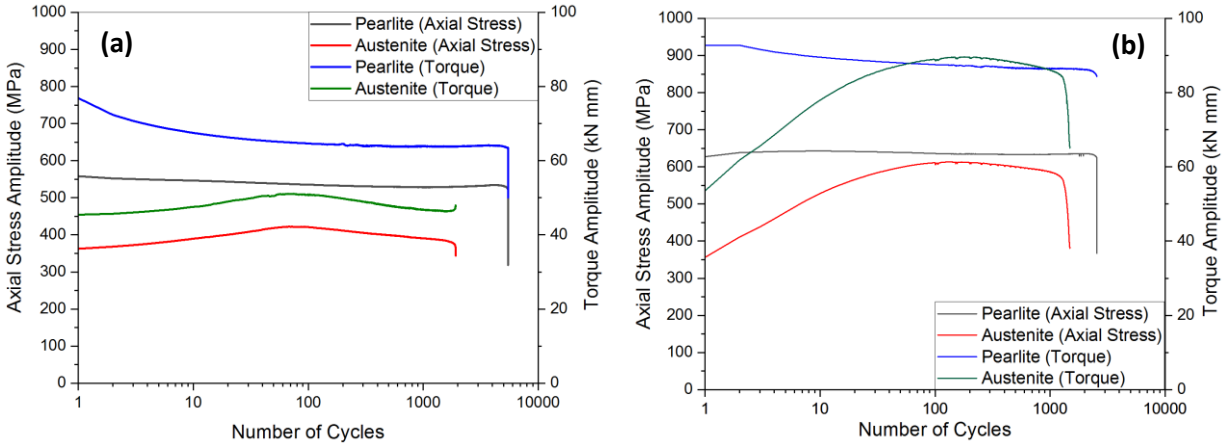

Figure 5: Biaxial LCF (axial + torsion) (a) in-phase proportional and (b) out of phase non proportional loading showing axial stress and torque amplitude vs number of cycles.

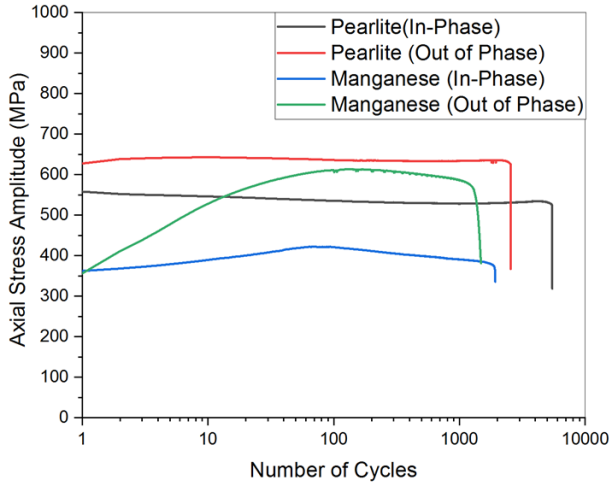

Figure 6: Comparison of uniaxial stress amplitude with number of cycles for both steels for biaxial loading.

Figures 4-6 shows the axial stress and torque amplitude development for the two materials under different conditions along with the plastic strain amplitude development for uniaxial loading.

For the manganese steel in all the three cases, there is strong initial hardening followed by softening and then failure. Hardening was observed only for the initial few percents of the fatigue life, whereas softening prevailed for most of the fatigue life. No saturation stage was observed. In strain controlled fatigue testing plastic strain amplitude is a major governing factor. The plastic strain amplitude decreased initially due to hardening in all cases. The cyclic hardening ratio (CHR) and the cyclic softening ratio (CSR) are two important parameters in characterizing cyclic deformation behaviors of metallic materials. CHR and CSR were determined using $CHR=(\sigma_{max}-\sigma_1)/\sigma_1$ and $CSR=(\sigma_{max}-\sigma_{half})/\sigma_{max}$, where σ_1, σ_{max} and σ_{half} are represented the stress amplitude at the first cycle, the maximum stress amplitude and the stress amplitude at the half life, respectively. The CHR and CSR are reported in Table 1. The manganese steel under uniaxial loading had a very high hardening ratio of nearly 0.3 compared to the softening ratio of 0.1 Under similar

conditions of strains, at 0.6% strain amplitude, the highest life is obtained for uniaxial loading and the lowest for non-proportional loading.

For pearlitic steel in uniaxial and biaxial in-phase loading, there are three stages present. First, there is a decrease in stress amplitude due to softening, followed by cyclic saturation and a slight increase in stress amplitude due to hardening until the final fracture. For biaxial non-proportional loading, there is an initial hardening within the first two cycles followed by softening, cyclic saturation and failure. The fatigue life is highest for the biaxial in-phase proportional loading followed by uniaxial loading and the lowest life is seen for biaxial non-proportional loading. It should be noted that this is valid in strain or displacement controlled load situations; if the loading is better characterized with a stress amplitude, the increased hardening caused by non-proportional loading will likely lead to lower plastic strains and thus less fatigue damage [22].

A comparison between uniaxial and biaxial low cycle fatigue cannot be made unless the equivalent stress values are obtained. However, use of solid specimens, as we use here, instead of tubular specimen restricts direct calculation of equivalent stress values. The normal stress is uniformly distributed whereas the general shear stress formula is dependent on the radius, shear stress being maximum at the surface and zero at the center. Due to plasticity, and non-linear response on plastic straining, the shear stress in each location is not readily computed. However, the strain is always well defined, and the uniaxial stress can be used as a comparison tool also on biaxial loading whether proportional or non-proportional. In case of pearlitic steel, in-phase proportional biaxial loading shows softening behavior like uniaxial loading. The softening ratios for the two conditions are nearly identical. This is expected as biaxial proportional loading does not cause any change in strain path and just adds on to the shear component. Out of phase non proprtional biaxial loading of pearlitic steel shows higher initial hardening due to strain path change after quarter cycle and activation of latent slip systems. Whereas the hardening ratio was zero for uniaxial and in-phase proportional loading, a hardening ratio of 0.024 was obtained for out of phase non proportional loading based on axial stress calculations. For manganese steel, the in-phase biaxial curve is similar to the uniaxial curve. Non-proportional loading gives a much increased hardening rate in out of phase loading. The cyclic hardening ratio was found to be around 0.7 based on normal stress calculations. In non-proportional out of phase loading the maximum shear stress plane rotates with time in every cycle causing activation of multiple slip systems and their mutual interactions [23]. The lowest hardening was observed in case of biaxial in-phase loading. For in-phase and uniaxial loading in manganese steel the amplitude developed is lower than pearlite but biaxial out of phase loading generates high hardening causing stress levels in line with the pearlitic steel.

The effect of mean strain on the two materials has been studied. The pearlitic steel is insensitive to mean strain hardening whereas for manganese steel, there is an increase in stress amplitude for the cases with negative mean strain as compared to those without mean strain for same strain amplitudes. This shows that manganese steel is sensitive to hardening due to mean strain. This additional hardening reduces the fatigue ductility and causes earlier occurrence of micro cracks and thereby reduces the fatigue life. This reasoning is valid in a displacement or strain controlled loading situation. The presence of mean strain did not seem to affect the life of pearlitic steel for similar strain amplitudes. For pearlitic steel, the strain hardening saturates within the initial cycle and thereafter softens till failure with the cyclic softening rates being identical to loading without mean strain for same strain amplitudes.

A comparison between the pearlite and manganese steels reveals the maximum stress amplitudes and torque amplitudes reached at all the strain amplitudes are higher for the pearlitic grade. This is due to the higher hardness of pearlitic grade steel. Also in all cases, the manganese steel has very high plastic strain amplitudes compared to pearlitic grade under similar conditions. This is due to lower yield strength of manganese steel. The fatigue life of the pearlitic steel is higher compared to the manganese steel under similar conditions. Higher hardness and strength leads to lower plastic strains in the material and thus increase in fatigue life. It is generally observed work hardened materials demonstrate cyclic softening whereas sofer material exhibit cyclic hardening in fatigue tests.

Table 1: The cycles to failure, CHR, and CSR of the different steels under different conditions of loading:

Loading Condition	**Strain amplitude**	**Material**	**N_f**	**CHR**	**CSR**
Uniaxial	0.6%	Head Hardened Pearlite Steel	3660	0	0.0522
		Manganese Steel	2278	0.2983	0.1066
	0.6% (0.9% compressive mean strain)	Head Hardened Pearlite Steel	2490	0	0.0453
		Manganese Steel	1480	0.2593	0.0714
Biaxial (proportional loading)	0.6% equivalent	Head Hardened Pearlite Steel	5471		
		Manganese Steel	1924		
Biaxial (non proportional loading)		Head Hardened Pearlite Steel	2556		
		Manganese Steel	1485		

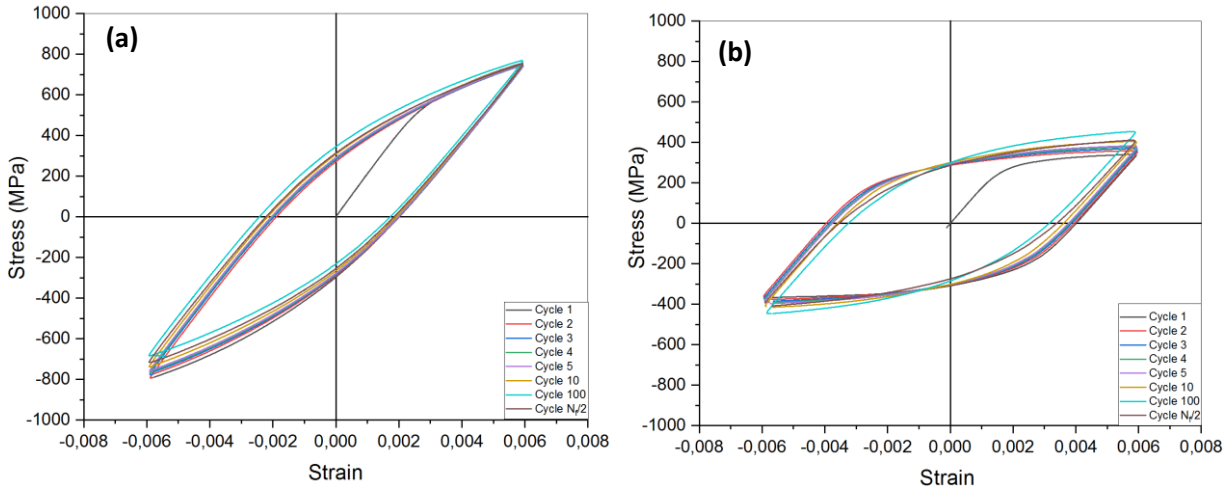

Figure 7: Hysteresis loops developed for 0.6% axial strain amplitude (a) pearlitic steel and (b) manganese steel.

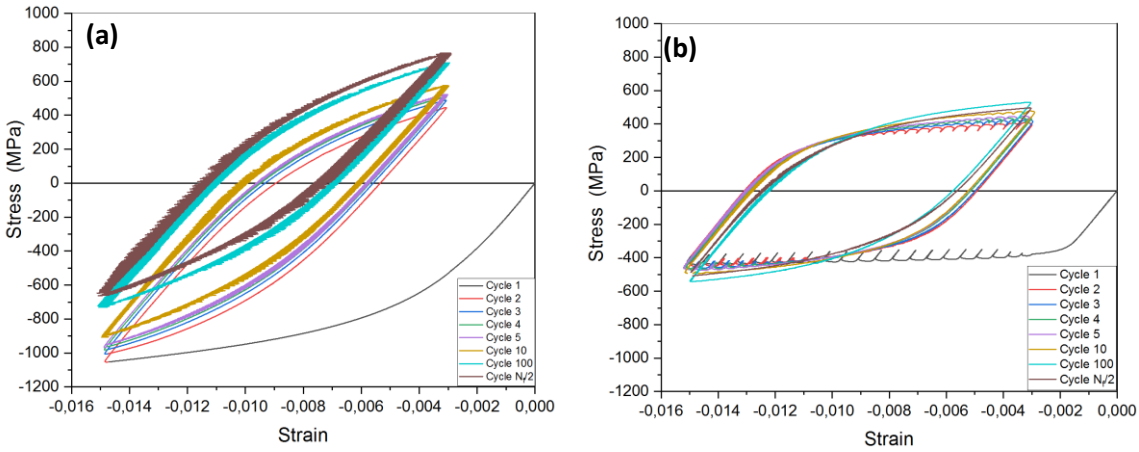

Figure 8: Hysteresis loops developed for 0.6% strain amplitude with -0.9% mean strain (a) pearlitic steel and (b) manganese steel.

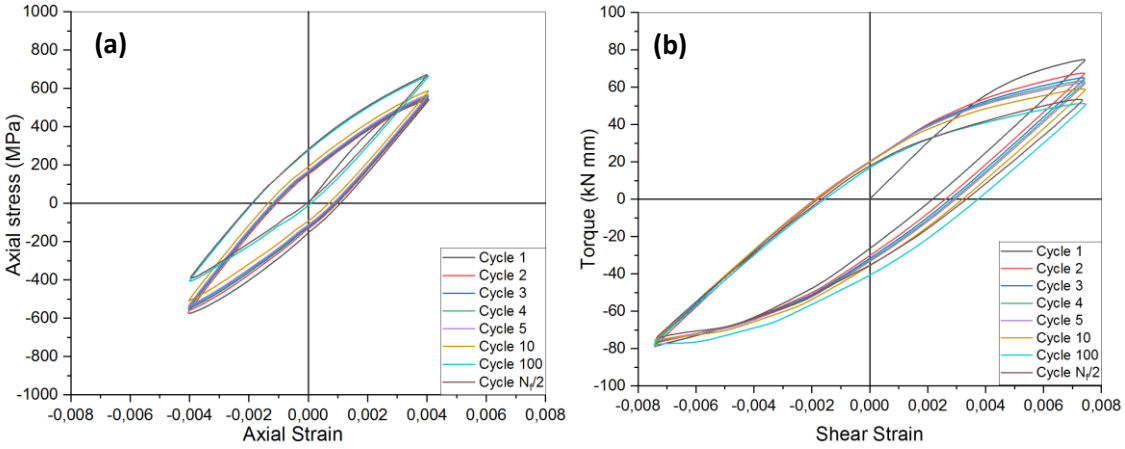

Figure 9: Hysteresis loop developed for 0.6% equivalent biaxial strains in proportional loading for pearlitic steel (a) axial stress-strain response and (b) shear stress-strain response.

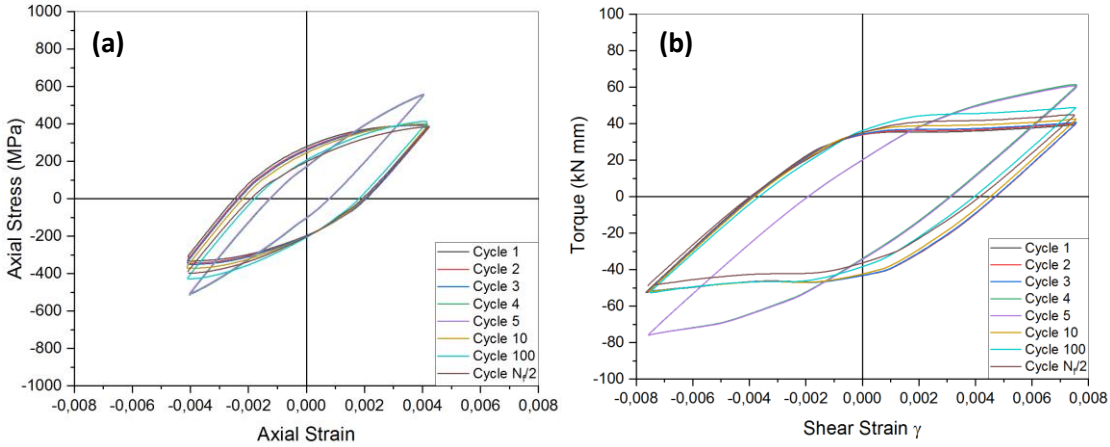

Figure 10: Hysteresis loop developed for 0.6% equivalent biaxial strains in proportional loading for manganese steel (a) axial stress-strain response and (b) shear stress-strain response.

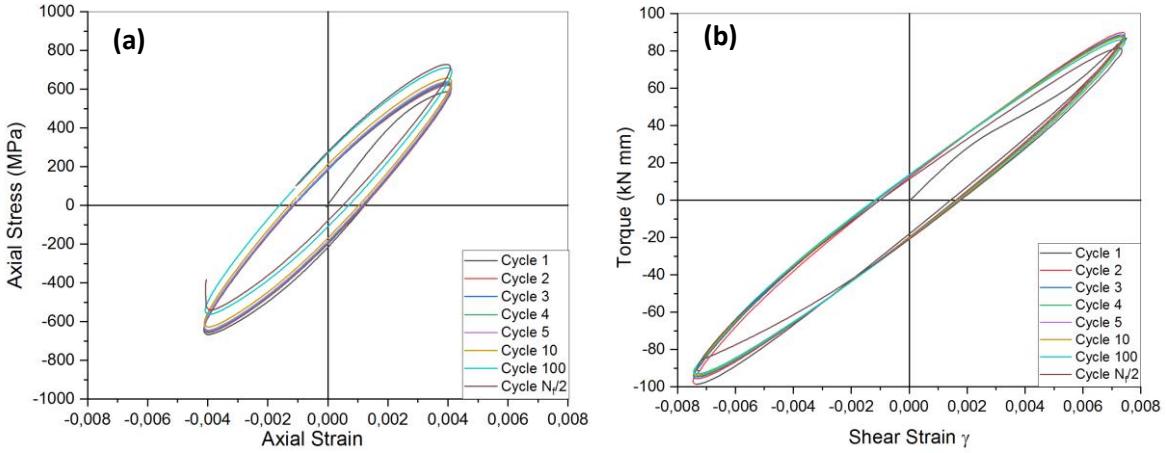

Figure 11: Hysteresis loop developed for 0.6% equivalent biaxial strains in non-proportional loading for pearlitic steel (a) axial stress-strain response and (b) shear stress-strain response.

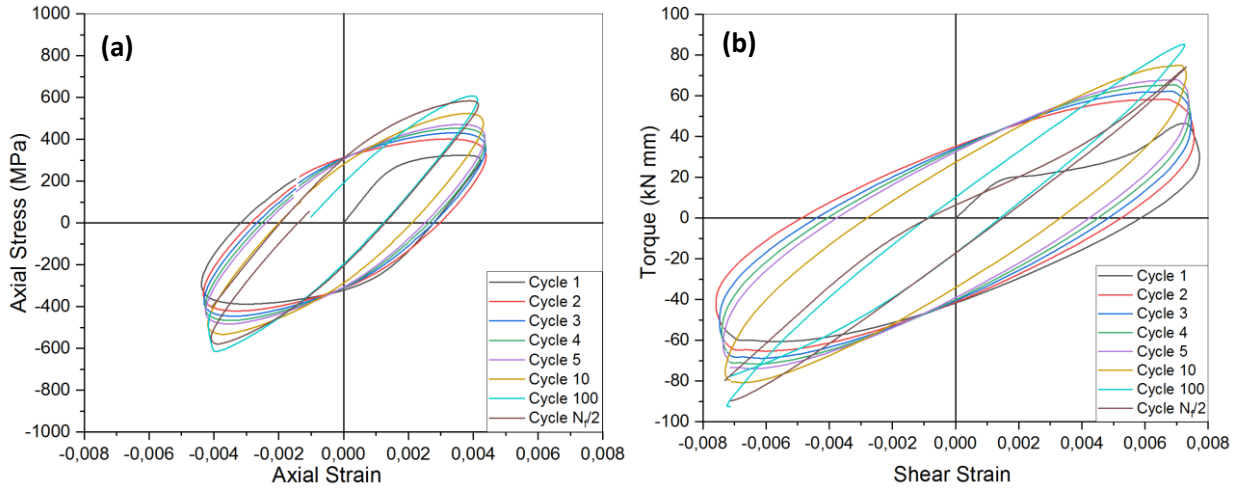

Figure 12: Hysteresis loop developed for 0.6% equivalent biaxial strains in non-proportional loading for manganese steel (a) axial stress-strain response and (b) shear stress-strain response.

Figures 7-12 show the hysteresis loops developed for the two different materials under different loading conditions. For the manganese steel under all conditions, there is a shift of the tip of the hysteresis loop upwards towards higher stress indicating cyclic hardening whereas the trend is reverse for pearlitic grade indicating cyclic softening for all cases except biaxial non-proportional loading. The shape of the loop is different for the two materials under similar conditions. For the pearlitic grade, the loops are generally narrower as compared to the manganese steel which has a broadened loop due to lower cyclic flow stress. In uniaxial and biaxial proportional loading, the hysteresis loops show a sharp tip at the maximum and minimum strains; however, under biaxial out of phase loading the tips of the hysteresis loop get rounded. In non-proportional loading, the maximum values of axial and shear strains do not occur simultaneously.

The hysteresis loops for the compressive mean strain conditions showed ratcheting behavior. In case of manganese steel, the loops were stabilized basically after the first compressive loading. Due to the low monotonic hardening rate,

no large mean stress was introduced by the mean strain imposed. Thus, the ratcheting could be easily described by monotonic plastic flow, and the continued cycling is little affected. However, the pearlite required more cycles to adjust to the mean strain and stabilize at low mean stress. Also, the stress range over which the stabilization occurred was higher in case of pearlite than manganese steel.

The area within the hysteresis loop correlates to the plastic strain energy density of the different materials under low cycle fatigue loading. Fatigue damage is characterized by absorption of irreversible plastic energy which influences fatigue life. In LCF the accumulated plastic deformation is the primary reason for the fatigue. Morrow [24] suggested that the plastic strain energy per cycle is a useful criterion to measure the fatigue damage per cycle since the cyclic plastic strain is related to the movement of dislocations and the cyclic stress is associated with the resistance against their motion. Hence, the fatigue resistance of a metal can be characterized in terms of its capacity to absorb and dissipate plastic strain energy. Due to use of solid specimens for the biaxial tests, it was not possible to calculate the exact values of the plastic strain energy density of the materials (as exact stress values could not be obtained) except for the uniaxial loading. However, a comparative analysis of the area under the loop from the above hysteresis curves indicates the manganese steel has higher plastic strain energy density compared to the pearlite at $N_f/2$. In the case of uniaxial loading, the plastic strain energies were comparable in both the materials. In the case of biaxial proportional loading both axial and shear plastic strain energy was higher for manganese steel than for pearlite. In the case of biaxial out of phase loading the axial plastic strain energy was higher but the shear plastic strain energy was lower for manganese than pearlite. A comparison between proportional and out of phase loading indicates out of phase loading has higher plastic strain energy density for both the materials.

Microstructure

Optical microscopy

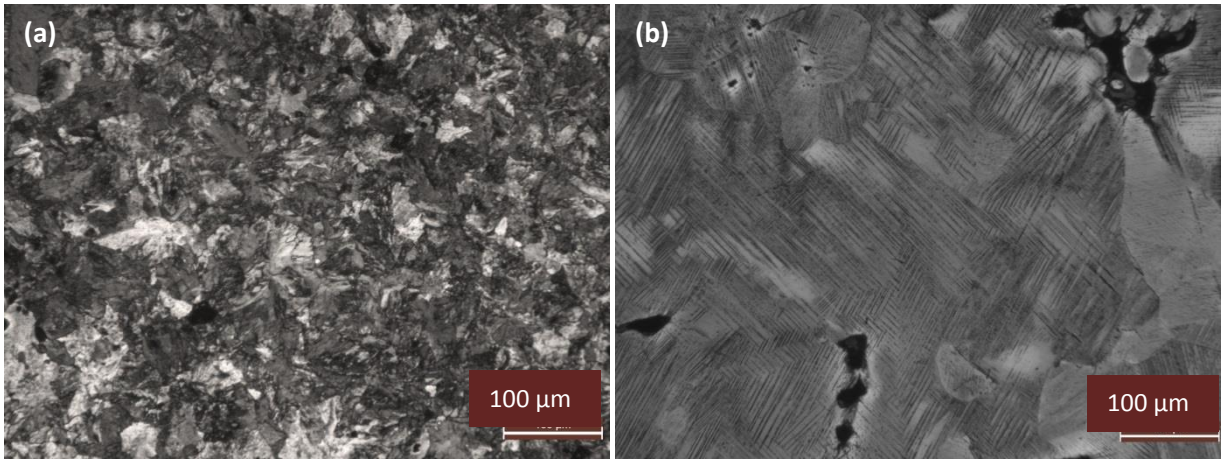

Figure 13: Optical micrographs of fatigue deformed specimens at 0.6% uniaxial strain amplitude (a) pearlitic steel and (b) manganese steel.

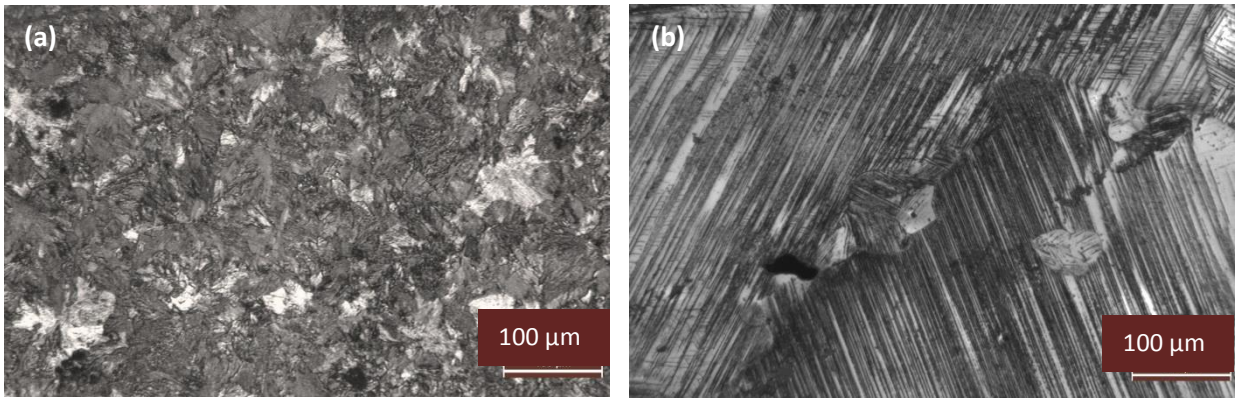

Figure 14 : Optical micrographs of fatigue deformed specimens at 0.6% strain amplitude biaxial proportional loading (a) pearlitic steel and (b) manganese steel.

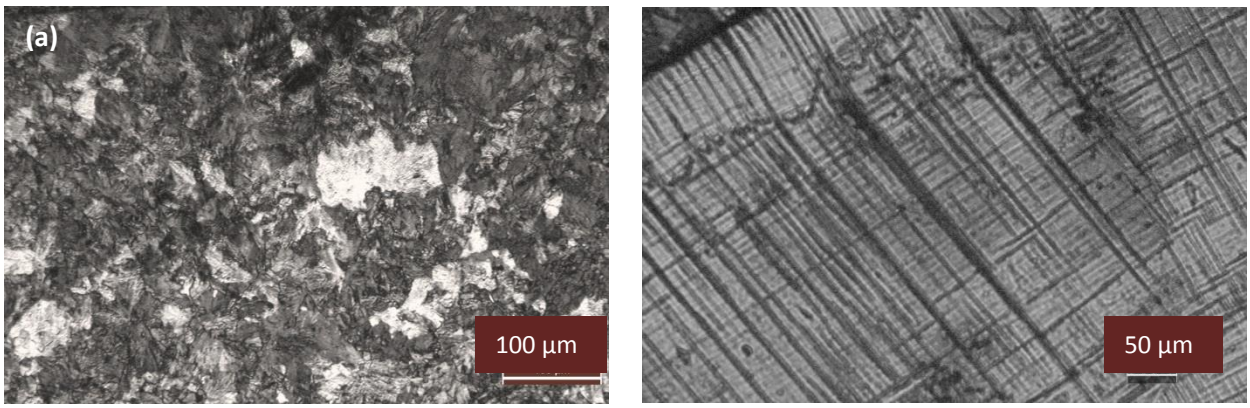

Figure 15: Optical micrographs of fatigue deformed specimens at 0.6% strain amplitude biaxial nonproportional loading (a) pearlitic steel and (b) manganese steel.

The optical micrographs of the fatigue deformed head hardened pearlitic steel do not show significant observable changes in the microstructure under the different conditions. The difference in the mechanical properties can, therefore, be attributed to dislocation density changes in the structure which will be evident from the TEM studies. The deformed microstructure of the manganese steel exhibits a banded structure. These bands can be deformation twins or stacking faults or dislocation boundaries which is not evident from the optical micrographs. The density and morphology of the bands differ under the different conditions of loading with increasing density and decreasing spacing of the bands for biaxial nonproportional loading. The bands are in different directions and in some grains, the bands are intersecting with each other. Inclusions are also evident in the micrographs.

TEM Analysis: Pearlitic steel

Figure 16 shows the pearlitic microstructures with alternating ferrite and cementite lamellae in the three different LCF samples. As 0.6% equivalent strain will not introduce observable changes in the main microstructural parameter, i.e. the interlamellar spacing, the present investigation focuses on the dislocation morphology and density in the ferrite lamellae. The dislocation morphologies in the three samples are similar, as shown in Fig. 16, and threading dislocations and dislocation tangles have been observed in all three samples, representing the typical low-strain pearlitic deformation

microstructure [25-26]. These dislocations are believed to nucleate at interfaces caused by elastic incompatibility stresses between the ferrite and cementite phases [27-29], and glide in the ferrite lamellae to form dislocation tangles.

However, it is interesting to note that the dislocation density is significantly different in the 3 samples; it increases from 4.9×10^{14} m^{-2} in the uniaxial sample, to 8.5×10^{14} m^{-2} in the in-phase biaxial sample, to 1.0×10^{15} m^{-2} in the out of phase biaxial sample. In biaxial LCF loading, slip systems in other directions are activated as compared to uniaxial loading. In biaxial out of phase loading, the change of strain path is suggested to be the main reason for the higher dislocation density.

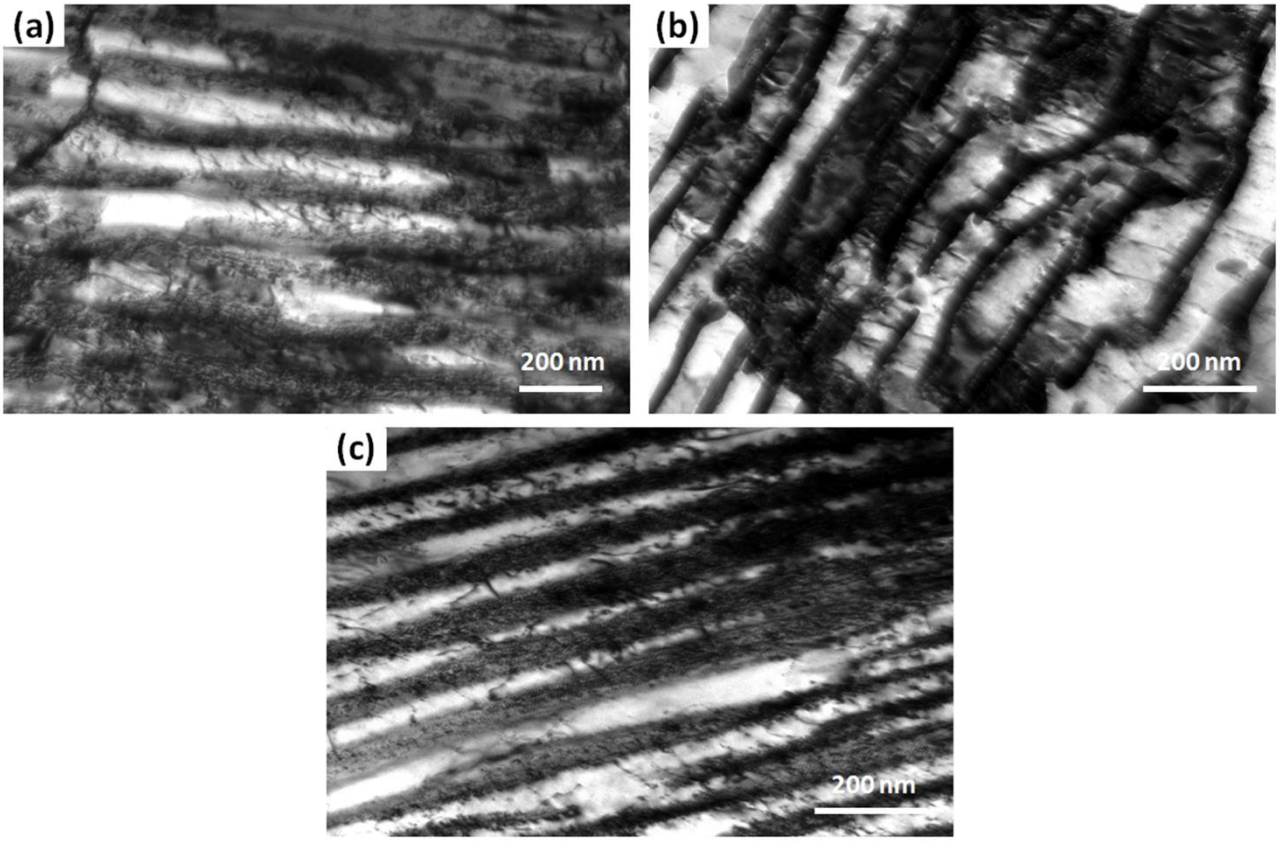

Figure 16: TEM micrographs showing the deformation microstructure in the low cycle fatigued (LCF) pearlitic samples: (a) 0.6 % uni-axial LCF, (b) 0.6 % in-phase biaxial LCF and (c) 0.6 % out-of-phase biaxial LCF.

TEM Analysis: Manganese steel

Figure 17 shows the different dislocation and stacking fault structures in the three samples of austenitic manganese steel deformed to the equivalent strain of 0.6%. The microstructures are composed of dislocation cells with dislocation tangles inside, intersected with straight stacking fault lamellae. In the uniaxial LCF sample, the dislocation cell size is ~ 500 nm, the dislocation density inside the cells is 3.4×10^{14} m^{-2} and the spacing between stacking fault lamellae is ~ 1.2 μm. Intersecting stacking fault lamellae with dislocation tangles between them are observed in the in-phase biaxial LCF sample where the average spacing between neighboring stacking fault lamellae is 330 nm and the dislocation density in the cells formed by intersecting stacking fault lamellae is 1.1×10^{14} m^{-2}. Dense parallel stacking fault lamellae with

dislocations and dislocation tangles between them are seen in the out-of-phase biaxial LCF sample where the average spacing between neighboring stacking fault lamellae is ~ 60 nm and the dislocation density between the parallel stacking fault lamellae is ~ 5×10^{14} m^{-2}.

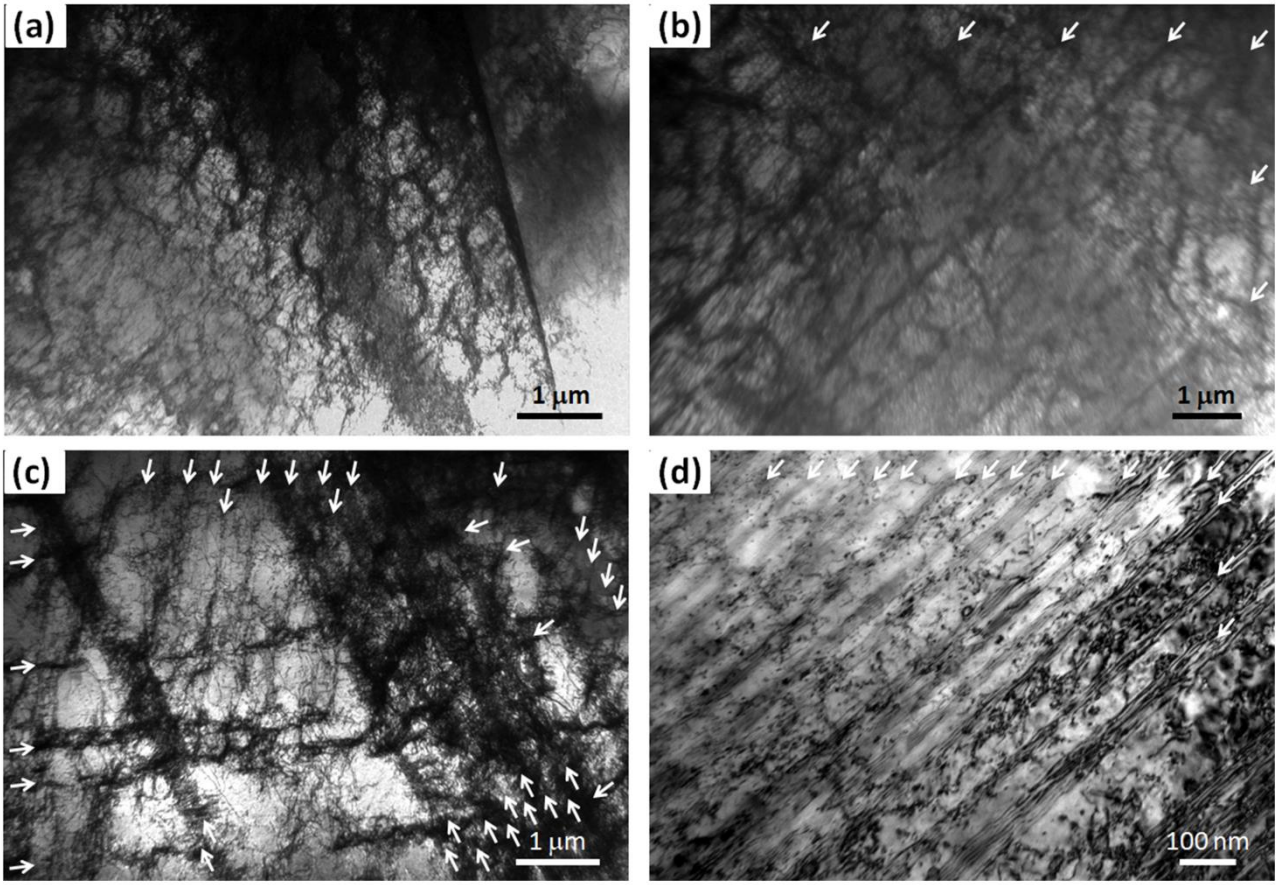

Figure 17: TEM micrographs showing the dislocation structures and stacking faults in the LCF samples (a) dislocation cells with dislocation tangles inside and (b) straight stacking fault lamellae across dislocation cells in 0.6 % uniaxial LCF sample, (c) intersecting stacking fault lamellae with dislocation tangles between them in 0.6 % in-phase biaxial LCF sample and (d) dense parallel stacking fault lamellae with dislocation tangles between them in 0.6 % out-of-phase biaxial LCF sample. The electron beam axis is close to the [213] direction of fcc austenite. The white arrows point out the stacking fault lamellae.

For the manganese steel, the microstructure is thus quite different for the 3 deformation modes deformed to the same equivalent strain. In the uniaxial LCF mode, multiple dislocation slip together with the increased friction stress against dislocation glide due to the high concentration of solute atoms are responsible for the formation of the observed dislocation cell structure. However, when the shear mode is introduced in the in-phase and out of phase biaxial LCF test, formation and growth of stacking faults play an important role together with dislocation nucleation, gliding and dislocation tangle formation. For the formation and growth of a stacking fault, any perfect dislocation with a Burgers vector can be dissociated into two partials, for example, two Shockley partials. The local applied stress generally exerts two different forces on the partials which determine the displacement of each dislocation and consequently the nature of

the stacking fault ribbons. Moreover, the low stacking fault energy of the manganese steel allows the width of the ribbons to increase enough to reach values giving an extended fault bounded by independent partial dislocations, where the density of independent partial dislocations, and therefore the density of extended stacking faults, increases with the strain [30]. For the present small strain, abundant stacking faults are observed for both in-phase and out of phase biaxial LCF samples, as previously reported in single-crystal manganese steel deformed to < 1% in tension [10]. However, the in-phase biaxial LCF results in parallel stacking faults in different directions while the out of phase biaxial LCF introduce a high density of parallel stacking faults with much smaller stacking fault spacing.

Table 2: the dislocation density of pearlite and manganese steel and stacking fault lamellae width for the manganese steel:

Condition	Dislocation Density		Stacking Fault lamellae
	Pearlite Steel	Manganese Steel	Manganese Steel
Uniaxial	4.9×10^{14} m^{-2}	3.4×10^{14} m^{-2}	~ 1.2 µm
Biaxial (Proportional)	8.5×10^{14} m^{-2}	1.1×10^{14} m^{-2}	330 nm
Biaxial (Non proportional)	1.0×10^{15} m^{-2}	5.0×10^{14} m^{-2}	~ 60 nm

Hardness measurement on fatigue deformed samples:

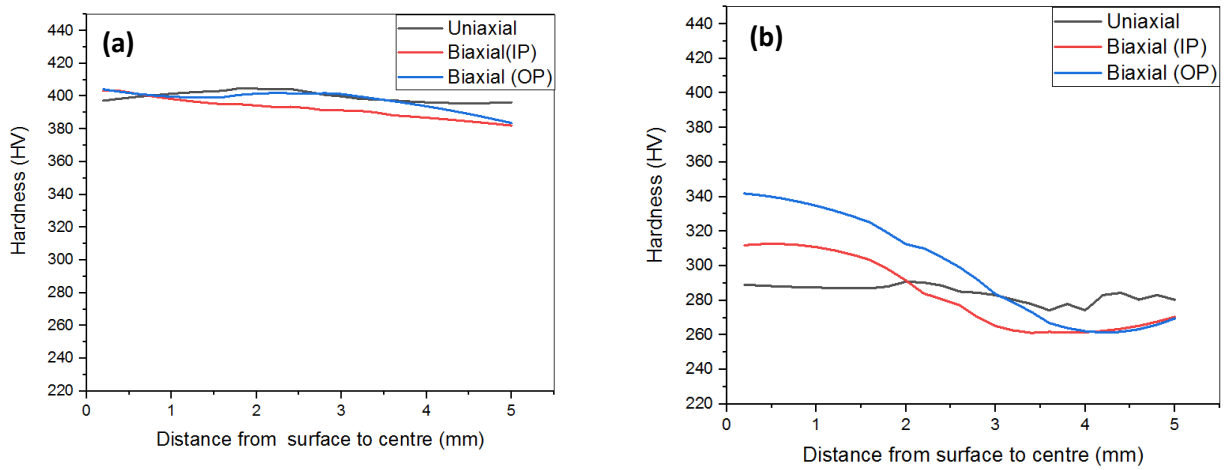

Figure 18: Hardness as a function for radial distance for a) pearlitic steel and b) manganese steel.

The hardness measurements across the radius of the deformed fatigue samples under the different conditions of loading are shown in Figure 18. For the pearlitic steel, there is no significant change in hardness after deformation under different conditions. It maintains a uniform average hardness of about 400 HV. For the manganese steel, a variation of hardness can be observed. The hardness is uniform for the uniaxial case across the radius due to uniform distribution of

strain. For the biaxial cases, the maximum shear strains are at the surface and zero at the center. Similarly, the maximum hardness is obtained at the surfaces of around 340 HV for out of phase loading and 310 HV for in phase loading which gradually falls to 260 HV at the center. The extent of hardening is significantly higher in manganese steels compared to pearlitic steel. The out of phase loading causes significant non-proportional hardening which is evident from the figure.

Discussion:

Pronounced hardening was observed in manganese steel under all conditions of loading. The cyclic hardening was more pronounced during the first 100 cycles and then softening follows. The evolution of total stress amplitudes of manganese steel is due to the combined contribution from both the internal and effective stress. The resistance to dislocation motion cause hardening in the manganese steel. TEM micrographs of uniaxially deformed manganese steel reveal that the microstructures are composed of dislocation cells with dislocation tangles inside, intersected with straight stacking fault lamellae. Fatigue straining causes dislocation generation in the material. The dislocations are obstructed at the stacking faults or are pinned down by obstacles causing pile-up which cause hardening and finally formation of dislocation tangles. The softening part in the life cycle is due to crack initiation and propagation. In-phase biaxial TEM micrographs reveal that the dislocation density of manganese steel for in-phase biaxial loading is lower compared to uniaxial loading but there are interactions of stacking faults with dislocations as well as a decrease in stacking fault lamellae width. Hence, the hardening cannot be explained with dislocation entanglement. The presence of intersecting stacking faults and their interaction with dislocations contribute to additional hardening behavior. For non proportional biaxial low cycle fatigue, the effect of strain path change is predominant with cyclic hardening. Higher non-proportional hardening clearly shows that the latent slip systems are active in this case [31]. The dislocation density is high and the width of the stacking fault lamellae decreases for non proportional biaxial low cycle fatigue loading in manganese steel.

The deformation mechanism of pearlitic steel is significantly different from manganese steel. The pearlitic steel has been hardened before and has already generated a high density of dislocation within the material. Further straining during fatigue testing causes very little hardening but rearrangement of the dislocations into a cell structure causing softening during the fatigue test. Out of phase biaxial loading of pearlitic steel shows higher initial hardening due to the strain path change and activation of latent slip systems (non-proportional hardening) [31]. For pearlitic steel, the sensitivity of activation of latent slip systems is not high. Thereafter, the cyclic softening is less compared to in-phase loading because it is compensated by non-proportional hardening.

The strain hardening capacity of manganese steels makes them a suitable choice for crossing material. The mode of deformation in pearlitic steels is limited only to slip whereas twinning, slip, and formation of stacking fault occur in manganese steel. These contribute to the additional hardening. In this study, the effects of mean strain and non-proportional loading were studied separately. The mean strain, which essentially leads to a monotonic pre-deformation (cf Figure 8b), caused a hardening effect of some 75 MPa that survived the following cyclic deformation (seen in Figure 4). The non-proportional loading gave a hardening that made manganese steel reach close to (some 25 MPa difference)

the cyclic strength of the pearlitic material deformed in an identical manner (seen in Figure 6). Thus, if those contributions are additive, the stress amplitude response would actually be higher for the manganese steel than for the pearlitic steel. This could be the reason why manganese steels do well in the application where monotonic pre-straining, as well as non-proportional straining, is generated by the rolling contact fatigue loading.

This study encompassed only one strain amplitude and pure biaxial loading, and can thus not fully explain why manganese steels perform well in the railway crossings. But since the loading in the crossings is even more complex, the manganese steel is likely to develop dislocation structures which increase the deformation resistance under such loads or cyclic strength. Since the loading is force controlled rather than displacement controlled, the plastic strain amplitude gets smaller for the developing very high strength manganese steel, thereby accumulating less plastic strain energy which typically correlates to fatigue damage. The reason for the shorter fatigue life of the manganese steel specimens in this study could be the presence of rather high tensile stresses and sensitivity of the microstructure due to very large grains and weak/brittle grain boundaries, whereas in the crossings, compressive stresses dominate to a larger degree.

Conclusion:

The low cycle fatigue behavior of the two different rail steels under different conditions of loading (uniaxial and biaxial) has been studied. The deformed microstructure after fatigue has been analyzed using TEM and relations between microstructural changes and mechanical properties are analyzed. The softer manganese steel exhibited cyclic hardening behavior under all conditions where fatigue straining caused dislocation and stacking fault generation and interaction between them. The highest hardening was obtained for biaxial non proportional loading due to activation of multiple slip systems due to a change in strain path. The harder pearlitic steel showed softening behavior. It was heat treated and had generated dislocations during the thermal treatment. Further straining caused reorganizing of the dislocations into cell structure and hence leads to softening. However biaxial non proportional loading showed some hardening in the initial cycles due to multiple slip systems being activated and also increased dislocation density. The pearlite steel had better fatigue life under all conditions. Whereas pearlite steel was insensitive to the mean strain, manganese steel showed mean strain hardening with a decrease in fatigue life. The dislocation morphology was found to be similar for pearlite under all conditions; the difference in mechanical behavior is due to a change in dislocation density with the biaxial non proportional loading having the highest dislocation density. For manganese steel, the in-phase loading results in parallel stacking faults in different directions while the out of phase loading introduces a high density of parallel stacking faults with much smaller stacking fault spacing and high dislocation density.

Acknowledgment:

The authors gratefully acknowledge support from the Innovation Fund Denmark through the project “INTELLISWITCH – Intelligent Quality Assessment of Railway Switches and Crossings” (Grant no 4109-00003B).

References:

[1] A. V. Olver, The mechanism of rolling contact fatigue: an update, Proceedings of the Institution of Mechanical Engineers, Part J: Journal of Tribology 219 (2005) 313-330.

[2] D. L. McDowell, Stress state dependence of cyclic ratcheting behavior of two rail steels, International Journal of Plasticity 11(4) (1995) 397-421.

[3] R. I. Stephens, A. Fatemi, R. R. Stephens and H. O. Fuchs, Metal fatigue in engineering, John Wiley and Sons, 2001.

[4] D. Rittel and I. Roman, Cyclic properties of coarse-grained cast austenitic manganese steels, International Journal of Fatigue 11(3) (1989) 177-182.

[5] M. Schilke, J. Ahlström and B. Karlsson, Low cycle fatigue and deformation behaviour of austenitic manganese steel in rolled and in as-cast conditions, Procedia Engineering 2 (2010) 623-628.

[6] J. Kang, F. C. Zhang, X. Y. Long and B. Lv, Cyclic deformation and fatigue behaviors of Hadfield manganese steel, Materials Science and Engineering A 591 (2014) 59–68.

[7] C. Chen, B. Lv, F. Wang and F. Zhang, Low-cycle fatigue behaviors of pre-hardening Hadfield steel, Materials Science and Engineering A 695 (2017) 144–153.

[8] E. G. Astafurova, M. S. Tukeeva, G. G. Zakharova, E. V. Melnikov and H. J. Maier, The role of twinning on microstructure and mechanical response of severely deformed single crystals of high-manganese austenitic steel, Materials Characterization 62 (2011) 588-592.

[9] C. Efstathiou and H. Sehitoglu, Strain hardening and heterogeneous deformation during twinning in Hadfield steel, Acta Materialia 58 (2010) 1479–1488.

[10] I. Karaman, H. Sehitoglu**,** Y. I. Chumlyakov and H. J. Maier, Deformation of single crystal Hadfield steel by twinning and slip, Acta Materialia 48(6) (2000) 1345-1359**.**

[11] W. S. Owen and M. Grujicic, Strain aging of austenitic Hadfield manganese steel, Acta Materialia 47 (1999) 111–126.

[12] P. H. Adler, G. B. Olson and W. S. Owen, Strain hardening of Hadfield manganese steel, Metallurgical Transactions A17 (1986) 1725–1737.

[13] J. Ahlstrom and B. Karlsson, Fatigue behaviour of rail steel-a comparison between strain and stress controlled loading, Wear 258 (2005) 1187–1193.

[14] P. P. Sarkar, P. S. Deb, S. K. Dhua and P. C. Chakraborti, Strain energy based low cycle fatigue damage analysis in a plain C-Mn rail steel, Materials Science and Engineering A 707 (2017) 125–135.

[15] G. Kang, Q. Gao and X. Yang, Experimental study on the cyclic deformation and plastic flow of U71Mn rail steel, International Journal of Mechanical Sciences 44 (2002) 1647–1663.

[16] A. Athukorala, D. V. De Pellegrin and K. I. Kourousis, Characterisation of head-hardened rail steel in terms of cyclic plasticity response and microstructure for improved material modelling, Wear 366-367 (2016) 416–424.

[17] H. Sunwoo, M. E. Fine, M. Meshil and D.H. Stone, Cyclic deformation of pearlitic eutectoid rail steel, Metal Transaction A 13A (1982) 2035-2047.

[18] C. L. Pun, Q. Kan, P. J. Mutton, G. Kang and W. Yan, Ratcheting behavior of high strength rail steels under bi-axial compression-torsion loadings: Experiment and simulation, International Journal of Fatigue 66 (2014) 138-154.

[19] G. Kang and Q. Gao, Uniaxial and non-proportionally multiaxial ratcheting of U71Mn rail steel: experiments and simulations, Mechanics of Materials 34 (2002) 809–820.

[20] G. Kang, Q. Gao, L. Cai, Y. Sun and X. Yang, Experimental study on non proportional multiaxial strain cycling characteristics and ratcheting of U71Mn rail steel, Journal of Materials Science and Technology 18(1) 2002 13-16.

[21] S. Dhar, H. K. Danielsen, S. Fæster, C. Rasmussen, Y. Zhang and D. Juul Jensen, Crack formation within a Hadfield manganese steel crossing nose, Submitted to Journal of Wear.

[22] Y. Jiang and H. Sehitoglu, A model for rolling contact failure, Wear 224(1) 1999 38–49.

[23] N. Shamsei, A. Fatemi and F. D. Socie, Multiaxial cyclic deformation and non-proportional hardening employing discriminating load paths, International Journal of Plasticity 26(12) (2010) 1680-1701.

[24] J. Morrow, Cyclic plastic strain energy and fatigue of metals, Internal Friction, Damping and Cyclic Plasticity, ASTM International STP378-EB (1965) 45-87.

[25] X. Zhang, A. Godfrey, X. Huang, N. Hansen and Q. Liu, Microstructure and strengthening mechanisms in cold-drawn pearlitic steel wire, Acta Materialia 59 (2011) 3422–3430.

[26] X. Zhang, A. Godfrey, N. Hansen and X. Huang, Hierarchical structures in cold-drawn pearlitic steel wire, Acta Materialia 61 (2013) 4898-4909.

[27] M. Dollar, I. M. Bernstein and A. W. Thompson, Influence of deformation substructure on flow and fracture of fully pearlitic steel, Acta Metallurgica 36 (1988) 311–320.

[28] S. A. Hackney and G. J. Shiflet, Anisotropy interfacial energy at pearlite lamellar boundaries in a high purity Fe - 0.80% C alloy, Scripta Materialia 20 (1986) 389–394.

[29] X. Zhang, N. Hansen, A. Godfrey and X. Huang, Structure and strength of sub-100 nm lamellar structures in cold-drawn pearlitic steel wire, Materials Science and Technology 34 (2018) 794–808.

[30] J. F. M. Vergnol and J. R. Grilhe, Relationship between extrinsic stacking faults and mechanical twinning in F.C.C. solid solutions with low stacking fault energy, Journal de Physique 45 (1984) 1479–1490.

[31] F. Barlat, J. M. Ferreira Duarte, J. J. Gracio, A. B. Lopes and E. F. Rauch, Plastic flow for non-monotonic loading conditions of an aluminum alloy sheet sample, International Journal of Plasticity 19(8) (2003) 1215-1244.

Part II- Additional Results

Characterization of failed crossings

Characterization of failed crossings

The detailed characterization of deformation and cracks on the nose of the manganese crossing ATP 110 and the wing rails of BTP 102 has been presented in Paper 1 and Paper 2 respectively. Further studies on deformation and degradation on the nose and wing rail of pearlitic (AP 104) and the wing rails of the manganese crossing (ATP 110) has been presented in this section.

1. Hardness measurements

The hardened pearlitic grade 350HT is often used as crossing material. Figure 1(a) shows the hardness profile of the undeformed 350HT hardened steel used in the crossing. The rail wheel contact surface has a hardness of around 400 Hv and the hardness drops off to a value of 300 Hv at the base of the rail head. The rail head does not have a uniform hardness but there is a gradual decline from the contact surface to the base. The head hardened part is confined within the first 20 mm from the contact surface. Figure 1(b) shows the hardness profile of the normal R260 grade pearlitic rail steel having a uniform hardness of around 300 Hv throughout the rail head.

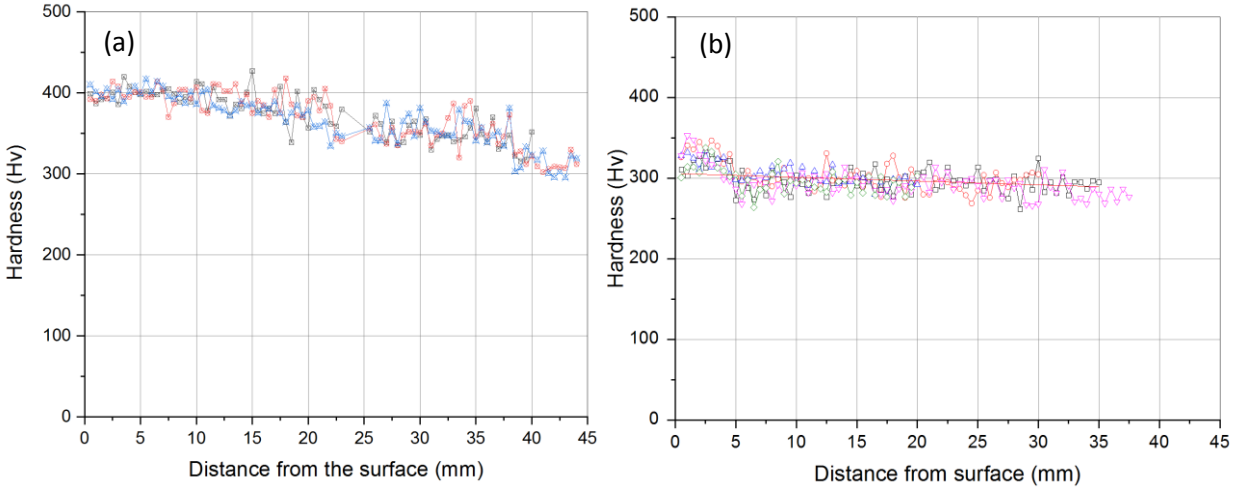

Figure 1: The hardness decrease as a function of distance from the rail wheel contact surface of (a) the undeformed 350HT head hardened pearlitic grade rail steel and (b) the non-head hardened pearlitic grade rail steel used in stock rail. The different colors refer to different measurements.

Figure 2 shows the variation of the hardness of the deformed part of the two wing rails and the damaged welded nose of the crossing (AP 104). Rail wheel contact induces deformation causing hardening of the surface of the running band. The hardness values on the contact surface of the wing rails reached as high as 500 Hv (See Figure 2a). The depth of hardening due to deformation caused by rail wheel contact was limited within the first 2-2.5 mm from the surface. A non-uniform hardness distribution is obtained for the nose of the crossing due to repair welding. The contact surface contained weld material with a hardness of around 500 Hv. Deformation hardening causes a gradient in hardness which falls off from the contact surface. After the weld material, a combination of microstructures is found consisting of bainite to fine pearlite which causes the variation in the hardness values in the middle region (HAZ). Finally, at 10 mm from the surface, the base material is found having hardness 400 Hv which is in agreement with Figure 1a.

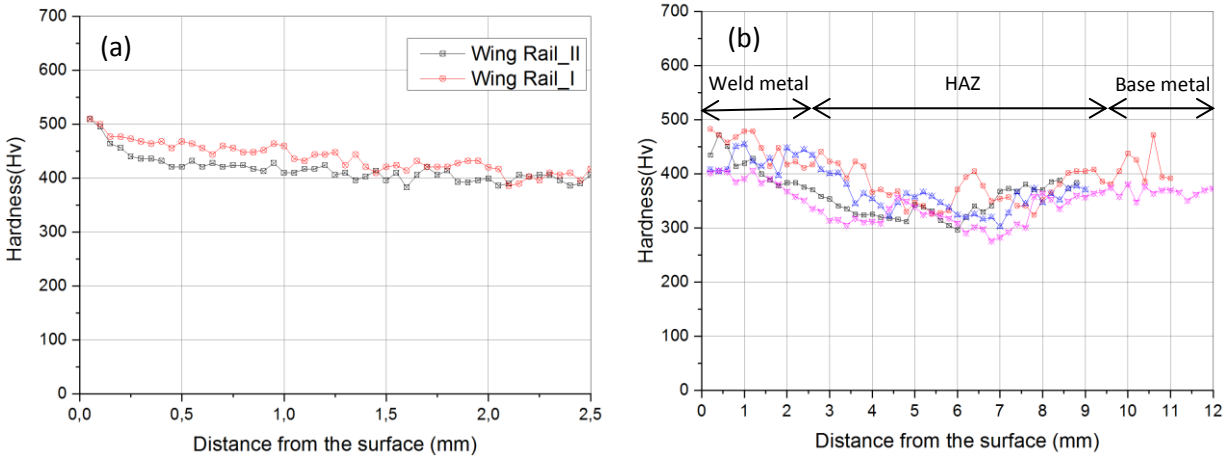

Figure 2: Hardness decrease trend as a function of distance from the rail wheel contact surface of the head hardened pearlitic crossing (AP 104) (a) deformed part of the two wing rails and (b) damaged welded nose. The different colors refer to different measurements.

The hardness profile in pearlite crossings is quite different from the ones in the manganese crossings. Figure 3 shows the hardness contour map of the transverse section of the wing rail of the manganese (ATP 110) crossing showing the gradient of deformation. The undeformed manganese crossing has a hardness of 220 Hv. The passage of wheels over the crossing causes hardening due to severe plastic deformation with the hardening being the most severe at the top layer showing hardness of around 600 Hv. Moving down from the contact surface into depths, the hardness values decrease indicating less deformation. The work hardened layer is observed to extend up to at least 10 mm below the surface. The depth of hardening is significantly higher in manganese grade crossings as compared to normal pearlite grade. The contact region of the wheel with the rail which causes this gradient of deformation hardening is on the left in Figure 3. On the right, the deformation hardening is limited to a few millimeters from the surface which could be due to other causes, such as profile grinding.

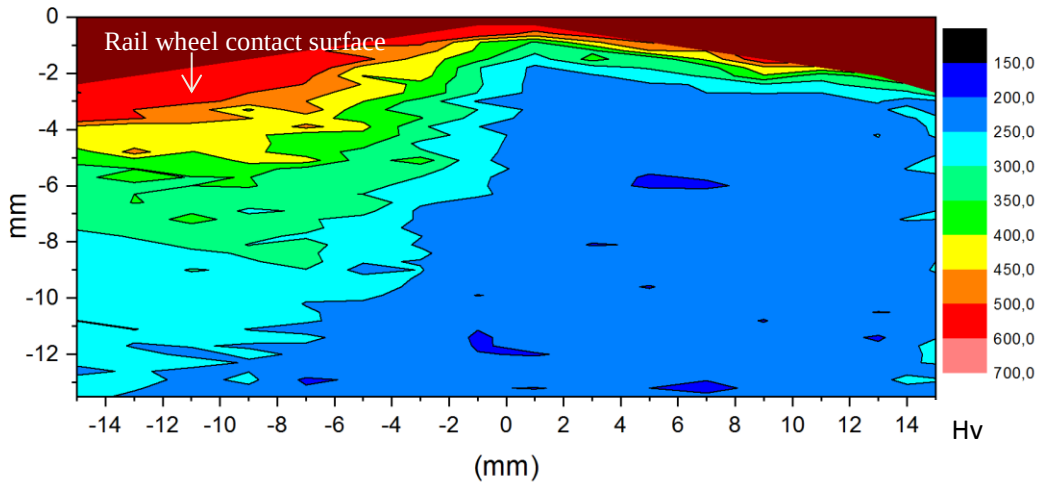

Figure 3: Hardness contour map of the transverse section of the wing rail of the manganese crossing (ATP 110) showing the gradient of deformation due to rail wheel contact.

2. Optical Microscopy

The microstructure of pearlite steel consists of ferrite and cementite. Figure 4 shows the deformed microstructure of the wing rail of the pearlitic crossing. Rolling contact fatigue causes deformation of the microstructure. The contact area of the wheel with the rail influences deformation. The normal and shear loads from the rail wheel contact had deformed the surface layers with material flow occurring in the shearing direction. As the plastic deformation diminishes with depth from the surface, the non-deformed microstructure becomes visible. The depth of plastic deformation varies depending on the contact zone. Figure 4(b) shows the deformed structure near the gauge corner which clearly shows higher depths of shearing than in regions near the center of rail head in Figure 4(a).

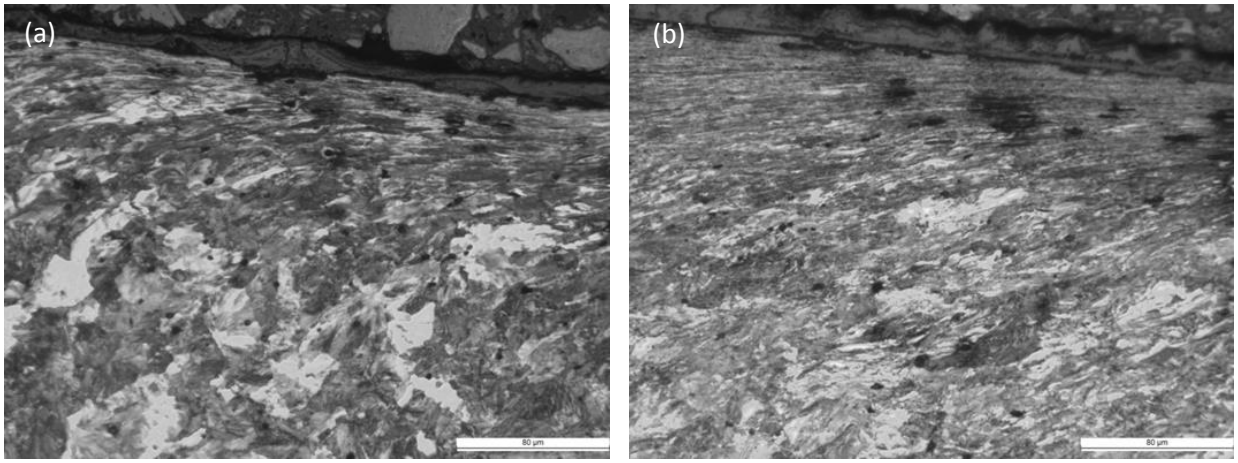

Figure 4: Deformed microstructure of the wing rail of pearlitic crossing (a) near the center of rail head and (b) near the gauge corner.

As mentioned above the nose of the pearlite crossing has been repair welded. Figure 5 shows the distinct layers formed due to etching due to the difference in microstructure formed due to welding on the nose of the pearlitic steel crossing. The microstructure of the welded nose at various depths from the surface is shown in Figure 6. The bright zone at the contact surface is the weld material (Figure 6d), followed by the heat affected zone (HAZ) having a combination of microstructures (Figure 6e-g), and finally the base metal (Figure 6i). Three distinct transition zones are visible in Figure 6a-c. The first transition zone is between the weld metal and the HAZ in Figure 6a. The weld appears bright with needle like structures bainite. The heat affected zone after the weld consists of needles of coarse bainite. The second transition zone is between the coarse bainite and the fine grained pearlite within the HAZ as evident in Figure 6b. The third transition zone is between the fine grained pearlite and large grained pearlite of the base metal (Figure 6c). The difference in the rate of cooling during welding has resulted in different types of structure in the HAZ within the nose of the crossing.

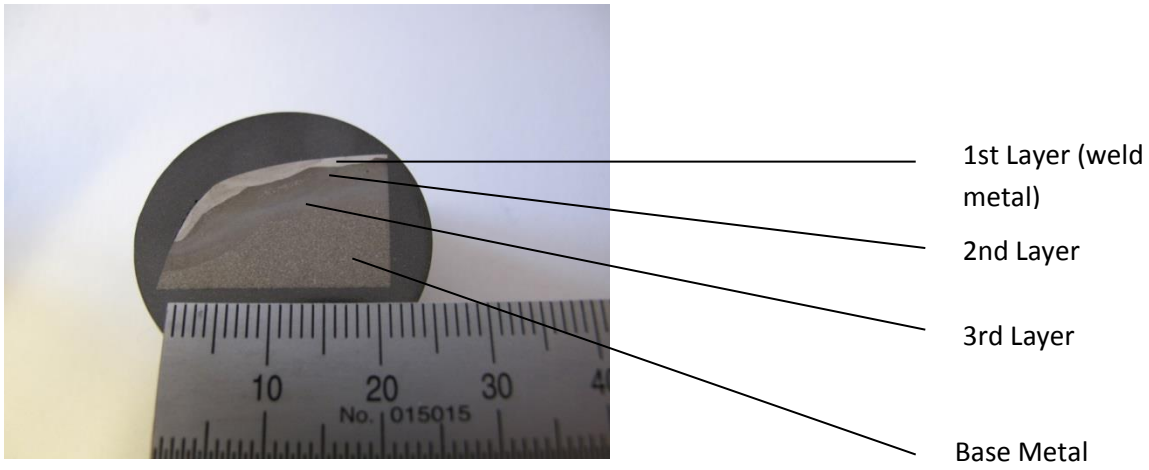

Figure 5: A small piece cut out from the nose of the pearlitic crossing for metallurgical investigation showing the various layers due to the presence of difference microstructures formed as a result of welding.

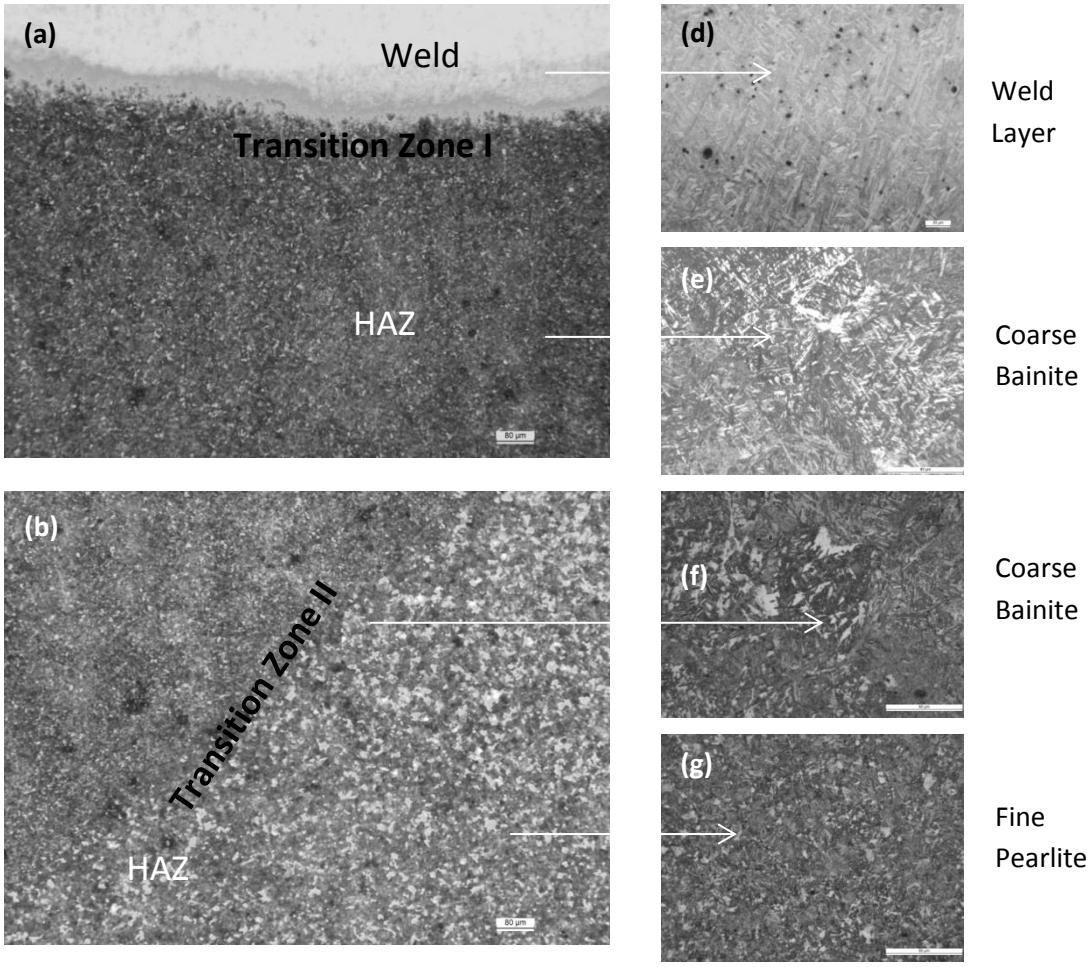

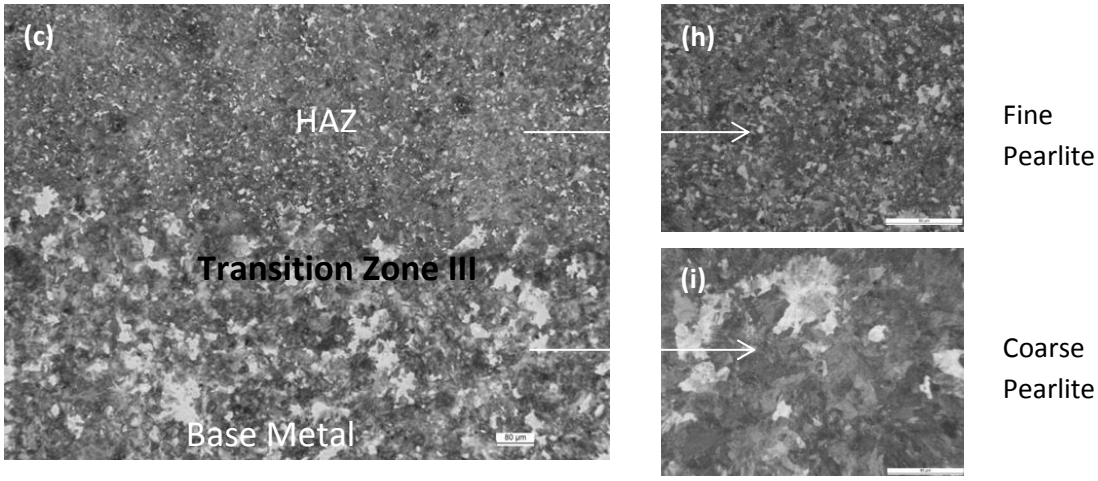

Figure 6: Optical microscopy images of the nose of the pearlitic crossing at different locations from the running surface (a-c) the three transitions formed due to welding, (d) the microstructure present in the weld metal at the contact surface consisting of a bainitic needle structure, (e) the microstructure present in the upper part of the HAZ near the welding consisting of coarse bainite, (f) the microstructure of the HAZ near the second transition zone consisting of coarse bainite, (g) the microstructure near the end of the HAZ consisting of a fine pearlite structure, (h) the fine pearlitic microstructure near the third transition zone and (i) the base material having coarse pearlite microstructure.

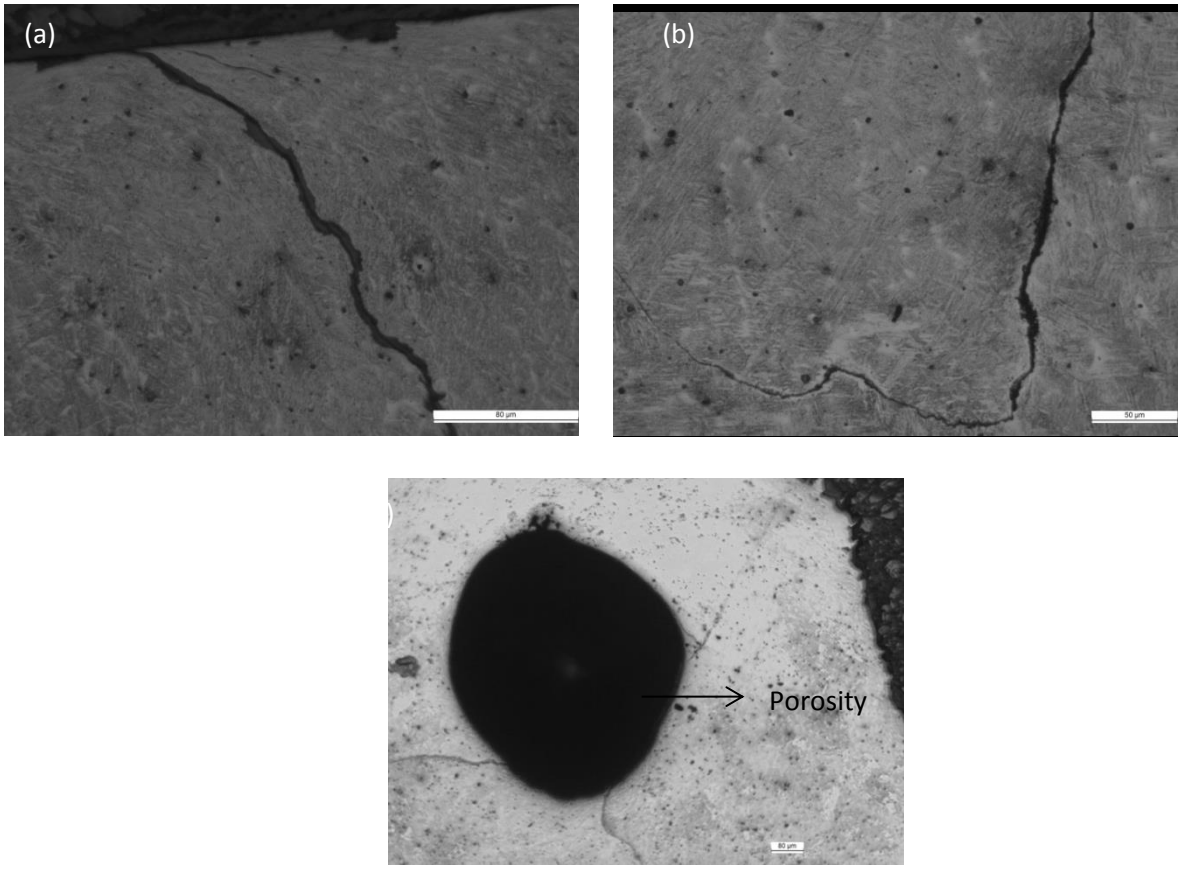

Figure 7: Defects present in the weld layer of the nose of the pearlitic crossing (a) and (b) multiple cracks present in the weld layer, and (c) porosity present in the weld layer.

Figure 7 shows the optical micrographs of the damages and defects present within the weld layer of the nose of the crossing. The contact surface gets strained in the direction of shear as seen in Figure 7a. Multiple surface and subsurface cracks were found in the weld layer (Figure 7a-b). Most of the cracks were confined within the weld layer. Crack branching and interaction between the cracks were also visible in the microstructure. Apart from cracks, presence of multiple pores of various dimensions was also evident from the optical microstructure. Some of the pores were more than 1 mm in size (Figure 7c) and had cracks originating from them. Improper welding has resulted in the formation of defects like porosities and cracks growing from them. These defects should be considered detrimental and could lead to rail failure in the future.

3. 3D X-ray tomography

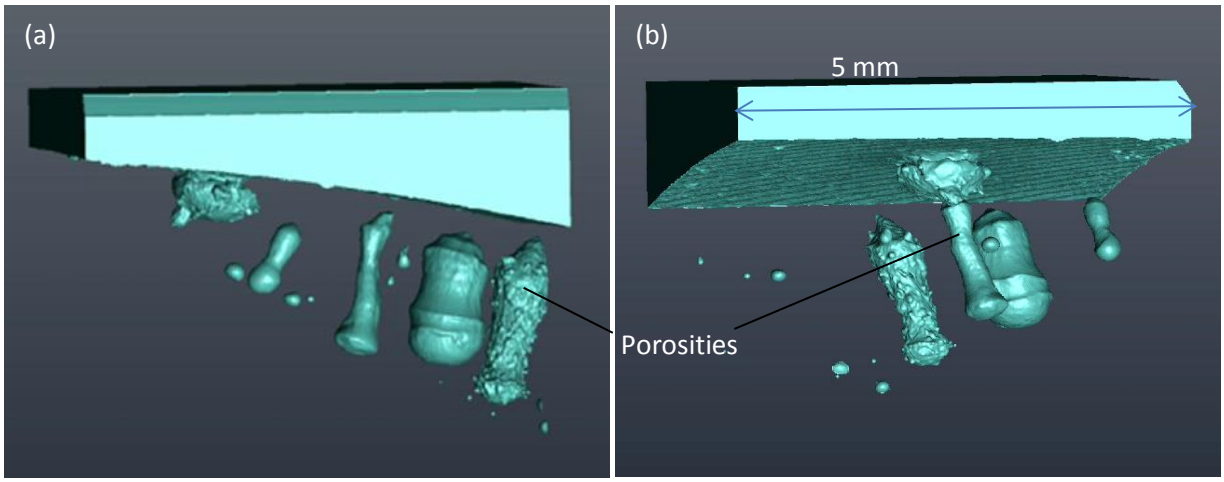

Figure 8: (a&b) 3-D tomographic representation of the defects and porosities in a small volume of the nose of the pearlitic crossing. The steel is represented as transparent and the blue colored area is the air which makes the porosities as well as the rail surface distinctly visible when performing global segmentation thresholding.

Multiple cracks and porosities were evident from the optical microcopy images of the nose of the pearlitic crossing. Figure 8 (a-b) shows the 3-D tomography images of defects in the nose of the pearlitic crossing. In this figure, the steel is represented as transparent and the blue colored area is the air which makes the porosities visible. Multiple pores of various shapes and dimensions with pores as long as 1 mm are present. Some of the pores are connected to the surface (for example through a crack) whereas many pores are deep inside the specimen. The pores run quite deep inside the material. Some of the pores have a smooth surface whereas some have rough surface due to oxidation as the crack is connected to the surface. The pores are sites of crack nucleation which might lead to failure of the material.

Mechanical testing of two different rail steels used in crossings

Mechanical Testing

The material behavior in service is strongly dependent on its mechanical properties. The following sections have a detailed description of the mechanical behavior of the two different grades of steel used in crossings. An attempt has been made to do a comparative analysis of the mechanical properties and deformation characteristics of two different steels.

1. Tensile test

Tensile tests were performed on the pearlitic and manganese steel at room temperature at 10^{-2} s^{-1} strain rate. Figure 1a shows the engineering stress-strain curve for the two materials. The pearlite grade steel has yield stress (0.2% offset) of 770 MPa and UTS of 1350 MPa. The tensile ductility measured in terms of percentage elongation is 12%. The necking behavior after UTS has a gradual drop in stress. The manganese steel has much lower yield stress and UTS compared to pearlitic steel. The yield stress is 203 MPa and the UTS is 750 MPa. The percentage elongation of manganese steel (22%) is much higher than the pearlitic steel. It is observed that there is very little necking with no significant drop in peak stress as the material fractures just after UTS. The true stress versus true strain curves are shown in Figure 1b. The strain hardening exponent and strain hardening coefficient for the pearlitic steel are 0.2 and 2208 respectively. The manganese steel has a higher strain hardening exponent (0.4) than pearlite. The strain hardening coefficient for manganese steel is 1636. Figure 1c gives the corresponding work hardening rate versus true strain curves. The work hardening rate of pearlitic steel was higher than manganese up to 0.05 strains, after which the manganese had much higher work hardening rate. The work hardening rate decreased throughout the test for the pearlite steel. For the manganese, initially there is a decrease, followed by a steady rate and then the rate decays somewhat towards the end of the test. The strain hardening in manganese steel is quite evident. The strain range over which the manganese steel hardens is large compared to pearlitic steel. This strain hardening ability of manganese steel makes it a suitable material to be used in crossings.

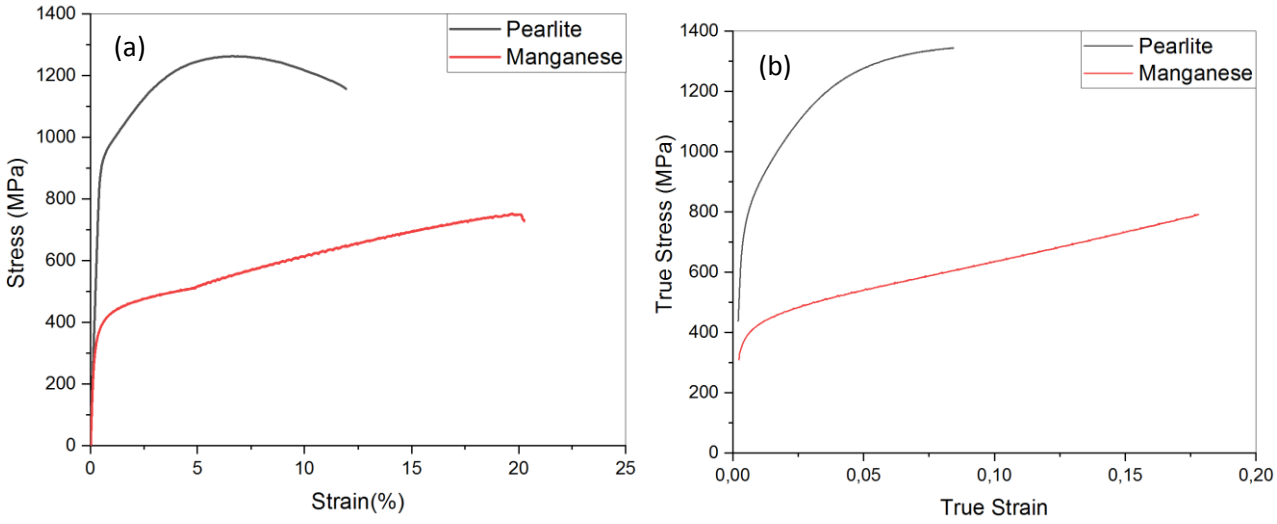

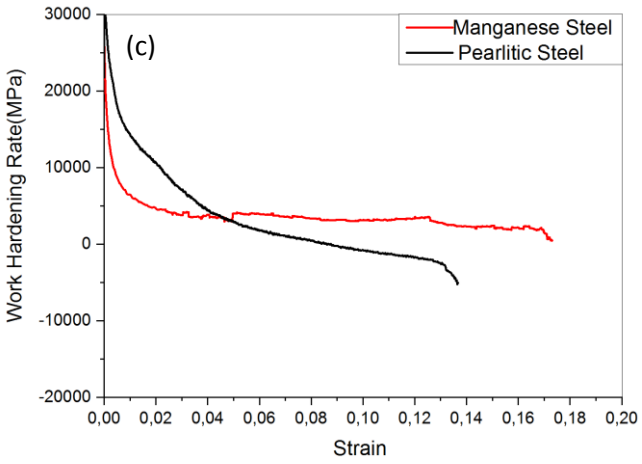

Figure 1: Tensile properties of pearlitic and manganese steel: (a) engineering stress-strain curves, (b) true stress-strain curves and (c) work-hardening rate versus true-strain curves.

The uniaxial tensile test results along with the hardness test results reveal that pearlitic steel which is harder compared to manganese steel strain hardens rapidly and saturates. This is also reflected in the low value of strain hardening exponent (n=0.2). Manganese steel is soft compared to pearlitic steel but strain hardens steadily, with constant work hardening rate over a higher strain range with a higher strain hardening exponent of 0.4.

2. Fatigue Results

The fatigue tests performed at 0.6% strain amplitude have been described in detail in Paper 5. The remaining test results are discussed in the following sections along with a comparison with the 0.6% strain amplitude low cycle fatigue data for a better comparative analysis of the low cycle fatigue behavior under different strains.

2.1 Uniaxial Low Cycle Fatigue

A material's response, when subjected to strain cycling, may range from hardening, softening, stabilization or a combination of all depending on its microstructural characteristics. The cyclic deformation behavior of the investigated rail steels corresponding to the development of stress amplitude σ_a with cycles N at various applied strain amplitudes is shown in Figure 2. Cyclic hardening/softening behavior of a material can be clearly seen from the variation of stress amplitude with elapsed loading cycles. For the pearlitic steel at all strain amplitudes, the cyclic behavior consists of three prominent stages. First, there is a decrease in stress amplitude leading to softening, followed by a stage of cyclic saturation and finally an increase in stress amplitude leading to hardening before the final fracture. For the 0.6% strain amplitude, the softening occurred for the first few cycles but the steel stabilized quickly in the next few cycles. With the increase in strain amplitude, the softening effect became almost negligible, and the stabilization occurred within fewer cycles. For the manganese steel at lower strain amplitudes, there is initial hardening followed by softening and then failure. Hardening was observed only for the initial few percent of the fatigue life (first 100 cycles), whereas softening prevailed for most of the fatigue life. No saturation stage was observed. At higher strain amplitudes, rapid hardening mostly predominates with little softening before failure. In strain controlled fatigue testing, the plastic strain amplitude is a major governing factor. The plastic strain amplitude development with the number of cycles is shown in Figure 3.

The plastic strain amplitude decreased initially due to hardening in all cases for manganese steel. At lower strain amplitudes, after an initial decrease, there was an increase in plastic strain amplitude due to softening. However, for higher strain amplitudes, the plastic strain amplitudes decreased throughout the fatigue life. For the pearlitic steel, the plastic strain amplitude increased initially due to softening, followed by stabilization before failure. The fatigue life decreased with increase in strain amplitude whereas the maximum stress amplitude increased with increase in strain amplitude for both the steels.

Application of compressive mean strain did not cause much change in the cyclic response of pearlitic steel as compared to without mean strain application as long as the strain amplitude remains the same. A compressive mean strain of 0.9% with a strain amplitude of 0.6% and a compressive mean strain of 0.5% with a strain amplitude of 1% were used respectively. The stress amplitude against number of cycles as well as the plastic strain amplitude developed curves for pearlitic steel is nearly coincident for the two cases of with and without compressive mean strain. Although the maximum and minimum strains in the fatigue tests with compressive mean strain were different, the stress response was found to be identical to the 0.6% strain amplitude without mean strain. The material adopted itself to the same cyclic response. In the case of 1% strain amplitude, however, little hardening was observed for the 1^{st} cycle but then the material adapted to the same cyclic response as without mean strain.

The material response for manganese steel towards mean strain application is different to one without mean strain. For both the strain amplitudes, the mean strain caused an increase (parallel shift) in the stress amplitude development. Higher stress amplitudes for each cycle was obtained compared to without mean strain. The cyclic response is identical in terms of hardening/softening. In the case of pearlite, the plastic strain amplitude was same for with and without mean strain. However, in the case of manganese steel, lower plastic strain amplitudes were obtained with mean strain application.

Mean strain in strain controlled loading causes mean stress relaxation. Initially, for negative mean strain, the positive stress peak is less and the negative peak is more showing negative mean stress. Gradually, the mean stress relaxed to zero showing symmetric loop as without mean strain, only shifted in negative strain axis. This is called mean stress relaxation. This happens with positive mean strain also where the shift is on the positive side of strain axis. Although the loops are symmetric, there may be an increase in stress amplitude due to extra hardening for the mean plastic strain. In this study, pearlitic steel is insensitive to mean strain hardening. However, manganese steel shows that there is an increase in cyclic yield stress due to extra hardening for the mean strain. Therefore, manganese steel is sensitive to hardening due to the mean strain, which causes a decrease in fatigue life.

A comparison between the pearlitic and manganese steel reveals the maximum stress amplitudes reached at all the strain amplitudes are higher for the pearlitic grade. This is due to the higher hardness of pearlitic grade steel. Also, in all cases, the manganese steel has higher plastic strain amplitudes compared to pearlitic grade under similar conditions. This is due to the lower yield strength of manganese Steel. The fatigue life of the pearlitic steel is higher compared to the manganese steel under similar conditions. The fatigue lives under different conditions of strain amplitude are given in Table 1. Higher hardness and strength leads to lower plastic strains in the material and thus increase in fatigue life. It is generally observed that work hardened materials demonstrate cyclic softening whereas softer material exhibit cyclic

hardening in fatigue tests [1]. For the present materials, the cyclic softening is higher in pearlite as compared to manganese steel.

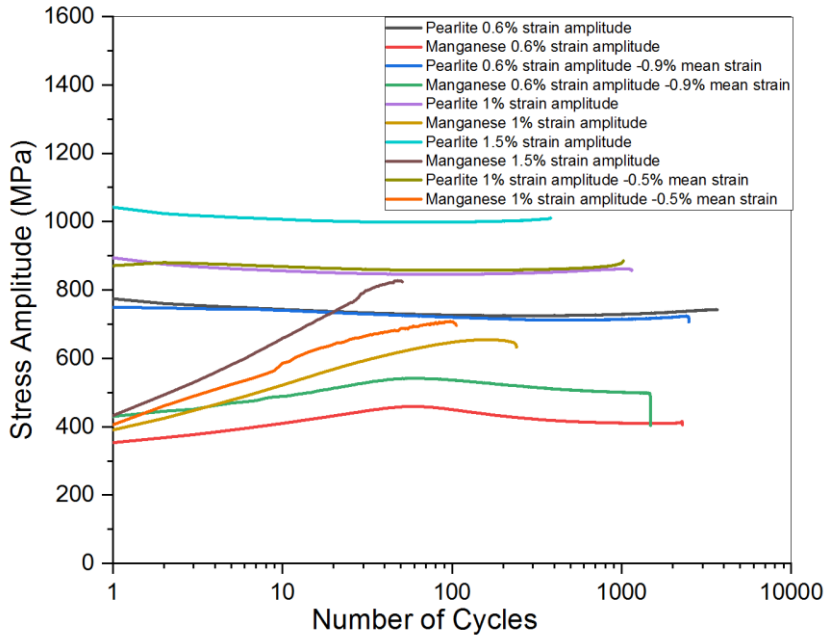

Figure 2: Stress amplitude development with number of cycles during uniaxial fatigue testing at different conditions of strain amplitude for pearlitic and manganese steels.

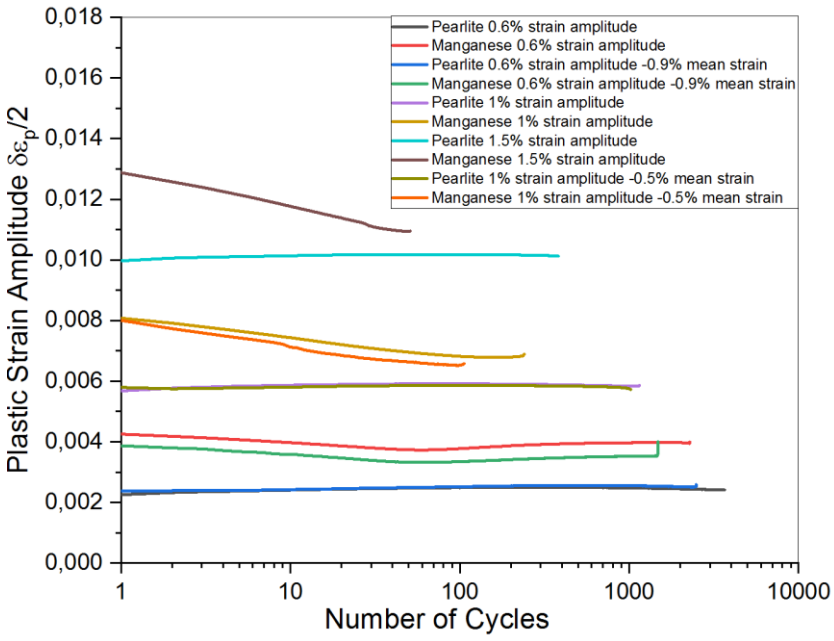

Figure 3: Plastic strain amplitude development as a function of number of cycles during uniaxial fatigue testing at different conditions of strain amplitude for pearlitic and manganese steels.

Table 1: Failure cycles for pearlitic and manganese steels for different strain amplitudes of uniaxial loading

Strain amplitude	Material	Number of Cycles to failure
0.6%	Pearlite	3660
	Manganese	2278
0.6% (-0.9% mean strain)	Pearlite	2490
	Manganese	1480
1%	Pearlite	1178
	Manganese	240
1% (-0.5% mean strain)	Pearlite	1028
	Manganese	107
1.5%	Pearlite	390
	Manganese	55

Cyclic hardening ratio (CHR) and cyclic softening ratio (CSR) are two important parameters in characterizing cyclic deformation behaviors of materials. CHR and CSR were determined using $CHR=(\sigma_{max}- \sigma_1)/\sigma_1$ and $CSR=(\sigma_{max}- \sigma_{half})/\sigma_{max}$, where σ_1, σ_{max} and σ_{half} represented the stress amplitude at the first cycle, the maximum stress amplitude, and the stress amplitude at the half lifetime, respectively. The degree of hardening and softening for both the steels is presented in Table 2. No hardening was observed for pearlitic steel except for 1% strain amplitude with 0.5% compressive strain, where very little hardening could be found in the first cycle due to mean strain hardening. Profound hardening was observed in case of manganese steel which was found to increase linearly with increase in strain amplitude. The softening was high at lower strain amplitudes compared to higher strain amplitudes for both the materials. The application of mean strain didn't cause a significant change in the hardening/softening behavior for the two steels.

Table 2: The cyclic hardening and softening ratios of the pearlitic and manganese steel for different conditions of strain amplitudes

Strain amplitude	Material	CHR	CSR
0.6%	Pearlite	0	0.0522
	Manganese	0.2983	0.1066
0.6% (-0.9% mean strain)	Pearlite	0	0.0453
	Manganese	0.2593	0.0714
1.0%	Pearlite	0	0.0432
	Manganese	0.6762	0.0051
1.0% (-0.5% mean strain)	Pearlite	0.0109	0.0195
	Manganese	0.7453	0.0311
1.5%	Pearlite	0	0.0389
	Manganese	0.9145	0.0759

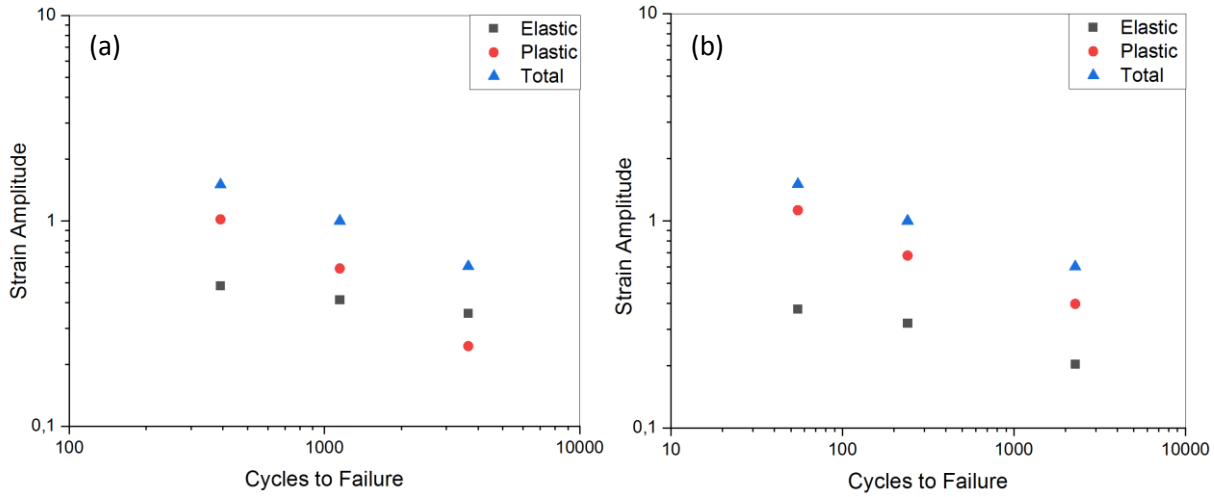

Figure 4: A graph showing the strain amplitudes (with zero mean strain) at half lifetime vs. the number of cycles to failure (a) pearlitic and (b) manganese steel.

The relationships among total, elastic and plastic strain amplitudes, as well as the number of reversals to failure of the pearlite and the manganese steels, are presented in Figure 4. As the number of cycles to failure increased, with decreasing the total strain amplitude, both the elastic and plastic strain amplitude decreased. In case of manganese steel, the elastic strain was less than the plastic strain in all conditions; however, for the pearlitic steel at lower strain amplitude of 0.6% the elastic strains were higher than the plastic strain. The decrease of plastic strain amplitude is higher compared to elastic strain amplitude. The transition life corresponds to the intersection of the elastic and plastic curve as we see in case of pearlitic steel. No transition life could be obtained for manganese steel. The difference of plastic strain amplitude between the two steels under cyclic loading might be the cause of different low cycle fatigue behaviors. The plastic strain amplitudes were always higher for the manganese steel compared to pearlitic steel. The relationship between plastic strain amplitude and fatigue life is given by the Coffin–Manson relationship [2],

$$\frac{\Delta\varepsilon_{pl}}{2} = \varepsilon_f'(2N_f)^c \quad (1)$$

Where ε'_f is the fatigue ductility coefficient and c the fatigue ductility exponent. The plastic strain amplitude ($\Delta\varepsilon_{pl}$) used in the analysis is obtained at $N_f/2$. The relation between the total stress amplitude and life time is given by the Basquin equation [3]:

$$\frac{\Delta\sigma_{total}}{2} = \sigma_f'(2N_f)^b \quad (2)$$

where σ'_f is the fatigue strength coefficient and b the fatigue strength exponent. The total stress amplitude ($\Delta\sigma_{total}/2$) used in the analysis is obtained at $N_f/2$.

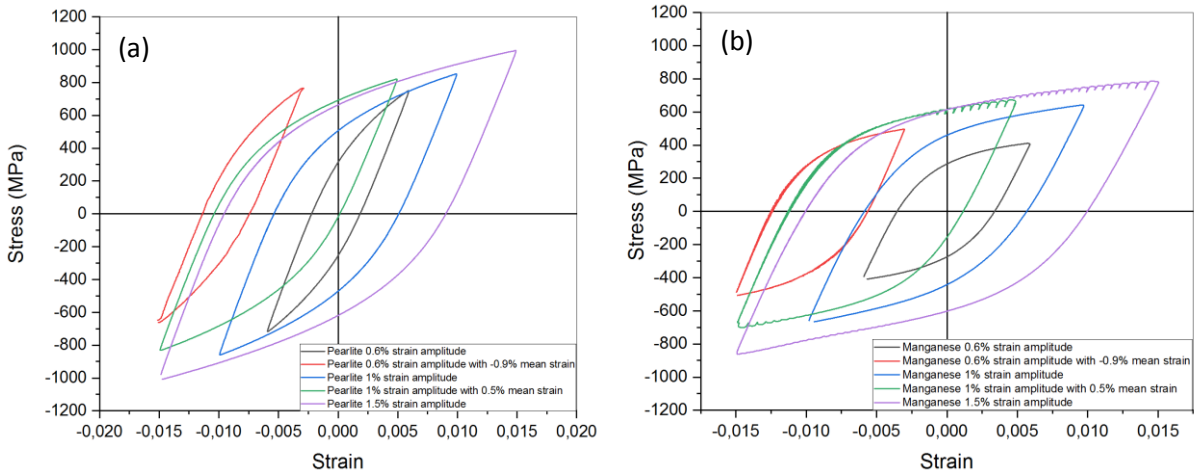

Figure 5: Stabilized hysteresis loop developed at half lifetime under different strain amplitudes of loading (a) pearlite and (b) manganese steel.

Figure 5 shows the hysteresis loops developed at stabilization for the two different materials under different strain amplitudes of loading. The shape of the loop is different for the two materials under similar conditions. The cyclic stress-strain curve is usually determined by connecting the tips of the stable hysteresis loop from the constant strain amplitude fatigue tests of the materials cycled at different strain amplitudes. The cyclic stress-strain curve is given by the equation [4]:

$$\Delta\sigma = K'(\Delta\varepsilon_p)^{n'} \tag{3}$$

Where $\Delta\sigma$ is the stress range, $\Delta\varepsilon_p$ is the plastic strain range at stabilization, and K' and n' are the cyclic strain hardening coefficient and cyclic strain hardening exponent respectively. The cyclic properties of the investigated rail steels are given in Table 3 below:

Table 3: Cyclic properties of the pearlitic and manganese rail steel used in this study

Material/Parameter	**Pearlite**	**Manganese**
Fatigue ductility coefficient, ε_f (%)	1.868	0.619
Fatigue ductility exponent, c	-0.636	-0.282
Cyclic strain hardening coefficient (K')	3.229	2.994
Cyclic strain hardening exponent (n)	0.2142	0.5976
Fatigue strength coefficient, σ'_f (MPa)	3.4	3.26
Fatigue strength exponent (b)	-0.1385	-0.1737

The area under the hysteresis loops gives an idea about the plastic strain energy density of the different materials under fatigue. Fatigue is characterized by absorption of irreversible plastic energy which influences fatigue life. In low cycle fatigue, the accumulated plastic deformation is the primary reason for the fatigue. Morrow [5] suggested that the plastic

strain energy per cycle is a useful criterion to measure the fatigue damage per cycle since the cyclic plastic strain is related to the movement of dislocations and the cyclic stress is associated with the resistance against their motion.

Table 4: Plastic strain energy density per cycle at half lifetime and accumulated plastic strain energy density at different strain amplitudes for pearlite and manganese rail steels

Strain amplitudes	**Wp @ $N_f/2$ (MJ/m^3)**		**Wp total ($x10^6$)**	
	Pearlite	**Manganese**	**Pearlite**	**Manganese**
$\Delta\varepsilon_t/2 = 0.6\%$	425	448	1.555	1.02
$\Delta\varepsilon_t/2 = 1\%$	1301	1186	1.533	0.312
$\Delta\varepsilon_t/2 = 1.5\%$	2720	2665	1.063	0.1599
$\Delta\varepsilon_t/2 = 0.6\%$ (ε_m= -0.9)	401	533	1	0.788
$\Delta\varepsilon_t/2 = 1\%$ (ε_m= -0.5)	1265	1370	1.3	0.15

The plastic strain energy density per cycle at $N_f/2$, as well as the accumulated plastic strains energy density for the two rail steels under different conditions, is reported in Table 4. At 0.6% strain amplitude the plastic strain energy density per cycle is nearly equivalent for both the materials. At higher strain amplitudes of 1% and 1.5%, the pearlite has higher plastic strain energy density per cycle compared to manganese. Higher number of cycles to failure in case of pearlitic steel caused much higher accumulated plastic strain energy for all cases. Presence of mean strain didn't cause an appreciable change in the plastic strain energy density per cycle of pearlitic steel compared to without mean strain application. However, in case of manganese steel, the presence of mean strain caused higher plastic strain energy density per cycle in both the strain amplitudes but the total accumulated strain energy density is less due to a lower number of cycles to failure. Comparing with pearlitic steel the plastic strain energy density was more in manganese steel in both strain amplitudes but the total energy was less. Energy dissipated in cyclic loading is related to the number of cycles (N_f) by a Coffin-Manson type power-law relationship: $W_p = W_f'(2N_f)^{\omega}$ where, where W'_f is the plastic strain energy coefficient or fatigue toughness co-efficient signifying the material's energy absorption capacity and ω is the plastic strain energy exponent. ω is correlated to b and c as ω = b + c. The log-log plot using experimentally obtained plastic strain energy density per cycle at about half-life and the number of reversals to failure ($2N_f$) is shown in Figure 6. The linear fit shows a correlation coefficient better than 0.99. The energy intercepts and slope (ω) of the curve is listed in Table 5.

Table 5: Hysteresis plastic work parameters of the rail steels

Material parameter	**Pearlite**	**Manganese**
Log (W'_f)	5.86	4.41
ω	-0.83	-0.4847
b+c	-0.774	-0.4557

It can be seen that for pearlitic steel the value of ω (−0.83) derived and as per the relation ω = b + c (−0.774) matched roughly, whereas for manganese steel it matched quite well. Therefore, the energy-life and strain-life relationships followed the same trend regarding their responses to the applied strain amplitude.

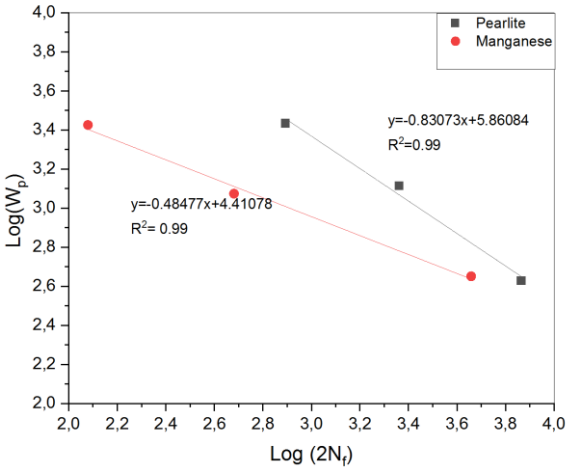

Figure 6: Plastic strain energy density per cycle at about half-life vs number of reversals to failure.

The accumulated plastic strain energy density is obtained by summing up the areas of all the hysteresis loops until failure. This total energy can be used to quantify the resistance to fatigue damage or fatigue toughness ($W_{p\ total}$).

$$W_{ptotal} = W_p . N_f .$$

With the increase in strain amplitude i.e. decrease in the number of cycles, the plastic strain energy density per cycle increased. But the total plastic strain energy density increased with increasing fatigue life. This phenomenon suggests that a higher amount of cumulative plastic strain energy was required for the process of crack initiation and propagation to occur at the lower level of strain amplitudes. At higher amplitudes local damage processes prevalent cause energy absorption leading to decrease in accumulated plastic strain energy density.

2.2 Pure Torsion Low Cycle Fatigue Testing

The torque amplitude developed with the number of cycles for the two steels at two different equivalent strain amplitudes of 0.8% and 1.3% is given in Figure 7. The load response indicates three stages are present in both the strain amplitude, as seen in the case of uniaxial straining for pearlitic steel. First there is a decrease of torque amplitude leading to softening, followed by a linear stage of cyclic saturation, and finally an increase in amplitude leading to hardening before the final fracture. Hardening followed by softening is observed in case of manganese steel for both the strain amplitudes. The hardening is present only for the initial few percents of the fatigue life whereas softening prevailed for most of the fatigue life with no saturation as was observed for uniaxial loading. The torque amplitudes developed are higher for pearlitic steel than for manganese steel. The cycles to failure at lower strain amplitudes are higher for manganese steel but at higher strain amplitudes pearlite and has a higher life time. Compared to uniaxial

testing, application of shear loading causes an increase in fatigue life time in both the steels. Shear loading causes delay in crack formation and increases fatigue life.

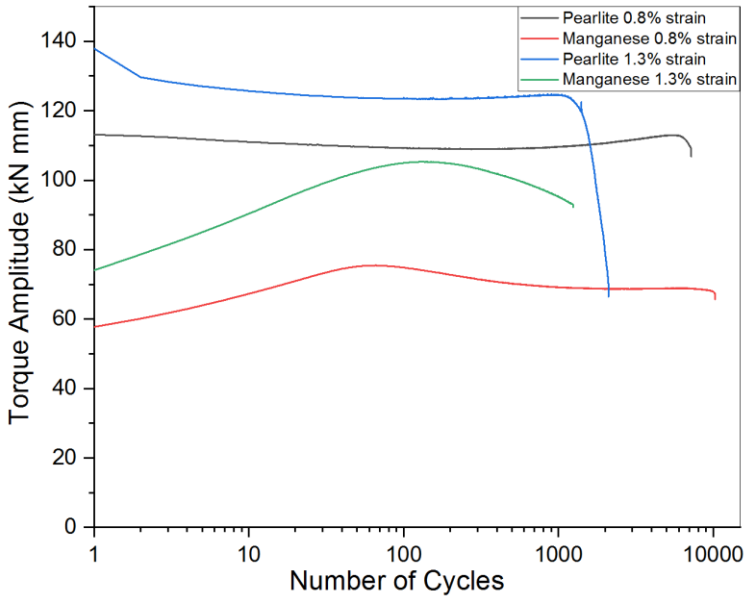

Figure 7: Evolution of torque amplitude with number of cycles in pure torsion loading under different strain amplitudes for pearlite and manganese steels.

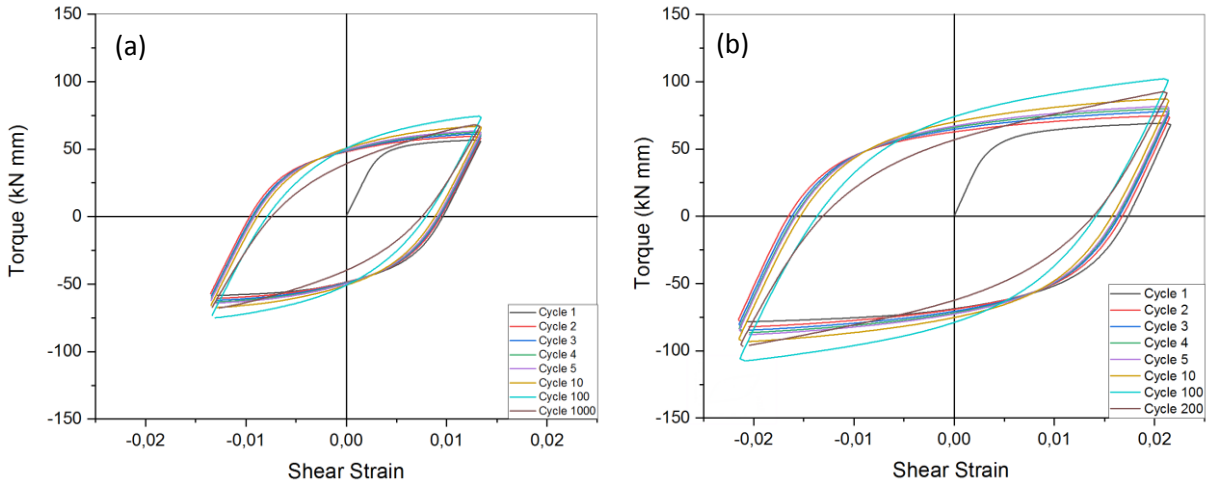

Figure 8: Hysteresis loop development for manganese steel at different cycles under pure torsion loading at (a) 0.8% equivalent strain amplitude and (b) 1.3% equivalent strain amplitude.

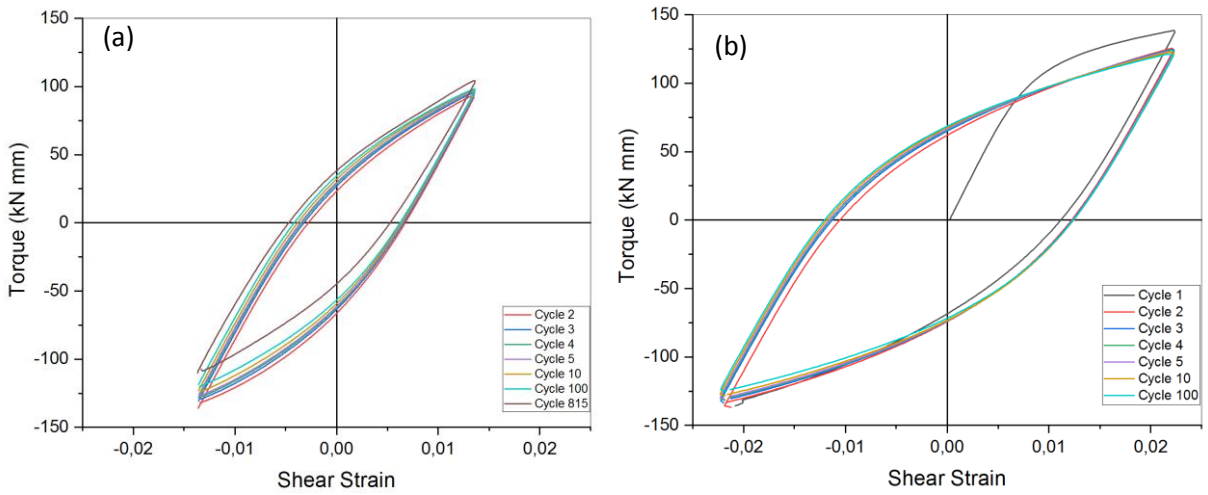

Figure 9: Hysteresis loop development for pearlite steel at different cycles under pure torsion loading at (a) 0.8% equivalent strain amplitude and (b) 1.3% equivalent strain amplitude.

Figures 8-9 show the hysteresis loops developed for the two different materials under different loading conditions. For the manganese steel initially under all conditions, there is a shift of the tip of the hysteresis loop upwards towards higher stress indicating cyclic hardening whereas the trend is reversed for pearlitic grade indicating cyclic softening. At half number of cycles, cyclic softening was observed for manganese steel. For pearlitic steel stabilized hysteresis loops are obtained at half cycles to failure. The area under the hysteresis loops gives the plastic strain energy density of materials under fatigue as mentioned before. The exact values of plastic strain energy density could not be calculated due to lack of stress data due to use of solid specimen. But a comparative analysis indicates the manganese steel and pearlitic steel have similar plastic energy density per cycle at lower strain amplitudes. But since the cycles to failure are higher for manganese steel, the accumulated plastic strain energy density is higher for manganese steel. At higher strain amplitudes, the pearlite has higher plastic strain energy density per cycle as well as higher cycles to failure leading to nearly double accumulated plastic strain energy density than manganese steel.

The torsion fatigue results show a similar trend as the uniaxial fatigue. The torque vs cycles results shows cyclic softening through the life for pearlitic steel whereas manganese steel shows cyclic hardening for almost 100 cycles, thereafter there is cyclic softening and failure. Cyclic hardening rate increases with strain amplitude leading to early microcrack initiations and reduction in failure life.

2.3 Biaxial Loading

A comparison between uniaxial and biaxial low cycle fatigue cannot be made unless the equivalent stress values are obtained. However, the present use of solid specimens instead of tubular specimen restricts direct calculation of equivalent stress values. The normal stress is uniformly distributed whereas the general shear stress formula is dependent on the radius, shear stress being maximum at the surface and zero at the center. Due to plasticity, and non-linear response on plastic straining, the shear stress in each location is not readily computed. However, the strain is always well defined, and the uniaxial stress can be used as a comparison tool also on biaxial loading whether proportional or non-proportional.

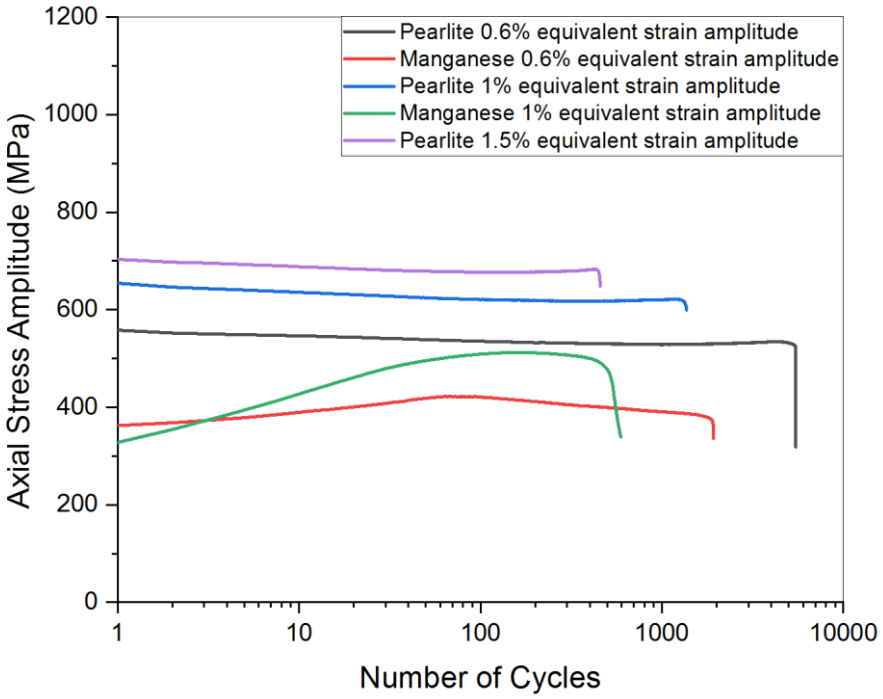

Figure 10: Evolution of axial stress amplitude with number of cycles in biaxial in-phase loading for the two rail steels under different equivalent strain amplitudes.

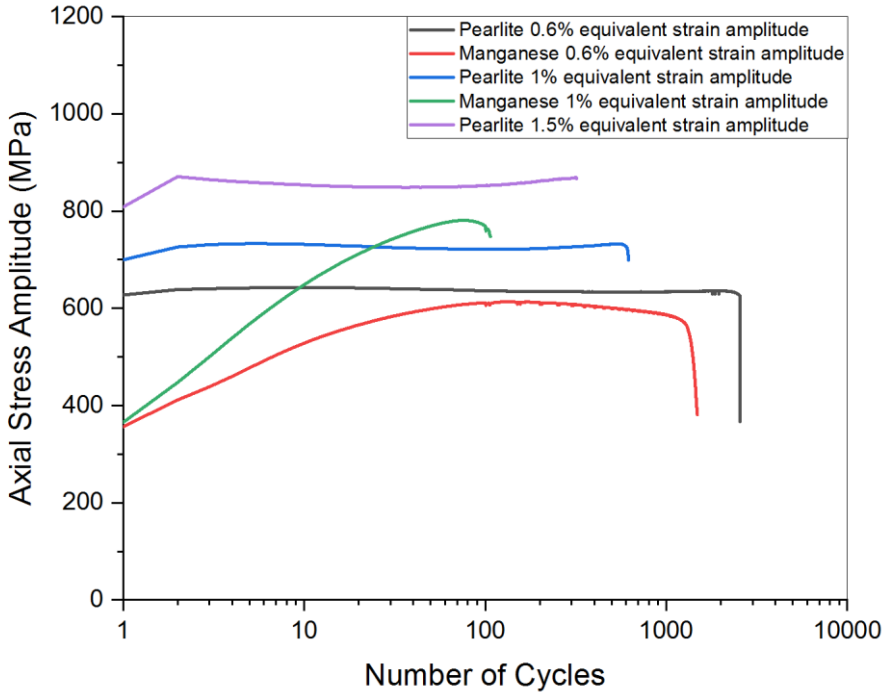

Figure 11: Evolution of axial stress amplitude with number of cycles in biaxial out of phase loading for the two rail steels under different equivalent strain amplitudes.

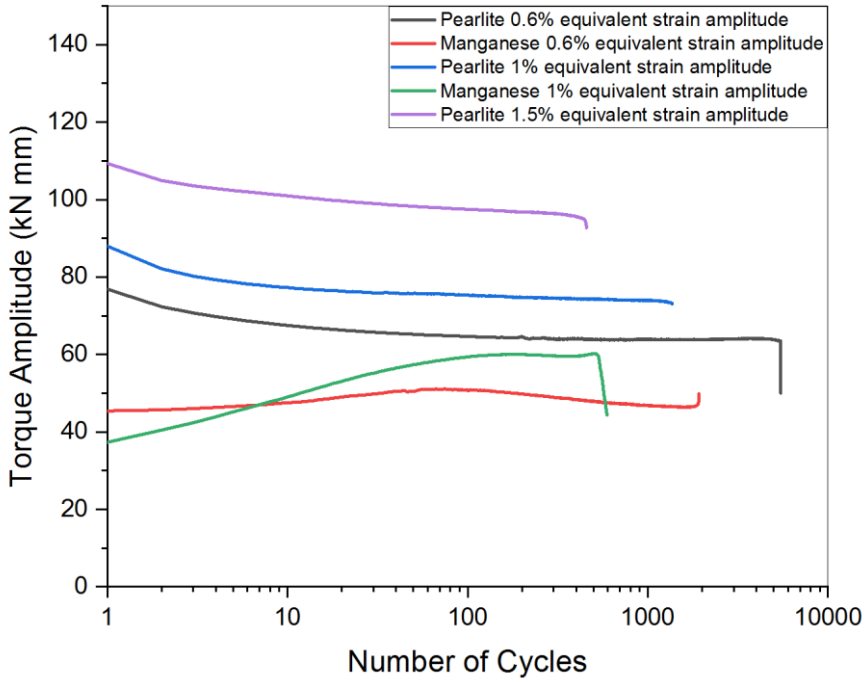

Figure 12: Evolution of torque amplitude with number of cycles in biaxial in-phase loading for the two rail steels under different equivalent strain amplitudes

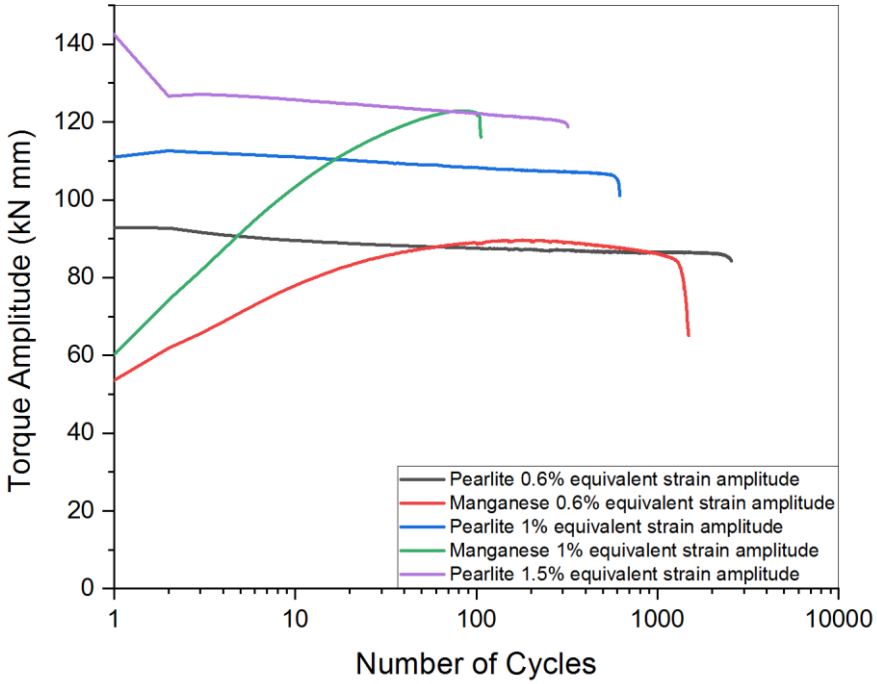

Figure 13: Evolution of torque amplitude with number of cycles in biaxial out of phase loading for the two rail steels under different equivalent strain amplitudes.

The material response in terms of stress and torque with number of cycles for biaxial loading for different equivalent strain amplitude is shown in the Figures (10-13) above. Similar trends as discussed in the case of uniaxial loading can be observed. With the increase in equivalent strain amplitude, the normal stress amplitude, as well as the torque amplitudes, increase for both the materials. The two materials behave very differently under in-phase and out of phase loading. Higher hardening and thus higher stress and torque amplitudes are observed for biaxial out of phase loading for both the materials. Due to rotation of maximum shear planes in biaxial out of phase loading additional slip systems get activated causing nonproportional hardening in addition to cyclic hardening. Nonproportional cyclic hardening depends on the strain path as well as the degree of straining. 90° out of phase loading causes the maximum degree of non-proportionality. Therefore higher strain amplitudes together with 90° phase difference cause the highest hardening compared to in-phase loading. The in-phase biaxial behavior is similar to uniaxial behavior.

During in-phase loading, the stress and torque amplitudes development for the manganese steel is less than the pearlite under all conditions of strain amplitudes. However, the non-proportional hardening in manganese steel at high equivalent strain amplitudes of 1% surpasses that in pearlite. The maximum stress and torque amplitudes developed are higher in manganese than pearlite in biaxial out of phase loading at 1% equivalent strain amplitude. At lower equivalent strain amplitude of 0.6%, the maximum torque amplitude for manganese steel is higher than pearlite whereas the normal stress amplitude is lower.

At lower strain amplitude during in-phase loading, both hardening and softening can be observed for manganese steel. But at higher strain amplitudes, hardening was more prominent with very little softening towards failure. As observed in the case of uniaxial loading, the hardening occurred within the first 100 cycles. For pearlitic steel, in biaxial in-phase loading, the behavior was similar as observed in case of uniaxial loading where there are three stages of cyclic softening, stabilization followed by little softening before fracture. Biaxial out of phase loading caused significant hardening in manganese steel even at lower strain amplitudes with very little softening. At higher strain amplitudes, the material strain hardened all the way to failure with no softening. For pearlite, there is little hardening in the first cycle, followed by softening and cyclic stabilization, softening and then failure.

Table 6: Failure cycles for pearlitic and manganese steel under different strain amplitudes of uniaxial loading

Condition	Equivalent Strain amplitude	Material	Number of Cycles to failure
Biaxial in-phase	0.6%	Pearlite	5471
		Manganese	1924
	1%	Pearlite	1368
		Manganese	594
	1.5%	Pearlite	456
Biaxial out of phase	0.6%	Pearlite	2556
		Manganese	1485
	1%	Pearlite	619
		Manganese	107
	1.5%	Pearlite	321

The biaxial out of phase loading causes a decrease in number of cycles to failure compared to biaxial in phase loading for both the materials. Like uniaxial loading, in biaxial loading also the pearlite can sustain higher cycles to failure.

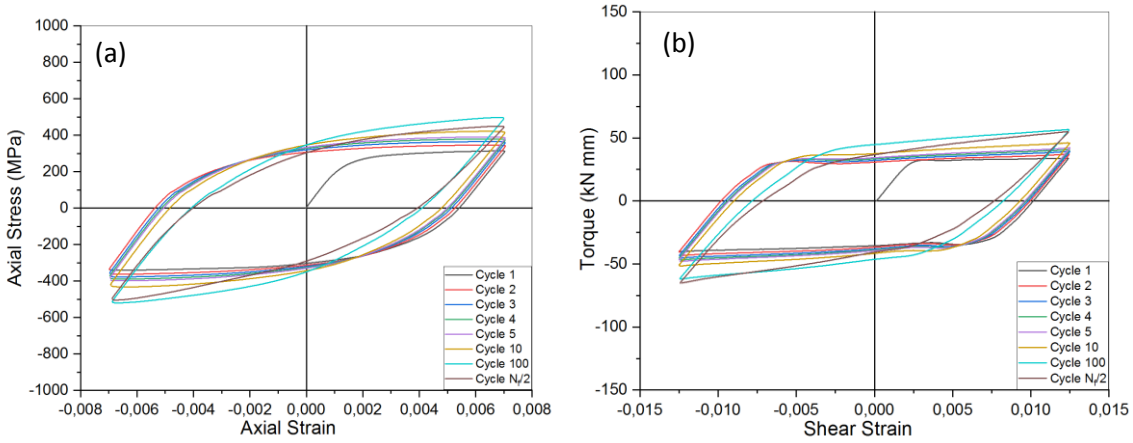

Figure 14: Hysteresis loop development for manganese steel at different cycles under biaxial in phase loading at 1% equivalent strain amplitude (a) axial stress-strain response and (b) shear stress-strain response.

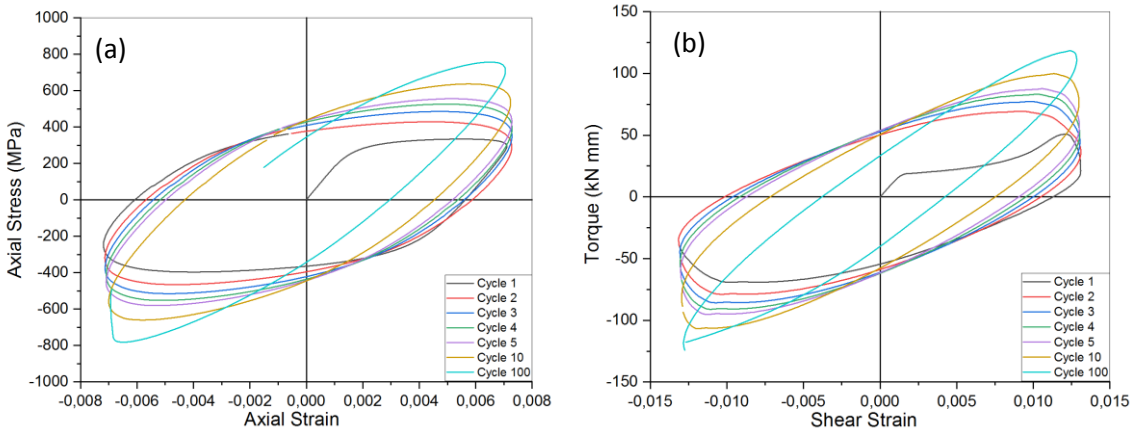

Figure 15: Hysteresis loop development for manganese steel at different cycles under biaxial out of phase loading at 1% equivalent strain amplitude (a) axial stress-strain response and (b) shear stress-strain response.

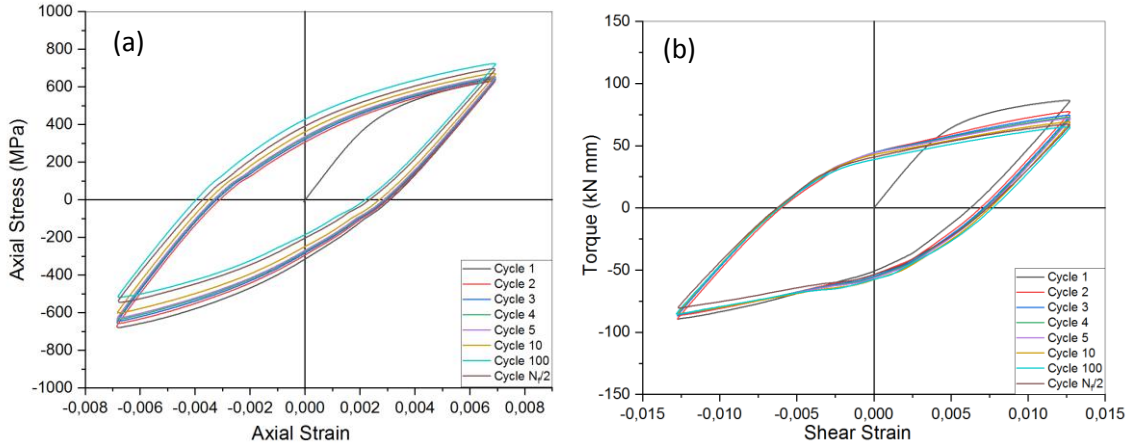

Figure 16: Hysteresis loop development for pearlite steel at different cycles under biaxial in phase loading at 1% equivalent strain amplitude (a) axial stress-strain response and (b) shear stress-strain response.

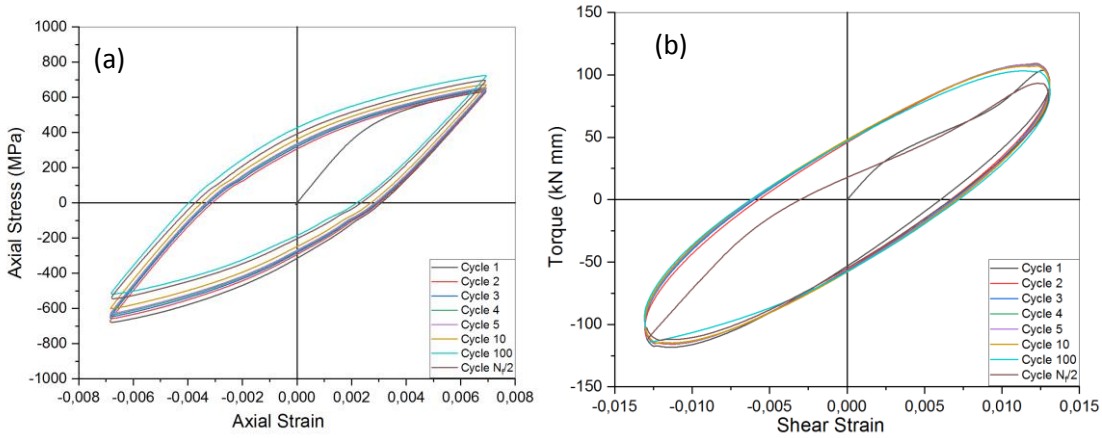

Figure 17: Hysteresis loop development for pearlite steel at different cycles under biaxial out of phase loading at 1% equivalent strain amplitude (a) axial stress-strain response and (b) shear stress-strain response.

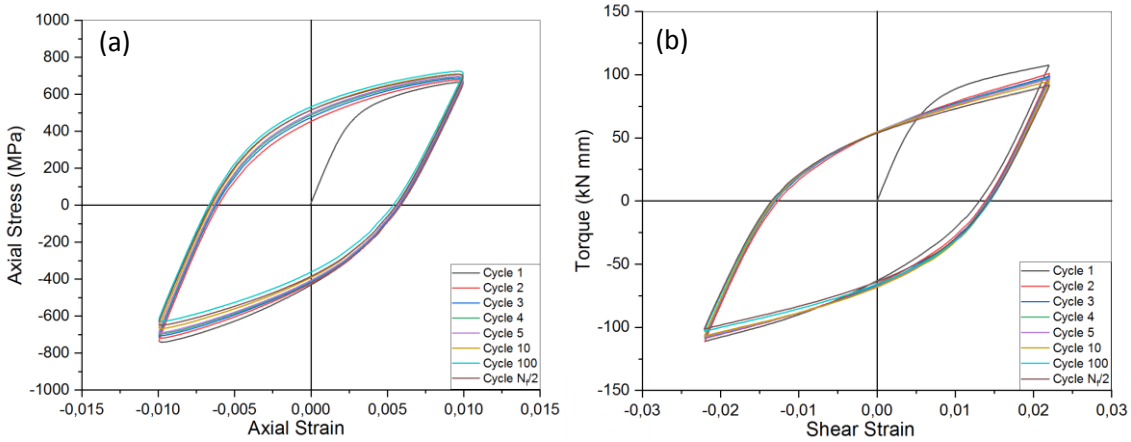

Figure 18: Hysteresis loop development for pearlite steel at different cycles under biaxial in phase loading at 1.5% equivalent strain amplitude (a) axial stress-strain response and (b) shear stress-strain response.

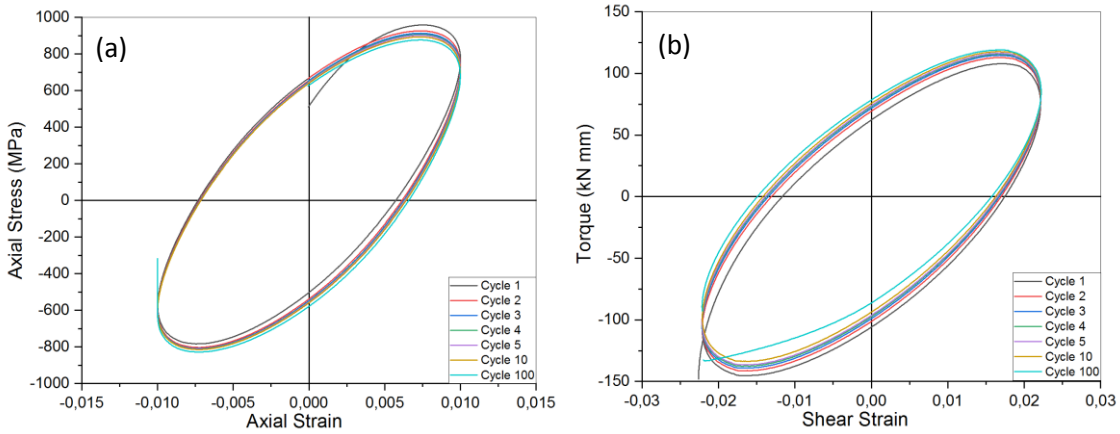

Figure 19: Hysteresis loop development for pearlitic steel at different cycles under biaxial out of phase loading at 1.5% equivalent strain amplitude (a) axial stress-strain response and (b) shear stress-strain response.

The hysteresis loops developed for the two materials at different equivalent strain amplitudes for biaxial loading are shown in Figures 14-19 above. The detailed description of hysteresis loops for 0.6% strain is described in paper 5. Similar to uniaxial loading, in biaxial in phase loading at 1% equivalent strain amplitude for the manganese steel under all conditions initially there is a shift of the tip of the hysteresis loop upwards towards higher stress indicating cyclic hardening, whereas the trend is reversed for pearlitic grade indicating cyclic softening for all cases except biaxial non proportional loading, where hardening can be observed in the first cycle. As discussed in the paper 5 in biaxial proportional loading, the hysteresis loops show a sharp tip at the maximum and minimum strains: however, under biaxial out of phase loading the tips of the hysteresis loop are rounded. Similar to tests done in pure torsion, the exact values of plastic strain energy density could not be calculated due to the use of solid specimens.

A comparative analysis of all the conditions of loading indicates, for manganese steel, there is prominent hardening for all conditions with the maximum hardening being observed in case of biaxial nonproportional loading for both the strain amplitudes with higher hardening and at the higher strain amplitudes. This is due to the combined effect of cyclic hardening and non-proportional hardening. The pearlitic steel exhibited softening for most of the cases except for biaxial loading with initial hardening in first 1-2 cycles. When comparing manganese and pearlitic steel, the pearlite has higher failure cycles under similar conditions of loading and strain amplitude. The softer manganese steel had lower stress or torque amplitudes than pearlitic steel for all conditions except for biaxial nonproportional loading at higher strain amplitudes where it surpasses the pearlitic steel.

2.4 Optical Microscopy:

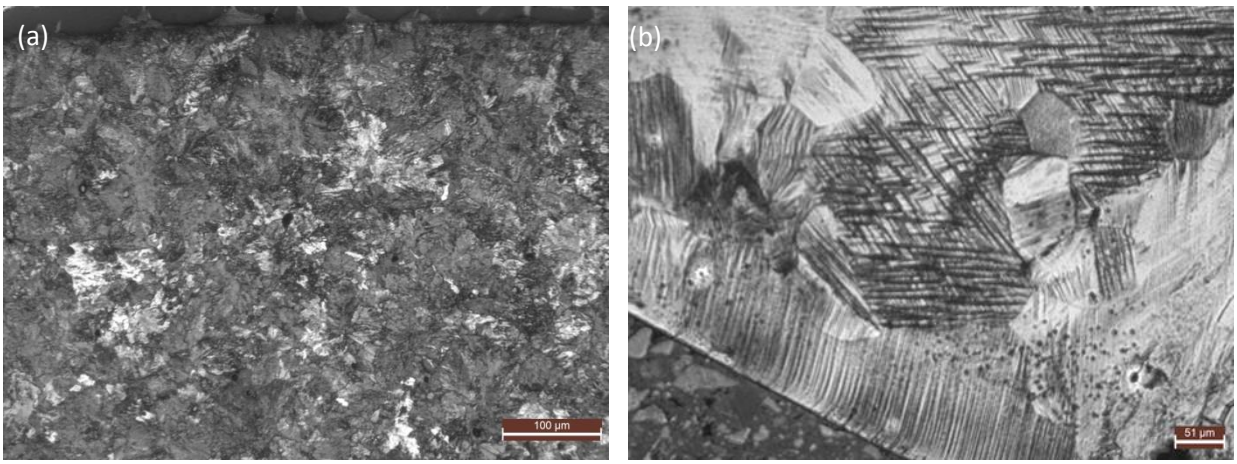

Figure 20: Optical micrographs of fatigue deformed samples for pure torsion at 0.8% strain amplitude for (a) pearlitic and (b) manganese steel.

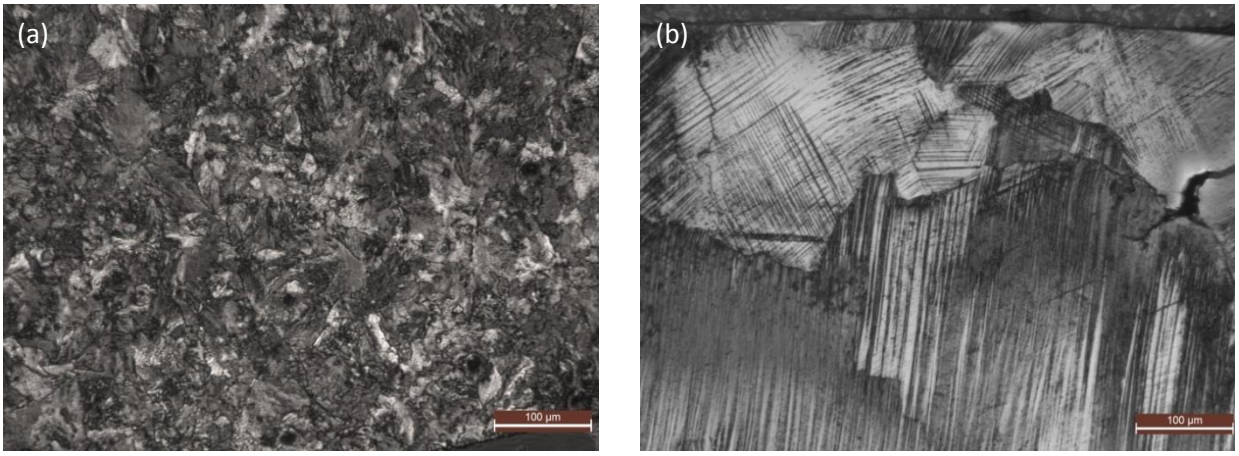

Figure 21: Optical micrographs of fatigue deformed samples for pure torsion at 1.3% strain amplitude for (a) pearlitic and (b) manganese steel.

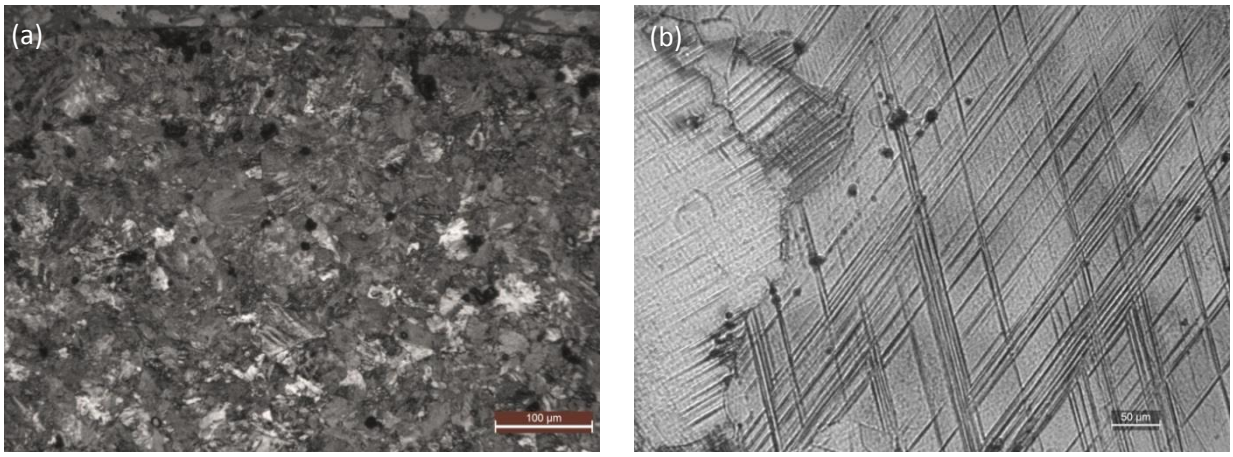

Figure 22: Optical micrographs of fatigue deformed samples for uniaxial loading at 1% strain amplitude for (a) pearlitic and (b) manganese steel.

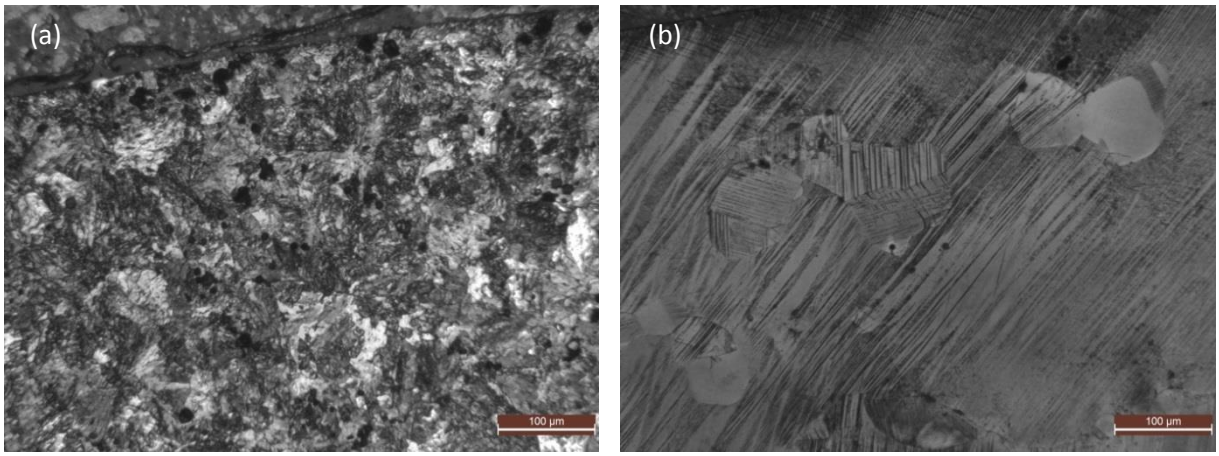

Figure 23: Optical micrographs of fatigue deformed samples for biaxial in-phase loading at 1% strain amplitude for (a) pearlitic and (b) manganese steel.

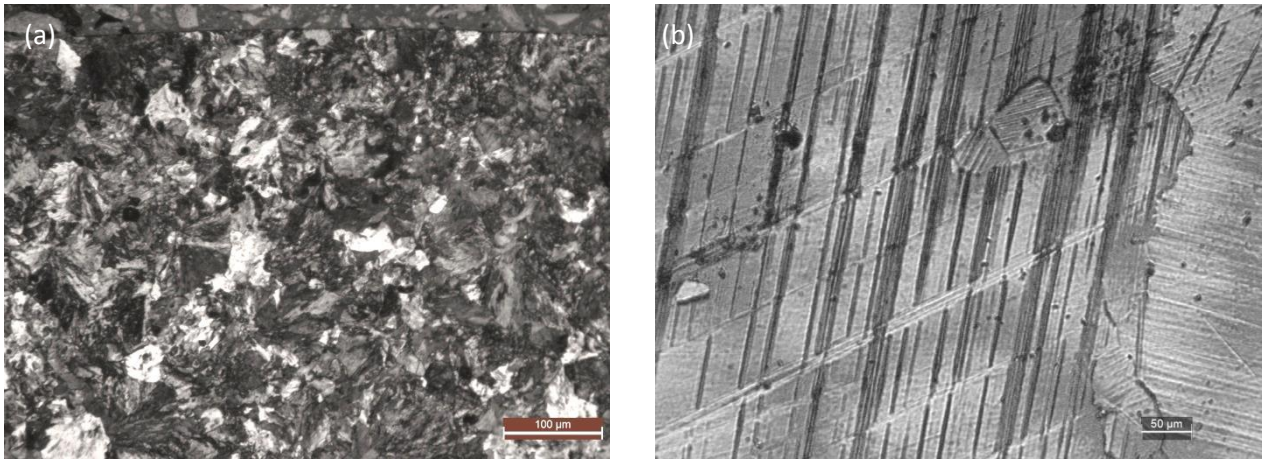

Figure 24: Optical micrographs of fatigue deformed samples for biaxial out of phase loading at 1% strain amplitude for (a) pearlitic and (b) manganese steel.

The optical micrographs of the fatigue deformed steels at 0.6% strain amplitude are discussed in paper 5. The optical micrographs of uniaxial and biaxially deformed fatigue specimens at 1% strain amplitude and pure torsion at 0.8% and 1.3% shear strain amplitude are shown in Figures 20-24. The pearlite microstructure does not show a much observable change in the microstructure under different conditions, similar to what is observed for 0.6% strain. The difference in the mechanical properties is therefore attributed to dislocation density changes in the structure which are not revealed by optical microscopy. The deformed microstructure of the manganese steel consists of banded structure. These bands can be deformation twins or stacking faults or dislocation boundaries which is not evident from the optical micrographs. The density and morphology of these bands differ under the different conditions of loading with increasing density and decreasing spacing of the bands at higher strains. The spacing between the bands is lowest for biaxial nonproportional loading. At higher strains in biaxial loading the bands appear finer, and under when viewed under higher magnification it can be seen they are as clusters of bands together. The bands are in different directions and in some grains, the bands are intersecting each other. This is similar to what is observed at 0.6% strain.

2.5 TEM Microstructure

Intermittent uniaxial fatigue testing at 0.4% strain amplitude with equal tension and compression was performed on the head hardened pearlite steel to study the evolution of damage and correlate it with microstructural changes at different time intervals. The change in mechanical response was analyzed in terms of dislocation density variation in the microstructure.

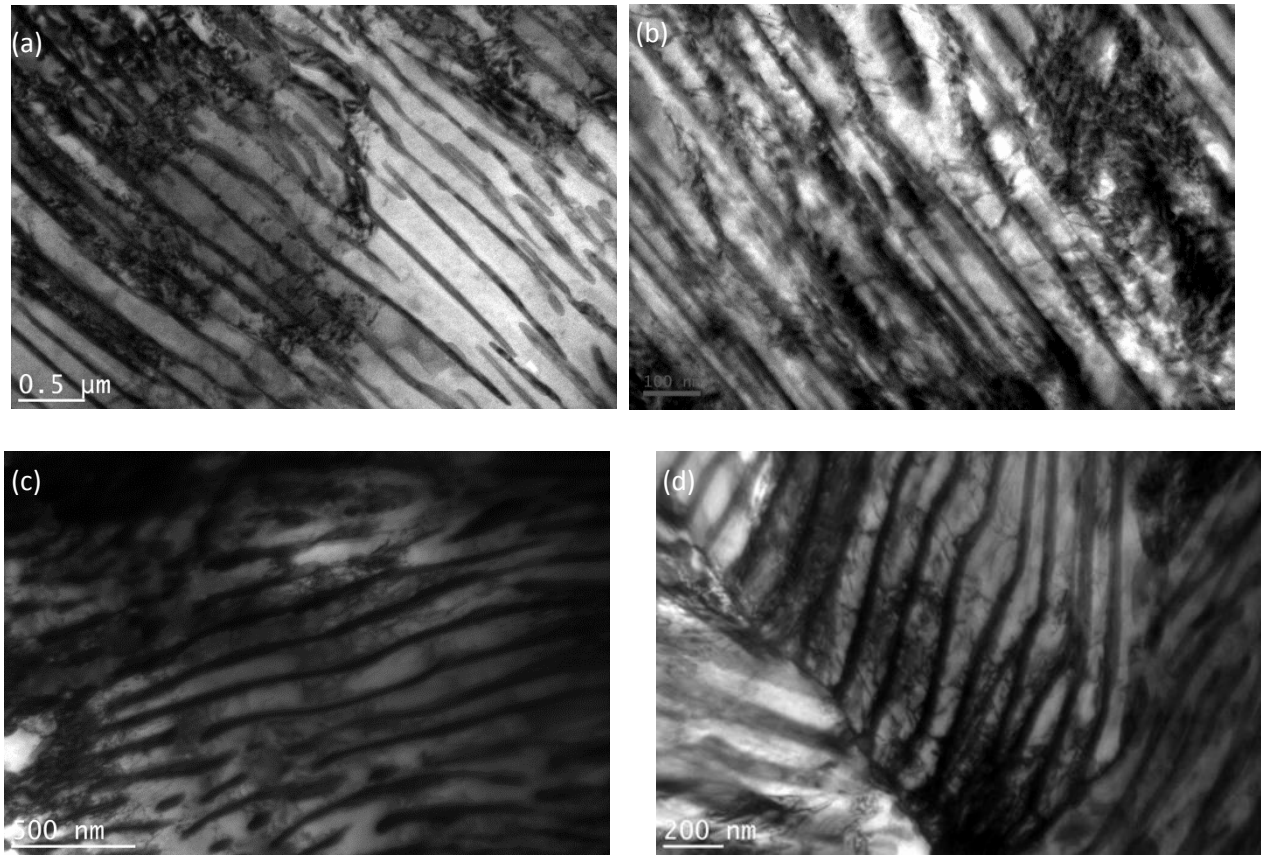

Figure 25: TEM micrographs of fatigue deformed pearlitic steel at 0.4% strain amplitude under uniaxial loading at (a) initial structure (b) 0.25 cycles (c) 100 cycles (d) at failure.

The TEM microstructure of the undeformed pearlitic steel specimen is shown in Figure 25a. The spacing between the ferrite and cementite indicates that it is a medium interlamellar spacing pearlitic structure with few scattered dislocations in the ferrite. The pearlite was given hardening treatment during processing which generated dislocations in the structure. The interface between the ferrite and cementite appears quite distinct and sharp. At 0.25 cycles, an increase in dislocation density in the ferrite channels randomly distributed is observed. The interface is still sharp and clear, free from dislocations. The ferrite and cementite microstructure is intact. No dislocation cells were found at this number of cycle. Dislocation structures with much higher dislocation densities were observed at 100 cycles and in the failed specimens. The dislocation densities are reported in Table 7 below. The significant increase in dislocation density after just one-quarter cycle indicates rapid strain hardening in early cycles. Thereafter, the rate of dislocation generation is slower and may reach saturation. Cell formation was observed after 100 cycles. The restructuring and formation of dislocation cells indicate the cyclic softening behavior in low cycle fatigue of pearlitic steel. After many cycles, dislocations are present within the ferrite channels as well as along the interfaces. Dislocations generally nucleate at ferrite cementite interfaces due to elastic incompatibility stresses between the ferrite and cementite phases and glide in the ferrite lamellae to form dislocation tangles.

Table 7: Dislocation densities observed in fatigue deformed pearlitic steel under uniaxial loading at 0.4% strain amplitude.

Cycles	Dislocation Density
0	5.06E+14
0.25	6.39E+14
100	6.73E+14
17000	7.55E+14

Discussion:

The tensile tests established high work hardening capacity of the manganese steel compared to the pearlitic steel with a strain hardening exponent of 0.4. Pearlite steel is a high strength steel. The work hardening is less (25% of the yield stress value) and saturates quickly (within 4% of the strain value, 3.4% of plastic strain value). It cannot accommodate large plastic deformation. For, high strength steel the deformation is mainly governed by elastic deformation due to higher yield strength, whereas, manganese steel is comparatively low strength steel with high work hardening capacity. The work hardening rate is constant for a large value of plastic strain (17.5% of plastic strain). Although, having a low yield stress value, manganese steel gains strength from work hardening with good ductility property.

Pearlite steel is designed to have a good strength with limited plastic deformation and work hardening confined to the top layers of rail wheel contact. This steel serves to prevent elastic damage like brittle cracking. The cracks will be confined to work harden top surface only. But it has less resistance to plastic strain induced damage. On the other hand, the manganese steel gains moderate strength from high work hardening property without sacrificing much of ductility. Thus, it can accommodate large plastic deformation. Although, manganese steel is less effective for elastic damage it is highly effective for plastic strain induced damage like exhaustion of ductility in low cycle fatigue.

From uniaxial low cycle fatigue test, apparently, it appears that pearlite steel is better choice compared to manganese steel because it can endure higher life cycles. However, laboratory scale fatigue testes were done under strain controlled mode. But, for stress controlled fatigue loading, which is the real life case in service, pearlite steel will suffer larger plastic deformation because the work hardening saturates quickly and will allow plastic deformation without any increase in stress. Moreover, in-service loading will result in mean stress above fluctuating load. This loading condition may result in ratcheting phenomenon. For cyclic softening material like pearlite steel, the ratcheting strain is higher and this may lead to failure due to ratcheting strain. The work hardening of manganese steel is also evident during the fatigue tests where it shows hardening behavior for all the test conditions. The cyclic hardening coefficient of manganese steel is found to be much higher compared to pearlite steel. For manganese steel, due to high work hardening capability, the plastic deformation is restricted for stress controlled fatigue loading. Moreover, due to cyclic hardening property, the ratcheting strain is also restricted.

The mean strain effect in strain controlled LCF test shows mean stress relaxation. For pearlite steel the mean stress relaxed within a few initial cycles and there is negligible effect as compared to LCF response without mean strain. But, for manganese steel mean stress relation occurs over a considerable number of initial cycles and mean strain hardening effect is noticeable.

Regarding fatigue life computation, fatigue ductility coefficient (ε_f) and fatigue ductility exponent (c) are derived from plastic strain life curve based on Coffin Manson equation. The fatigue ductility coefficient shifts the curve parallel to the plastic strain amplitude axis whereas the fatigue ductility exponent 'c' gives the negative slope of the curve of plastic strain amplitude vs number of failure cycles in a log-log plot. Therefore, the fatigue strength deterioration rate with elapsed cycle (damage rate) is governed by fatigue ductility exponent 'c'. In this analysis the fatigue ductility exponent 'c' is coming out as -0.636 and -0.282 for pearlite steel and manganese steel respectively. The higher negative value of fatigue ductility exponent for pearlite steel shows the higher plastic strain induced damage rate for pearlite steel compared to manganese steel.

However, from stress life curve (Basquin equation) the fatigue strength coefficient and fatigue strength exponent 'b' are calculated. The result shows that the fatigue strength exponents 'b' are -0.1385 and – 0.1737 for pearlite steel and manganese steel respectively. The lower negative value of fatigue strength exponent 'b' for pearlite steel shows that elastic stress induced damage rate is less for perlite steel compared to manganese steel.

Regarding, plastic energy absorbing capability, it is observed from the test results that , the deterioration of plastic energy absorbing capacity (exhaustion of ductility) in low cycle fatigue is more for pearlite steel (ω= -0.83) compared to manganese steel (ω= -0.485).

From these observations it can be concluded that if the fatigue process is dominated by elastic deformation, pearlite steel is preferable whereas the manganese steel gives benefit if the fatigue process is dominated by plastic deformation. In fact, the use of high strength steel is to keep the deformation dominated by the elastic strain.

Strain controlled uniaxial low cycle fatigue tests show that the fatigue life is more for pearlite steel compared to manganese steel for the same strain amplitude. Pure torsion LCF tests show that the difference in fatigue life for both the steels are not so prominent for the same strain amplitude. For 0.8% equivalent strain amplitude, the fatigue life of manganese steel is slightly higher compared to pearlite steel. This is due to the fact that for pure shear the deformation is due to the slip activity which is mainly plastic strain dominated. However it is to mention that the fatigue lives of both the steels are considerable higher in pure shear loading compared to uniaxial loading. Pure shear causes delay in crack initiation and thus improves fatigue life. In biaxial fatigue testing for low equivalent strain amplitude (0.6%) pearlite steel shows higher fatigue life for in-phase biaxial loading compared to uniaxial loading. This may be due to the contribution of shear deformation in biaxial loading which enhances the fatigue life compared to pure axial deformation. For manganese steel there is not much change in fatigue lives for uniaxial and biaxial in-phase loading. For out of phase loading for pearlite steel non proportional hardening is 12% whereas for manganese steel it is 37%. Higher non proportional hardening of manganese steel is due to its capability to accommodate large plastic deformation by activating more number of slip systems or other deformation mechanisms.

The difference in mechanical response can be correlated with the microstructure obtained. TEM studies of fatigue deformed pearlitic steel reveal threading dislocations and dislocation tangles which nucleate at the ferrite cementite interface due to strain incompatibility. The different loading causes difference in the dislocation density which affects the fatigue strength and fatigue life. Slip is the only deformation mode for pearlitic steel. The softening behavior of the pearlitic steel can be explained in terms of the hardening treatment during processing which generated dislocation density already in the material. Further straining only increased little dislocation density in the initia1 few cycles and finally, the material gets stabilized causing softening. Cyclic softening takes place through a dynamic recovery process owing to the rearrangement of dislocations into a stable lower energy configuration [6]. At higher strain amplitudes, the stress amplitudes are also sufficiently high and thus the rearrangement occurs earlier in less number of cycles. The softening rate decreased as the strain range was increased.

For manganese steels, a combination of dislocation cells with dislocation cells as well as intersecting straight stacking fault lamellae governs the microstructure. Uniaxial loading is dislocation density dominant but when the shear mode is introduced in the in-phase and out-of-phase biaxial LCF test, formation and growth of stacking faults play an important role together with dislocation nucleation, gliding and dislocation tangle formation. Cyclic hardening is believed to occur due to increase in dislocation density by multiplication and intense interaction among themselves during cyclic straining [6]. FCC materials like manganese steels have lower stacking fault energies (SFE). Lower SFE results in easy dislocation splitting and facilitates increase in stacking fault density. Therefore the excellent hardening in manganese steel is due to both dislocations as well as stacking faults which imparts additional hardening.

Refernces:

[1] R. I. Stephens, A. Fatemi, R. R. Stephens and H. O. Fuchs, Metal fatigue in engineering John Wiley and Sons, 2001.

[2] L. F. Coffin, Transactions of the ASME 76 (1954) 923–950.

[3] O. H. Basquin, The exponential law of endurance tests, American Society of Testing and Material 10 (1910) 625-630.

[4] G. E. Dieter, Mechanical Metallurgy, McGraw-Hill Book Company, 1988.

[5] J. Morrow, Cyclic plastic strain energy and fatigue of metals, Internal Friction, Damping, and Cyclic Plasticity, ASTM International, STP378-EB (1965) 45-87.

[6] P. P. Sarkar, P. S. Deb, S. K. Dhua and P. C. Chakraborti, Strain energy based low cycle fatigue damage analysis in a plain C-Mn rail steel, Materials Science & Engineering A 707 (2017) 125–135.